Henning Trill

Sodalite Solid Solution Systems:

Synthesis, Topotactic Transformations, and Investigation of Framework-Guest and Guest-Guest Interactions

2002

Meinem Vater
zum 65. Geburtstag

Physikalische Chemie

Sodalite Solid Solution Systems:

Synthesis, Topotactic Transformations, and Investigation of Framework-Guest and Guest-Guest Interactions

Inaugural-Dissertation
zur Erlangung des Doktorgrades
der Naturwissenschaften im Fachbereich Chemie und Pharmazie
der Mathematisch-Naturwissenschaftlichen Fakultät
der Westfälischen Wilhelms-Universität Münster

vorgelegt von

Henning Trill

aus Ahaus

- 2002 -

Dekan:	Prof. Dr. V. Leute
Erster Gutachter:	Prof. Dr. H. Eckert
Zweiter Gutachter:	Prof. Dr. R. Pöttgen
Tag der mündlichen Prüfung:	12. 11. 2002
Tag der Promotion:	12. 11. 2002

Table of Contents

1 Introduction

Sodalite is a naturally occurring mineral similar to lazurite or “lapis lazuli”, which has been used as jewelry combined with gold, silver and gemstones by ancient cultures already more than 5000 years ago. Similarities between sodalite and lazurite were already suggested 1890 by Brögger and Böckstrom[1], but it was not until 1930, when the crystal structure was solved by Pauling[2] and later refined by Löns and Schulz.[3]

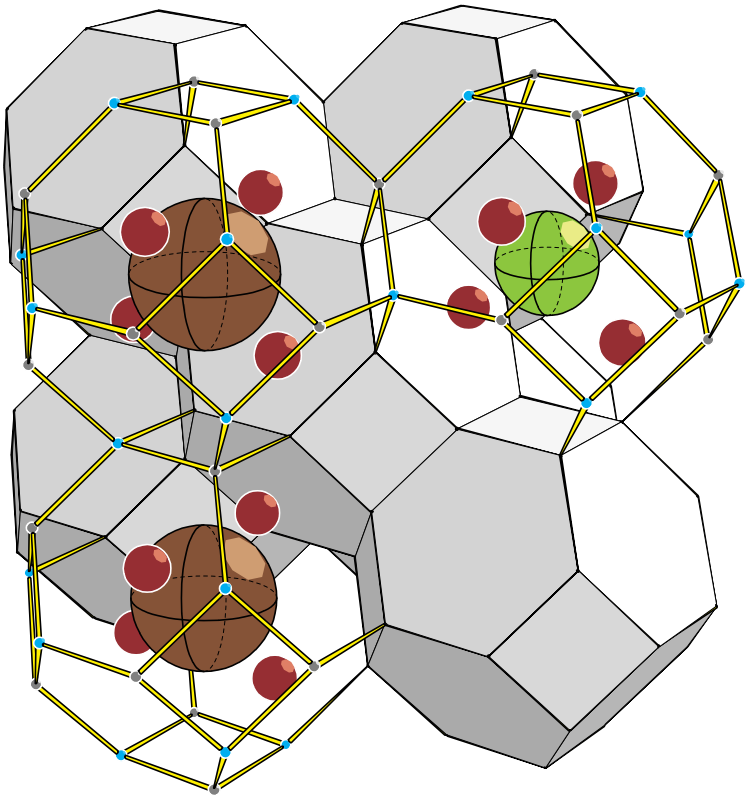

Figure 1-1: *A bcc packing of corner truncated octahedra representing sodalite cages. The sodalite framework is comprised of regularly alternating AlO_4 and SiO_4 tetrahedra with Al and Si residing at the corners of the truncated octahedra. Depicted here is a salt-bearing sodalite solid solution with mixed halide occupancy. The extra-framework species sodium (small, plain), chlorine (large, light, crossed) and bromine (large, dark, crossed) are shown in the open cages. Oxygen atoms each linking two T-sites are not printed to increase the clarity.*

As portrayed in Figure 1-1, the sodalite mineral is an alumosilicate and its structure can be viewed as a space filling bcc lattice built from truncated octahedra (or β-cages), where aluminum and silicon reside on the 24 vertices in alternating order linked via oxygen atoms. The sodalite framework is flexible and can expand to accommodate various extra-framework species, which is accomplished by cooperative changes in the Al-O-Si bond angles. The compositional formula of the framework is given by $[Al_6Si_6O_{24}]^{6-}$ and comprises two cages. Even though only three monovalent cations per sodalite cage are required for charge compensation of the negatively charged framework, an excess mineral salt unit, NaX, is typically incorporated during the synthesis. Inside the cages of such *salt-bearing* sodalites one finds a central anion surrounded tetrahedrally by four sodium cations. The naturally occurring sodalite hosts a sodium chloride unit, which is just one example of a vast variety of

monovalent salts that have been successfully incorporated into the sodalite lattice.[4] S*alt-bearing* sodalites are classified as feldspatoides[5] and are different from sodalites with no excess salt molecule present, which were recently dubbed *salt-free* sodalites.[6]

Such salt-free sodalites can be obtained from hydroxo ("basic") sodalites, containing an $H_3O_2^-$ anion at the center. While synthetic OH^- containing sodalites synthesized under hydrothermal conditions were reported already in 1967 by Bukin & Makarov,[7] much confusion existed about the actual hydroxide and water content, until Hassan[8] found the *basic* sodalite to have the composition $Na_8[Al_6Si_6O_{24}](OH)_2*2H_2O$ and refined the extra framework oxygen positions. In 1992 Wiebke et. al[9] finally refined the hydrogen positions and identified the extra framework species as a hydrogen dihydroxide $(H_3O_2)^-$. It then had been known for a long time that the anion with its corresponding sodium cation can be exchanged for water molecules. The crystal structure of the resulting *hydro* sodalite $Na_6[Al_6Si_6O_{24}]\cdot 8H_2O$ was first reported by Felsche et al.[10] Within the same paper these authors also reported the high temperature crystal structure of anhydrous hydro sodalite (or *dry* sodalite), which they had previously found upon dehydration of hydro-sodalite.[11] While the confusion about a variety of hydroxide and water containing sodalite phases was removed by Engelhardt,[12] the room temperature structure of dry sodalite was only solved recently.[13,14] It was found to be a tetragonal distorted superstructure of the regular sodalite structure with lattice constants of about $\sqrt{2}a \times \sqrt{2}a \times a$, where *a* is the cell edge of common cubic sodalite. Salt-free sodalites are thus much closer to zeolites than to feldspatoides.[15]

Upon application of γ-radiation, F-centers can be created in annealed salt bearing sodalites, which has already led to applications for data storage in the 1970s.[16] An alternate route to creation of F-centers by exposure of annealed sodalite to sodium vapor was invented by Barrer.[17] Such F-centers were successfully identified by EPR as Na_4^{3+} centers through their characteristic 13 line spectrum.[18] The extra electron is delocalized over the volume of the sodalite cage and absorbs light in the visible region. The color of F-center containing sodalites turns from purple to black with increasing number of such centers. Thus pure salt-free sodalites completely "doped" with sodium were dubbed "*black sodalites*" or "*sodium electro sodalites*" (SES) and were first reported in 1996 by Engelhardt et al.[19], who also showed ^{27}Al and ^{29}Si MAS NMR spectra of this material. An antiferromagnetic coupling at 48K was discovered by Srdanov,[20] who first managed to produce SES free of paramagnetic impurities. Due to the fact that sodalites contain only one type of alkali metal clusters, which are ordered

in a strict bcc manner, black sodalite has attracted a lot of interest by theoretical chemists, since it can serve as a model substance for the investigation of the properties of metal nano-clusters, as well as their interaction.[21-24]

So far, the transition from isolated F-centers to ordered F-center lattices has not been explored, but promises interesting magnetic behavior due to a distribution of antiferromagnetically coupled spins.[25] The creation of disordered F-center lattices requires solid solution materials as precursors. The key characteristic of a solid solution X_uY_{1-u} ($0 \leq u \leq 1$) is the random distribution of its constituents *X* and *Y*. For cubic lattices and under solid solution conditions, such as sodalites or many metals, the cell edge, a_o, is expected to obey Vegard's rule: $a_o = u \cdot a_o(X) + (1-u) \cdot a_o(Y)$. This rule is used as a convenient tool for determining the actual stoichiometry of the solid solution, while the deviations from it may indicate an onset of phase separation. Sodalites form an unusual type of solid solution consisting of spatially separated molecular species inside the central cages whose interactions are mediated by the aluminosilicate framework. Since direct interaction between the molecular units is weak, such mixed sodalites differ from classical solid solutions. Sodalite solid solutions were first reported by Barrer[26] who investigated the kinetics of the salt entrainment of sodalites. Unfortunately, the results were compromised by the fact that the possible combinations of extra framework species within the sodalite cage were overestimated at that time. Another approach to sodalite solid solutions was undertaken by Weller, who prepared mixed halide sodalites by solid state routes, followed by crystallographic analysis[27] In 1992 Sieger showed that mixed sodalites with similar extra-framework species obey Vegard's rule,[28] but may deviate from it when these species differ substantially from each other in size. Thus, using the same procedure as Barrer[17] for transforming basic sodalite into *salt-free* hydro sodalite, and then into dry sodalite, $Na_6[Al_6Si_6O_{24}]$, one can transform mixed Br/basic into Br/hydro and Br/dry sodalites without altering the bromine content.[29]

Solid solution systems are likely to show properties that are not present in any of the pure phases. An excellent way to study such systems on a microscopic scale is nuclear magnetic resonance (NMR), since this method gives an insight into the local structure of these materials, while commonly used techniques such as x-ray diffraction and UV- spectroscopy give only averaged information over the bulk or the surface of such phases. Fortunately each of the interesting elements with the exception of oxygen occurring in halide sodalites (these are ^{1}H, ^{23}Na, ^{27}Al, ^{29}Si, ^{35}Cl, ^{81}Br and ^{127}I) possess a sufficiently abundant nuclear isotope applicable for NMR studies. In this connection, it is interesting to note that in sodalites all the NMR active nuclei are separated by oxygen, which weakens direct interaction of the nuclear

spins via dipole coupling and thus allows the observation of single particle signals. However, with the exception of ^{1}H and ^{29}Si, these nuclei have quadrupole moments, which in general cause specific linebroadening effects, preventing easy analysis of the spectra. It has only been in recent years that high magnetic fields, high spinning speeds and sophisticated techniques, such as Double Rotation (DOR)[30,31], Dynamic Angle Spinning (DAS)[32] and Multiple Quantum Magic-Angle-Spinning (MQ-MAS)[33] have been developed, producing well resolved NMR spectra of such quadrupolar nuclei in the solid state. Due to these advances quadrupolar nuclei now offer a wider variety of information than spin ½ nuclei, since their spectra also contain information about the symmetry of their local electronic environment.

The intent of this study is to gain synthetic control of sodalite solid solution systems with the ultimate goal of creating lattices with randomly distributed F-centers and to investigate their interactions among each other as well as with the host lattice. To this end, a comprehensive study on the preparation and characterization of sodalite solid solution systems has been carried out and NMR has been applied along the way from the mixed hydroxy/halide sodalite through the step of water exchange, dehydration and metal doping.

Chapters 2 and 3 summarize the theoretical background on the techniques applied, including the current state of the literature on their specific applications to sodalite systems. Chapter 4 reports the synthetic procedures and all the experimental specifications of the characterization studies. In Chapter 5 I will develop a model of the growth of solid solutions, with Chapter 6 devoted to the synthetic aspects of extra framework species exchange. Chapter 7 gives a comprehensive overview of the capabilities of NMR to investigate such solid solution systems and fundamental relations between lattice and NMR parameters are presented. This knowledge is applied in Chapter 8 to understand the effects of topotactic transformation on the local and bulk structure of sodalite solid solution systems. Chapter 9 analyses delocalized electrons without a central attractor (Na_4^{3+}-centers or F-centers) captured inside sodalite cages and randomly distributed throughout the crystallites in concentration ranges between 10 % and 90 % cage occupancy. While the interactions between the F-centers and the framework are studied by NMR, the interactions between the electrons themselves resulting in magnetic coupling are also reflected in the NMR spectra and are further studied by magnetic susceptibility measurements. Finally Chapter 10 summarizes the results of this thesis from a broader perspective and outlines further possible research directions.

2 Theory

2.1 Nuclear Magnetic Resonance

2.1.1 Semi-classical Description

The Nuclear Spin in a Static Magnetic Field

All nuclei, except those with even numbers of protons and neutrons do have angular momentum *J*, resulting in a magnetic moment μ by:

$$\vec{\mu} = \gamma \cdot \vec{J} \qquad \text{Equ. 2-1}$$

where γ is the gyromagnetic ratio, characteristic for each nucleus.

$$\vec{\mu} = g_n \mu_n \vec{J} \qquad \text{Equ. 2-2}$$

The latter is given by the nuclear g-value g_n and the nuclear magneton $\mu_n = e/(2m_pc)$, where *e* is the unit charge, m_p is the proton mass and *c* is the vacuum speed of light. If an external magnetic field B_0 is applied (let B_0 be parallel with the z-axis), the component of the angular momentum parallel to B_0 is quantized, as will be elaborated in more detail below. Only discrete values are allowed:

$$\left|\overrightarrow{J_z}\right| = \hbar \cdot m \qquad \text{Equ. 2-3}$$

where *m* is an integer number with $-I \geq m \geq -I$ (I is the spin quantum number that is given for any nucleus). In general, the energy of a nucleus in the state *m* interacting with the magnetic field is given by:

$$E = -\vec{\mu} \cdot \vec{B} = -\gamma \cdot \hbar \cdot m \cdot B_z \qquad \text{Equ. 2-4}$$

Thus, the magnetic field removes the degeneracy of the nuclear orientational states. This effect can be exploited for spectroscopy if the nuclei absorb photons in order to switch between these states. According to the selection rules, for interactions between nuclei and photons to the first order only nuclear transitions with $\Delta m = \pm 1$ are allowed if the photon is to be absorbed. Thus the energy of the photon is given by:

$$\Delta E(m \rightarrow m+1) = \gamma \cdot \hbar \cdot B_z = \hbar \cdot \omega_L \qquad \text{Equ. 2-5}$$

where ω_L is the Larmor frequency.

The macroscopic magnetization M_z parallel to the external field B_0 results from the summation of the microscopic magnetic moments, whose population distribution is given by the Boltzmann law:

$$\frac{N_-}{N_+} = \exp\left[\frac{-\gamma\hbar B_0}{kT}\right] \cong 1 - \frac{\gamma\hbar B_0}{kT} \qquad \text{Equ. 2-6}$$

where $N_\pm$ are the numbers of spins parallel and antiparallel to the magnetic field (B_0)-direction. For sufficiently high temperatures (above 2K) the macroscopic magnetization is given by:

$$M_z = \frac{N}{V}\frac{\gamma^2\hbar^2 J(J+1)}{3kT} B_0 \qquad \text{Equ. 2-7}$$

Interaction of Spins with External Radiofrequency Fields

A magnetic moment not aligned with an external magnetic field B_0 is subject to a torque $\vec{T} = \vec{\mu} \times \vec{B}_0$, that rotates the momentum about the direction of the external field:

$$\frac{d\vec{M}}{dt} = \sum_i \frac{d\vec{\mu}_i}{dt} = \gamma \cdot \sum_i \frac{d\vec{J}_i}{dt} = \gamma \cdot \sum_i \left(\vec{\mu} \times \vec{B}_0\right) = \gamma \cdot \left(\vec{M} \times \vec{B}_0\right) \qquad \text{Equ. 2-8}$$

This is also true for the magnetization of an assembly of *i* magnetic moments. Since B_0 is oriented along the z-axis, the result is a set of first order differential equations:

$$\begin{aligned} \frac{dM_x}{dt} &= \gamma \cdot B_0 \cdot M_y \\ \frac{dM_y}{dt} &= -\gamma \cdot B_0 \cdot M_x \\ \frac{dM_z}{dt} &= 0 \end{aligned} \qquad \text{with the solutions:} \qquad \begin{aligned} M_x &= m_0 \cdot \cos(\omega_L \cdot t) \\ M_y &= -m_0 \cdot \sin(\omega_L \cdot t) \\ M_z &= const. \end{aligned} \qquad \text{Equ. 2-9}$$

where $m_0 = (\vec{M} \times \vec{B_0}) / B_0$ and $\omega_L = -\gamma \cdot B_0$ is the Larmor frequency. While an isolated magnetic moment could theoretically spin forever (or at least for a very long time) the macroscopic magnetization returns to its equilibrium value by spin-lattice relaxation, while loosing its amplitude in the xy-plane independently also by spin-spin relaxation. The latter process describes the exchange of spin states for neighboring nuclei, causing a loss of phase coherence and therefore reducing the number of spins in phase with the macroscopic magnetization. Spin-lattice relaxation occurs, when a spin aligns its magnetic moment with the external field (increasing its orientational quantum number m). These spin flips occur through a transfer of the excess energy to the lattice in the form of phonons. Both relaxation processes are described by the Bloch equations:

$$\begin{aligned}\frac{dM_x}{dt} &= \gamma \cdot B_0 \cdot M_y - \frac{1}{T_2^*} M_x \\ \frac{dM_y}{dt} &= -\gamma \cdot B_0 \cdot M_x - \frac{1}{T_2^*} M_y \\ \frac{dM_z}{dt} &= -\frac{1}{T_1}(M_0 - M_z)\end{aligned} \qquad \text{Equ. 2-10}$$

$1/T_1$ is the spin-lattice relaxation rate and $1/T_2^* = 1/T_2 + 1/T_2'$ is the observed transverse relaxation rate. The latter is composed of $1/T_2$ which is due to spin exchange and $1/T_2'$, which is caused by local field inhomogenities. Transformed into a rotating frame reference system, spinning around B_0 with the angular frequency of the applied rf field ω_0, the Bloch equations have the form:

$$\begin{aligned}\frac{dM_{x'}}{dt} &= -\frac{1}{T_2^*} M_{x'} \\ \frac{dM_{y'}}{dt} &= -\frac{1}{T_2^*} M_{y'} \\ \frac{dM_{z'}}{dt} &= -\frac{1}{T_1}(M_{z'} - M_0)\end{aligned} \quad \text{with} \quad \begin{aligned}M_{x'} &= M_{x'0} \cdot e^{-t/T_2^*} \\ M_{y'} &= M_{y'0} \cdot e^{-t/T_2^*} \\ M_{z'} &= \left(M_{z'0} - M_0\right) \cdot e^{-t/T_1} + M_0\end{aligned} \qquad \text{Equ. 2-11}$$

as their solutions.

Dynamics in a Time-dependent Magnetic Field

In order to tilt the macroscopic magnetization *M* out of its equilibrium state aligned with the external magnetic field, it is necessary to apply a second magnetic field B_1 (or B_{rf}) which is always perpendicular to B_0 and *M* and which precesses around B_0 with the angular frequency ω_0. This can be achieved by a linearly polarized electromagnetic wave oscillating with ω_0. The latter consists of two circular polarized magnetic fields, one spinning with ω_0 and one with $-\omega_0$.

$$\begin{aligned}\overrightarrow{B_x} &= 2\overrightarrow{B_1}\cos(\omega_0 \cdot t) \\ \overrightarrow{B_R} &= B_1(\overrightarrow{e_x}\cos\omega_0 t + \overrightarrow{e_y}\sin\omega_0 t) \\ \overrightarrow{B_L} &= B_1(\overrightarrow{e_x}\cos\omega_0 t - \overrightarrow{e_y}\sin\omega_0 t) \\ \overrightarrow{B_1}(t) &= B_1(\overrightarrow{e_x}\cos\omega_0 t + \overrightarrow{e_y}\sin\omega_0 t)\end{aligned} \qquad \text{Equ. 2-12}$$

Now the Bloch equations are given by:

$$\frac{d\overrightarrow{M}}{dt} = \gamma \cdot \overrightarrow{M} \times (\overrightarrow{B_0} + \overrightarrow{B_1}(t)) \qquad \text{Equ. 2-13}$$

or in the rotating frame:

$$\left(\frac{d\vec{M}}{dt}\right)_{rot} = \gamma \cdot \vec{M} \times (\vec{B_0} + \vec{B_1}(t)) - \vec{\omega}_0 \times \vec{M}$$

$$\Leftrightarrow \quad \left(\frac{d\vec{M}}{dt}\right)_{rot} = \vec{M} \times \left\{(\omega_0 + \gamma \cdot B_0) \cdot \vec{e_{z'}} + \gamma \cdot B_1 \cdot \vec{e_{x'}}\right\} \qquad \text{Equ. 2-14}$$

$$\Leftrightarrow \quad \left(\frac{d\vec{M}}{dt}\right)_{rot} = \gamma \cdot \vec{M} \times \vec{B}_{eff}$$

$$\text{with} \quad B_{eff} = \left(B_0 - \frac{\omega_L}{\gamma}\right) \cdot \vec{e_{z'}} + B_1 \cdot \vec{e_{x'}}$$

This is essentially the same equation as Equation 2-8. Within the rotating frame the magnetization therefore precesses around B_{eff} with an angular frequency (ω_L -ω_0) . In case ω_0 is chosen to be ω_L, the Larmor frequency, B_{eff} is parallel to $e_{x'}$ and the magnetization is rotated in the y´z-plane.

The B_1 field can now be applied for a certain time in order to rotate the magnetization from the z-direction into the xy-plane. This process is called a 90° pulse. A measure for the amplitude of B_1 is the nutation frequency, which is given by the number of 360° rotations of the magnetization in the y´z-plane per second. The nutation angle α is then given by:

$$\alpha = \gamma B_1 t \qquad \text{Equ. 2-15}$$

In general the same coil that induced the B_1 field is used to detect the oscillating magnetization within the NMR probe, resulting in a nuclear induction signal (free induction decay or FID) having the general form

$$g(t) = \sum_i M_{0i} \cdot \cos(\omega_i - \omega_0) \exp\left\{\frac{-t}{T_{2i}^*}\right\} \qquad \text{Equ. 2-16}$$

where i denotes all of the nuclei of the isotope species under investigation. The signal is then processed by a Fast Fourier Transformation in order to extract the frequency information, which is usually displayed in the form of a frequency spectrum:

$$S(\omega) = \int_{-\infty}^{+\infty} g(t) \exp\{-i\omega t\} dt \qquad \text{Equ. 2-17}$$

2.1.2 Quantum Mechanical Description

Angular Momentum

Most NMR experiments cannot be described classically. Therefore, instead of vectors, dimensionless operators and observables are used:

$$\hat{\mu} = \gamma \cdot \hat{J} \qquad \text{and} \qquad \hat{J} = \hbar \cdot \hat{I} \qquad \text{Equ. 2-18}$$

where the angular momentum operator is given by:

$$\hat{J} = \vec{r} \times \frac{\hbar}{i} \frac{\partial}{\partial \vec{r}} \qquad \text{Equ. 2-19}$$

If the system is described by an eigenket $|\hat{I},m\rangle$ of $\hat{I}^2$ and $\hat{I}_z$, the corresponding eigenvalues are given by:

$$\hat{I}^2 |I,m\rangle = I(I+1)|I,m\rangle \qquad \text{Equ. 2-20}$$

$$\hat{I}_z |I,m\rangle = m|I,m\rangle \qquad \text{Equ. 2-21}$$

$\hat{I}_x$ and $\hat{I}_y$ can be combined into ladder operators,

$$\hat{I}^+ = \hat{I}_x + i\hat{I}_y$$

$$\hat{I}^- = \hat{I}_x - i\hat{I}_y \qquad \text{Equ. 2-22}$$

which link the eigenstates $|I,m\rangle$ and $|I,m\pm1\rangle$

$$\hat{I}^+ |I,m\rangle = \sqrt{I(I+1) - m(m+1)} \cdot |I,m+1\rangle$$

$$\hat{I}^- |I,m\rangle = \sqrt{I(I+1) - m(m-1)} \cdot |I,m-1\rangle \qquad \text{Equ. 2-23}$$

One might keep in mind, that $\hat{I}^+$ and $\hat{I}^-$ are adjunct, but not Hermitian, while $\hat{I}_x$, $\hat{I}_y$, $\hat{I}_z$ and $\hat{I}^2$ are Hermitian with real eigenvalues. The ladder operators describe the transitions from one nuclear eigenstate to another, as they occur in NMR experiments. For example, a spin 3/2 quadrupolar nucleus has a probability ratio of 3 : 4 : 3 for the $|3/2\rangle \leftrightarrow |1/2\rangle$, the $|1/2\rangle \leftrightarrow |-1/2\rangle$ and the $|-1/2\rangle \leftrightarrow |-3/2\rangle$ transitions, respectively.

In the most general form, nuclear magnetic states can be written as linear combinations of Zeeman eigenstates:

$$|\Psi\rangle = \sum_m c_m |I,m\rangle \qquad \text{Equ. 2-24}$$

The same relation is true for an ensemble of nuclear spins, as it is typical for an NMR experiment, where the ensemble consists of about 10^{21} spins. In this case each state is multiplied with the probability operator w_i and $\Sigma\, w_i = 1$.

Spin Density Formalism:

In quantum-mechanics, a physical measurement on a system is represented by an operator $\left(\hat{H}\right)$ acting on a wavefunction ($|\Psi\rangle$). In NMR we are again dealing with an ensemble of spins and the average expectation value is given by:

$$\left[\left\langle \hat{H} \right\rangle\right] = \sum_i w_i \left\langle \Psi_i \middle| \hat{H} \middle| \Psi_i \right\rangle \qquad \text{Equ. 2-25}$$

Now the density operator is defined as:

$$\hat{\rho} = \sum_i w_i \left| \Psi_i \right\rangle \left\langle \Psi_i \right| \qquad \text{Equ. 2-26}$$

to yield the mean expectation value simply as the trace of the product of density operator and "experiment" operator:

$$\left|\left\langle \hat{H} \right\rangle\right| = tr\left\{\hat{\rho}\hat{H}\right\} \qquad \text{Equ. 2-27}$$

Time Dependence

In the Schrödinger picture, the time dependence of a wavefunction is introduced by a time evolution operator $U(t_0,t)$ such that:

$$\left|\Psi, t_0; t\right\rangle = \hat{U}(t_0, t) \left|\Psi, t_0\right\rangle \qquad \text{Equ. 2-28}$$

In NMR the time evolution is given by the Hamiltonian operator $\hat{H}$.

$$\hat{U}(t_0, t_0 + dt) = 1 - i\frac{\hat{H}}{\hbar} dt \qquad \text{Equ. 2-29}$$

leading to the famous SCHRÖDINGER Equation:

$$\boxed{i\hbar \frac{d}{dt} \left|\Psi, t_0; t\right\rangle = \hat{H} \left|\Psi, t_0; t\right\rangle} \qquad \text{Equ. 2-30}$$

If the Schrödinger equation is applied to an ensemble of spins given by the density matrix discussed above it can be shown that the time development of the density matrix is given by the LIOUVILLE- VON NEUMANN equation:

$$\boxed{i\hbar \frac{d\hat{\rho}}{dt} = -\left[\hat{\rho}, \hat{H}\right]} \qquad \text{Equ. 2-31}$$

where the commutator is defined by: $\left[\hat{\rho}, \hat{H}\right] = \hat{\rho}\hat{H} - \hat{H}\hat{\rho}$ Equ. 2-32

In the most general form, $\hat{H}$ is a linear combination of several operators describing each interaction of the nucleus with external and internal fields in its environment.

$$\hat{H}_{total} = \hat{H}_Z + \hat{H}_{rf} + \hat{H}_{CS} + \hat{H}_{HF} + \hat{H}_D + \hat{H}_Q + \hat{H}_{relax} \qquad \text{Equ. 2-33}$$

Here $\hat{H}_Z$ is the Hamiltonian of the Zeeman interaction, $\hat{H}_{rf}$ describes the interaction between the spin system and the radiofrequency field, $\hat{H}_{CS}$ is the Hamiltonian for the chemical shielding interaction, $\hat{H}_{HF}$ describes the hyperfine shift arising from unpaired electron density, $\hat{H}_D$ represents the dipolar interaction, the quadrupolar interaction is given by $\hat{H}_Q$ and finally the relaxation of the spin system is described by $\hat{H}_{relax}$.

2.1.3 Zeeman Interaction

Interaction with Static External Fields

The Hamiltonian for the Zeeman interaction is given by:

$$\hat{H}_Z = -\gamma\hbar B_0 \hat{I}_Z \qquad \text{Equ. 2-34}$$

Its eigenvalue is E = -μB_0. The time development operator can be derived by insertion of $\hat{H}_z$ into the Schrödinger equation, yielding:

$$\hat{U}(t_0 = 0, t) = e^{i\omega_L \hat{I}_z t} \qquad \text{Equ. 2-35}$$

It then can be shown that, with proper starting conditions, the expectation values of $\langle \hat{I}_x \rangle$ and $\langle \hat{I}_y \rangle$ are $h/4\pi\cos(\omega_L t)$ and $h/4\pi\sin(\omega_L t)$, respectively. Therefore the spins are oscillating in the xy-plane with the Larmor frequency. This result is consistent with the semi-classical description.

Interactions with Time Dependent External Fields

The Hamiltonian $\hat{H}_{rf}$ in the rotating reference frame is time independent and describes the interaction of the spin system with the magnetic field B_1, arising from the applied radio-frequency field (rf pulse).

$$\hat{H}_{rf} = -\gamma\hbar \vec{B}_1 \hat{I}_x \qquad \text{Equ. 2-36}$$

where $\hat{I}_x$ is the component of the angular momentum along the x-axis in the rotating frame. The Zeeman and the rf Hamiltonians have by far the largest contributions to the total Hamiltonian. The other interactions are therefore treated by first and second order perturbation theory.

2.1.4 Internal Interactions

The Chemical Shielding Interaction

The chemical shielding Hamiltonian is an extension of the Zeeman Hamiltonian due to the induced magnetic field.

$$\hat{H}_{CS} = \hbar\gamma_N \hat{I}\overleftrightarrow{\sigma}\vec{B}_0 \qquad \text{Equ. 2-37}$$

Here the gyromagnetic ratio is labeled γ_N to be not confused with one of the Euler angles introduced below. At the site of the nucleus under investigation, the magnetic field consists of the external magnetic field and an induced magnetic field, which is caused by the interaction between the external field and the local electronic environment. The induced field is not necessarily aligned with the external field and therefore conveniently described by a second rank tensor $\overleftrightarrow{\sigma}$ acting on the external field.

$$\vec{B}_{eff} = (1-\overleftrightarrow{\sigma})\vec{B}_0 \qquad \text{Equ. 2-38}$$

The shielding tensor $\overleftrightarrow{\sigma}$ is composed of a diamagnetic shielding contribution, due to electron circulation in closed shells, and a paramagnetic de-shielding contribution, which arises from the orbital angular momentum of higher electronic states mixed into the ground state under the influence of the magnetic field. While the diamagnetic contribution due to the core electron, is rather constant for different chemical environments of the atom, the paramagnetic contribution is sensitive to changes of valence electron distributions caused by chemical bonding, making the chemical shift a valuable tool for structure determination. Since $\overleftrightarrow{\sigma}$ is Hermitian, it can be diagonalized by rotation into the principal axis coordinate system (PAS)

$$T^{-1}\begin{pmatrix}\sigma_{xx} & \sigma_{xy} & \sigma_{xz}\\ \sigma_{xy} & \sigma_{yy} & \sigma_{yz}\\ \sigma_{xz} & \sigma_{yz} & \sigma_{zz}\end{pmatrix}T = \begin{pmatrix}\sigma_{11} & 0 & 0\\ 0 & \sigma_{22} & 0\\ 0 & 0 & \sigma_{33}\end{pmatrix} \qquad \text{Equ. 2-39}$$

where by definition $|\sigma_{33} - \sigma_{iso}| \geq |\sigma_{11} - \sigma_{iso}| \geq |\sigma_{22} - \sigma_{iso}|$. By full expansion of the product of the tensor and B_0 the orientational dependence of the precession frequency, or chemical shift anisotropy (CSA), is written as:

$$\omega_0 = \gamma_N B_0\left(1-\sigma_{11}\sin^2\beta\cos^2\gamma + \sigma_{22}\sin^2\beta\sin^2\gamma + \sigma_{33}\cos^2\beta\right) \qquad \text{Equ. 2-40}$$

where β and γ are the Euler angles relating the principal axis system to the laboratory coordinate system. The isotropic shielding is given as:

$$\sigma_{iso} = \tfrac{1}{3}\left(\sigma_{11} + \sigma_{22} + \sigma_{33}\right) \qquad \text{Equ. 2-41}$$

If the chemical shielding tensor has axial symmetry, the expression simplifies as follows:

$$\omega_0 = \gamma_N B_0\left(1-\sigma_{iso} + \tfrac{1}{3}\left(\sigma_{\perp} - \sigma_{\parallel}\right)\left(3\cos^2\beta - 1\right)\right) \qquad \text{Equ. 2-42}$$

where $\sigma_{\perp} = \sigma_{11} = \sigma_{22}$ and $\sigma_{\parallel} = \sigma_{33}$ are the shielding components parallel and perpendicular to the symmetry axis in the PAS. In case of spherical symmetry all three tensor components are the same. Also in liquids, due to rapid molecular motion, the shielding tensor is averaged to its trace value σ_{iso}. In a powder sample, there is a statistical distribution of all possible orientations, thus the resulting line shape is a superposition of precession frequencies for all angles, multiplied with their respective probabilities. Examples are given in Figure 2-1:

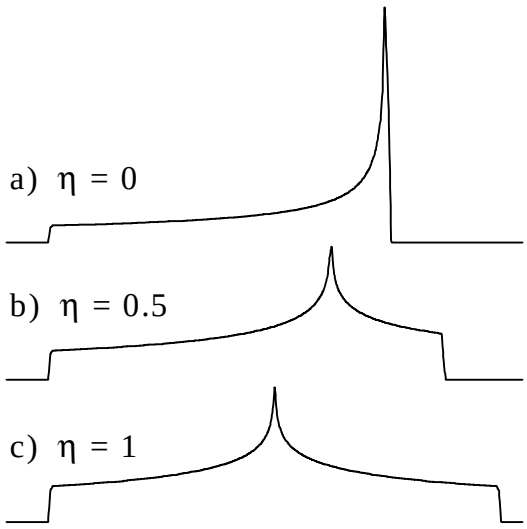

Figure 2-1: *Example of NMR spectra displaying chemical shielding anisotropy (CSA). In this figure the frequency increases from right to left. All the spectra have the same isotropic chemical shielding.* ***a)*** $\eta = 0$, ω_{33} *is at high frequency edge (left side of the spectrum) and* $\omega_{22} = \omega_{11}$ *at the low frequency edge of the spectrum.* ***b)*** $\eta = 0.5$. ω_{33} *is at the high frequency edge,* ω_{11} *at the low frequency edge and* ω_{22} *at the peak position.* ***c)*** $\eta = 1$. ω_{33} *is at the high frequency edge,* ω_{11} *at the low frequency edge and* ω_{22} *at the peak position.*

Since the shielding effect is linearly dependent on the magnitude of the external field, the *chemical shift* can be defined as the relative deviation from a reference precession frequency. In many cases, this reference is a 1 molar aqueous solution of hydrated ions.

$$\delta = \frac{\omega_{sample} - \omega_{ref}}{\omega_{ref}} \qquad \text{Equ. 2-43}$$

Dipolar Coupling

The dipolar coupling interaction describes the interaction of nuclear spins through space. Its Hamiltonian has a strong distance dependence and is given by:

$$\hat{H}_D = \frac{\mu_0}{4\pi}\gamma_i\gamma_k\hbar \cdot \hat{I}^i D_{ik} \hat{I}^k \qquad \text{Equ. 2-44}$$

where i and k are the indices for the two nuclei and D_{ik} is the dipolar coupling tensor:

$$\left(D_{ik}\right)_{\alpha\beta} = \frac{3(e_\alpha r_{ik})(e_\beta r_{ik}) - e_\alpha e_\beta}{r_{ik}^3} \qquad \text{Equ. 2-45}$$

e_α and e_β are unity vectors in Cartesian coordinates and r_{ik} is the distance between the two nuclei. After transformation into the laboratory reference frame, for nuclei of the same species, the Hamiltonian can be written as:

$$\hat{H}_D = -\frac{\mu_0}{4\pi} \cdot \frac{\gamma^2 \hbar}{2r_{ik}^3} \left(3\cos^2 \beta - 1\right)\left\{3\hat{I}_z^i \hat{I}_z^k - \hat{I}^i \hat{I}^k\right\} \qquad \text{Equ. 2-46}$$

Analogously the heteronuclear dipolar coupling Hamiltonian is given by:

$$\hat{H}_D = -\frac{\mu_0}{4\pi} \cdot \frac{\gamma_I \gamma_S \hbar}{2r_{IS}^3} \left(3\cos^2 \beta - 1\right)\hat{I}_z \hat{S}_z \qquad \text{Equ. 2-47}$$

where $\hat{I}$ and $\hat{S}$ are the nuclear spin operators of the two nuclei.

Hyperfine Coupling

The hyperfine coupling in NMR describes the interaction between an unpaired electron spin and the nuclear spin. As long as both spins are far apart from each other the interaction can be described as a dipolar interaction, as is the case for electrons in pure p or d orbitals. For unpaired electrons with s-state character, however, this approximation is no longer valid and the resulting Hamiltonian is given by:[34]

$$\hat{H}_{HF} = \frac{8\pi}{3}\gamma_S \gamma_I \hbar^2 \hat{I}\hat{S}\delta\left(\vec{r}\right) + \frac{\gamma_S \gamma_I}{r^3}\left[3\frac{\left(\hat{I}\cdot\vec{r}\right)\left(\hat{S}\cdot\vec{r}\right)}{r^2}\right] \qquad \text{Equ. 2-48}$$

Here the first term represents the Fermi-contact interaction by the Dirac δ function, which is only non-zero at the site of the nucleus. The second term is due to the dipolar coupling between the electron and nuclear spins. $\hat{I}$ and $\hat{S}$ denote the nuclear and electron spin and r gives the distance between these two. Rapid spin flips of the paramagnetic electron average contributions of the second term to zero on the NMR timescale. The resulting interaction energy solely depends on the electron density at the site of the nucleus and the magnetic moments of the two spins.

$$E_{HF} = \frac{8\pi}{3}\overrightarrow{\mu_S}\overrightarrow{\mu_I}\left|\Psi(0)\right|^2 \qquad \text{Equ. 2-49}$$

Applying the high temperature approximation for the magnetic moment of a paramagnetic electron by Bloembergen[35] combined with Curie´s law for the magnetic susceptibility of interacting electrons, the hyperfine shift (in ppm) of the nuclear resonance is given by:[36]

$$\Delta\delta = -A_N \frac{\gamma_S}{\gamma_I} hS(S+1)\frac{10^6}{3k(T-\theta_W)} \qquad \text{Equ. 2-50}$$

where $A_N = \frac{8\pi}{3h} g_e \mu_B g_N \mu_N \left|\Psi(0)\right|^2$ is the hyperfine coupling constant in Hz as known from EPR, $\gamma_S = g_e\mu_B\hbar$, $\gamma_I = g_N\mu_N\hbar$ and θ_W is the Weiss temperature. Due to the finite size of the

nucleus, $|\Psi(0)|^2$ will vary over its expansion, which is the cause for hyperfine anomalies, for example resulting in slightly different coupling constants for isotopes of the same atom. Although the electron density at the nucleus is available through Equation 2-50, additional shielding by closed shells and de-shielding by excited electronic states occur. Thus direct conclusions about the electron density around the atom are not possible on the basis of the shift measurement alone.

The contact term of the hyperfine coupling is similar and sometimes confused with the Knight shift, which was first observed by Knight[37] as the shift of copper in metal compared to diamagnetic copper compounds. While the hyperfine shift is due to a time average of electron density of the unpaired electron at the nucleus, the Knight shift is due to a spatial average of all conduction electrons at the Fermi level mixing with the atomic s-orbitals. Thus the Knight shift is temperature independent due to temperature independence of the metallic susceptibility, while the hyperfine shift varies according to Curie´s law.[38]

Quadrupolar Coupling

Nuclei with spin quantum numbers I > ½ are characterized by an asymmetric charge distribution described by a nuclear electric quadrupole moment, which will interact with electric field gradients. The Hamiltonian describing this interaction is given by:

$$\hat{H}_Q = \frac{eQ}{2I(2I-1)\hbar}\hat{I}\overleftrightarrow{V}\hat{I} \qquad \text{Equ. 2-51}$$

where eQ is the nuclear electric quadrupole moment and $\overleftrightarrow{V}$ is a second rank tensor giving the second derivative of the electric potential Φ:

$$(V)_{\alpha\beta} = \frac{\partial^2\Phi}{\partial r_\alpha \partial r_\beta} \qquad \text{with } \alpha,\beta = x;y;z \qquad \text{Equ. 2-52}$$

$\overleftrightarrow{V}$, like $\overleftrightarrow{\sigma}$, can be diagonalized by transformation into the principal axis system (PAS) with the remaining components $V_{zz} > V_{xx} > V_{yy}$. Commonly the largest component is called the electric field gradient eq = V_{zz}. Since further $\Sigma V_{ii} = 0$ (Laplace Equation), all the components can be comprised into the asymmetry parameter $\eta = (V_{xx} - V_{yy})/ V_{zz}$. The quadrupolar coupling constant is then defined as:

$$C_Q = \frac{e^2qQ}{\hbar} \qquad \text{Equ. 2-53}$$

If the quadrupolar interaction is weak compared to the Zeeman interaction, it can be treated with first order perturbation theory. In this case the Hamiltonian can be expressed in the laboratory reference frame as follows:

$$\hat{H}_{Q1} = \frac{C_Q}{8I(2I-1)}\left(3\cos^2\beta - 1 + \eta\sin^2\beta\cos(2\gamma)\right)\left\{3\hat{I}_z^2 - \hat{I}(\hat{I}+1)\right\} \quad \text{Equ. 2-54}$$

where β and γ are the Euler angles relating the principal axis system to the laboratory coordinate system. Its eigenvalues simply add to the Zeeman eigenvalues:

$$E_{Q1} = \frac{C_Q}{8I(2I-1)}\left(3\cos^2\beta - 1 + \eta\sin^2\beta\cos(2\gamma)\right)\left\{3m^2 - I(I+1)\right\} \quad \text{Equ. 2-55}$$

Since to first order, the energy arising from the quadrupolar interaction is a function of m^2 rather than m, the energy of the central transition ($\left|\tfrac{1}{2}\right\rangle \leftrightarrow \left|-\tfrac{1}{2}\right\rangle$) is not altered.

For strong quadrupolar coupling (about $C_Q \geq 1$ MHz), the perturbation treatment has to be extended to second order. The perturbation is no longer field independent and also affects the central transition lineshape. The Hamiltonian which describes the second order effects given by:

$$\hat{H}_{Q2} \propto \frac{1}{\omega_L}\frac{e^2qQ}{4I(2I-1)}\sum_{k=0}^{2}\sum_{n=k}^{-k} A^{2k}(\hat{I},m)B_{2n}^{2k}(\eta)D_{2n,0}^{2k}(\beta,\gamma) \quad \text{Equ. 2-56}$$

where:

$A^0 = I(I+1) - 3m^2$ $\quad A^2 = 8I(I+1) - 12m^2 - 3$ $\quad A^4 = 18I(I+1) - 34m^2 - 5$

$B^0{}_0 = -(3+\eta^2)/5$ $\quad B^2{}_0 = (\eta^2-3)/14$ $\quad B^2{}_{\pm2} = \eta\,(3/14)^{1/2}$

$B^4{}_0 = (18+\eta^2)/140$ $\quad B^4{}_{\pm2} = 3\eta(5/140)^{1/2}$ $\quad B^4{}_{\pm4} = \eta^2(3/2240)^{1/2}$

$D^{2k}{}_{2n,0}(\beta,\gamma)$ are the Wigner matrices in which again β and γ are the Euler angles which describe the quadrupolar PAS with respect to the laboratory reference frame. The second order quadrupolar effects cause an increase in linewidth and a distinct, asymmetry parameter dependent, line shape.

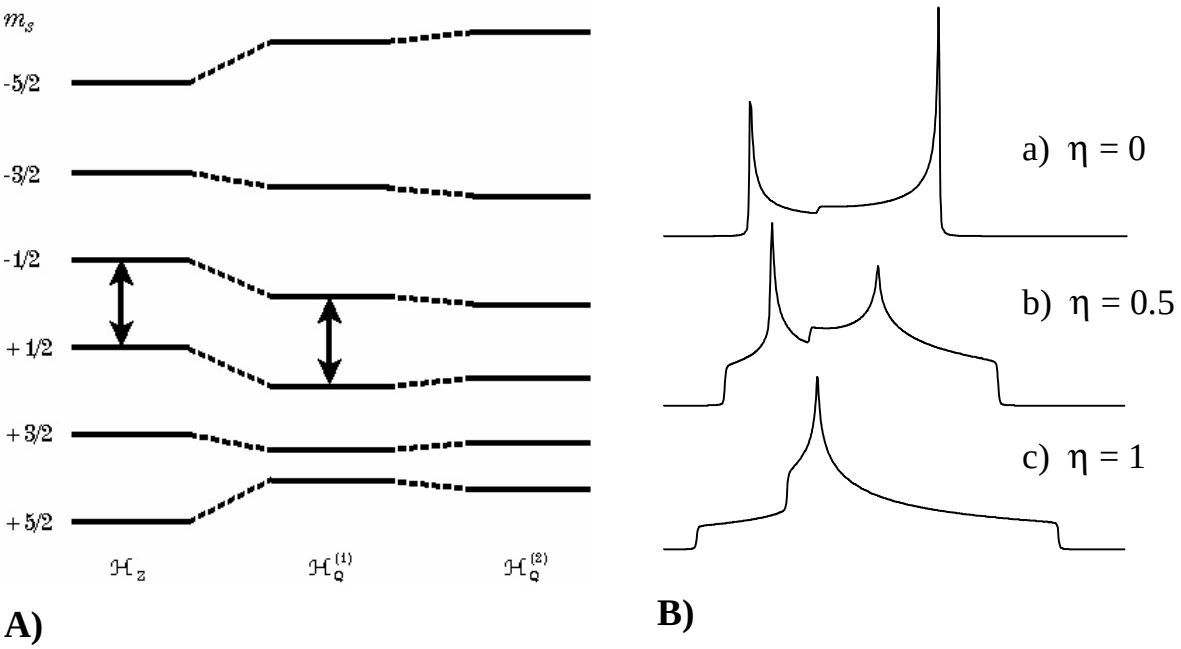

***Figure 2–2**: **A)** Change of nuclear Zeeman states upon first and second order quadrupolar perturbation of an I = 5/2 spin system. The first order quadrupolar interaction does not alter the central transition. **B)** Static quadrupolar lineshapes due to second order quadrupolar broadening. All lineshapes correspond to the same chemical shift and quadrupolar coupling constant. The values of* η *are given in the figure.*

2.1.5 Modern Experimental Methods

Single Pulse Time-domain NMR

The most basic NMR experiment is the one pulse experiment, in which an RF pulse is applied to the spin system as discussed above. The pulse sequence is shown in Figure 2-2, where the duration *t* of the pulse is $t = \alpha/\gamma_N B_1$, and the flip angle is $\alpha = \pi/2$. Consequently such a pulse is called a 90° pulse. After application of the pulse, the oscillating magnetization can be detected in the xy-plane, where it disappears with the relaxation rate $1/T_2^*$. A common problem in NMR experiments is the noise, which can be countered by the accumulation of FIDs (signal averaging). From statistics, it is known, that the error of an n-count is $(n)^{½}$. If the relaxation rate is sufficiently large, several thousand FIDs can be acquired within a few minutes. This is especially true for quadrupolar nuclei, where energetic exchange between the nuclei and the vibrational modes of the lattice is facilitated by quadrupolar coupling. This mechanism is generally by a factor 10 to 100 more efficient than dipolar coupling, leading to T_1 values of less than one second in many systems.

For acquisition of quantitative spectra with several resonances, all nuclei have to be excited similarly, which can be achieved by application of short pulses $\{t < \pi/(4(I + ½))\}$. In addition the intensities of the MAS centerbands (most conveniently used for quantification purposes)

depend on the quadrupolar coupling constant itself, the magnetic field strength and the spinning speed. A method to correct for these influences has been developed by Massiot et. al.[39]

Magic Angle Spinning (MAS)

Static NMR suffers from poor resolution due to extensive line broadening caused by chemical shift anisotropy as well as dipolar and quadrupolar interactions. The Hamiltonians of the latter interactions all show an angular dependent term ($3\cos^2\beta$-1). Broadening caused by these terms can artificially be averaged out by ra idly s innin the sa le at an an le = between the external field and the spinning axis. Such a rotation introduces a time dependence of the a iltonian he tensor describin the interaction of interest is now not directly transformed from the principal axis system (PAS) to the laboratory axes system (LAS), but via the spinner axis system (SAS).

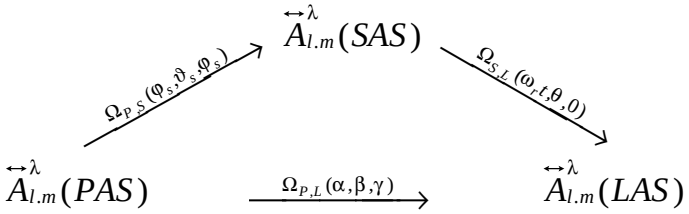

The transformation can be described by a Wigner rotation matrix:

$$\overleftrightarrow{A}^{\lambda}_{l.m}(LAS)=\sum_{m'} D^{l}_{m',m}\left(\Omega_{P,L}\right)A^{\lambda}_{l.m'}(PAS)=\sum_{m''} D^{l}_{m'',m}\left(\Omega_{S,L}\right)\sum_{m'} D^{l}_{m',m}\left(\Omega_{P,S}\right)A^{\lambda}_{l.m'}(PAS) \quad \text{Equ. 2-57}$$

The Hamiltonian can then be computed by ignoring terms with l = 1 and is then given by:

$$\hat{H}^{LAS}_{\lambda}=C_{\lambda}X^{\lambda}_{0,0}\left\{A^{\lambda}_{0,0}+X^{\lambda}_{2,0}\left[A^{\lambda}_{2,-2}(LAS)+A^{\lambda}_{2,0}(LAS)+A^{\lambda}_{2,2}(LAS)\right]\right\} \quad \text{Equ. 2-58}$$

where C_λ is an interaction dependent constant and $X^{\lambda}_{l,m}$ are components of a 3x3 matrix $\hat{X}_{\lambda}$ comprising spin components or components of spin and magnetic field. Explicit computation of the Hamiltonian results in:

$$\hat{H}^{LAS}_{\lambda}=\hat{H}^{iso}_{\lambda}+\hat{H}^{aniso}_{\lambda}+\hat{H}_{\lambda}(t) \quad \text{Equ. 2-59}$$

where $\hat{H}^{iso}_{\lambda}=C_{\lambda}X^{\lambda}_{0,0}A^{\lambda}_{0,0}$ is not angular dependent and therefore isotropic, $\hat{H}^{aniso}_{\lambda}=X^{\lambda}_{2,0}\sqrt{3/2}\delta_{\lambda}\frac{1}{2}\left(3\cos^2\theta-1\right)\left\{\frac{1}{2}\left(3\cos^2\beta-1\right)+\frac{\eta_{\lambda}}{2}\sin^2\beta\cos 2\gamma\right\}$ contains angular

dependent terms and $\hat{H}_\lambda(t) = C_\lambda \sqrt{3/2}\delta_\lambda X^\lambda_{2,0}\{C_1 \cos\omega_r t + S_1 \sin\omega_r t + C_2 \cos 2\omega_r t + C_2 \sin 2\omega_r t\}$ is the time and angular dependent fraction of the total Hamiltonian. C_i and S_i are time-independent constants,[40] β and γ are Euler angles. Spinning at the magic angle θ = 54.7° nulles the anisotropic term. The time dependent term $\hat{H}_\lambda(t)$ changes periodically with the spinner rotation. Its average value over one rotor period ($2\pi/\omega_r$) can be determined applying the Average Hamiltonian Theory,[41] according to which the Hamiltonian can be developed as follows:

$$\hat{H}_\lambda = \sum_{n=0}^{\infty} \hat{H}_{\lambda,n} \qquad \text{Equ. 2-60}$$

$$\hat{H}_{\lambda,0} = \frac{1}{t_r}\int_0^{t_r} \hat{H}_\lambda(t')dt' \,,\; \hat{H}_{\lambda,1} = \frac{1}{2it_r}\int_0^{t_r}\int_0^{t'} \left[\hat{H}_\lambda(t''),\hat{H}_\lambda(t')\right]dt'dt'', \ldots..$$

where t_r is the rotor period $\omega_r/2\pi$. The $(n+1)^{th}$ element can thereby be approximated by: $\hat{H}_{\lambda,n+1} \approx t_r \Delta\nu \hat{H}_{\lambda,n}$ where ν is the spectral width of the static spectrum.

For $t_r\ \nu << 1$ the first element of the sum is a sufficient approximation of the average time dependent Hamiltonian. In this case, the integral over $\hat{H}_\lambda(t)$ equals zero and the spectrum consists only of one sharp resonance. If $t_r\ \nu > 1$ it is necessary to take elements of higher order into account. As a result the time vanishes, where $t = nt_r$ holds. After Fourier transformation, the spectrum not only consists of the central line, but also of a set of sidebands that are separated by $1/t_r$. In the slow spinning limit the envelope of the sideband amplitudes resemble the static lineshape.

2.1.6 MAS of Quadrupolar Nuclei

Under MAS conditions the first order quadrupolar line broadening is removed, however, the second order effects are not averaged to zero, causing characteristic powder patterns of the central transition. The resulting lineshapes are portrayed in Figure 2-3. The position of the center of gravity is changed by the quadrupolar shift δ_{QS} from the position of the chemical shift, discussed above:

$$\delta_{CG} = \delta_{CS} + \delta_{QS} \qquad \text{Equ. 2-61}$$

For the central transition, the quadrupolar shift is given by:

$$\delta_{QS}(m) = -D_{\mathrm{Im}} \frac{P_Q^2}{\nu_0^2} \,, \qquad D_{\mathrm{Im}} = \frac{3}{40}\frac{I(I+1) - 9m(m-1) - 3}{I^2(2I-1)^2} \qquad \text{Equ. 2-62}$$

where ν_0 is the resonance frequency and $P_Q = C_Q\left(1+\frac{\eta^2}{3}\right)^{1/2}$ is the quadrupolar interaction parameter (or second order quadrupolar effect parameter (SOQE)), comprising the quadrupolar coupling constant and the asymmetry parameter. It is worthy to note that, since η can only adopt values between 0 and 1, if η is unknown, P_Q overestimates C_Q always by less than 13% and is therefore in itself a good measure for the quadrupolar interaction strength. Table 2-I gives the resulting *I* and *m* dependent values of D_I.

I	m	D_{Im}/ppm
1.5	-0.5	-50000
1.5	0.5	25000
1.5	1.5	-50000
2.5	2.5	-21000
2.5	1.5	-750
2.5	0.5	6000
2.5	-0.5	-750
2.5	-1.5	-21000

Table 2-I:

D_{Im} values as a function of I and m.

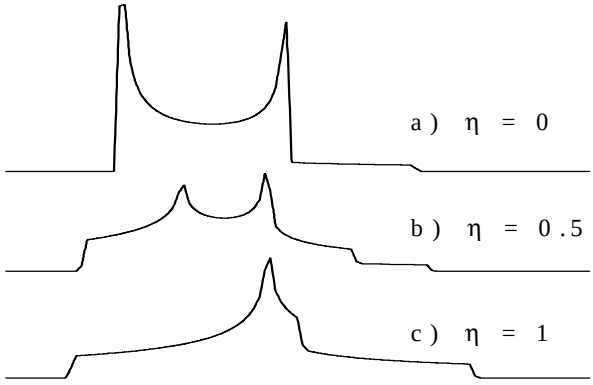

Figure 2–3: *MAS lineshapes due to second order quadrupolar broadened powder patterns. All lineshapes correspond to the same chemical shift and quadrupolar coupling constant. The values of* η *are given in the figure.*

If different magnetic fields are available, the dependence of the quadrupolar shift δ_{QS} on the precession frequencies allows extraction of the second order quadrupolar effect parameter from the resonance shifts δ_{CG} (center of gravity) at high (H) and low (L) field experiments:

$$P_Q^2 = \frac{1}{D_I}\frac{\delta_{CG}^H - \delta_{CG}^L}{\frac{1}{(\nu_0^L)^2} - \frac{1}{(\nu_0^H)^2}} \qquad \text{Equ. 2-63}$$

where $\nu_0 = \omega_0/2\pi$. The chemical shift then follows from Equation 2-61 and 2-62. For rather small P_Q values (< 500 kHz), this method is strongly affected by the frequency resolution and has proven impractical. A solution to this problem is SATRAS (see below).

Satellite Transition Spectroscopy (SATRAS)

Observation of the spinning sidebands associated with the non-central Zeeman transitions ("*satellite transitions*") can be a valuable tool in accurate determination of quadrupolar coupling parameters up to C_Q = 1 MHz. While the central transition usually shows only few sidebands, the satellite transitions generally show a large manifold of sidebands over a wide

spectral range. In order to evenly excite the satellite transitions, short high power pulses (t ~ 0.5 μs) are necessary. Also a probe with a rather low quality factor is essential in order to detect resonances as far as 500 kHz from the central transition.

As shown in Equation 2-62, the quadrupolar shift is different for the central (CT) and the satellite transitions (ST). Therefore the second order quadrupolar coupling parameter can be determined from comparison of the spinning sidebands of the satellite transition manifold and the central transition.

$$P_Q = \left\{ \nu_L^2 \frac{\delta_{CG}(CT) - \delta_{CG}(ST)}{D_{\mathrm{Im}} - D_{\mathrm{Im=0.5}}} \right\}^{1/2}, \qquad \text{Equ. 2-64a}$$

$$\delta_{iso} = \delta_{CG}(CT) - \frac{\delta_{CG}(CT) - \delta_{CG}(ST)}{D_{\mathrm{Im}} - D_{\mathrm{Im=0.5}}} \qquad \text{Equ. 2-64b}$$

Here δ_{CG} are the respective centers of gravity of the CT and two corresponding ST spinning sidebands, and the D_{Im} are the constants from Table 2-I.

The envelope function also allows a guess of P_Q. While for I = 3/2 the overall frequency range over which sidebands are observed corresponds to the value of C_Q, for nuclei with I = 5/2 the difference between the outermost sidebands is about 2 C_Q. A simulation of the sideband pattern, as shown by Jakobsen,[42] also allows extraction of η.

Multiple Quantum (MQ) MAS NMR

The determination of quadrupolar coupling parameters by regular MAS NMR becomes more difficult if multiple lineshapes overlap. Early techniques invented to conquer that problem are double rotation (DOR)[30] and dynamic angle spinning (DAS)[32] NMR. These techniques are capable of the removal of second order quadrupolar linebroadening and therefore allow better resolution of quadrupolar lineshapes. Their disadvantage lies, however, in the challenging experimental difficulties, since they require special probes and sophisticated spinning techniques. Frydman and Harwood[33] developed a two dimensional NMR technique in which one dimension is free of quadrupolar broadening. Multiple Quantum (MQ) MAS NMR takes advantage of the fact that the angular dependent terms in the resonance frequency expansion of the central transition of quadrupolar nuclei have quantum coherence order (p) dependent pre-factors.

$$\omega_p = -p\omega_{CS} + \frac{\omega_Q^2}{\omega_L}\left[A_0 C_0^I(p) + A_2(\beta,\gamma) C_2^I(p) P_2(\cos\theta) + A_4(\beta,\gamma) C_4^I(p) P_4(\cos\theta)\right] \qquad \text{Equ. 2-65}$$

where $\omega_Q = \frac{3e^2qQ}{2I(2I-1)\hbar}$ is the quadrupolar frequency, $A_2(\beta,\gamma)$ and $A_4(\beta,\gamma)$ are orientation dependent functions, responsible for residual broadening, θ is the angle between the external field and the spinning axis, $P_2(\cos\theta) = \frac{1}{2}(3\cos^2\theta - 1)$ and $P_4(\cos\theta) = \frac{1}{8}(35\cos^4\theta - 30\cos^2\theta + 3)$ are the second and fourth order Legendre Polynomials, $C_0^I(p) = -p\left[I(I+1) - \frac{3}{4}p^2\right]$ and $C_4^I(p) = -p\left[18I(I+1) - \frac{34}{4}p^2 - 5\right]$ are the pre-factors and p is the quantum coherence order, defined as the difference between the magnetic quantum numbers of two Zeeman Eigenstates. In the spin density matrix, this is equivalent with the difference between column and row number of the matrix element. Under MAS conditions Equation 2-65 simplifies to:

$$\omega_p = -p\omega_{CS} + \frac{\omega_Q^2}{\omega_L}\left[A_0 C_0^I(p) + A_4(\beta,\gamma)C_4^I(p)P_4(\cos\theta)\right] \qquad \text{Equ. 2-66}$$

The idea of the experiment is to let the spin density matrix evolve for times t_1 and t_2 for different coherences. This can be achieved by a two pulse spin echo experiment whose quantum coherence pathway is plotted in Figure 2-4.

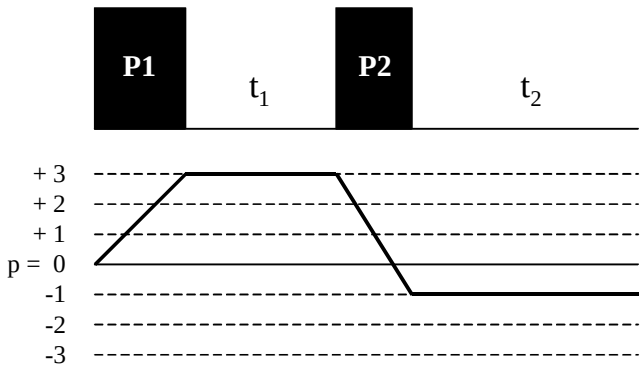

***Figure 2-4**: Two pulse MQ MAS NMR pulse sequence. The first hard pulse transfers magnetization to all elements of the density matrix, while the last one refocuses them. The coherence pathway is selected by phase cycling, which selects the shown path, while other coherences are cancelled out over one cycle.*

The signal is given as:

$$S(t_1,t_2) = S_{p,-1}(0)\exp\{-i\omega_p t_1\}\exp\{-i\omega_{-1}t_2\} \qquad \text{Equ. 2-67}$$

$$S(t_1,t_2) = S_{p,-1}(0)\exp\left\{-i\left\{-p\omega_{CS} + \frac{\omega_Q^2}{\omega_L}\left[A_0 C_0^I(p) + A_4(\beta,\gamma)C_4^I(p)P_4(\cos\theta)\right]\right\}t_1\right\}$$

$$\cdot \exp\left\{-i\left\{\omega_{CS}+\frac{\omega_Q^2}{\omega_L}\left[A_0C_0^I(-1)+A_4(\beta,\gamma)C_4^I(-1)P_4(\cos\theta)\right]\right\}t_2\right\} \qquad \text{Equ. 2-68}$$

we now define the MQ ratio: $R(I,p)=-\frac{C_4^I(p)}{C_4^I(-1)}$ and rearrange Equation 2-68:

$$S(t_1,t_2)=S_{p,-1}(0)\exp\left\{-i\left\{-p\omega_{CS}+\frac{\omega_Q^2}{\omega_L}A_0C_0^I(p)\right\}t_1\right\}$$

$$\cdot \exp\left\{-i\left\{\omega_{CS}+\frac{\omega_Q^2}{\omega_L}A_0C_0^I(-1)\right\}t_2\right\} \qquad \text{Equ. 2-69}$$

$$\cdot \exp\left\{-i\left\{\frac{\omega_Q^2}{\omega_L}A_4(\beta,\gamma)C_4^I(-1)P_4(\cos\theta)\right\}(-R(I,p)t_1+t_2)\right\}$$

Thus, by introduction of the times t_1' and t_2' with $t_1=\frac{t_1'}{1+R}$ and $t_2=\frac{Rt_1'}{1+R}+t_2'$, the equation can be rewritten in a way that the t_1' dependent fraction of the signal is independent of any angular dependent terms and therefore free from quadrupolar broadening.

$$S(t_1',t_2')=S_{p,-1}(0)\exp\left\{-i\left\{[R-p]\omega_{CS}+\frac{\omega_Q^2}{\omega_L}\left[A_0C_0^I(p)+RC_0^I(-1)\right]\right\}t_1'\right\} \qquad \text{Equ. 2-70}$$

$$\cdot \exp\left\{-i\left\{\omega_{CS}+\frac{\omega_Q^2}{\omega_L}\left[A_0C_0^I(-1)+A_4(\beta,\gamma)C_4^I(-1)P_4(\cos\theta)\right]\right\}t_2'\right\}$$

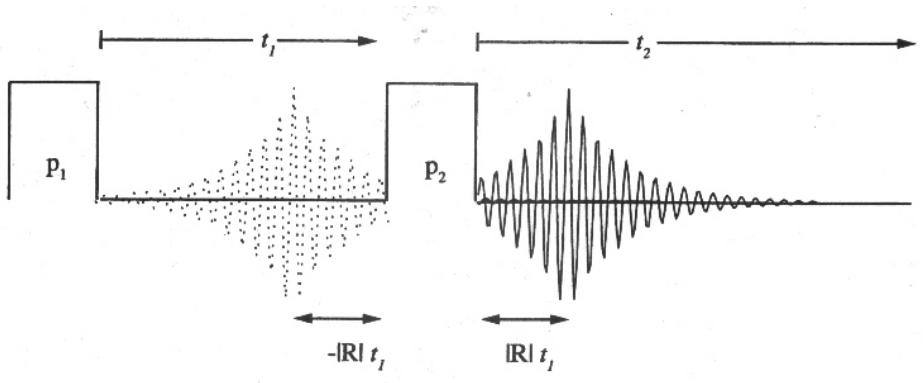

***Figure 2-5**: Relations between t_1, t_2 and t_1' and t_2' according to equation 2-70.*

The signal acquired and Fourier transformed in both dimensions, t_1 and t_2, shows the quadrupolar perturbed resonances as diagonal ridges with slopes, dependent on the MQ-ratio for the nucleus and transition observed. For triple quantum (TQ) MAS NMR spectra of

sodium and aluminum, for example, these slopes are $R\left(\frac{3}{2},\frac{3}{2}\right)=\frac{-7}{9}$ and $R\left(\frac{5}{2},\frac{3}{2}\right)=\frac{19}{12}$, respectively. The slopes are due to the mixing of t_1' and t_2' into t_1 and t_2 and can be brought to zero (ridges parallel to the F_2 axis), by a shearing transformation of the F_1 dimension. Practically, this shearing is achieved by multiplication of the time dependent signal with $e^{-i\omega_{-1}Rt_1}$. This also guarantees that, independent of *p* and *I*, the resonance shifts extracted from the center of gravity of each resonance are given as:[43,44]

$$\delta_{F2}=\delta_{CS}+\delta_{QS} \qquad \delta_{F1}=\delta_{CS}-\frac{10}{17}\delta_{QS} \qquad \text{Equ. 2-71}$$

This allows the extraction of the second order quadrupolar parameter and the chemical shift by:

$$\delta_{iso}=\frac{17\delta_{F1}+10\delta_{F2}}{27} \qquad \text{and} \qquad P_Q=\frac{1}{D_{\mathrm{Im}}}\frac{17}{27}\nu_L^2\left(\delta_{F1}-\delta_{F2}\right) \qquad \text{Equ. 2-72}$$

where D_{Im} is the same as in Equation 2-62. In the sheared 2D spectrum, resonances with the same P_Q values show up on a diagonal, parallel to $F_1 = F_2$ and resonances with same chemical shifts show up on a line with the slope *R(I,p).*

Zero Quantum Filtered MQMAS[45]

A problem with MQ MAS, especially if applied to higher coherence orders than p = 3 is, that the efficiencies of the (0,p) and the (p,-1) transitions are not equal. This leads to phasing problems and dispersion components in the spectra. It has been shown by Amoureux,[45] that these effects can be significantly reduced, by application of a z-filtered pulse sequence (0, ±p, 0, -1).

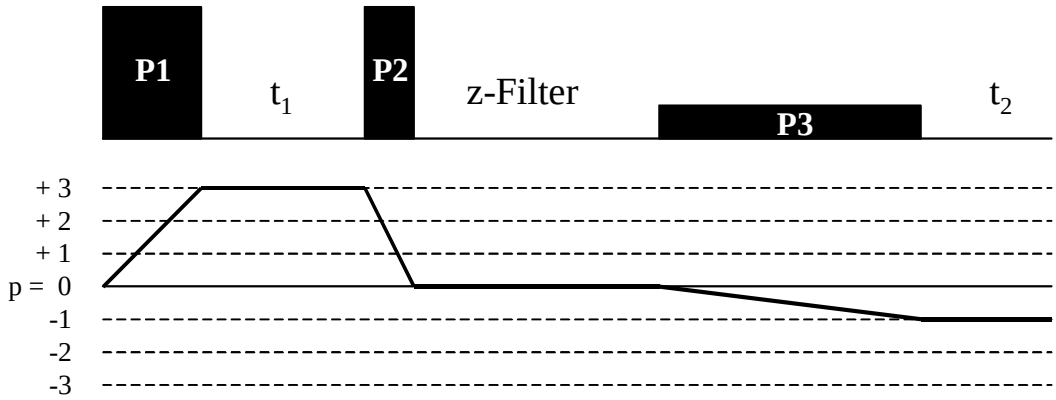

Figure 2-6: *Zero quantum filter MQ MAS NMR pulse sequence. The first two pulses are similar to the two pulse experiment. The time between second and third pulse is called z-filter, due to the fact, that all components of magnetization perpendicular to the external field dissipate during this period. The third soft pulse transfers the magnetization back to the xy plane, where it can be detected.*

In such an experiment, the first pulse specifications are similar to those of the two pulse sequence discussed above, creating the maximum amount of ±p quantum-symmetrical coherences. Both coherences evolve during t_1 and are refocused along p = 0 by the second pulse. By applying appropriate phase cycling and a delay t_z sufficient to eliminate transverse magnetization, only populations of the ± ½ Zeeman states are not negligible after the z-filter. The final soft 90° pulse transforms both magnetizations into an observable signal. Despite the removal of dispersion from the spectrum, a second advantage of this pulse sequence is the cosine dependence on t_1 of the signal intensity, allowing for pulse optimization applying the first (t_1 = 0) spectrum.

2.2 Magnetic Measurements

2.2.1 The SQUID

The direct-current (dc) SQUID (Superconducting Quantum Interference Device) consists of two Josephson junctions arranged on a superconductive ring. A current applied to the SQUID, called a bias current, divides between the junctions and, if greater than the critical current, produces a voltage across the SQUID. Plotting this current against the voltage yields characteristic curves. Steadily increasing the magnetic flux threading through the ring (for instance, by bringing in a small magnet) causes the critical current to decrease and then increase successively. The critical current is a maximum for zero flux (or an integer number of flux quanta) and a minimum for a half-integer number of flux quanta. The period of these oscillations is the flux quantum. This effect closely resembles the double-slit experiment in optics. When coherent light (such as that from a laser) passes through two parallel slits, the merging beams "interfere" with each other to produce a series of light and dark fringes. In a superconductor a single wave function describes all the Cooper pairs. The wavefunctions at the two Josephson junctions interfere with each other to produce the current and voltage swings. In practice, one can detect changes that are smaller than the flux quantum. A tiny flux signal produces a corresponding voltage swing across the SQUID, which conventional electronics can measure.

2.2.2 Methods

Hysteresis Loop

At zero field, the sample is cooled to the desired temperature. After temperature stabilization, the magnetic field is increased, usually in increasing steps to reach the maximum magnetic field of the instrument. The magnetic field is then brought down to the negative value of same magnitude and back up to the maximum field. Susceptibility measurements are undertaken at every step. Ferro, superparamagnetic and spin glass- materials show hysteresis loops, below their Curie (ferromagnetic) or blocking (superparamagnetic and spin-glass) temperatures. The characteristics are the remanence and the coercive field. The remanence is the residual magnetization in zero field after the second fifth of the loop. The coercive field is the negative field necessary to bring the magnetization of the sample back to zero after the second fifth of the loop. Ferromagnetic materials usually have large remanences (about saturation magnetization) and high coercive fields on the order of 1T. Soft ferromagnets,

superparamagnets and spin glasses show small remanences and coercive fields on the order of 10 to 100 mT.

Saturation

Saturation is reached when all the magnetic moments of the sample are aligned with the external magnetic field. Paramagnetic materials approach this point at B/T = 3 Tesla/Kelvin, where B is the external field and T the temperature. The saturation magnetization is determined by the atomic angular momentum quantum number of J, and is achieved, when all magnetic moments are aligned, which is usually the case for B/T = 3 Tesla/Kelvin. This value could only be approximated experimentally, since the maximum field was 5 T at 2 K.

Field Cooling (FC)

Field cooling experiments are performed at a constant external magnetic field (usually 10 to 1000 mT), while the temperature is lowered, usually from room temperature to the minimum temperature of the instrument. The experiment is capable of distinguishing between paramagnetic, diamagnetic, antiferromagnetic and ferromagnetic interactions.

Zero Field Cooling (ZFC)

If the FC run shows deviations from the above mentioned forms of magnetism, ZFC experiments can be performed to yield further information about the material. The sample is cooled down to the minimum temperature in zero field. Then a small field is applied (usually 1 to 20 mT) and the temperature is increased above all transitions observed to be cooled back down to the minimum Temperature. Superparamagnetic and spin glass materials show a deviation between the FC and the “field warmed” branch of the susceptibility data. Usually the “field warmed” curve also shows a maximum, which gives the blocking temperature. The temperature difference between blocking temperature and onset of branch separation is a measure of the dispersion of magnetic clusters.

If no other information about the material rules out either superparamagnetic or spin glass phenomena, neutron diffraction is the only experimental method to distinguish between these effects, since it is capable of showing the order of the antiferromagnetic spins of the spin-glass.

3 Structural Aspects of Sodalite Solid Solutions

3.1 Relations between Lattice Parameters and Sodalite Cage Geometry

As shown in the Introduction, the crystal structure of sodalite can be viewed as an aluminosilicate framework with alternating Si-O-Al bonds, built of 14 face-sharing truncated octahedra, which are stacked in a space filling bcc manner as portrayed in Figure 1-1. The building blocks of these cages are SiO_4 and AlO_4 tetrahedra. The flexibility of the sodalite framework and therefore its wide range of lattice constants between 8.47 Å (LiCl-SOD) and 9.34 Å ($KClO_4$-SOD) is achieved by a tilt of the tetrahedral edges, which, in the theoretical fully expanded structure with a lattice constant of 9.40 Å, are parallel to the cell edges, as shown in figure 4-1. The description of such structures based on a tilt angle was first introduced by Taylor[46] for silicates with one type of tetrahedra. Hassan and Grundy [47] later applied this principle to sodalites with their two types of slightly distorted tetrahedra. In the latter case different tilt angles occur for the aluminum and silicon tetrahedra.

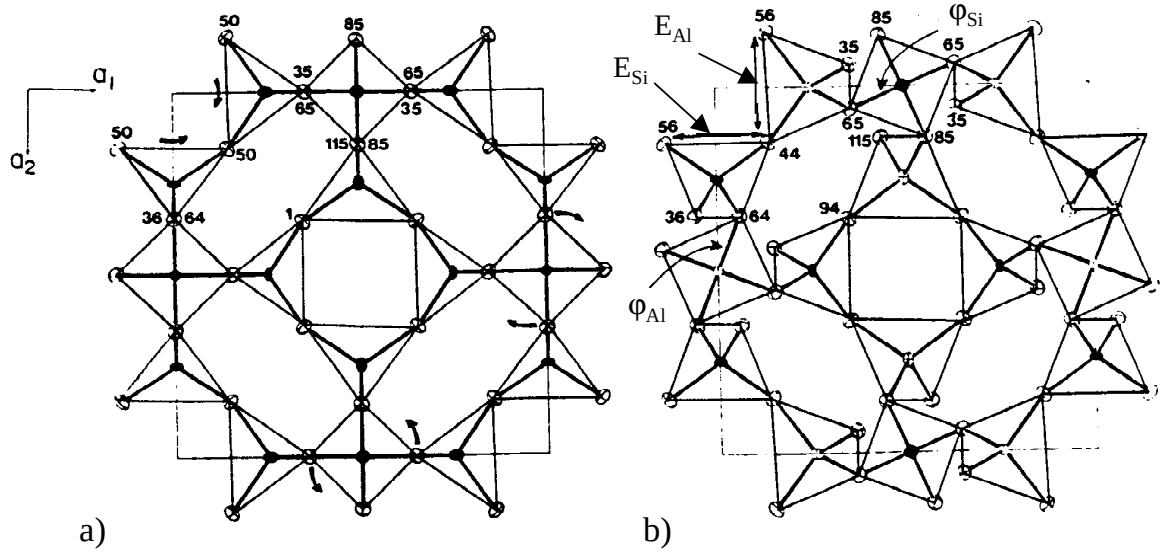

***Figure 3-1**: Upper half of the unit cell. **a)** the fully expanded framework of regular tetrahedra of equal sizes (space group Im3m). The arrows indicate the rotation of tetrahedra about axes parallel to the cell edges which reduce the cell edge. Along each row of tetrahedra oriented with their $\bar{4}$ axes parallel to a cell edge, alternating tetrahedra are rotated clockwise and counter-clockwise. **b)** A partially "collapsed" structure of the sodalite lattice showing tilt angles φ_{Si} and φ_{Al} and also O-O distances E_{Si} and E_{Al}. The Al and O atoms are shown as open and the Si atoms as filled ellipsoids. Numbers indicate heights in % of the cell edge a_0.*[47]

The remarkable property of the sodalite structure is that the positions of all framework atoms can be determined, solely from the lattice constant, if the properties of the tetrahedra are known. So far all crystal structures of aluminosilicate sodalites known are built of similar

SiO_4 and AlO_4 tetrahedra (where the SiO_4 tetrahedra have Si-O distances of 1.620 Å and edges of 4*2.626 Å and 2* E_{Si} = 2.701 Å, and the AlO_4 tetrahedra have Al-O distances of 1.742 Å and edges of 4*2.831 Å and 2* E_{Al} = 2.871 Å).[47]

Thus the Al-O-Si bond angle α solely depends on the cell edge a_0 and is given by:

$$\alpha = \frac{180°}{\pi}\arccos\left(\frac{\overline{SiO}}{2\overline{AlO}} + \frac{\overline{AlO}}{2\overline{SiO}} - \frac{a_0{}^2}{16\overline{SiO}\cdot\overline{AlO}}\right) \qquad \text{Equ. 3-1}$$

The tilt angles are then given by:

$$\cos\varphi_{Si} = \frac{1}{2E_{Si}}a_0 - 4\sqrt{4\overline{AlO}^2 - (E_{Al}/2)^2} \qquad \text{Equ. 3-2}$$

where the equation for φ_{Al} is analogous to the one for φ_{Si}. The coordinates of the oxygen position closest to the origin of the coordinate system are then given by:

$$x_{Ox} = \frac{E_{Si}}{2a_0}\cos\varphi_{Si} \quad , \; y_{Ox} = \frac{E_{Al}}{2a_0}\cos\varphi_{Al}$$

$$z_{Ox} = \frac{1}{2} - \frac{1}{2a_0}\left(E_{Al}\sin\varphi_{Al} + E_{Si}\sin\varphi_{Si}\right) \qquad \text{Equ. 3-3}$$

If, in addition, the Na-O distance is known, also the position of the sodium (X_{Na}, X_{Na}, X_{Na}) and the Na-halide distance (= $3^{½}a_0X_{Na}$) are directly deductible from the following quadratic equation:

$$X_{Na}^2 - \frac{2}{3}\left(x_{Ox} + y_{Ox} + z_{Ox}\right)X_{Na} + \frac{1}{3}\left[\left(x_{Ox}^2 + y_{Ox}^2 + z_{Ox}^2\right) - \frac{\overline{NaO}^2}{a_0^2}\right] = 0 \qquad \text{Equ. 3-4}$$

The Na-O distances for all salt-bearing sodalites studied are 2.355 Å, while for dry sodalites and hydro sodalites Na-O distances of 2.33 and 2.51 Å have been reported.[10] Thus, all lattice parameters of the systems investigated are accessible from the lattice constant and the Na-O distance. Na-halide distances, to be discussed below, have been always computed according to the previous equations.

3.2 Statistical Description of Sodalite Solid Solutions

Another important property of the systems studied and directly connected to the flexible size of the sodalite cage is its ability to incorporate different central anions and thus forming a special type of solid solution, where the interactions between the mixed species are moderated by the framework. Solid solutions are characterized by a random distribution of their constituents. Thus to understand the variety and intensity of NMR resonances occurring in these systems, knowledge about theoretically expected distributions will be very helpful in assigning observed peaks to certain local environments.

If *A* and *B* are the two species being distributed among the cage centers with probabilities of *P(A)* and *P(B)* = 1 – *P(A)*, the probability that *n* chosen cages are filled with *i* elements of species *A* is given by the binomial distribution:

$$P(iA) = \binom{n}{i} P(A)^i \cdot (1 - P(A))^{n-i} \qquad \text{with} \binom{n}{i} = \frac{n!}{i!(n-i)!} \qquad \text{Equ. 3-5}$$

Each T-atom is part of four sodalite cages. Thus the resulting probabilities of 0 to 4 neighbors can be determined directly from Equation 3-5 with n = 4. If two different kinds of environments have to be considered, such as the influence of first and second order neighbors, the probabilities for any combination are just the products of the single probabilities. Simulations for special environments of interest to this study will be discussed in the upcoming chapters, along with the experimental data.

3.3 NMR Studies of Sodalites

Among the first applications of solid state NMR to sodalites were correlations between lattice parameters and ^{29}Si chemical shifts[48,49] where a correlation between the average T-O-T bond angle and the chemical shift was observed. Jacobsen et. al showed that a similar correlation is true for ^{27}Al in 1:1 aluminosilicate sodalites,[50] and also systematic variations of the ^{27}Al chemical shift with the average Al-O-Si bond angle in all aluminum sodalites could be shown.[51]. Nielsen established exact shift and quadrupolar coupling parameters for several sodalites via Satellite Transition (SATRAS) NMR.[52] ^{1}H NMR studies on sodalites were for the first time undertaken by Engelhardt in order to solve the phase diagram of basic/hydro

sodalites, where ^{23}Na MAS NMR also proved to be a valuable tool in the observation of such transformations.[9,12] Silver-sodium solid solution systems were studied by Jelinek and Stein using ^{23}Na NMR, .[53-56] and they also conducted ^{35}Cl and ^{81}Br NMR in order to distinguish between Na_4Halide and Ag_xNa_{4-x}Halide clusters.[54] Several subsequent papers use NMR to investigate crystal growth or to report NMR spectra of newly synthesized sodalites,[57,58] and a good overview is given by Engelhardt.[59] Recently an extensive ^{27}Al, ^{29}Si and ^{71}Ga NMR study appeared in the literature where the T-atom shifts were correlated against each other, as well as against several parameters derived from the T-O-T bond angle.[60] It was found that under similar conditions, shift effects of ^{71}Ga are twice as large as for ^{27}Al. Sodium electro sodalites were characterized by NMR, which shows quantized shifts due the distribution of Na_4^{3+} centers around the T atom environments.[19] These resonances are shifted with decreasing temperature to higher frequencies, as expected for hyperfine coupling between nuclei and paramagnetic electrons.

3.3.1 NMR of Framework Atoms.

The analysis of the chemical shift of T atoms has become a valuable tool in the characterization of aluminosilicates. Besides the fact that different coordination numbers can be distinguished,[61] for tetrahedral environments the chemical shift is correlated with the average T-O-T bond angle. It has been shown, that the paramagnetic contribution to the chemical shift can be calculated from the charge distribution of a tetrahedral SiX_4 silicon unit with four σ MOs and that it is the dominant contribution to the chemical shift.[62] The polarity of the MOs can be described by the electronegativities (EN) of the ligands and can be linearly correlated with the chemical shift.

$$\delta = -a\,EN + b \qquad \text{Equ. 3-6}$$

A relation between EN and the bond angle is given by the degree of s-hybridization ρ of the oxygen bond orbitals, which is related to both, EN and the Si-O-Si bond angle α.

$$\rho = \cos\alpha / (\cos\alpha - 1) \qquad \text{Equ. 3-7}$$

$$EN = EN_p + \rho(EN_s - EN_p), \qquad \text{Equ. 3-8}$$

where EN_s and EN_p are the electronegativities of pure s and pure p oxygen bond orbitals. Thus a linear relation results between δ and ρ. Due to the fact that ρ and α also correlate approximately linearly over the range of angles studied, it has become customary to use the linear relation between α and δ rather than between ρ and δ. Since α and the cell edge a_0 correlate linearly to a second order approximation as well, δ has also been correlated to the

cell edge. Comparative studies usually give the best experimental correlation for δ and α.[48,49,59] The same considerations are true for aluminum, and it is not surprising that similar correlations have been established for aluminum and gallium.[50,60]

^{27}Al and ^{71}Ga both have a nuclear electric quadrupole moment, thus interactions with their local electric field gradients have to be taken into account. In sodalites, aluminum resides in the center of a slightly distorted tetrahedron (see above), resulting in P_Q values around 0.8 MHz. The ^{27}Al signal thus contains information about the average T-O-T angle as well as on the degree of distortion from tetrahedral symmetry. A relation between the shear strain and the quadrupolar coupling constant C_Q was proposed by Engelhardt[63] and confirmed by Weller.[64] The shear strain, as defined by Depmeier[65] is given by: $|\Psi| = \sum_{i=1}^{6} |\tan(\alpha_i - 109.48°)|$

and the correlation found is C_Q = uch a correlation can also be rationali ed by si le point charge model calculations.

3.3.2 NMR of extra Framework Species

The point charge model has also been useful for computing P_Q values for ^{23}Na. While for ionic bonds, partial ligand charges can be calculated according to Brown and Altermatt[66], covalency effects can be taken into account by artificially increasing ligand charges. Point charge computations within this study are based on a computer program written by Arno Kentgens, which had been previously successfully employed to correlate ^{23}Na C_Q values with various oxygen environments, and will be elaborated in more detail in Chapter 4.[67] Electric field gradients computed by this program are transformed into quadrupolar coupling constants.

Recently distance dependent relations between the ^{23}Na chemical shift and oxygen ligand environments have been established theoretically by Hartree-Fock based calculations,[68] but systematic experimental studies are still lacking. Furthermore, except for publications by the author of this study,[6,69] halide NMR has so far only once been applied to aluminosilicates, where ^{35}Cl and ^{81}Br MAS NMR spectra were exploited to distinguish between sodium and silver ligands in mixed Na-Ag bromo-sodalites.[54]

Besides many applications in liquids, where a comprehensive overview was given by Akitt,[70] halide NMR of alkali halide salts has been a valuable tool in understanding the nature of chemical shifts. Kondo and Yamashita[71] have proposed a relation between the overlap integrals and paramagnetic shielding σ_p of such compounds:

$$\sigma_p = -\frac{8\mu_B^2\mu_0}{\left\langle r^3 \right\rangle_p}\frac{S_{XX} + S_{XM} + S_{XS}}{\pi\Delta E} \qquad \text{Equ. 3-9}$$

where E is the average excitation energy, $\langle r^3 \rangle_p$ is the expectation value of r^3 for an outer p electron of the halide, and the S terms are the sums of squares of overlap integrals between the outer p orbitals of the halide ion ($_X$) and the orbitals of other halide, alkali cations ($_M$) or solvent ($_S$) ions. While Hafemeister and Flygare have computed and tabulated overlap integrals between alkaline metal and halide ions[72] as well as relativistic corrections[73] the basis of the semiempirical results are the alkali and halide shifts of these salts at their equilibrium distances. The sums of overlap integrals (S_{XM}) as computed could always be fitted very precisely by exponential functions such as:

$$S_{XM} = C \cdot e^{-\frac{r}{\rho}} \qquad \text{Equ. 3-10}$$

C and ρ are constants and r is the distance between the two ions. Tests of such relations have been undertaken by the application of high pressure to the heavier halide salts of Rb and Cs[74] or high temperature measurements.[75] The correlations found were linear in both cases, thus pressure and temperature dependent side-effects always have to be accounted for, which significantly complicates the data analysis. Finally it is worth mentioning that Hartree-Fock based computations with much more extensive basis sets of atomic orbitals than used by Hafemeister and Flygare, essentially result in similar decay functions, however with somewhat different coefficients C and ρ.[72]

3.4 Magnetically Coupled Spins

The Heisenberg Hamiltonian describes the magnetic coupling between single electrons located on sites i and j by the exchange integral J_{ij}:

$$\hat{H} = -J_{ij}\hat{S}_i\hat{S}_j \qquad \text{Equ. 3-11}$$

where $_i$ and $_j$ are the spin operators. A negative value of J_{ij} is associated with antiferromagnetic (AFM) coupling. The two major effects regarding mutual coupling of electrons are kinetic and potential exchange.[76] AFM is the result of gain in kinetic exchange energy. In this case the two electrons have antiparallel spins and their spin functions are orthogonal, thus they may overlap. Ferromagnetic (FM) coupling is the result of a gain in potential exchange energy and is dominant between electrons in spatially separate orbitals that

are orthogonal by symmetry and thus cannot overlap. Generally potential exchange is weaker than kinetic exchange. It has been shown by various theoretical approaches[21-24,77] and experiments,[20,78] that the F-center electrons in sodium electro sodalite (SES) couple antiferromagnetically and the kinetic exchange interaction can be described by second order perturbation theory.[76]

$$J_{ij} = -\frac{4b_{ij}^2}{U} \qquad \text{Equ. 3-12}$$

Here b_{ij} describes the virtual transfer of an electron from site i to site j between the localized single occupied molecular orbital (SOMO) and U is the on site Coulomb repulsion energy:

$$U = \iint d\vec{r}_1 d\vec{r}_2 |\psi(\vec{r}_1)|^2 \frac{1}{|\vec{r}_1 - \vec{r}_2|} |\psi(\vec{r}_2)|^2 \qquad \text{Equ. 3-13}$$

U can also be approximated by:[79]

$$U = 1 + \left(S_{12}^{\alpha\beta}\right)^2 \qquad \text{Equ. 3-14}$$

where $S_{12}^{\alpha\beta}$ is the overlap integral between the magnetically interacting orbitals α and β at the centers 1 and 2. Thus it is reasonable to assume that for n interacting spins, the Coulomb repulsion potential is approximately:

$$U = 1 + n \cdot \left(S_{12}^{\alpha\beta}\right)^2 \qquad \text{Equ. 3-15}$$

while the parameter b_{ij} is not affected.

The high temperature volume susceptibility caused by paramagnetic electrons is given by

$$\chi = \frac{C}{T - \theta_W} \qquad \text{Equ. 3-16}$$

where $C = \frac{N\mu_0 g_e^2 \mu_B^2 S(S+1)}{3k_B}$ is the Curie constant, *N* the number of spins per unit volume, T is the temperature and θ_W is the Weiss temperature. A negative value of θ_W indicates AFM coupling while a positive value indicates FM coupling between the spins. From the molecular field treatment of ferromagnetism and antiferromagnetism,[80] the Weiss temperature can be calculated from the number of nn (nearest neighbors) and nnn (next nearest neighbors) spins coupling to the spin under observation and their corresponding coupling constants *J*.

$$\theta_W = \frac{2S(S+1)}{3k_B}\left(z_{nn}J_{nn} + z_{nnn}J_{nnn}\right) \qquad \text{Equ. 3-17}$$

For a bcc packing, as present for the F-centers in the sodalite lattice, two arrangements of nn and nnn spins are possible, resulting in overall AFM coupling.[80]

a) All 8 nn are oriented antiparallel to the central spin (AFM-I), while the 6 nnn are ordered parallel, yielding a Néel Temperature of:

$$T_{NI} = \frac{2S(S+1)}{3k_B}(-8J_{nn} + 6J_{nnn}) \qquad \text{Equ. 3-18}$$

b) The 8 nn are alternatingly oriented parallel and antiparallel with the central spin (AFM-II), while all 6 nnn are ordered antiparallel with respect to the central spin. The resulting Néel Temperature is then given by:

$$T_{NII} = \frac{2S(S+1)}{3k_B}(-6J_{nnn}) \qquad \text{Equ. 3-19}$$

Thus the ratio T_N/θ_W allows the identification of the type of magnetic ordering, if the ratio of J_{nn}/J_{nnn} is known. For SES this ratio has not been determined experimentally and was guessed to be between 6:4[78] and 1:0.[24]

4 Experimental

4.1 Synthesis

Sodalites can be synthesized by high temperature conversion of other alumino-silicates such as kaolin or Zeolite A^{27} or via hydrothermal routes from basic solutions containing aluminum and silicon precursors. Since the latter methods offer a wider range for inclusion of intra-cage species, all sodalites discussed here were synthesized from solutions or gels under hydrothermal conditions.

In order to be able to characterize the magnetic properties of these materials, it was important to gain knowledge and control over the inclusion of magnetic species. In all sodalites, the dominant paramagnetic impurity is iron, which is usually introduced by the aluminum precursor. In a common precursor, kaolin, for example, an average of 0.2 to 1.5% of the aluminum sites are occupied by iron(III). Aluminum oxide has an iron impurity of about 0.05% and aluminum isopropoxide of less than 10ppm. Since the quality of crystallinity decreases and the reaction time increases in the order kaolin, Al_2O_3, $Al(ipr)_3$, sodalites which were not magnetically studied such as the mixed halide sodalites series were synthesized from kaolin (process 1). Sodalites which were artificially iron enriched were prepared from a 1:2 mix of Al_2O_3 and SiO_2 (process 3), and "diamagnetic" sodalites pure enough to study the interaction among the F-center electrons had to be prepared from aluminum isopropoxide (process 2).

4.1.1 Mixed Halide Sodalites

The synthesis of the mixed halide sodalites was carried out in Teflon-coated 20 ml stainless-steel autoclaves. The inlays were filled with 3 mmol calcined kaolin as a precursor, 0.18 mol NaOH (as Na_2CO_3 free pellets) and 20 mmol of the desired mixture of sodium-halide salts. Distilled water was added to give a total volume of 18 ml and the gel was stirred until all of the sodium hydroxide was dissolved. After stirring for another 30 minutes the autoclaves were sealed off and heated at 450K under autogenous pressure for 10 days. After decanting the basic solution, the sodalites were washed several times with distilled water to remove excess sodium hydroxide from the surface of the crystallites.

4.1.2 Mixed Salt-bearing/Salt-free Sodalites

The synthesis of the halide/basic sodalites, free of iron impurities, was carried out in Teflon-coated 40 ml stainless-steel autoclaves. A desired amount (ranging between 6 and 15 mmol) of aluminum-isopropoxide (Aldrich: 22,940-7) and 0.36 mol of NaOH pellets (Aldrich: 30,657-6) free of carbon-dioxide impurity was topped off with 30 ml of distilled water and stirred until a clear solution was obtained. A known amount (between 0.5 and 40 mmol) of NaBr (Aldrich: 22,034-5) required for the bromine content desired in the mixed sodalite was added to the solution. After stirring for 15 minutes, the corresponding stoichiometric amount (6 to 15 mmol) of tetra-ethyl-ortho-silicate (Aldrich: 33,385-9) was added to the solution. The autoclave was topped off with distilled water until 90 % of its volume was occupied, closed tightly and kept at 350 K for 10 to 20 days.

After opening the containers, the highly basic solution above the sample was decanted and the sodalite samples were washed (through a plastic membrane filter) to remove sodium hydroxide adhered to the crystal surfaces. Only 50 ml of deionized water was used for this purpose since prolonged washing may extract NaOH from basic sodalite cages (see below).

The samples of the halide/hydro series were obtained by stirring Br/basic sodalites in deionized water for several days. The pH of the suspension was kept at 6 ± 0.5 during extraction by frequent addition of diluted H_2SO_4. The washing process was terminated when the pH did not change significantly for a day, indicating a complete transformation of Br/basic sodalite into halide/hydro sodalite.

Halide/dry sodalite samples were obtained by heating halide/hydro sodalites to 670 K under vacuum (~$5 \cdot 10^{-8}$ Pa) for eight hours.

4.1.3 Halide/Electro Sodalites

Dry sodalites can be doped with alkali atoms from liquid or vapor. Since an alkali metal liquid was found to damage the sodalite structure, I used the vapor method: Under an argon atmosphere about 200mg of dry sodalite were filled into a glass tube (Pyrex© or Duran©) of 9mm (outer) diameter and 200mm length. A chunk of alkali metal, having a length of about 20mm is then carefully positioned at a distance of about 120mm from the sodalite end of the tube. The alkali metal easily sticks to the glass walls, so one has to be very careful introducing it into the ampoule while, on the other hand, it is quite easy to fix it at the desired position. The tubes were then attached to a vacuum valve (either to a metallic valve via Swagelock© attachments, or to a glass valve using glass joints). This device was taken out of the argon atmosphere and attached to a high vacuum system. It is important to achieve pressures below

10^{-3} Pa (10^{-5} mbar, $7.6 \cdot 10^{-6}$ Torr) in order to achieve a sufficient mean free path for the alkali metal vapor during the doping procedure. The tubes were then sealed off above the alkali metal chunk and heated inside a horizontal tube furnace in a way that the sodalite end is at a temperature of 290 °C and the alkali metal chunk about 20 °C below as shown in Figure 4-1.

Figure 4-1: *Glass ampoules inside an opened tube furnace. The sodium metal is on the cooler side of the tubes. The sodalite powder is located near the center of the furnace. The two tubes on the right clearly show the black frontier of already doped sodalite moving through the undoped part. The central sample on the left side is already completely doped. The sample in the upper left part is being distilled (one end of the glass tube sticks out of the furnace. The white material is glass-wool.*

It is helpful to distribute the sodalite within the glass tube such that it takes up less than 30% of the diameter, but still has no contact with the alkali metal. During the doping procedure, which takes between 5 and 24h, a border separating the undoped white and doped black parts of the sodalite can be observed moving slowly across the sample. In order to evaporate excess sodium on the crystallites´ surfaces, the tubes were exposed to a temperature gradient of about 190 °C, condensing the sodium vapor at the non sodalite end of the tube. The latter process took significantly longer when the sodalite was doped with potassium, since the potassium tends to displace sodium from the crystallites, leaving them covered with a liquid mixed alkali metal phase at room temperature. Complete doping was only successful with sodium and potassium, while rubidium diffusion into the cages was found to be limited to the surface layers.

It is noticeable that sodium electro sodalites decompose slowly while potassium electro sodalites catch fire instantly when exposed to air. Even potassium electro sodalites with more than 90% cages filled with bromine decompose immediately under these conditions. The residual material mainly contains silicon and aluminum oxide, as well as strongly distorted sodalite crystals. It is likely that this effect is caused by an alkali metal layer that cannot be removed from the sodalite surface at the moderate temperatures applied.

4.2 X-ray Diffraction

X-ray diffraction is a standard method of analysis for crystalline materials. Radiation with a wavelength of about 10^{-11} m is scattered by atoms from crystal surfaces and a few layers below. Constructive interference is observed under reflection angles (θ), dependent on the spacing (d) between atomic layers in the sample according to the Bragg equation: $n\lambda = 2d \cdot \sin\theta$, where n is an integer and λ is the x-ray wavelength. When the crystal structure is known, the lattice constant can be derived from the reflection angles of a powder pattern, while the intensities allow distinction between atoms occupying the crystal sites.

X-ray diffraction powder patterns in the $12^o < 2\theta < 66^o$ region were taken with Cu-K_α (1.54178 Å) radiation on a Scintag-X2 spectrometer in 0.02^o steps and at a scanning rate of 2^o/min. Silicon powder was used as an internal standard. The background correction, removal of the Bragg reflections due to the $K\alpha_2$ line, and the subsequent determination of the lattice constants by the least squares fitting procedure were done with the DMSNT 1.37 software package from Scintag. The lattice constants were calculated from the corrected peak data to an accuracy of about 0.001 Å. The halide/dry and halide/electro sodalite samples were kept inside a hermetically sealed beryllium cell during the data acquisition in order to avoid rehydration or oxidation.

4.3 Thermogravimetric Analysis (TGA)

Thermogravimetric analysis allows to monitor the weight loss of a sample compared to a reference, while both, sample and reference, are heated up in a specific atmosphere at a certain rate. Sample and reference are placed on a balance, thus the relative weight loss of the sample can be monitored. For sodalites, the percentage of water filled cages can be calculated directly from the weight loss (in mg or % of the sample mass). Mixed halide/hydro sodalites loose their water between 400°C and 500°C. Two sodium hydroxides in halide/basic sodalites turn into $H_2O\uparrow$ and Na_2O at about 800°C. The weight loss w as a fraction of the total mass is then given by:

$$w = 1 - \frac{M(\,framework) + 2(1-x)\cdot M(NaHal)}{M(\,framework) + 2(1-x)\cdot M(NaHal) + 8x\cdot M(H_2O)} \qquad \text{Equ. 4-1a}$$

where the M( ) are the molar masses and x is the fraction of cages filled with water under the assumption that non-halide filled cages are always occupied by four molecules of water, as is

the case for pure hydro sodalite. The calculation of the fractional water content is then straightforward:

$$x = w \cdot \frac{M(\,framework) + 2 \cdot M(NaHal)}{8(1-w) \cdot M(H_2O) + 2w \cdot M(NaHal)} \qquad \text{Equ. 4-1b}$$

The thermogravimetric analysis (TGA) was carried out on a Netzsch 609 Simultaneous Thermal Analyzer. About 50 mg of sample were heated at 10 K/min from room temperature to 1373 K against a dry Al_2O_3 standard and background corrected. The weight loss between 383 and 800 K was ascribed to intra cage water, while the weight loss below 383 K was attributed to surface water.

4.4 Nuclear Magnetic Resonance

^{1}H, ^{23}Na, ^{27}Al, ^{29}Si, ^{35}Cl, ^{81}Br and ^{127}I MAS NMR spectra were obtained with a Bruker "HP WB73A MAS 4BL CP BB VTN" probe head on a high resolution Bruker DSX 500 NMR spectrometer. Complementary experiments were undertaken on Bruker DSX 400 and CXP 200 spectrometers in order to extract chemical shift and quadrupolar coupling parameters from field dependent data. The corresponding resonance frequencies are given in Table 4-I. 1M aqueous solutions of $(AlNO_3)_3$, NaCl, NaBr and NaI were used as chemical shift references at zero ppm. For the halide resonances secondary referencing was done on the basis of solid KCl, KBr and KI, respectively. Hydrogen and Silicon were referenced with a standard of liquid tetramethylsilane (TMS). Typical spinning speeds ranged from 10 to 15 kHz. For all samples simple one-pulse MAS NMR spectra were obtained with 30^{o} pulses of 1.0 μs duration. High resolution triple quantum (TQ) MAS NMR spectra were acquired using the three-pulse sequence with zero quantum filtering.[33,45] For ^{27}Al TQ MAS, the first two hard pulses were 3.8 and 1.4 μs in length, respectively. The third selective 90º pulse had a length of 10 μs. A total of 64 to 128 spectra, containing 72 to 144 scans each, were acquired in the F_1 dimension. In the case of ^{23}Na TQ MAS, the first two hard pulses were 3.1 and 1.1 μs in length, respectively. The third selective 90º pulse had a length of 10 μs. A total of 64 to 128 spectra, containing 48 to 96 scans each, were acquired in the F_1 dimension.

Variable temperature NMR was carried out with a Bruker "HP WB73A MAS 4BL CP BB WVT" probe in the temperature range between 160 K and 575 K at spinning speeds around 7000 Hz. The high temperature experiments were undertaken in a 9.4 T field, where active frame cooling was available.

Nucleus	Spin	Natural Abundance	ν_L /MHz at 11.7 T	ν_L /MHz at 9.4 T	ν_L /MHz at 4.7 T	eQ / $10^{-30}m^2$	γ_∞ [Ref 70]
^{1}H	1/2	99.985	500.13	400.11	200.04		
^{23}Na	3/2	100	132.26	105.81	52.9	10.98	-4.1
^{27}Al	5/2	100	130.29	104.23	52.11	14.03	-2.3
^{29}Si	1/2	4.67	99.33	79.46	39.73		
^{35}Cl	3/2	75.77	48.99	39.19	19.6	-8.17	
^{81}Br	3/2	49.31	135.03	108.03	54.01	27.6	
^{127}I	5/2	100	100.04	80.03	40.01	-78.9	

Table 4-I: *Nuclear parameters for the nuclei studied by NMR.* ν_L *is the Larmor frequency, eQ is the nuclear electric quadrupole moment and* γ_∞ *is the Sternheimer antishielding constant (see section 4.5).*

4.5 Computational Methods

4.5.1 Ab Initio Calculations

The primary objective of the chemical shielding calculations was to obtain insight into the dependence of these shieldings on Na-halide distances. To this end, the GAUSSIAN98[81] program package was used to calculate the ^{23}Na, ^{35}Cl and ^{81}Br chemical shieldings by the Hartree-Fock method applying mainly the 6-31G* and the 6-311++G(3df,3pd) basis sets. In the case of iodo-sodalites, the SDD basis set was applied, which gives similar results as 6-31G* but includes heavier atoms. Other basis sets were used to study the influence of the basis set. Since GAUSSIAN is not designed for periodic boundary conditions one important step in the calculation of NMR parameters of nuclei embedded in crystals is to identify representative atomic environments. Sodium is coordinated by three oxygen atoms and by the halide ion at the center of the cage. Therefore I chose the framework six-ring, where aluminum was exchanged for silicon, all open bonds were terminated with hydrogen and the halide ion with its three additional sodium ligands. The six-ring model has previously been employed for ^{23}Na shift calculations by other workers,[68] as the environment for most calculations, as portrayed in Figure 3-1.

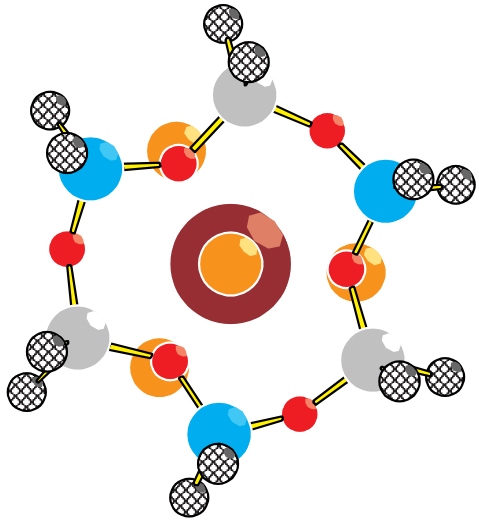

Figure 4-1. *Bottom up view of the sodium environment chosen for computation. In front the sodalite six-ring, where all the T sites are occupied by silicon (light gray spheres) and bridged (these bonds are marked) by oxygen atoms (small dark spheres). The bonds connecting the six-ring with the residual sodalite lattice are terminated with hydrogen atoms (white spheres, crossed). The sodium ion of interest is centered. On the far side the halide (large dark sphere) resides with its additional three sodium ligands, which can be seen behind every other oxygen atom.*

I also evaluated a variety of other environments, such as isolated Na-halide "molecules", sodium environments of six-rings containing three aluminum ions, terminated with OH groups and a whole cage, surrounded by four sodium ions and terminated with hydrogen. All atomic positions (except those for the terminating ions) were computed from the sodalite lattice constant and an Na-O distance of 2.355 Å, using the correlation by Hassan et al.[47] Additional computations were undertaken for environments without halide ions using Na-O distances of 2.330 Å, as found in dry sodalite. Only the hydrogen positions were allowed to equilibrate prior to the shielding calculations. For sodium, it was found that the variation of basis set and local environments gives results that scatter by about ± 5 ppm around the values obtained from 6-31G* and the hydrogen terminated six-ring environment. Therefore, we decided to use the latter as a model for comparison with the experimental results. For the halide resonances, shielding calculations were also attempted, however, even when using the 6-311++G(3df,3pd) basis set only qualitative agreement with the experimental data was obtained. We ascribe this to the fact that the halogen basis sets are optimized for covalent, rather than ionic bonds.

4.5.2 The Point Charge Model

A rather simple but sometimes efficient way to compute the quadrupolar interaction parameters C_Q and η is based on a point charge model. The idea is to compute the electric field gradient (EFG) at the site of the nucleus based on the Cartesian coordinates of all ligands and their charges. For ionic bonds, the charge $n_\lambda e$ of the ligand can be derived from empirical relationships according to the model by Brown and Altermatt.[66,82] If the origin of the coordinate system is the site of the central nucleus, the matrix elements of the EFG tensor are computed as follows, summing up the contributions from all ligands:

$$\sum_{\lambda} V_{\alpha\beta}^{\lambda} = n_{\lambda} e \frac{3\alpha\beta - r_{\lambda}^2}{r_{\lambda}^5} \qquad \text{Equ. 4-3}$$

where $(\alpha,\beta) = (x_\lambda, y_\lambda, z_\lambda)$ and $r_\lambda = \sqrt{x_\lambda^2 + y_\lambda^2 + z_\lambda^2}$. The final electric field gradient tensor is then diagonalized by orthogonal rotations using a program by Kentgens.[67]

The largest principal value found, $V_{zz} = eq$, can be used to calculate the nuclear quadrupolar coupling constant:

$$C_Q = (1-\gamma_\infty)\frac{eqeQ}{h} \qquad \text{Equ. 4-4}$$

where eQ is the nuclear quadrupole moment and γ_∞ is the Sternheimer antishielding factor (see Table 4-I), giving the relation between the external EFG caused by the surrounding ligands and the internal EFG. The internal EFG is caused by anisotropic charge distributions of the core and valence electrons as a result of the external EFG.[70] The asymmetry parameter is computed according to Equation 2-52 (also see text).

The values computed are based on the atoms in the first coordination sphere. Although introduction of more distant charges was in some cases capable of changing this value by up to 30%, the values yielded from computations based on the first coordination were found to be in best agreement with experimental results. This is reasonable, since atoms of the first coordination sphere have a partially covalent bond with the atom of interest and thus a more polarizing effect on its electrons, compared to the more remote atoms.

4.6 Magnetic Measurements

All magnetic measurements were carried out on a QUANTUM DESIGN SQUID (Superconducting Quantum Interference Device) which allows detection of AC and DC susceptibilities down to 10^{-7}emu at temperatures between 2K and 400K. About 40mg of the air sensitive samples were centered in a gel capsule (6mm*12mm), pressed into the center of a standard soft drink straw and inserted into the bore of the SQUID through a vacuum port at room temperature. All data points were acquired in the DC mode. Above 60 K the sample temperature was usually continuously ramped at a rate of 2 K/min and the data points were acquired with one scan during the ramping process. At lower temperatures, the instrument was allowed to equilibrate at the desired temperature before the measurement. In this case the data was averaged over three scans. Field dependent measurements were carried out at various temperatures in the “no overshoot” mode, approaching the desired temperature without crossing it to assure correct measurements in case, the sample shows a hysteresis effect.

5 Halide inclusion

5.1 Experimental Observations

The sodalite solid solution systems synthesized are quasi binary systems with two different anions incorporated. They fall into two groups: Mixed halide/basic sodalites have a fraction of their cages occupied by halide ions, while the remaining cages contain $H_3O_2^-$ anions. The mixed halide sodalites have two different halide species distributed among their cages. The Cl/Br, Br/I and Cl/I containing sodalites were synthesized according to Chapter 4 and their summarized NMR and lattice parameters are given in Tab 5-I. The samples were characterized by powder XRD, which allows the determination of the lattice constant. All mixed Cl/Br and Br/I sodalites show one set of sharp x-ray reflections corresponding to a lattice with $P\bar{4}3n$ group symmetry and varying lattice constants between 8.880 and 9.012 Å. Mixed Cl/I sodalite samples having comparable concentrations of Cl and I show significant peak broadening, indicating the occurrence of domains with different lattice constants and/or phase separation, to be discussed later. Narrow peaks are again observed for mixed Cl/I sodalites near the corresponding endmember compositions, indicating single phase materials.
The halide fractions inside the sodalite matrix were based on a quantitative ^{23}Na MAS NMR procedure (see below) and are plotted in Figure 5-1 as a function of the lattice constant.

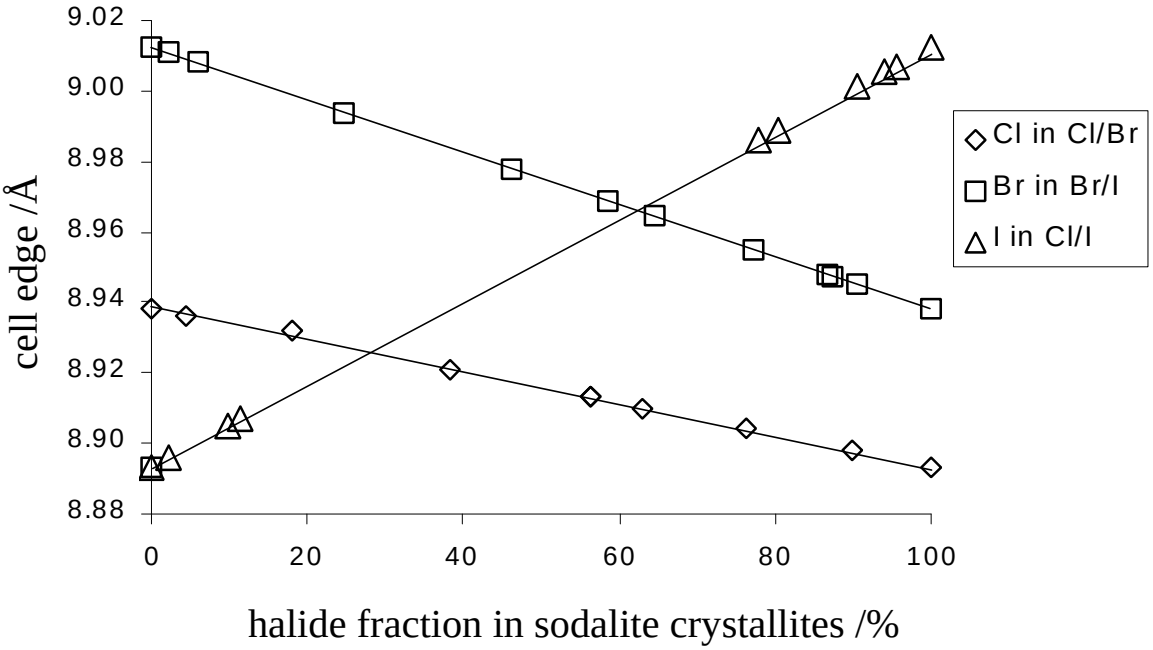

***Figure 5-1**: Lattice constants of various mixed halide sodalites, as a function of composition.*

Thus, in case of Cl/Br and Br/I sodalites, as well as some Cl/I sodalites Vegard's rule is obeyed indicating the formation of solid solutions.

Using the course of the sol-gel synthesis of these materials, it was found that, the concentration ratio of the halides in the sodalite product is not solely dependent on their ratio in the synthesis solution (see Figure 5-2). While in mixed Cl/Br sodalites, the halide fractions in the sodalite reflect their concentrations in the solution, we find that in Br/I sodalites, bromine incorporation is generally favored, except for the sample with the lowest bromine concentration. Cl and I containing precursor solutions having one halide species in excess result in single phase sodalites containing 80 to 100% of the dominant halide species. At intermediate compositions domain separation occurs.

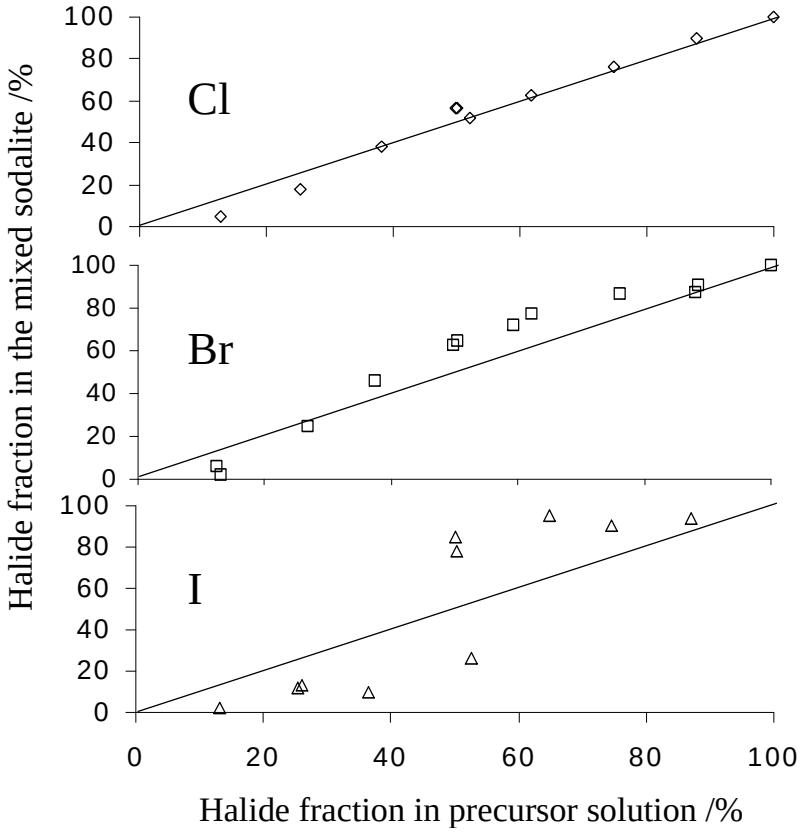

***Figure 5-2**: Halide incorporation during the synthesis. The x axis gives the halide fractions in the precursor solution, while fractions of the corresponding halide included into the sodalite framework are given on the y-axes. a) chlorine in Cl/Br sodalites, b) bromine in Br/I sodalites and c) chlorine in Cl/I sodalites. Generally more than 98% of sodalite cages are halide filled.*

In order to further investigate the effect of domain or phase separation, mixed Cl/I sodalites where synthesized at 120°C. For these samples XRD reveals the existence of two lattices shown in Figure 5-3.

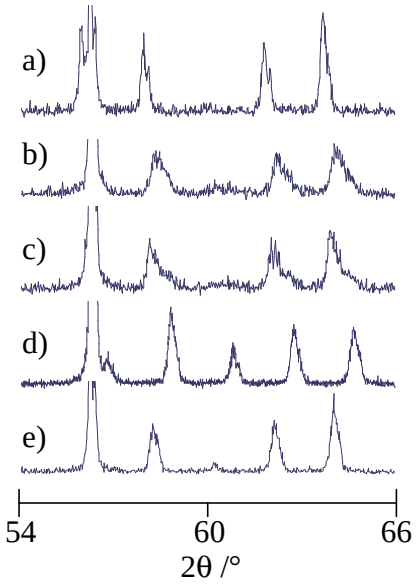

***Figure 5-3**: Bragg reflections at 54° ≤ 2θ ≤ 66° corresponding to the 521, 440, 441, 433 and 442 hkl planes. The 521 peaks partially overlap with the peak at 2θ = 56.121° from the internal silicon standard. a) I sodalite, b) Cl/I sodalite synthesized at 180°C, c) Cl/I sodalite synthesized at 120°C, d) Cl sodalite, e) Br/I sodalite synthesized at 180°C. While the peaks in b) are noticeably broadened compared to a), d) and e), the peaks of the Cl/I sodalite synthesized at 120°C clearly show two components, a broad one evidencing Cl sodalite and a sharper one indicating I sodalite.*

The powder sample of the Cl/I sodalite synthesized at 120°C clearly shows two separate lattices with lattice constants of 8.91 and 9.00 Å corresponding to nearly pure iodo and distorted chloro sodalites, while the Cl/I sample synthesized at 180°C shows single, however, broad reflections corresponding to a_0 = 8.95 Å. The powder pattern of the mixed Cl/Br sample shows sharp reflections corresponding to a lattice constant of a_0 = 8.9 Å in perfect agreement with a solid solution of 50% chloro and bromo sodalite cages.

Similar mixed sodalite systems can be formed with halide and $H_3O_2^-$ filled ca es he relations between lattice constants and composition are linear over the solid solution range with a well-defined lattice constant as portrayed in Figure 5-4. The corresponding data is given in Table 6-I in the Appendix. For these mixed halide/basic sodalites, the halide contents can be determined independently using TGA and NMR as will be discussed later. This is important, since especially pure basic and pure chloro sodalite have similar lattice sizes. Thus halide contents derived from Vegard's rule for mixed Cl/basic sodalites have errors around ± 15 %. All halide fractions for the mixed halide/basic sodalites were derived from NMR. They always lie within the confidence interval of the of X-ray and TGA measurements.

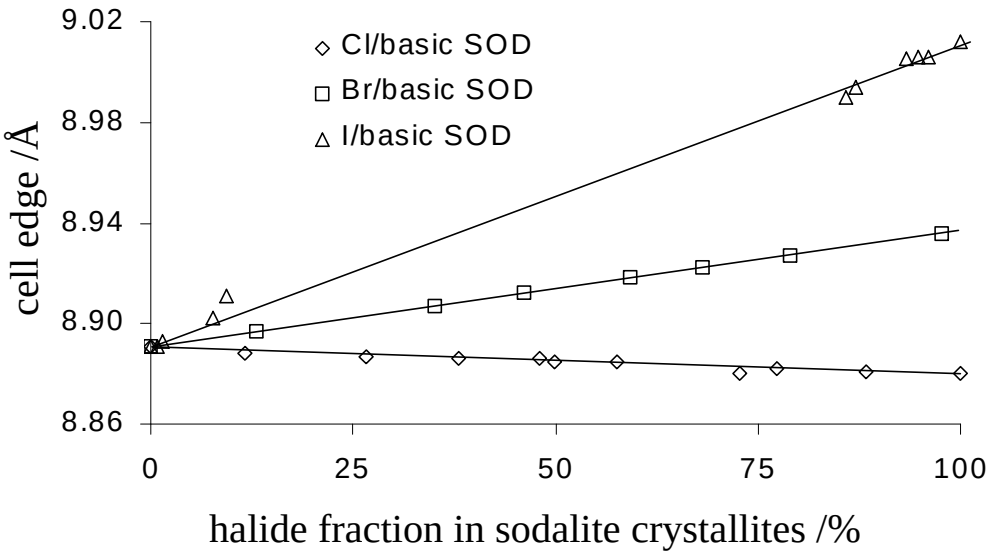

Figure 5-4: *Lattice constants of the three mixed halide/basic sodalite systems: diamonds: Cl/basic-sodalites, squares: Br/basic-sodalites, triangles: I/basic-sodalites. Mixed I/basic sodalites with halide contents around 50% could not be synthesized (see text).*

As can be seen from Figure 5-4 the lattice constants of Cl/basic and Br/basic sodalites are in excellent agreement with those predicted from Vegard's rule on the basis of the composition determined by NMR. It is noticeable, that just like Cl/I sodalites, I/basic sodalites show a pronounced solubility gap, which is wider in the latter case. Due to the fact that formation of halide centers is generally preferred over formation of basic centers by a factor of about 100, plots as given in Figure 5-2 for mixed halide sodalites turn out to be unsuitable for evaluating the mixed halide/basic sodalite systems. In order to gain deeper insight into the growth of sodalites with different extra framework species, a growth model was developed, which will later be applied to analyze and discuss the data.

5.2 Growth Simulations

Based on the findings of the previous paragraph, it seemed necessary to develop a mathematical model capable of describing the experimental findings by few parameters. In addition a measure for the deviation of these quasi solid solution systems from a perfect binomial distribution must be developed. The approach chosen here is based on a simple model: The sodalite cages form a bcc lattice and the growth was investigated in the (111) direction. On each new plane, each cage built is connected to four sodalite cages in the plane below by six-ring windows and to one cage two planes below by a four ring window (see Figure 5-5).

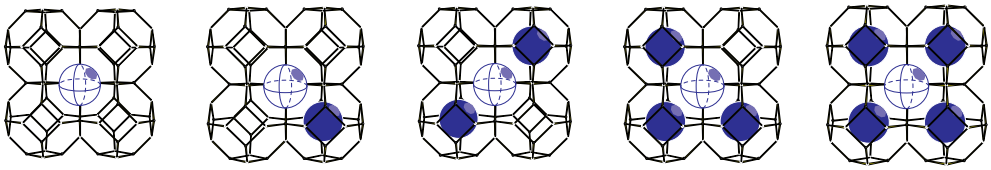

Figure 5-5: *Different formation scenarios for the growth of a new sodalite cage in the 111 direction. The probabilities of the new cage (transparent sphere) to be occupied by X (blue sphere) or species Y (empty cage) are given in Table 5-I.*

Also the cage can be connected to four cages in the same plane through four-ring windows. To simplify the model, it was assumed that the preferred size of the new cage and therefore a preference for a certain halide species is influenced by all surrounding cages, but mainly by those connected to the cage in question by the larger six-ring windows. (It should be possible to show that similar statistics can be achieved if all windows are taken into account, but due to the extensive computational demand, the four neighbor model was chosen here.)

A 1000 x 1000 matrix with random (binomial) distribution of two halide species (X and Y) according to the given concentrations of the precursor solution ($[X]_l$ and $[Y]_l$) was computed. With the first matrix as a starting point, a second matrix was calculated, where the probabilities of inclusion of the species X were modified based on four matrix elements (according to the occupancies of the cages in the lower plane) of the prior matrix. Periodic boundary conditions were chosen to eliminate surface effects. The modification of the inclusion probability was introduced by a "separation factor" *f*, which covers values between 0 and 1, where 0 causes no deviation from the binomial distribution and 1 causes the maximum deviation and thus complete phase separation. The probabilities of inclusion of the species X and Y ($P(X_s)$ and $P(Y_s)$) are then defined, based on their concentrations in the precursor solution, with the occupancies of the lower four sodalite cages and the separation factor as shown in Table 5-I.

Base plane occupation (X:Y)	Incorporation of minor halide	Incorporation of X
(0 : 4)	$P(X_s) = [X]_l \cdot (1-f)^2$	$P(X_s) = [X]_l \cdot (1-f)^2$
(1 : 3)	$P(X_s) = [X]_l \cdot (1-f)$	$P(X_s) = [X]_l \cdot (1-f)$
(2 : 2)	$P(X_s) = [X]_l$, $P(Y_s) = [Y]_l$	$P(X_s) = [X]_l$
(3 : 1)	$P(Y_s) = [Y]_l \cdot (1-f)$	$P(X_s) = [X]_l \cdot (1-f) + f$
(4 : 0)	$P(Y_s) = [Y]_l \cdot (1-f)^2$	$P(X_s) = [X]_l \cdot (1-f)^2 + f(2-f)$

Table 5-I*: Simulated probabilities of halide inclusion for cages built in the $n+1^{st}$ layer as functions of their occupancy distribution in the four connected cages of the lower crystal layer.*

Thus, the composition of the n+1st layer of the fictive crystallite can be calculated based solely upon the occupancy distribution in the nth layer. The fractional occupation of both halides usually converges against constant values after a few layers, only affected by statistical deviations due to the finite size of the matrix used. As a result, the convergence limits of the halide occupations can be considered as the halide fractions inside the sodalite crystal. Examples of such growth matrices are displayed in Figure 5-6.

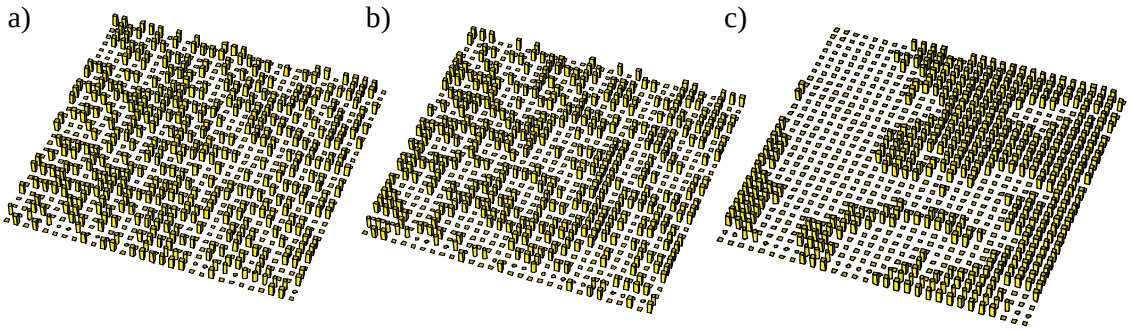

Figure 5-6: *30x30 matrices, extracted from convergent 1000x1000 matrices for precursor fractions of 0.5 and separation factors of a) 0.0, b) 0.4 and c) 0.9. The columns represent the species X, while empty spaces denote the species Y.*

As can be seen from Figure 5-6, larger separation constants obviously cause agglomeration of a given type of halide occupied cage; while for $f = 0$, agglomerations are in perfect agreement with a binomial distribution, a value of $f = 0.4$ already produces small domains of each species and a value of $f = 0.9$ can be considered to produce phase separation.

Motivated by a possible NMR probe to find a numerical measure for these effects, it is reasonable to determine the probabilities of the 5 possible combinations of 4-cage environments present. The probabilities counted from the computed matrix can then be compared to probabilities expected from binomial distribution at the same overall halide content; this can be done for all halide compositions. The differences can then be summed up over all environments resulting in a deviation factor *h*.

$$h = \sum_{i=0}^{4} \left| P_{comp}(iX) - P_{bin}(iX) \right| \qquad \text{Equ. 5-1}$$

with $P_{bin}(iX)$ according to Equation 3-4. $P_{comp}(iX)$ is the probability of an environment with *i* X-species, as determined from the convergent matrix and $P_{bin}(iX)$ is the probability resulting from the binomial distribution at a given $[X]_s$, where $[X]_s$ is the fraction of the species X in the convergent matrix.

The advantage of this method is that, as will be shown later in more detail, the ^{27}Al spin, located at the joint of four sodalite cages exactly serves as such a probe and its NMR resonances resemble the summation of the five possible environments. The effects of certain separation constants *f* and precursor concentrations $[X]_l$ and $[Y]_l$ on the halide fractions in the crystallites and the deviation factor *h* are shown in Figure 5-7.

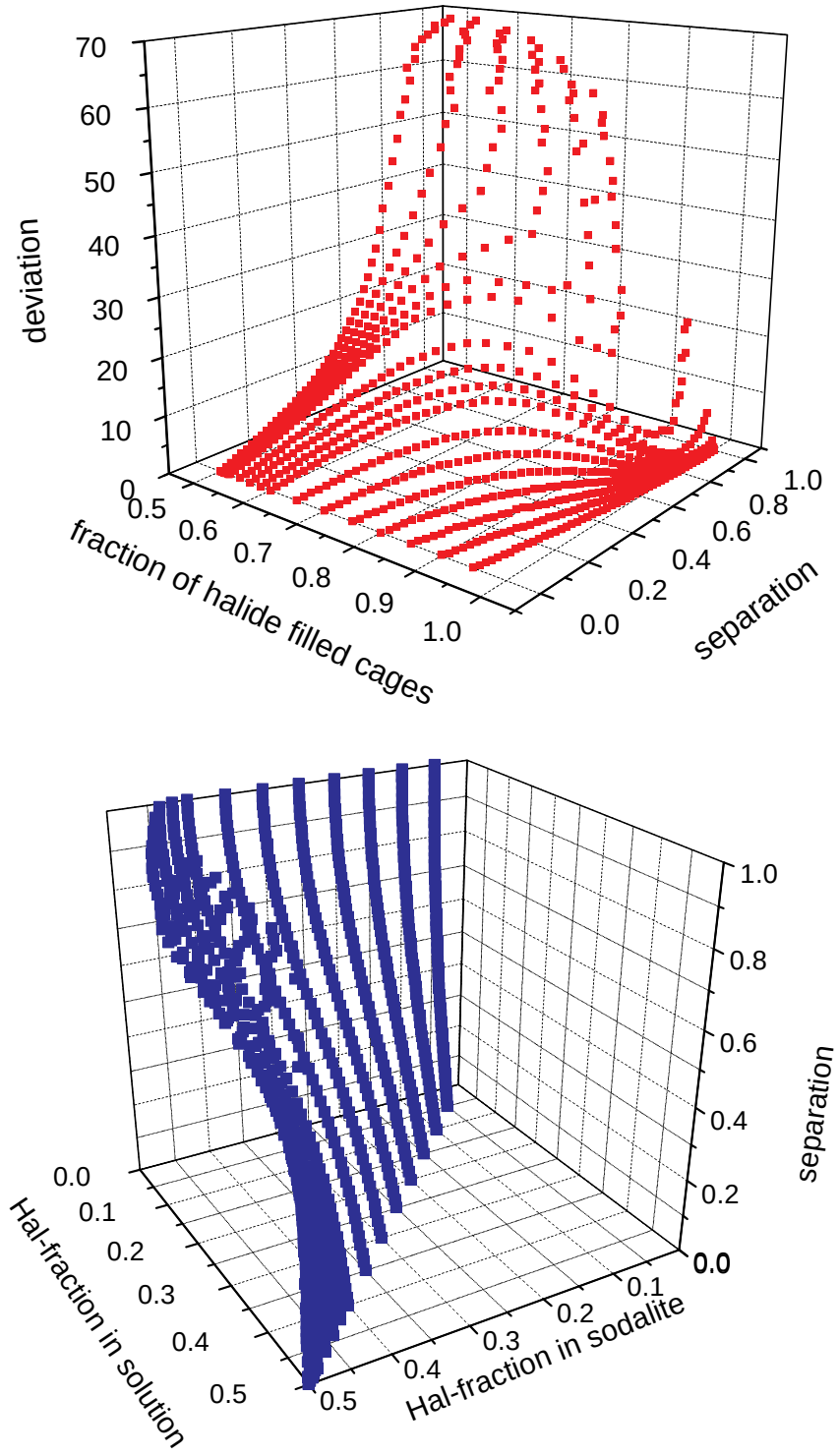

Figure 5-7: *Effects of the separation constants between the solid solution species.*

a) *deviation of probabilities of the five aluminum environments from the probabilities resulting from perfect binomial distribution, as a function of the separation factor and the overall halide fraction. The data has a mirror symmetry in the yz-plane at x = 0.5.*

b) *incorporation of one species from the precursor solution. The data has a C2 axes parallel to the z-axes at x = y = 0.5.*

Figure 5-7a shows the calculated deviation factor as a function of the halide fraction and the separation factor. Since the halide fractions of sodalite solid solutions are easy accessible and

the deviation factor can be determined experimentally via NMR, Figure 5-7a allows the identification of the separation factor and therefore allows a simulation of the species distribution inside the crystallite. Figure 5-7b shows the calculated dependence of the species fraction $[X]_s$ on its fraction in the synthesis solution $[X]_l$ at different values of the separation factor. In this figure the xy-planes are comparable to the upper left quarters of the diagrams in Figure 5-2. For small separation factors, the relation between precursor fractions and incorporated fractions is linear, while for higher separation factors the curve becomes more S-shaped to turn into a step function for a separation factor of 1. Comparison of experimental and theoretical halide incorporation curves therefore also allows the determination of the separation constant and thus gives an insight into the likely distributions of the halide species throughout the crystallite.

So far the results of this growth model are symmetrical with respect to the halide species X and Y, that is no species is *a priori* preferred. In order to include this possibility into the model it will first be discussed for the case f = 0 and later be extended for the cases f > 0. If the cages already formed have no influence on the new cages being built, the two species X^- and Y^- will compete for the inclusion into the growing sodalite lattice.

$$\left(X^-\right)_l + \left(Y^-\right)_s \underset{k_Y}{\overset{k_X}{\rightleftharpoons}} \left(X^-\right)_s + \left(Y^-\right)_l \qquad \text{Equ. 5-2}$$

where *l* and *s* denote the liquid and solid phases, respectively. Under equilibrium conditions, an equilibrium constant $K_{X/Y}$ (*selectivity factor*) is given by:

$$K_{X/Y} = \frac{k_X}{k_Y} = \frac{[Y^-]_l}{[X^-]_l} \cdot \frac{[X^-]_s}{[Y^-]_s}$$

$$\text{or} \quad \frac{[X^-]_s}{[Y^-]_s} = K_{X/Y} \cdot \frac{[X^-]_l}{[Y^-]_l} \qquad \text{Equ. 5-3}$$

Here $[X^-]_s$ and $[Y^-]_s = 1 - [X^-]_s$ are the fractional occupancies of sodalite cages by anions X and Y, respectively. The selectivity factor, $K_{X/Y,}$ denotes how many times the X^- species is more likely to be incorporated into the lattice than the Y^- species. Equation 5 – 3 thus allows to determine this selectivity factor for a system where no separation occurs (or where this case can reasonably be expected), by the plot of the X^- fractions in the solid against that in the liquid precursor solution, yielding the selectivity factor as the slope of a linear function.

The two effects of separation and selectivity can now be combined in the following way. The halide fractions of the synthesis solution, included in the probability determination

for halide inclusion in the growth model, have to be exchanged for effective halide fractions in the synthesis solution according to the selectivity factor:

$$[X^-_{eff}]_l = \frac{K_{X/Y}[X^-]_l}{K_{X/Y}[X^-]_l + [Y^-]_l}$$

$$[Y^-_{eff}]_l = \frac{[Y^-]_l}{K_{X/Y}[X^-]_l + [Y^-]_l} \qquad \text{Equ. 5-4}$$

The latter equation can actually also be expressed similar to the first, where $K_{X/Y} = 1/K_{Y/X}$ in accordance with Equation 5-3. It is now interesting to note that the selectivity factor can also be easily determined for systems which show separation effects, by analysis of those synthesis solution compositions ($[X_{0.5}]_l$ and $[Y_{0.5}]_l$), producing the sodalite species fractions $[X]_s = [Y]_s = 0.5$ in the solid state. In this case Equation 5-3 turns into:

$$\frac{0.5}{0.5} = K_{X/Y} \cdot \frac{[X^-_{0.5}]_l}{[Y^-_{0.5}]_l} \quad \text{or} \quad K_{X/Y} = \frac{[Y^-_{0.5}]_l}{[X^-_{0.5}]_l} \qquad \text{Equ. 5-5}$$

The point $[X]_s = [Y]_s = 0.5$ is exceptional, because the influence of the separation factor is eliminated due to equal incorporation of both species. The effects of selectivity and separation factors on the "incorporation diagrams" such as Figure 5-2 are shown in Figure 5-8:

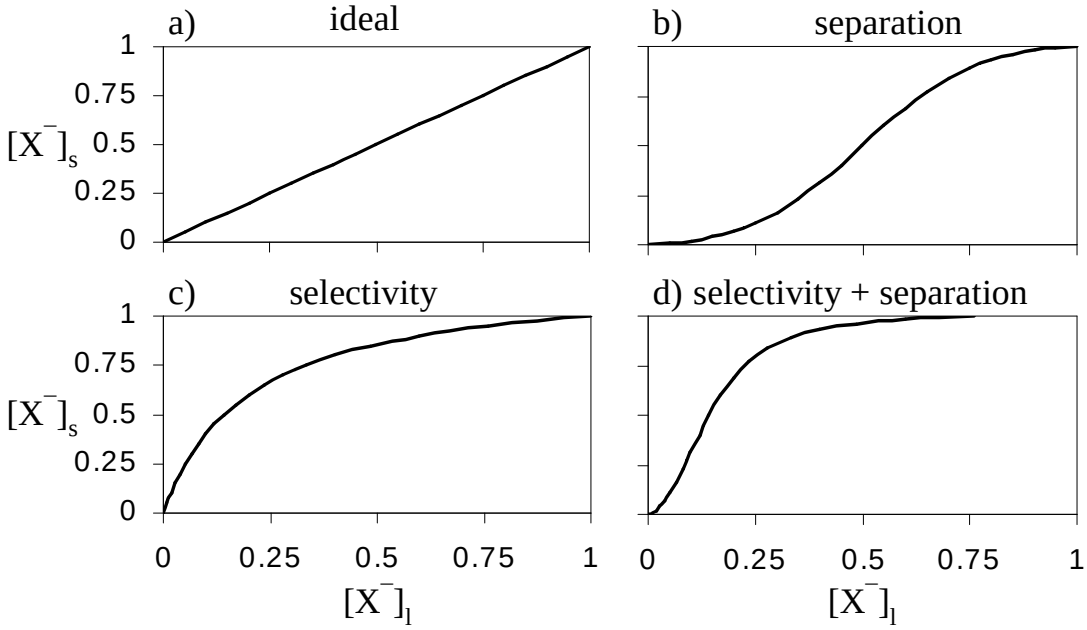

Figure 5-8: *Incorporation diagrams:* ***a)*** *ideal case: $K_{X/Y} = 1$ and $f = 0$;* ***b)*** *domain separation occurs: $K_{X/Y} = 1$ and $f = 0.3$;* ***c)*** *binomial distribution is still present, but one species is generally preferred: $K_{X/Y} = 6$ and $f = 0$;* ***d)*** *while one species is preferred, also domain separation occurs. $K_{X/Y} = 6$ and $f = 0.3$. In c) and d) the selectivity factor $K_{X/Y} = 6$ can be determined from $[X^-_{0.5}]_l = 0.143$ and $[Y^-_{0.5}]_l = 0.858$ according to Equation 5.5.*

5.3 Discussion of the Experimental Data along the Growth Model

Equipped with such tools, we can express the preference of the mixed halide/basic sodalite for the halide by the selectivity factor. In order to extract these values, Figure 5-9 plots the fractional compositions according to Equation 5-3. Clearly the quality of these fits expressed by the R value decreases from Cl to Br to I. While the fits for the Cl/basic and the Br/basic sodalite are reliable, the extremely low quality fit for I/basic sodalites suggest that the model applied is no longer valid. As discussed above Equation 5-3 is only valid for systems without a trend to separation. Such trends are likely to be caused by different cage size requirements of the two competing species, favoring spatial agglomeration of cages containing the same anion. The differences of the equilibrium lattices between chloro sodalite, bromo sodalite and iodo sodalite on one hand and basic sodalite on the other are 0.009 Å, 0.045 Å and 0.121 Å, respectively. While the sodalite lattice itself is very flexible in hosting these guests, the formation of a solid solution requires the anions to accommodate inside a cage with unfavorable diameter, changing its natural Na-halide distance and/or putting strain on the lattice. With an increase of differences in equilibrium cage diameters, however, these systems tend to deviate from solid solutions, first forming domains, dominated by one species, and eventually leading to total phase separation such as known for ClO_4/basic sodalites.[83] Therefore it is not surprising that the deviation from the ideal behavior increases in the observed order. Apparently in the case of I/basic sodalite the selectivity factor cannot be determined the same way as for the other two mixed halide/basic sodalite systems. In Figure 5-8d the halide fraction in the I/basic sodalite lattice is plotted against the corresponding value in the synthesis solution. Although a data point with $[I^-]_s = 0.5$ is missing because no single phase material with this composition could be synthesized, an approximated fitting according to Figure 5-7d yields a value of $[I^-_{0.5}]_l = 0.0125 \pm 00.25$. According to Equation 5-5 this corresponds to a selectivity factor of about 80 ± 20.

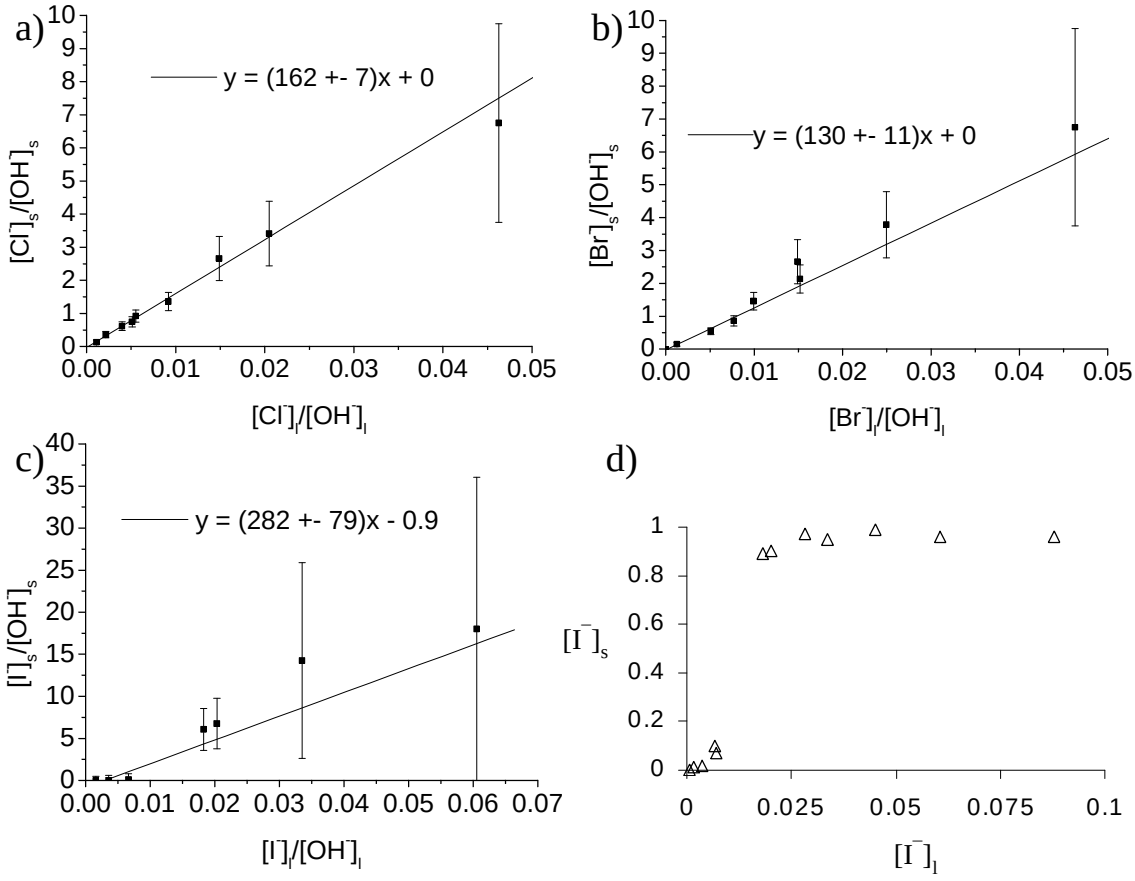

Figure 5-9: *a-c: plots of the fractional ratios of halide and OH ratio in solution:* ***a)*** *Cl/basic sodalites,* $K_{Cl/OH}$ *= 162 ± 7;* ***b)*** *Br/basic sodalites,* $K_{Br/OH}$ *= 130 ± 11;* ***c)*** *I/basic sodalites,* $K_{I/OH}$ *= 282 ± 79 is only an apparent value. Accuracy of the fits decreases from Cl/basic to Br/basic to I/basic from R = 0.994 to R = 0.984 to R = 0.73, respectively.* ***d)*** *I/basic sodalites: plot of halide fraction in the sodalite versus the fraction in the solution (see text).*

If the incorporation diagrams in of the mixed halide sodalites (Figure 5-2) are analyzed according to the growth model, it is obvious, that the separation factors for the mixed halide sodalite systems increase with increasing difference of the equilibrium cell edge of the pure sodalite species. From comparison with the data plotted in Figure 5-7b, the *f*-values can be estimated to be about 0.05 for Cl/Br sodalites, 0.2 for Br/I sodalites and 0.8 for Cl/I sodalites and thus give an idea of the clustering and the deviations from perfect binomial distribution. In addition, we can also extract the selectivity factors according to Equation 5-5: $K_{Cl/Br}$ = 1 ± 0.2, $K_{Br/I}$ = 1.5 and $K_{I/Cl}$ = 1.3 ± 0.8. These values are in good agreement with the corresponding ratios of selectivity factors in the mixed halide/basic sodalite systems. The precision of $K_{I/Cl}$ is actually this small, because the outcome of 1:1 halide ratios in the synthesis cannot be related to any of the observed factors and might be highly sensitive to preparation times or warming rates of synthesis vessels in the furnace.

It is interesting to compare these values with values observed for growth rates of pure halide sodalites at a synthesis temperature of 95°C.[84]

		Selectivity factor at 180°C	Growth rate ratio at 95°C
a)	Cl/basic	162	6
b)	Br/basic	130	3
c)	I/basic	80	1

Overall the results indicate that the preference for the smaller species decreases with increasing temperature, which is in fine agreement with the results of high temperature solid state synthesis, where no preference for any specific halide is reported at all.[27] This clearly indicates that synthesis at sufficiently high temperatures can overcome any enthalpic preferences for anions of certain sizes resulting in the entropy favored, thermodynamically most stable solid solutions. Therefore we conclude that at 180°C the formation of mixed sodalites is still controlled by enthalpy differences between different sodalite cages. The preferred cage size appears to be somewhere between the values of pure chloro and pure bromo sodalite. This would explain the symmetry of chlorine and bromine intake, while in the Br/I case bromine is preferred. The inability of forming Cl/I sodalite solid solutions over the whole concentration range is then due to the different size requirements of both halide ions, which, at this temperature, cannot be overcome energetically.

6 Mixed Halide Sodalites

As shown in the paragraph above, in all series of sodalites having different extra framework species, the lattice parameters vary continuously with the compositions, obeying Vegard's rule. Investigation of the variation of NMR parameters throughout these series provides a unique opportunity to observe the dependence of chemical shielding and quadrupolar coupling, with respect to distance changes between the atoms and small changes in the ionic environments, respectively, without the application of high pressure or high temperatures, which always involve unwanted side effects. Representative ^{27}Al, ^{23}Na, ^{35}Cl, ^{81}Br and ^{127}I MAS NMR spectra of the various solid solution series are portrayed in Figure 6-1 to 6-3. The corresponding NMR parameters are given in Table 6-I in the Appendix.

6.1 Experimental Observations

6.1.1 ^{27}Al MAS NMR

As can be seen from Fig. 6-1A and 6-2A all of the Cl/Br and Br/I mixed halide sodalites show single ^{27}Al NMR resonances which vary only slightly in shift and linewidth. The quadrupolar coupling parameters P_Q, determined from field dependent measurements, scatter around 0.8 MHz and are in agreement with values for pure halide sodalites.[52] For all the solid solution series, the chemical shift varies linearly with the lattice constant. For mixed Cl/I sodalites, with compositions close to 1:1 the observed lineshapes consist of two overlapping resonances which are also not well resolved in ^{27}Al TQ MAS NMR spectra. The average chemical shifts and quadrupolar coupling constants of those resonances, however, are close to the values of pure Cl- and I- sodalite. This finding is in good agreement with the x-ray data indicating the presence of two domains as shown in Figure 5-3. Apparently the different halide anion sizes would cause too much strain on the framework if they were incorporated into a single lattice, thus phase separation is preferred.

6.1.2 ^{23}Na MAS NMR

Fig. 6-1B to 6-3B show the ^{23}Na MAS NMR spectra of the three series of mixed halide sodalites. In the Cl/Br series, two sodium resonances are clearly separated from each other. Based on the compositional evolution of their intensities, it is obvious that the high frequency resonance has to be assigned to sodium in bromo-cages, while the low frequency resonance originates from sodium in chloro-cages. The quadrupolar coupling constants are about 0.8 MHz and 0.4 MHz for the high and low frequency resonance, respectively and scatter by only 0.1 MHz throughout the whole series. A representative TQ MAS NMR spectrum is shown in Figure 6-4a. Besides the variation in intensity also a variation of the chemical shift with composition is observed. As the lattice constant increases, both ^{23}Na resonances are shifted to lower resonance frequencies.

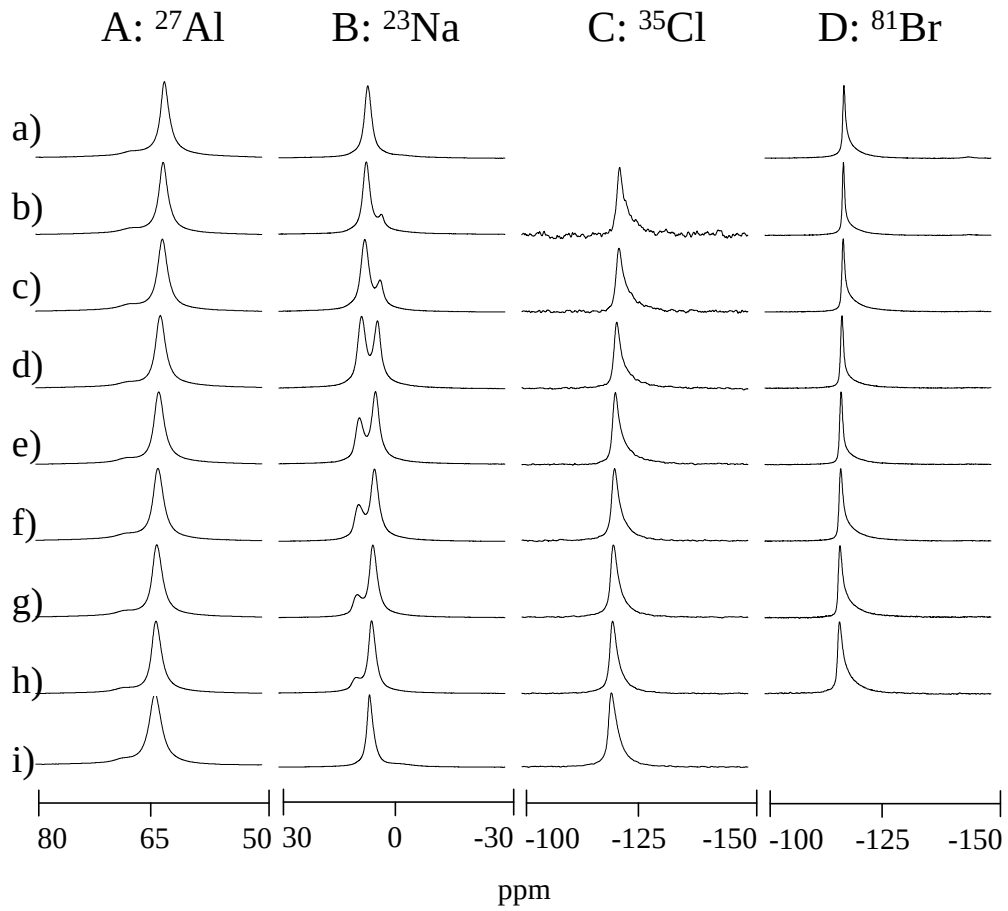

Figure 6-1 (above): *^{23}Na, ^{27}Al, ^{35}Cl and ^{81}Br MAS NMR spectra of mixed Cl/Br sodalites. The spectra were taken in a 11.7 T magnetic field at a spinning speed of 10 kHz. The sodalite cages are over 98% occupied by halide ions of which a) 0%, b) 5%, c) 18%, d) 38, e) 56%, f) 62%, g) 76%, h) 90%, i) 100% are chlorine.*

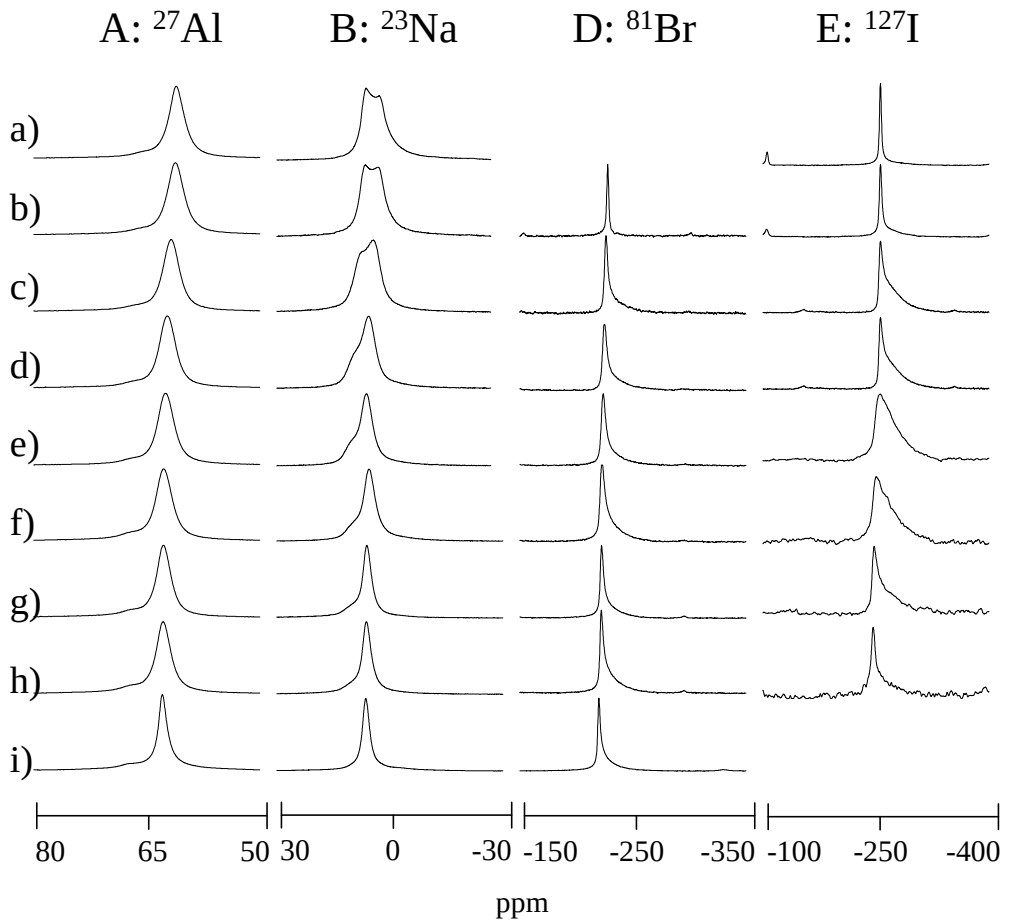
A: 27Al
B: 23Na
D: 81Br
E: 127I
a)
b)
c)
d)
e)
f)
g)
h)
i)
80 65 50
30 0 -30
-150 -250 -350
-100 -250 -400
ppm

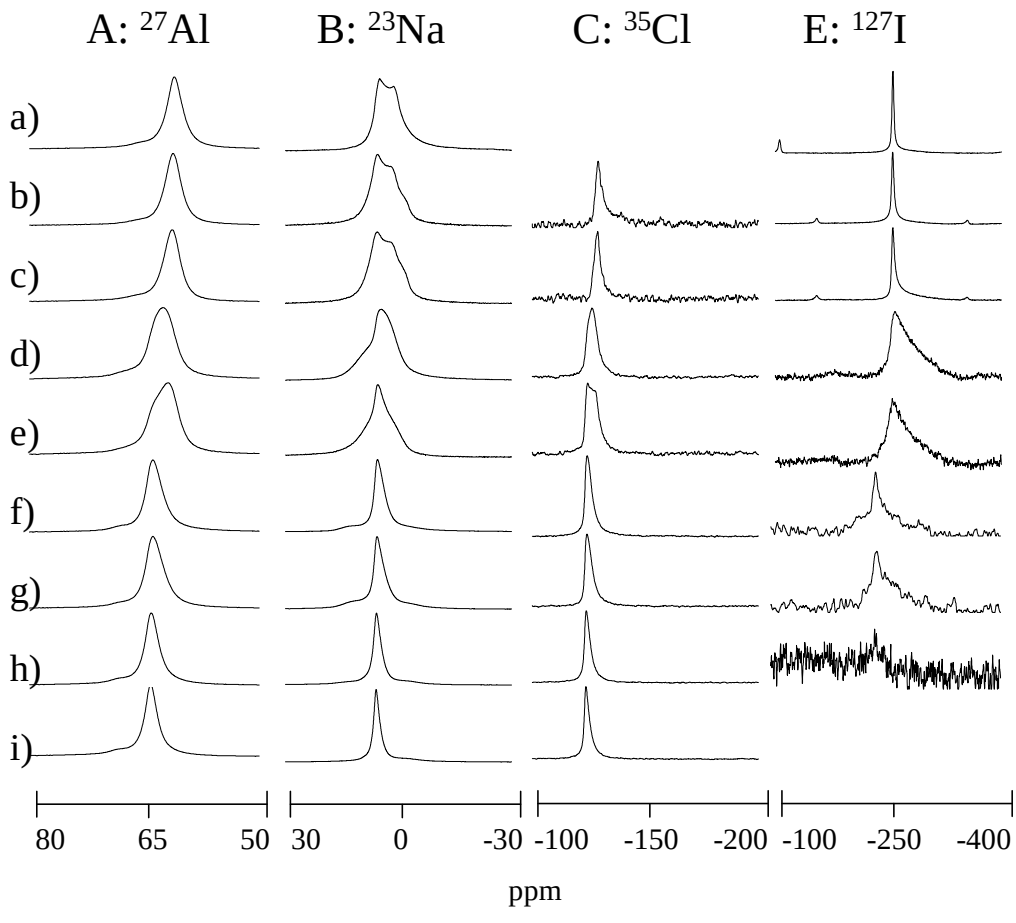
A: 27Al
B: 23Na
C: 35Cl
E: 127I
a)
b)
c)
d)
e)
f)
g)
h)
i)
80 65 50
30 0 -30
-100 -150 -200
-100 -250 -400
ppm

Figure 6-2 (previous page top): *^{23}Na, ^{27}Al, ^{81}Br and ^{127}I MAS NMR spectra of mixed Br/I sodalites. The spectra were taken in a 11.7 T magnetic field at a spinning speed of 10 kHz. The sodalite cages are over 98% occupied by halide ions of which a) 0%, b) 6%, c) 25%, d) 46, e) 65%, f) 77%, g) 86%, h) 91%, i) 100% are bromine.*

Figure 6-3 (previous page bottom): *^{23}Na, ^{27}Al, ^{35}Cl and ^{127}I MAS NMR spectra of mixed Cl/I sodalites. The spectra were taken in a 11.7 T magnetic field at a spinning speed of 10 kHz. The sodalite cages are over 98% occupied by halide ions of which a) 100%, b) 95%, c) 94%, d) 89, e) 78%, f) 11%, g) 10%, h) 3%, i) 0% are iodine.*

In the series of Br/I sodalites, also two resonances can be observed, albeit less well resolved. Again, the areas underneath the simulated lineshapes reflect the corresponding halide fractions. The quadrupolar coupling parameter P_Q for sodium in bromo-cages is 0.8 MHz, similar to the one in the Cl/Br series. For sodium in iodo-cages, P_Q is 1.75 MHz and increases to 2.1 MHz for sodalites containing little iodine. These quadrupolar parameters had to be deduced from TQ MAS spectra as shown in Figure 6-4b, which clearly separate the two spectral components.

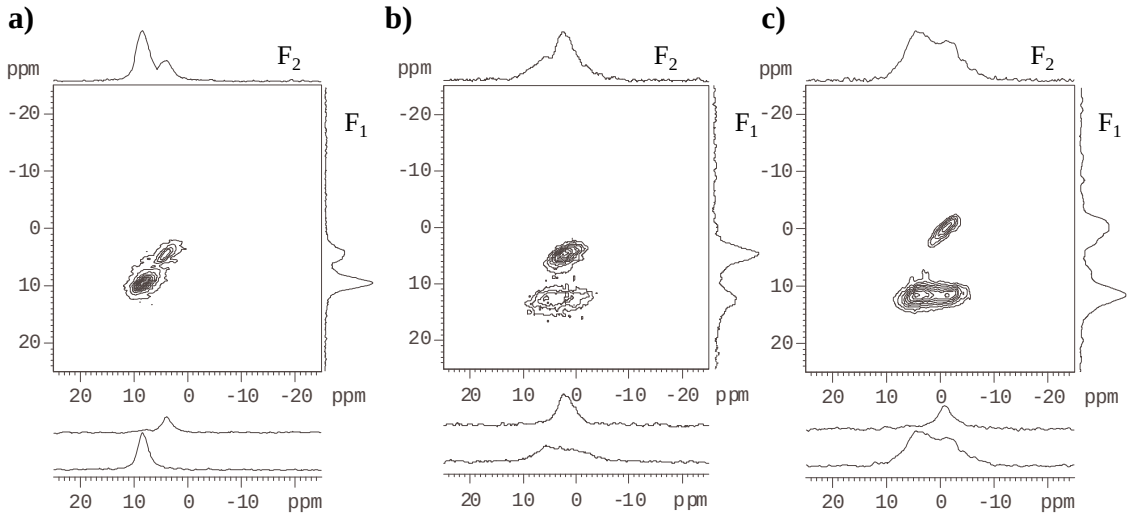

Figure 6-4: *^{23}Na TQ MAS NMR spectra of a) mixed Cl/Br sodalite corresponding to sample 6-1 d, b) mixed Br/I sodalite corresponding to sample 6-2 f, c) mixed Cl/I sodalite corresponding to sample 6-3 g. All spectra were acquired at a spinning speed of 15 kHz in a 11.7 T magnetic field. The 1D spectra shown below the 2D graphs represent slices in the F_2 dimension cutting through the centers of gravity of each resonance in the F_1 dimension.*

As seen above, Cl/I sodalites do not form solid solutions over the entire compositional range. The ^{23}Na MAS NMR spectra of the high and low Cl containing mixed Cl/I sodalites, however, show the same trends in intensities as in chemical shifts and P_Q values as do the ^{23}Na NMR spectra of the other series. For the 25% Cl containing mixed Cl/I sodalites, the ^{23}Na TQ MAS NMR spectrum (Figure 6-4c) clearly resolves the two environments. All

parameters in this series had to be determined by TQ MAS, since the broad lineshape of the sodium ions in the I-bearing cages cannot be fitted accurately in 1D spectra.

^{23}Na NMR shieldings and electric field gradients were also calculated by GAUSSIAN98[81] as described in the Experimental section. As a reference point the sodium NMR shielding of a sodium ion, coordinated by six water molecules was chosen. The equilibrium Na-O distances were found to be 2.383 Å, resulting in an absolute shielding σ_{ref} = 578 ppm. The absolute shielding of a free sodium ion was 631 ppm. Sodium shieldings were calculated for six-ring arrangements with chlorine, bromine and iodine, as well as with "empty" cages (dry sodalite). The shielding values are given in Table 6-II in the Appendix and can be converted into chemical shifts as follows:

$$\delta = -(\sigma - \sigma_{ref}) \qquad \text{Equ. 6-1}$$

In good agreement with the experimental data, the calculations reveal that ^{23}Na is increasingly deshielded along the series Cl r urther ore within each series the shieldin increases with increasing Na-halide distance. With increasing halide atomic number the sensitivity of the ^{23}Na shielding to this distance variation increases significantly; in contrast for sodium in dry cages almost no dependence on the cage diameter is found in agreement with previous experimental results.[6]

For the ^{23}Na quadrupolar coupling constant, our experimental results show an increase from Cl to Br to I ligands of 0.4, 0.8 and 1.75 MHz, respectively, in good agreement with values determined previously from SATRAS NMR spectroscopy of the pure halide sodalites.[52] In contrast this trend is not revealed by the ab-initio calculations. Furthermore the computed C_Q-values are found to be highly sensitive on the Na-halide distance at variance with the experimental findings. These discrepancies are ascribed to the intrinsic limitations of the theoretical model, which lacks appropriate charge balance needed to produce more accurate results. A sufficiently charge balanced environment would require more than 100 atoms, which is beyond our computational capabilities.

6.1.3 ^{35}Cl, ^{81}Br and ^{127}I MAS NMR

All ^{35}Cl MAS NMR spectra of the chloride-containing mixed sodalite series show (with one exception) a single resonance (Figure 6-1C, 6-3C). The chemical shifts observed vary between -123.9 and –128.7 ppm for pure chloro sodalite and 5% chloride containing iodo sodalite, respectively. The lineshapes are in all cases nearly symmetric and only weak

quadrupolar coupling constants (C_Q = 0.4 ± 0.3 MHz) could be estimated from field dependent measurements. For pure chloro-sodalite a P_Q value of 55 ± 5 kHz was estimated from the satellite transition spinning sideband manifold (SATRAS) portrayed in Figure 6-5a. In the case of 50% Cl containing mixed Cl/I sodalite the spectrum can be fitted with two main resonances with chemical shifts of 127.6 and 124.6 ppm suggesting the existence of two separate regions or phases in agreement with the segregated character of this sample. A distribution of chemical shifts between these values can be noted as well, suggesting the occurrence of domains with intermediate compositions.

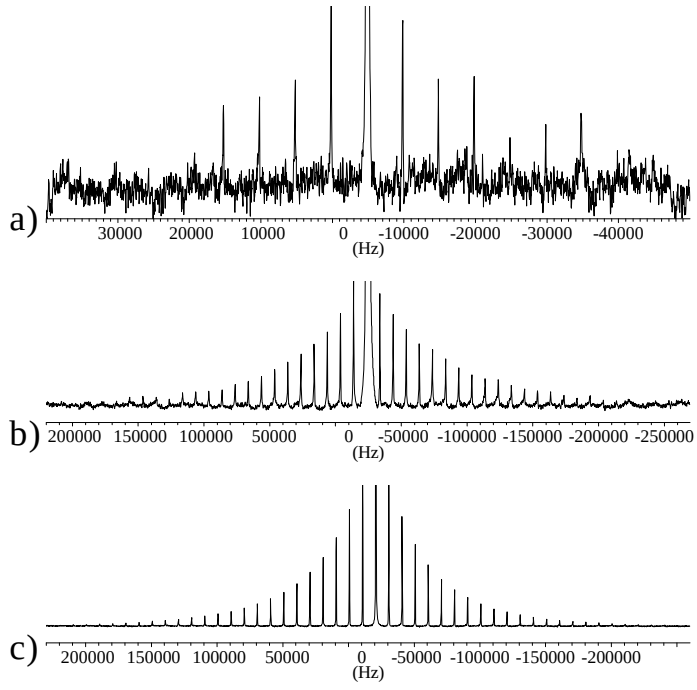

Figure 6-5: *a)^{35}Cl, b) ^{81}Br and c) ^{127}I SATRAS NMR spectra of pure chloro, bromo and iodo sodalites at 39.19, 108.02 and 80.03 MHz, respectively. The spinning speeds were 7kHz for a) and 10kHz for b) and c). The central resonance is plotted off-scale to enhance the weaker spinning sideband manifolds generated by the effect of MAS on the first order quadrupolar satellite powder pattern.*

The ^{81}Br spectra of all Br containing sodalites, displayed in Figures 6-1D and 6-2D, also show only one resonance, the chemical shift of which depends on the composition and varies between -217.4 and -227.8 ppm for low bromide containing chloro and iodo sodalites, respectively. Except for pure bromo sodalite, all lines show a low frequency asymmetry, which becomes more pronounced with decreasing bromine content. The P_Q values also increase with decreasing bromine content and vary between 0.5 MHz and 0.9 MHz. These must be considered average values, since the lineshape indicates a distribution of quadrupolar coupling constants.

The values given here were deduced from the peak positions measured at 9.4 and 11.7 T, using Equation 2-63. The SATRAS spectrum of pure bromo sodalite is shown in Figure 6-5b and indicates a distribution of P_Q values around a mean value 400 kHz.

The ^{127}I spectra (Figure 6-2E and 6-3E) reveal the strongest dependence on composition. While the chemical shift varies between –236 and –256 ppm within the range of the samples studied, the ^{127}I lineshape proves extremely sensitive to the composition of the sample. For pure I sodalite, a linewidth of 270 Hz was observed, which increases to more than 4000 Hz with decreasing iodine content in these mixed Cl/I and Br/I sodalites. In the low iodide concentration limits, the linewidths decrease to about 1000 and 400 Hz for Cl/I and Br/I sodalites, respectively. A similar trend is observed in the P_Q parameters, which change between 400 ± 20 kHz and 4.0 ± 2 MHz throughout these series. The ^{127}I SATRAS spectrum (Figure 6-5c) again indicates a distribution of P_Q values for the pure iodo sodalite around a mean value of 0.8 MHz.

6.2 Discussion

6.2.1 Solid Solution Effects on the Framework

The first two coordination spheres of aluminum in mixed halide sodalites are similar for all aluminum atoms. Therefore it is not surprising that only single ^{27}Al resonances are observed for all mixed sodalites in this study, except in those samples with incipient phase separation (sample 6-3e). Nevertheless this observation shows that none of the central anions has a noticeable effect on the electronic environment of the framework building T-atoms. While the P_Q values for all the aluminum resonances scatter around 0.8 MHz, the chemical shifts show a linear dependence on the calculated T-O-T bond angle as shown in Figure 6-6:

$$\delta = 167.6 \text{ ppm} - \alpha_{TOT} \cdot 0.744 \text{ ppm/°} \qquad \text{Equ. 6-2}$$

Over the T-O-T bond angle range observed, Equ. 6-2 agrees with in 0. 5 ppm with the correlations established in the literature.[48,49,59] Since these systems obey Vegard's rule, in principle the observation of the ^{27}Al resonance can be used instead of X-ray data for the determination of the lattice constant. In case of deviations from solid solution behavior, the ^{27}Al signal is even more sensitive to domain separation than x-ray diffraction. The latter will be of importance throughout the paper, since various cell parameters, such as T-O-T bond angles and Na-halide distances, will be derived from lattice constants according to Chapter 3, assuming solid solution behavior.

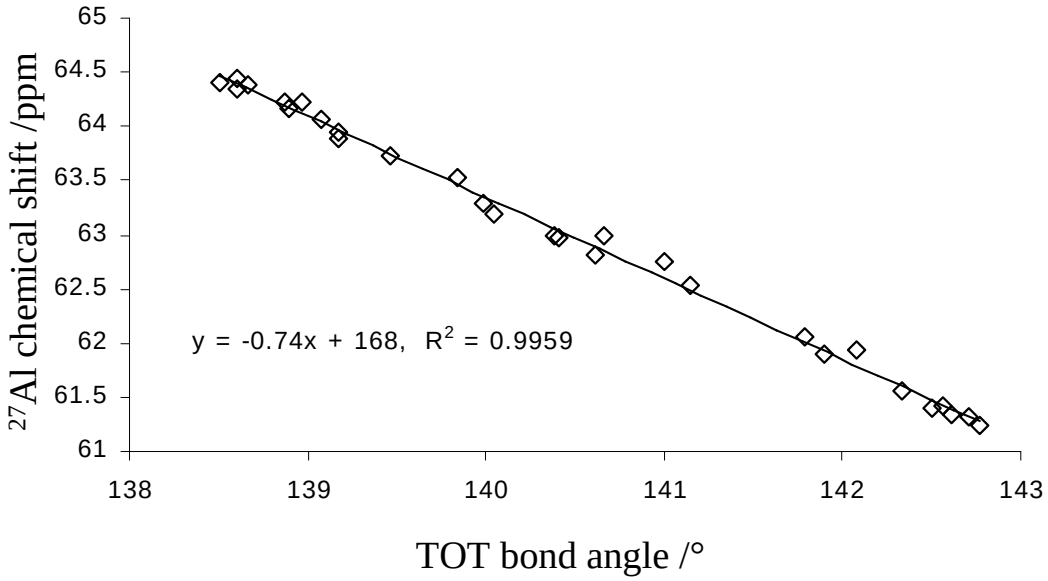

Figure 6-6: *^{27}Al chemical NMR shift as a function of the average T-O-T bond angle, derived from the lattice constant according to Equation 3-2.*

6.2.2 The extra Framework Species

The sodium ions in halide sodalites are four coordinated by three framework oxygen atoms, which are all part of one Al-Si six-ring and the halide in the center of the cage. Since it has been shown that the Na-O distance for the three pure halide sodalites is (2.355 ± 0.005)Å it is reasonable to assume that this is also valid for sodium in the cages of mixed halide sodalites. Based on this assumption, the Na-halide distance is directly computable from the cell edge length of the sodalite lattice as shown in Equation 3-4. Since it could be shown that this cell edge can be tuned easily between 8.870 Å and 9.012 Å, the Na-halide distance can be varied between 2.7 Å and 3.07 Å, giving an experimental insight into the dependence of chemical shift on Na-halide distances, both for the ^{23}Na and the halide resonances.

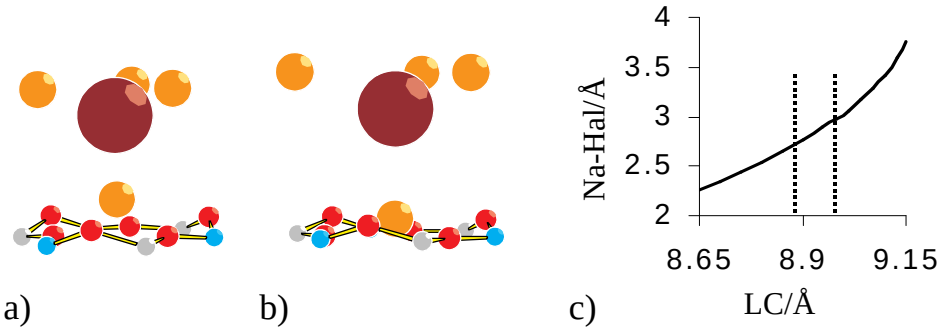

Figure 6-7: *Visualization of the Na-halide distance dependence upon lattice expansion.* ***a)*** *and* ***b)*** *show a six-ring window with its sodium atom and the residual atoms within the corresponding cage for a cell edge of 8.88 and 9.10 Å, respectively.* ***c)*** *illustrates the functional relation. The Na-halide distance range of mixed halide sodalites is marked by dotted lines.*

As discussed in Chapter 3, it has been generally established that the magnitude of the (dominant) paramagnetic deshielding effect in ionic materials arises from the extent of anion-cation and anion-anion overlap[71] and that the distance dependences are given by rather simple exponential decay functions as in Equation 3-10. Recently Tossell[68] has shown that the ^{23}Na NMR shielding can be reliably computed by the Restricted-Hartree-Fock method applying rather simple basis sets. Also, the shielding of a ligand environment could be successfully computed, by summation of the shielding contributions of every single ligand, while no significant angular dependence was observed. Based on these ideas and the fact that the sodium-oxygen distance remains constant among the studied samples, the different shielding contributions can be separated in order to identify the influence of the Na-halide distance on the sodium shielding.

$$\sigma_{cs} = \sigma_{fi} + 3\sigma_{Ox} + A_{NaHal} \cdot e^{-\frac{r}{r_{0\,NaHal}}} \qquad \text{Equ. 6-3}$$

Here σ_{CS} is the absolute shielding for ^{23}Na in the sodalite, σ_{fi} is the absolute shielding of the free sodium ion and $3\sigma_{Ox}$ is the shielding contribution due to the three oxygen ligands, A_{NaHal} and r_{0NaHal} are ligand dependent constants, r is the distance between sodium and the halide ion. A_{NaHal} and $3\sigma_{Ox}$ represent paramagnetic deshielding contributions and are thus negative in sign. In order to facilitate a comparison between experimental and computational data, Equation 6-3 separates the shielding contribution dependent on the Na-halide distance from all other contributions.

According to the calculations based on the 6-31G** basis set, the shielding of the free sodium ion is 631 ppm and the contribution of the oxygen atoms was found to be -42 ppm, resulting in $\sigma_{fi} + 3\sigma_{Ox} = 589$ ppm (see Figure 6-8).

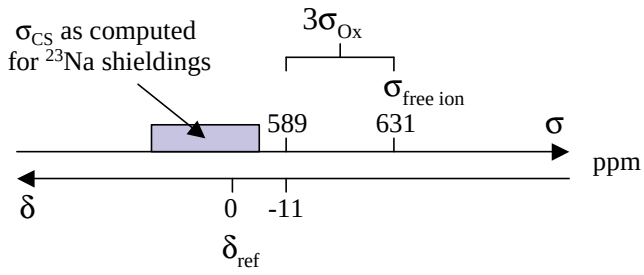

Figure 6-8: *the relation between calculated shieldings (σ) and observed chemical shifts for the ^{23}Na environments. $3\sigma_{Ox}$= -42 ppm and δ = + 11ppm are the offsets of the exponential fits and represent the shielding of the sodalite environment without the halide ion.*

Figure 6-9 thus plots $-\sigma_{CS}$ + 589 ppm versus the Na-halide distance for the three series investigated, resulting in fitting parameters of A and r_0 listed in Table 6-III. The original computed data points are given in Table 6-II in the Appendix. Figure 6-9 also includes

calculated data based on the Na-O distance of 2.330 Å (as found in dry sodalite[13,14]). The calculated shieldings based on this value are very similar, indicating a minor influence of the exact Na-O distance on the results. In addition, calculated shielding values of halide lacking environments as found in "dry" sodalite cages are shown. The fact that in this case (589 ppm - σ_{CS}) is not quite zero can be attributed to the three sodium ions, still present in the environment. In case of a halide filled cage, however, their influence is apparently screened by the halide ion.

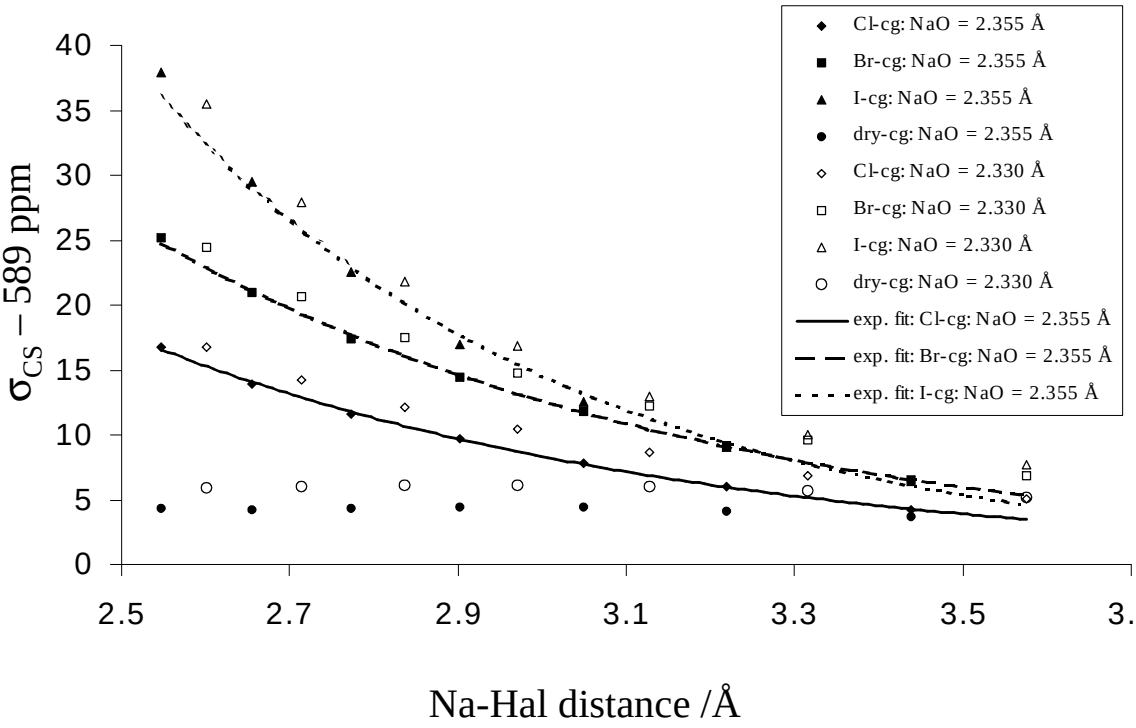

Figure 7-9: *Computed ^{23}Na chemical shifts for sodium in dry (circles), Cl (diamonds), Br (squares) and I (triangles) occupied cages. The empty symbols show shifts calculated on the basis of Na-O distances of 2.330 Å, while the filled symbols show shifts determined from Na-O distances of 2.355 Å.*

The sodium shielding for Na-halide "molecules" were also calculated disregarding the oxygen environments altogether. Even in this simplified model the trends are followed, and the corresponding fitting parameters are given in Table 6-III. In addition Table 6-III contains the exponential fits to the sums of squared overlap integrals as given by Hafemeister and Flygare. Experimentally, not absolute shieldings are measured but chemical shifts against a reference sample. Thus Equation 6-3 turns into:

$$-\delta_{CS} = \sigma_{cs} - \sigma_{ref} = \left[\sigma_{fi} + 3\sigma_{Ox} - \sigma_{ref}\right] + A_{NaHal} \cdot e^{-\frac{r}{r_{0\,NaHal}}} \qquad \text{Equ. 6-4}$$

The experimental δ_{CS} values measured for all three mixed halide sodalite series could be fitted to Equation 6-4 by fixing the value in the brackets to –11 ppm yielding: δ_{CS} + 11 ppm = -*A*exp{r/r_0} (see Figure 6-10). Table III includes the corresponding fitting parameters for *A* and r_0 from the experimental data. For sodium in chloro and bromo cages the agreement with the calculated data is quite good, especially in view of the fact that the best fit parameters for *A* and r_0 are very sensitive to the chosen offset values.

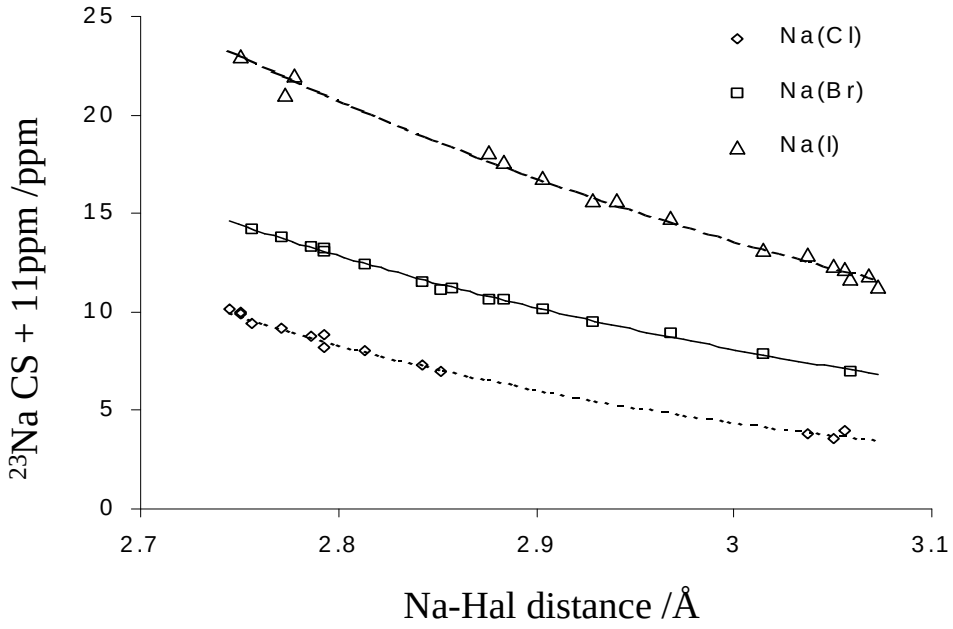

Figure 6-10: *^{23}Na chemical shifts as a function of Na-halide distance, as determined from the lattice constant, revealing the influence of the residual halide cages. The shifts plotted include a 11 ppm correction for the oxygen ligands, allowing exponential fits, as described in the text.*

distance dependence of	NaCl		NaBr		NaI	
	-A /ppm	**r_0 /Å**	**-A /ppm**	**r_0 /Å**	**-A /ppm**	**r_0 /Å**
δ_{iso} (exp)	1260	0.63	1110	0.68	1930	0.65
δ_{iso} (GAUSS. 6-ring)	800	0.65	1120	0.67	5900	0.51
δ_{iso} (GAUSS. NaHal)	3100	0.57	3200	0.61	1300	0.78
$\sum S^2$ [Ref. 72]	51	0.35	32	0.36	31	0.38

Table 6-III: *Fitting parameters for exponential decay functions of experimental and calculated sodium shifts, as well as literature values.*

While trends in the fitting parameters are not obvious, the de-shielding caused by the halide at a fixed distance increases with atomic number and decreases with increasing Na-halide distance. It also becomes more sensitive to this parameter with increasing atomic number of the halide ion. Overall the trends in the magnitude of the computed de-shielding contributions are in good agreement with the experimental results. The computed sodium shieldings for

iodo sodalites, however, deviate from the experimental data, which is due to the fact that because of computational limitations only the less extensive and non relativistic basis set SDD was used.

The summed squared overlap integrals, which should be proportional to the shielding, generally show much smaller characteristic lengths r_0. However, they have been tested only for the equilibrium interatomic distances in the halide salts, where they qualitatively agree with the absolute shielding values found experimentally. The only distance dependent data included into the model were pressure dependent resonance shifts of Rb and Cs halide salts.[74]

6.2.3 Halide Chemical Shift Trends in the Mixed Sodalites

Concerning the halide resonances, the chemical shifts compared to the 1 M aqueous solutions decrease from –123.5 ppm for ^{35}Cl to –220.6 ppm for ^{81}Br to –256 ppm for ^{127}I. Since experimental estimates for the chemical shifts of all free halide ions are not available, exponential fits of the data would lead to more or less arbitrary values for A_i, r_i and δ_0. Therefore the fitted halide chemical shifts were fitted in Figure 6-11 with linear expressions, the slopes of which increase from ^{35}Cl to ^{81}Br and further to ^{127}I always by a factor of about two from 17 ppm/Å to 35 ppm/Å and to 75 ppm/Å, respectively. This increased sensitivity with increased atomic number agrees with general shift trends in the Periodic Table.

The halide centers of the sodalite cages might also be viewed as molecular fragments present in hypothetical halide salt polymorphs with tetrahedral (instead of octahedral) coordination geometry. When the chemical shifts of the sodalite halides, corrected for their different Na-halide distances by the linear fits from Figure 14 are compared to the chemical shifts of the rock-salt like halide salts, the differences (δ_{SOD} - δ_{NaHal}) of –77.8 ppm, -210.5 ppm and -456.6 ppm for ^{35}Cl, ^{81}Br and ^{127}I, respectively, indicate, that the chemical shifts in the rocksalt structures are much more paramagnetic than those of the isolated tetrahedral fragments. The reason for this large effect can be attributed to the strong deshielding contribution arising from the anion-anion overlap in the rocksalt structures, which is absent in the sodalites. Furthermore, these data illustrate the dramatic increase of the anion-anion overlap effect with increasing atomic number of the halide.

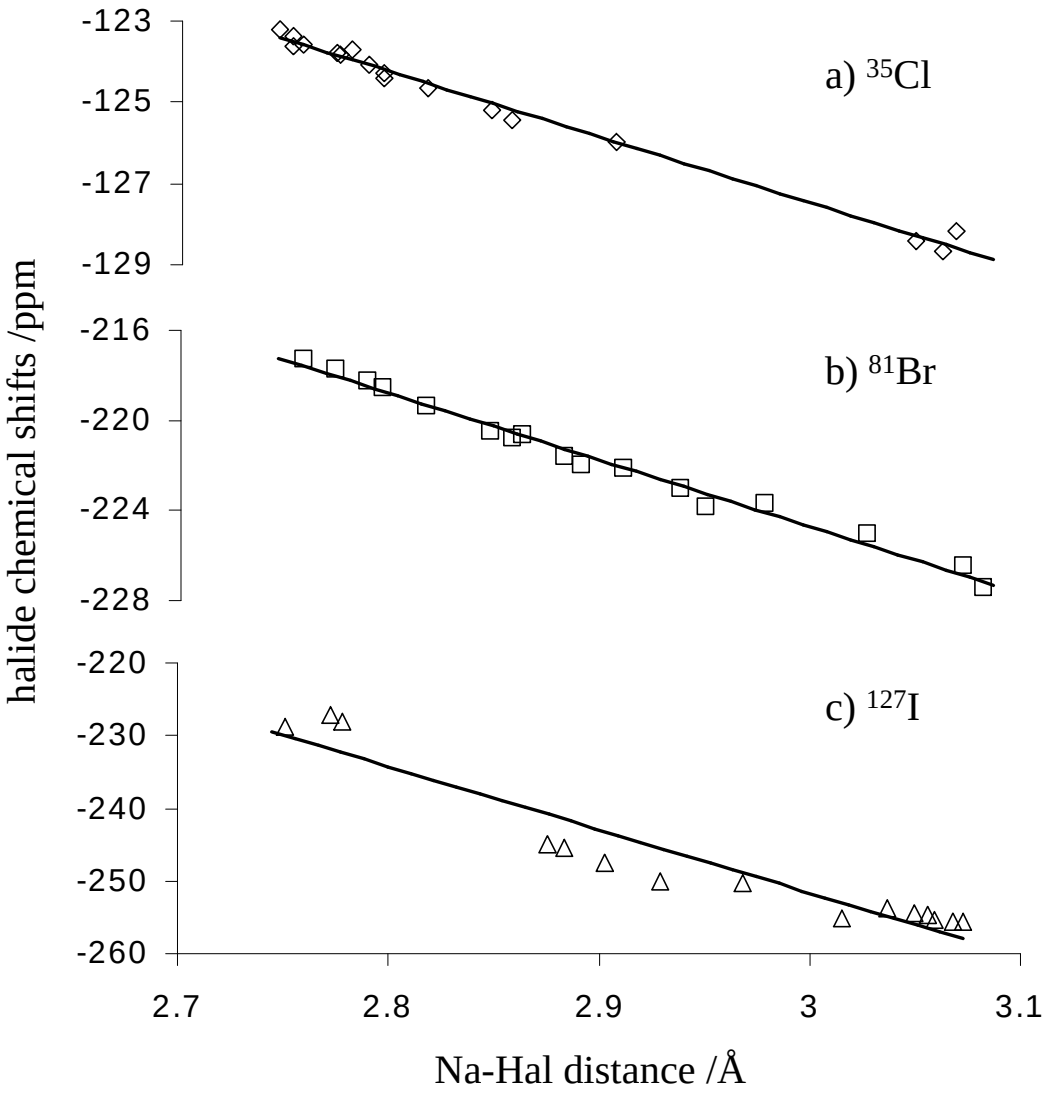

Figure 6-11: *Experimental NMR chemical shifts of ^{35}Cl, ^{81}Br and ^{127}I as a function of Na-halide distance, as computed from the lattice constants in all the sodalite solid solution samples according to Equation 3-4.*

6.3 Ion Mobility

Similar to the situation in sodalites, sodium ions in zeolites also occupy six-ring windows, where it has been an open question whether or not they are capable of performing jumps along the symmetry axis of the six ring window. Due to the m symmetry of this process, no changes in the quadrupolar coupling constant can be expected in zeolites or dry sodalites. Thus mixed halide sodalites offer the opportunity to study this process, since in a 1:1 mixed Cl/Br sodalite, 50% of each sodium species (in the Cl and Br cages, respectively) would change their bond partner and therefore experience different chemical shielding before and after the jump. In mixed Cl/Br sodalites, the two resonance lines of sodium species in Cl and Br cages are well separated, which makes them an ideal probe for this process. Figure 6-12 shows the results of this investigation on the basis of temperature dependent MAS-NMR studies.

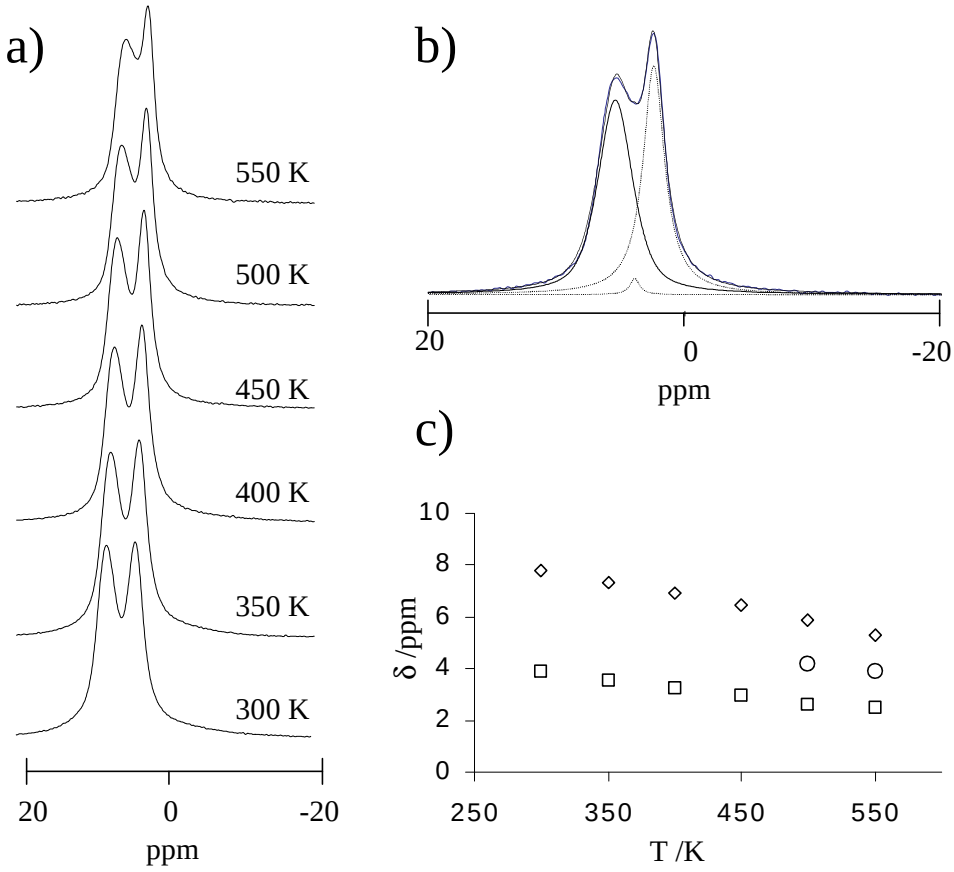

Figure 6-12: *High temperature study of mixed Cl/Br sodalite with a 1:1 halide ratio.* ***a)*** *temperature dependent ^{23}Na MAS NMR, recorded at 105.81 MHz with spinning speeds of 6500 KHz.* ***b)*** *Fitting curves of the 550 K ^{23}Na spectrum from a.* ***c)*** *resonance shifts of the sodium resonances portrayed in a). The diamonds represent sodium in Cl-cages, the squares represent sodium in Br cages and the circles give the position of a third line which had to be introduced into the 500 and 550 K spectra to reproduce the experimental lineshape.*

As can be seen from this figure, the frequency difference between the two sodium resonances decreases with increasing temperature. Over the range of these temperatures, the ^{27}Al resonance shifts from 63.48 ppm at 300 K to 62.60 ppm at 550K. The ^{81}Br resonance shifts from –219.5 to –217.8 ppm. The sodium resonances shift by 2.48 and 1.44 ppm for Br and Cl associated sodium, respectively. Neglecting direct thermal influences on the shift, the ^{27}Al shift suggests an increase in lattice constant from 8.92 Å to 8.96 Å, which theoretically goes along with an increase of the average Na-O distance of about 0.1 Å. At room temperature such an increase would correspond, according to the relations derived above, to low-frequency displacements of the sodium resonances by 2.4 and 1.9 ppm for the Br and Cl sites, respectively. This is in good agreement with the experimental shift trends found, however, deviations especially in the spectrum at 550K are noticeable. In this temperature range it is necessary to introduce a third sodium resonance at an intermediate chemical shift to fit the experimental data. This extra sodium line is attributed to sodium ions that are exchanging fast

on the NMR timescale between both halide environments. From the frequency separation we can conclude that for a fraction of the sodium ions the hopping rate at 550 K is faster than 400 Hz.

Although these findings are yet an initial indication of sodium mobility, they reveal that the mixed Cl/Br sodalite is a good probe for investigating such hopping processes, and that a more detailed study of this case is possible as soon as equipment for higher temperatures is available. It is interesting to note that the ^{81}Br resonance at 550 K is shifted to higher frequencies, compared to the 300 K spectrum. Since the paramagnetic deshielding of sodium decreases, this is also expected for bromine. The opposite trend observed is on the other hand likely to be caused by reduction of the asymmetries in the lattice and therefore the quadrupolar coupling constant of the central cage species at higher temperatures. Thus, the quadrupolar shift is a low frequency shift and its reduction can explain the high frequency shift observed.

7 Topotactic Transformations of the Sodalite Lattice

As already described in Chapter 1, it is possible to exchange the $H_3O_2^-$ anion and a corresponding sodium cation by four molecules of water, by boiling the sodalites in a slightly acidic (pH = 6) environment for up to a day. The water can then be removed at 400°C under vacuum, which causes a severe expansion of the lattice. Exposure to sodium vapor then leads to incorporation of sodium atoms forming Na_4^{3+} centers. The procedure is sketched in Figure 7-1.

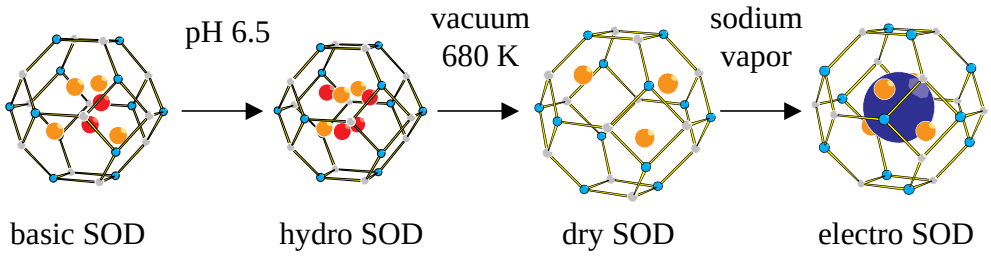

***Figure 1-1**: visualization of the changes in the sodalite cage during the topotactic exchange of the extra- framework species. Inside the cage, only sodium ions (light) and oxygen atoms (dark) are shown for simplicity.*

7.1 Experimental Lattice Constants

7.1.1 Halide/Hydro Sodalites

The exchange of the basic for hydro centers in these mixed sodalite series also changes the lattice constants as portrayed in Figure 7-2.

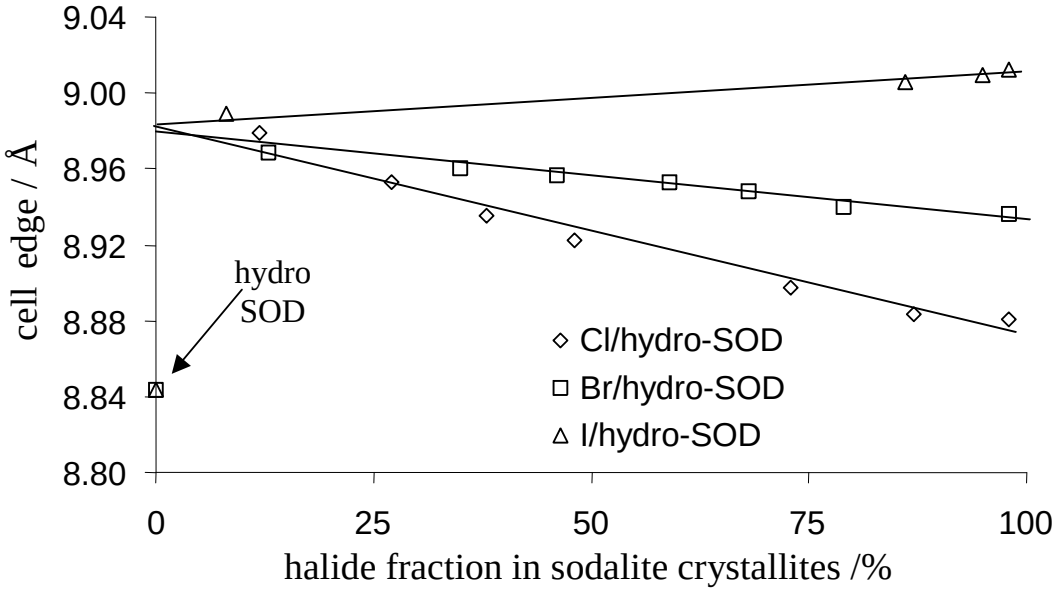

***Figure 7-2:** Lattice constants of the three mixed halide/hydro sodalite systems. Note that the lattice constant of pure hydro sodalite is 8.844 Å violating Vegard's rule.*

While for Cl/hydro sodalites and Br/hydro sodalites the lattice constant decreases with increasing halide content, the I/hydro sodalites show the opposite trend. Furthermore mixed I/OH sodalites with iodine contents between 20% and 80% could not be synthesized as pure phases. For all sodalites, the lattice constants seem to approach a value around 8.99 Å for the pure hydro sodalite. This value stands in marked contrast to that of pure hydro sodalite (8.844 Å). Apparently these mixed phases do not obey Vegard's rule at their lowest halide concentrations. Figure 7-2 implies that the water containing cages appear to have different equilibrium sizes in the pure and the mixed phases. Table 7-I illustrates that the concentrations calculated from the relative mass losses of those samples, according to Equation 4-1b, agree well with those compositions inferred from XRD data of the parent mixed Br/basic sodalites. This result suggests that the washing procedure used to remove NaOH from the cages does not alter the halide content.

Sample		Xray: Br/basic SOD		TGA: Br/hydro SOD	
abbr.	code	cell edge	Br fract.(%)	mass loss	Br fract.(%)
a)	H209	8.936Å	98	0.25%	98.2
b)	H214	8.926Å	76.2	2.60%	81.1
c)	H183	8.922Å	67.5	5.93%	62.6
d)	H200	8.919Å	61	6.69%	55.4
e)	H182	8.913Å	47.9	8.67%	38.6
f)	H199	8.908Å	37	9.60%	32.3
g)	H172	8.897Å	13	12.79%	11
h)	H227	8.891Å	0	14.10%	2.4
error		± 0.002Å	± 6	± 0.40%	± 3.9

Table 7-I: *Comparison of halide contents by XRD and TGA assuming four water molecules per hydro cage. The agreement is within the experimental error. The slight systematic overrepresentation of hydro cages from TGA is most likely due to an unspecific mass loss around 100°C due to surface water.*

All halide contents given in Table 7-I are in good agreement with each other, indicating that the water content per cage is the same throughout the whole mixed Br/hydro sodalite series. Thus, the reason for the extreme contraction of sodalite cages in pure hydro sodalite is not related to the water content. This point will be investigated below by various NMR techniques.

7.1.2 Halide/Dry Sodalites

The whole Br/hydro series and selected samples of mixed Cl/hydro and I/hydro sodalites were dried under the conditions mentioned above, yielding halide/dry sodalites. While the structure of pure dry sodalite is distorted (space group Pnc2) and thus non-cubic, departures from the

cubic symmetry could not be found in any of the mixed halide/dry sodalites prepared, however, the peaks in the x-ray diffraction patterns are somewhat broader than those for halide/basic and halide/hydro sodalites. The observed lattice constants of Cl/dry, Br/dry and I/dry sodalites are given in Table 8-I in the Appendix.

In the case of halide/dry sodalites, Vegard's rule is again obeyed within the precision limits of the measurements. The lattice constants of the members of all three series of mixed halide/dry sodalites are, according to their compositions, the weighted averages of the lattice constants of the pure phases. The lattice constant for a hypothetical pure dry cubic sodalite at room temperature is $a \approx 9.1$ Å, yielding the same Z as the other cubic sodalites.

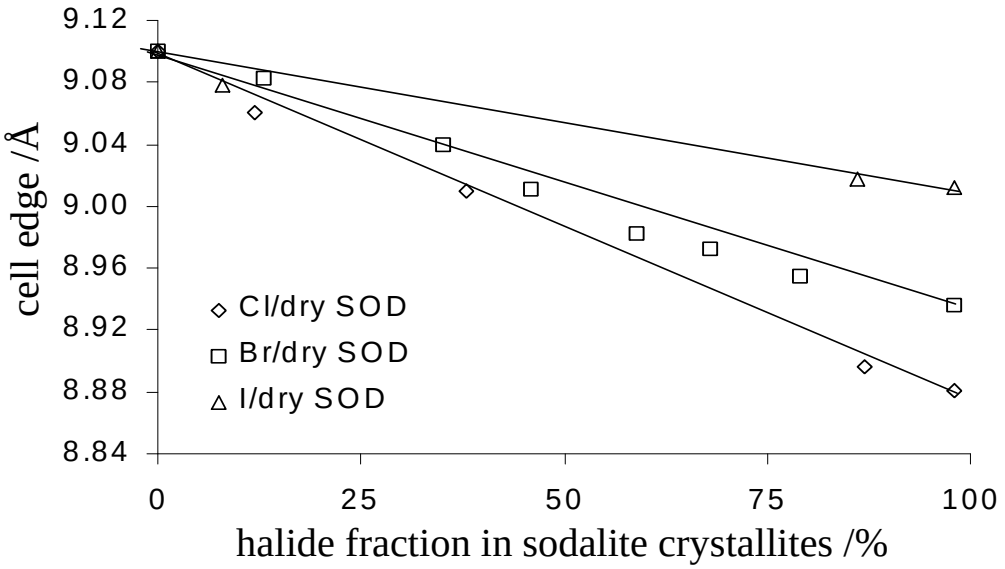

Figure 7-3: *Lattice constants of the three mixed halide/dry sodalite systems. The lines mark perfect obedience of Vegard's rule. The actual mixed halide phases deviate slightly from Vegard's rule, but these deviations still fall within the experimental error. Data points are presented only for those sodalites, which where doped with sodium and are further characterized in Chapter 9.*

7.1.3 Halide/Electro Sodalites

For the halide/electro sodalite series, so far only preliminary x-ray data is available due to the fact that pure phase samples were only available recently. The halide/electro sodalites are highly air-sensitive and since x-ray diffractometry is surface sensitive, data is easily corrupted by surface oxidation, even if this is hardly visible in NMR. A discussion of lattice constants determined from NMR experiments can be found in Chapter 9.

7.2 Discussion

When the water molecules are removed from the cages of hydro-sodalite, the sodalite framework expands rather than contracts. Similarly, the lattice of salt-free sodalite is expanded in comparison with that of salt-bearing sodalites. The underlying reason for this unusual behavior is the Coulomb repulsion between the charge compensating alkali cations. In the absence of the central anion or some polar molecular species such as water, the unscreened Coulomb repulsion pushes the alkali cations away from the center of the sodalite cage. This in turn increases the average Al-O-Si bond angle leading to lattice expansion. Because of the unusually large Al-O-Si bond angles, the aluminosilicate framework of dry sodalite is strained and eager to absorb small atoms or molecules that can help screen Coulomb repulsion.

The above considerations can help rationalize the observed trends in the lattice parameters of mixed sodalites shown in Figures 7-2 and 7-3. In the halide/basic mixed halide sodalite series, Coulomb repulsion between sodium cations is screened in both cages, which allows lattice contraction to the point required to accommodate the two different central anions. Contrary to this, in the halide/dry series there is an apparent competition between two opposing forces. Coulomb repulsion is efficiently screened in *halide* cages, thus allowing for their contraction, but not in *dry* cages hence favoring their expansion. The repulsive forces prevail in all the three series for the whole lattice expands monotonically as the halide content decreases. The trends in the lattice parameters of the halide/hydro series are more complex. The Coulomb repulsion of the sodium cations in hydro cages appears to be screened to some extent, yet repulsive forces prevail so that the Cl/hydro and Br/hydro lattices expand slightly with the decrease of the halide content. It appears that such a trend persists for the entire solid solution series except at its very end where the lattice of *hydro* cages suddenly shrinks.

8 Mixed Salt-bearing/Salt-free Sodalites

The mixed halide/salt-free sodalites discussed in Chapter 5 and 7 were investigated by NMR similar to the mixed halide sodalites in Chapter 6. The substantial difference between these two types of sodalites is that the tetrahedral symmetry of the extra framework species is not preserved for the salt-free cages. While in halide/basic sodalites only the symmetry of the anion $H_3O_2^-$ does not confor with the tetrahedral sy etry in halide hydro and halide basic sodalites vacant sodium sites occur, which, since they are directly coordinated to the framework are also likely to break the framework symmetry. The main focus in this study has been placed on the Br/salt-free sodalite systems and the more extensive experiments have been performed on these series. Nevertheless room temperature NMR spectra will be presented for all 9 mixed salt-bearing/salt-free sodalite systems to show halide dependent similarities and differences between these groups of sodalites.

Although an extensive amount of data is presented in this chapter, all of the data are discussed jointly to demonstrate the close relationship between the NMR parameters for all the nuclei used in these systems. First the basic 1 D room temperature NMR data will be presented for each NMR isotope and supplemented by 2D and VT data to identify the observed resonances. In the subsequent sections trends in the NMR parameters and their correlation with structural properties will be discussed. Finally, NMR data relating to ionic mobility will be presented.
The extracted NMR parameters corresponding to the NMR spectra shown in this Chapter are listed in Table 8-I in the Appendix.

8.1 Observation and Assignment of NMR Resonances

8.1.1 ^{27}Al MAS NMR

In cubic sodalites, with identical extra framework species of tetrahedral symmetry, aluminum has only one crystallographic site, located at the joint of four adjacent sodalite cages. In mixed sodalites, however, the degeneracy of the aluminum site is removed thus potentially giving rise to multiple environments associated with different cage occupancies. As shown in Chapter 7, this removed degeneracy is not detected by ^{27}Al MAS NMR if the extra framework species differ only in their central anions, but not in their symmetry. From Figure 8-1, 8-2 and

8-3 it can be seen that this is no longer true, if the symmetry of the extra framework species changes along the series halide/basic halide hydro halide dry

Each of the first columns of Figure 8-1 to 8-3 shows the ^{27}Al MAS-NMR spectra of the respective halide/basic series. In all cases only a single resonance with a nearly symmetric lineshape was found, whose full width at the half maximum (FWHM) varies between 80 and 270 Hz. Evidently the chemical shift differences between the various ^{27}Al sites are smaller than the inhomogeneous broadening caused by solid solution disorder, thus no resolved resonances are detected. While for the Cl/basic sodalites, the chemical shift of the ^{27}Al resonance remains constant at 64.5 ppm, for the Br/basic and I/basic sodalites, it shifts linearly to higher frequencies (from 63.4 to 64.5 ppm for Br/basic and from 61.4 to 64.5 ppm for I/basic sodalites) with decrease of the halide content.

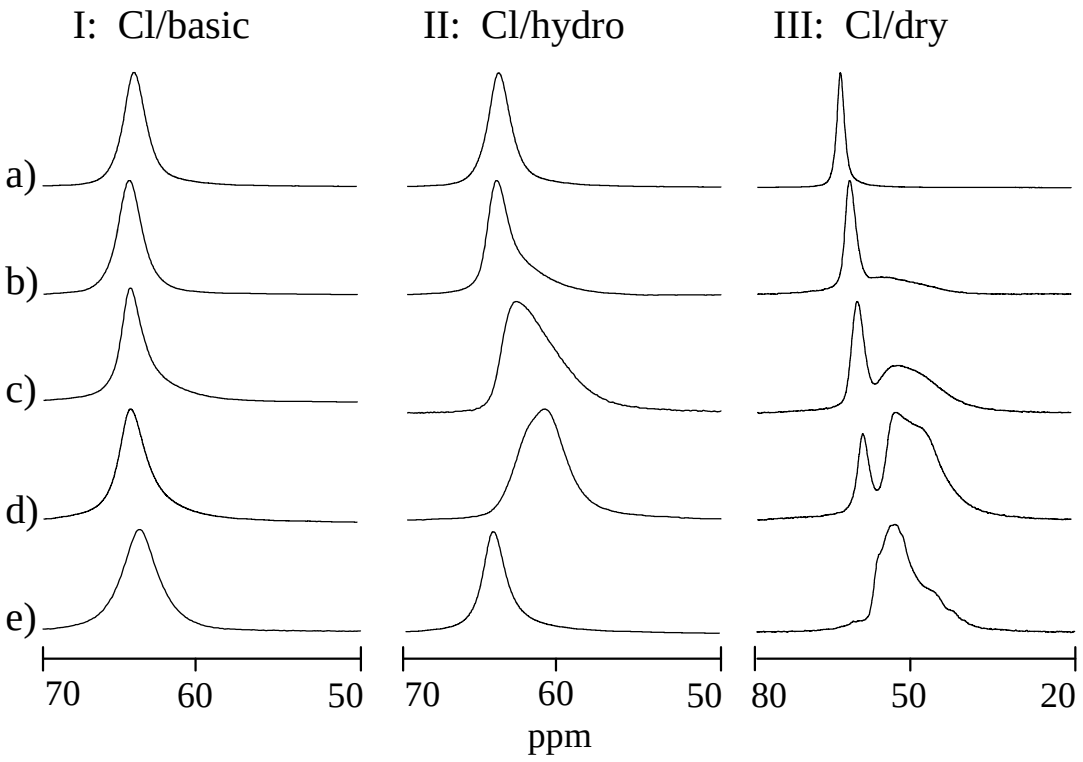

Figure 8-1. *^{27}Al MAS NMR spectra (observed at 130.28 MHz) of the Cl/basic, Cl/hydro, and Cl/dry series. The percentages of chloro cages, identical for all three series within the same row, are as follows: (a) 98%, (b) 73%, (c) 45%, (d) 16%, (e) 0%.*

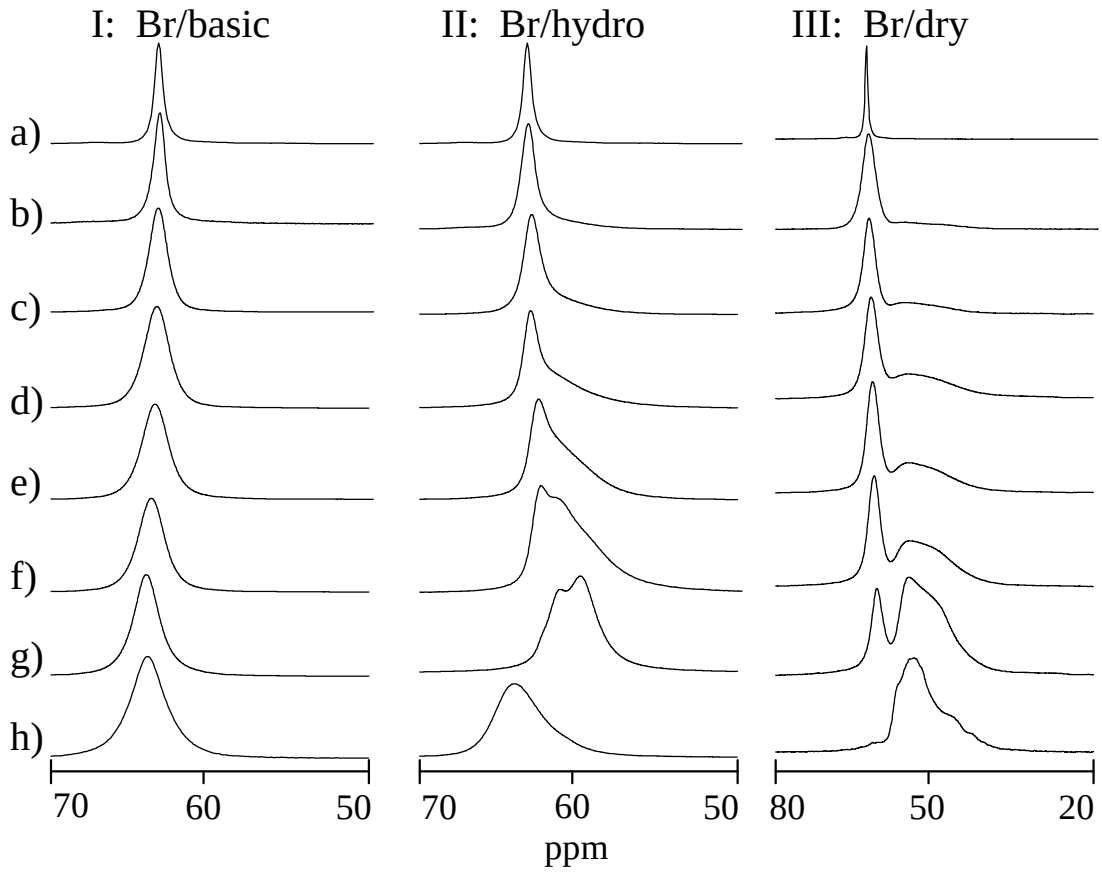

Figure 8-2. *^{27}Al MAS NMR spectra (observed at 130.28 MHz) of the Br/basic, Br/hydro, and Br/dry series. The percentages of bromo cages, identical for all three series within the same row, are as follows: (a) 98%, (b) 78%, (c) 67%, (d) 61%, (e) 45%, (f) 36%, (g) 10%, (h) 0%.*

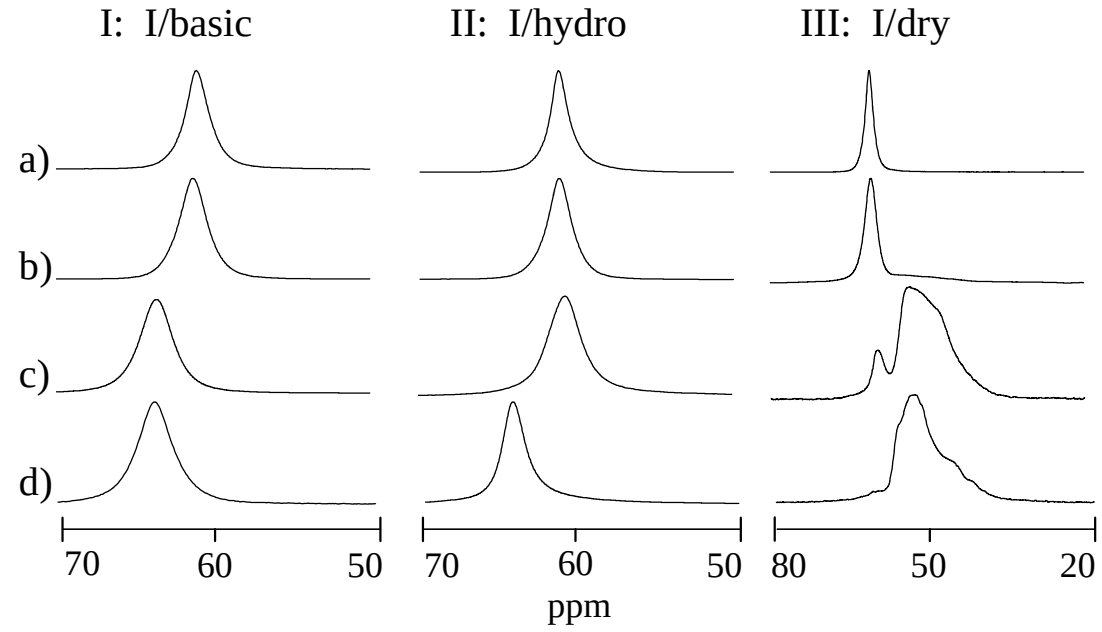

Figure 8-3. *^{27}Al MAS NMR spectra (observed at 130.28 MHz) of the I/basic, I/hydro, and I/dry series. The percentages of iodine cages, identical for all three series within the same row, are as follows: (a) 98%, (b) 86%, (c) 9%, (d) 0%.*

As shown in Figure 6-2, the substitution of $H_3O_2^-$ by Br^- or I^- anions expands the sodalite lattice and thus increases the average Si-O-Al bond angle, which changes the isotropic chemical shift of the ^{27}Al resonance to more positive values (less de-shielding), as discussed below. Simultaneously P_Q remains unchanged at 0.8 ± 0.1 MHz in agreement with previous studies on the end-members of this series.[52,85] This indicates that the ion substitution does not alter significantly the electric field gradient (EFG) around the aluminum site, consistent with the fact that all the sodalite cages in the Br/basic series contain a central anion and four Na^+ cations.

The ^{27}Al NMR spectra of the halide/hydro and halide/dry series are given in column II and III of the latter three figures. These spectra display two distinct resonances that are more widely separated in the halide/dry series. While the high-frequency resonances in all series are narrow and nearly symmetric, the low-frequency resonances show a marked shape asymmetry indicating strong second order quadrupolar coupling.

In the halide/hydro series (with the exception of pure hydro sodalite), the chemical shifts range between 64.5 and 62.2, 63.4 and 62.4, and 61.4 and 61.8 ppm for Cl/hydro, Br/hydro and I/hydro sodalites, respectively. The P_Q values of these series increase from 0.8 to about 1.6 MHz with decreasing halide concentration. The low frequency resonance, which for the low halide containing sodalites is only visible as a shoulder becomes more pronounced for the low halide containing species. For sample 8-2IIf the ^{27}Al TQMAS NMR spectrum as shown in Figure 8-4b reveals the multiple site character of the 1D spectrum, where two aluminum sites with P_Q values of 1.6 MHz and 2.1 MHz for the high and the low-frequency resonances can be detected. Note that both resonances have the same chemical shift within the experimental error. While at room temperature, the low frequency resonance although having only one peak might consist of multiple components, from temperature dependent NMR data between 273 and 373 K, as shown in Figure 8-4a, two symmetric resonances can be distinguished, indicating that at 373 K only two sites can be identified.

The ^{27}Al NMR spectrum of pure hydro sodalite shows one resonance which is characterized by a chemical shift of 65.6 ppm and a strong high-frequency shoulder. As shown in Figure 8-5b the TQ MAS spectrum only resolves only one site, but indicates a distribution of quadrupolar coupling constants. The temperature dependent spectra given in Figure 8-5a show that the low-frequency shoulder decreases with increasing temperature. At 373 K only one ^{27}Al resonance, which is nearly symmetric and narrow can be observed. Thus from an NMR

point of view, in contrast to the Br/hydro sodalite, pure hydro sodalite has only a single aluminum site.

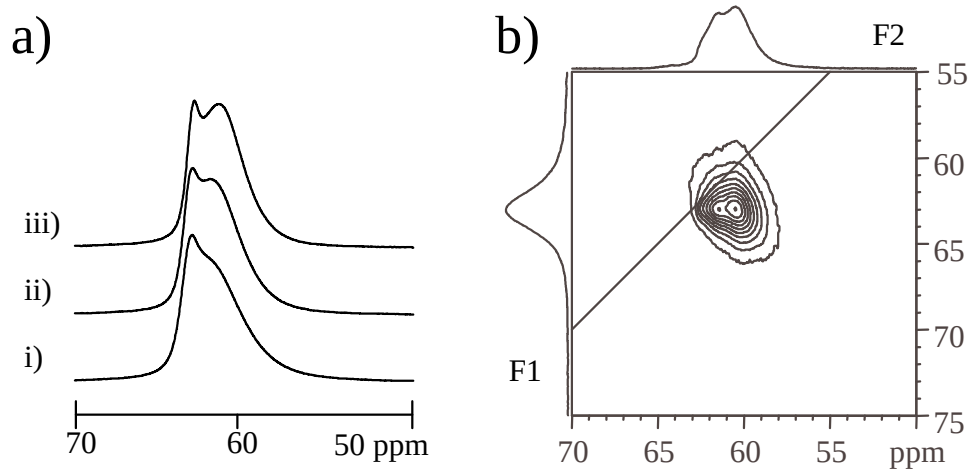

Figure 8-4: a) *temperature dependent ^{27}Al MAS NMR at i) 273 K, ii) 323 K and iii) 373 K of the Br/hydro sodalite sample corresponding to Figure 8-2IIf.* ***b)*** *^{27}Al TQ MAS NMR spectrum of the Br/hydro sodalite sample with 11% of bromo cages (Figure 8-2IIIf)*

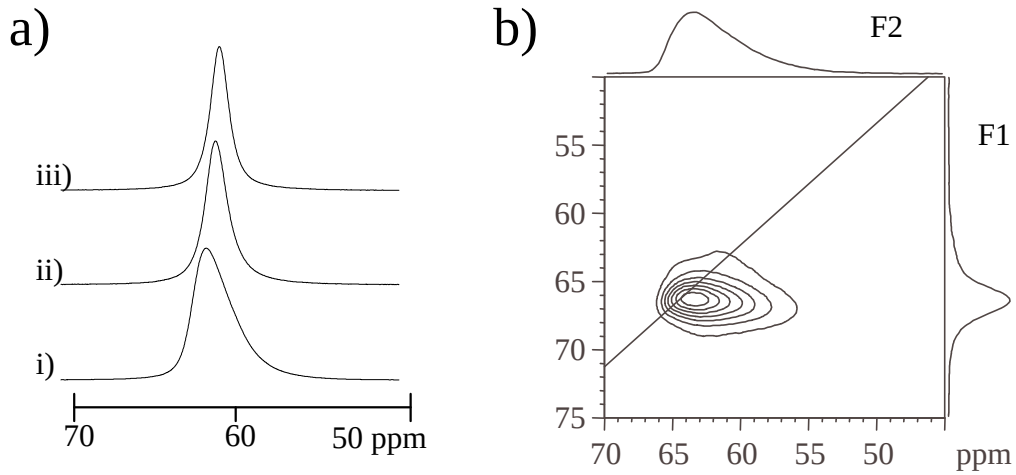

Figure 8-5: a) *temperature dependent ^{27}Al MAS NMR at i) 273 K, ii) 323 K and iii) 373 K of pure hydro sodalite (e.g. Figure 8-2IIh).* ***b)*** *^{27}Al TQ MAS NMR spectrum of the same sodalite.*

In the halide/dry series, two well separated ^{27}Al resonances occur. The low frequency ones are narrow and have chemical shifts ranging between 64.6 and 58.5, 63.4 and 58.5 and 61.4 and 58.5 ppm for the Cl/dry, Br/dry and I/dry series, respectively. The P_Q values of these series increase between the pure halide sodalites and the low halide halide/dry sodalites from 0.8 to about 1.6 MHz. The low frequency resonances are broad and have a pronounced, but smeared lineshape, thus their characterization had to be undertaken by TQ MAS NMR. A representative spectrum is given in Figure 8-6a.

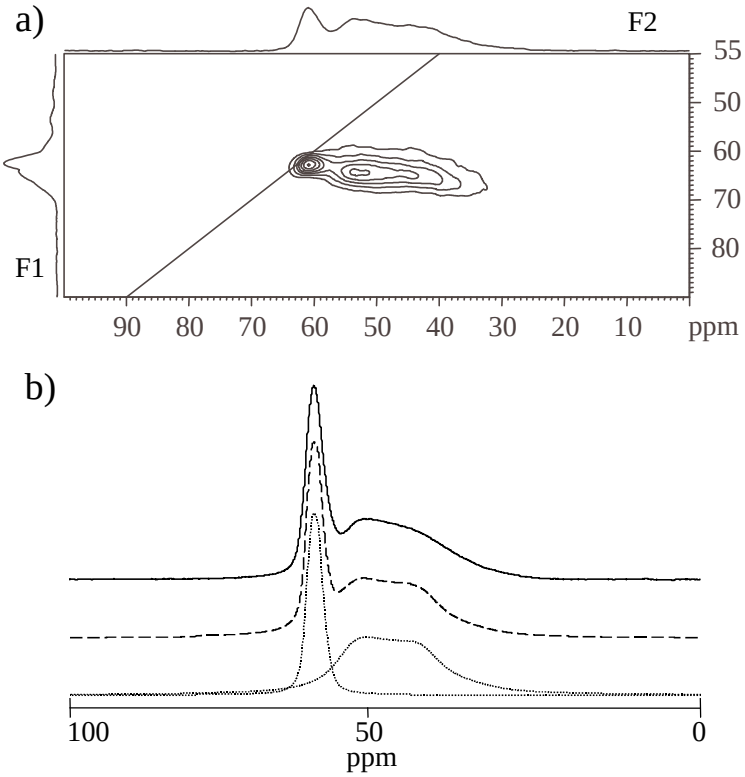

Figure 8-6: a) *^{27}Al TQ MAS NMR spectrum of the Br/dry sodalite sample with 36% of bromo cages (Figure 8-2IIIf)* ***b)*** *^{27}Al MAS NMR spectrum of the same sample (solid line), the simulated spectrum (dashed line), and deconvolution into the two line-components (dotted curves). Both spectra were observed at 104.22 MHz.*

Figure 8-6a shows the ^{27}Al TQMAS spectrum of sample 8-2IIIf from the Br/dry series where the two aluminum sites are clearly differentiated on the basis of their P_Q values. As will be elaborated in more detail in the Discussion section, the very large P_Q value of the low-frequency resonance (4.4 MHz) indicates a substantial distortion of the tetrahedral aluminum environments in that series. Using the Hamiltonian parameters derived from this experiment a satisfactory simulation of the MAS lineshape can be achieved, as shown in Figure 8-6b. Both the MAS and the TQMAS results suggest the presence of a distribution of P_Q values thereby limiting the precision with which the average values can be determined. Within the Cl/dry and I/dry series, the same trends are observed for the low frequency resonance. The chemical shifts range between 60 and 58 ppm and will be discussed in more detail below.

The ^{27}Al MAS NMR spectrum of pure dry sodalite merely shows one resonance. This resonance with a center of gravity at 52 ppm is comparable to the low-frequency resonance in the ^{27}Al NMR spectra of mixed halide/dry sodalites. However, it has a detailed structure, indicating an overlap of several resonances due to different aluminum sites. The ^{27}Al TQ MAS NMR spectrum, shown in Figure 8-7a, supports the assignment. A possible fit to the NMR spectra is given in Figure 8-7b. The three aluminum sites have quadrupolar coupling constants of 3.5, 4.6 and 5.4 MHz with chemical shifts of 58.0, 59.0 and 58.5 ppm, respectively. The observed integrated intensities decrease with increasing quadrupolar coupling constants in the order of 1.0 : 0.78 : 0.48. It has to be taken into account, however,

that the fraction of signal with strong quadrupolar coupling found in the central MAS resonance decreases with increasing quadrupolar coupling constant. An approximation of this effect, based on a method developed by Massiot[39] yields correction factors of 0.2, 0.15 and 0.12 resulting in a ratio of 1: 1.04 : 0.80, for the latter resonances, which supports comparable populations of all three sites in the sample. This finding is in good agreement with a recently published room temperature structure of dry sodalite and will be discussed further below.[13] The small high-frequency shoulder of the overall lineshape can be ascribed to a negligible number of cages from which the fourth sodium has not been removed during the process of topotactic transformation. While the chemicals shift of this site is also around 58.5 ppm, it does not show quadrupolar broadening.

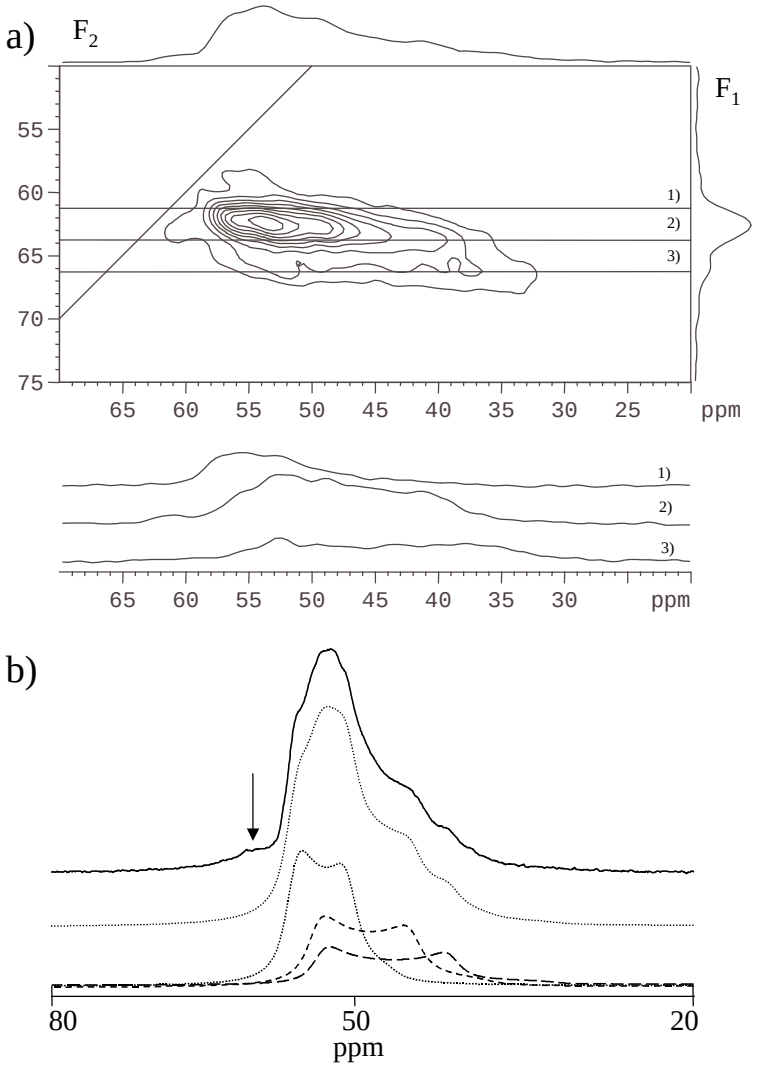

Figure 8-7: a) *^{27}Al TQ MAS NMR spectra of dry sodalite acquired at 104.22 MHz. The F_2 slices corresponding to the resonances are given below.* ***b)*** *^{27}Al MAS NMR spectrum of the same sample (solid line) observed at 130.28 MHz corresponding to Figure 8-2IIIh. The lineshape could be simulated by three overlapping quadrupolar broadened contributions (see text). The high-frequency shoulder is most likely due to rather undistorted AlO_4 tetrahedra resulting from residual cages with four extra framework sodium ions. (see arrow)*

8.1.2 The Halide NMR Spectra

The mixed sodalites considered in this study are expected to have only one halide site where the anions are coordinated by four Na^+ cations in a tetrahedral geometry.

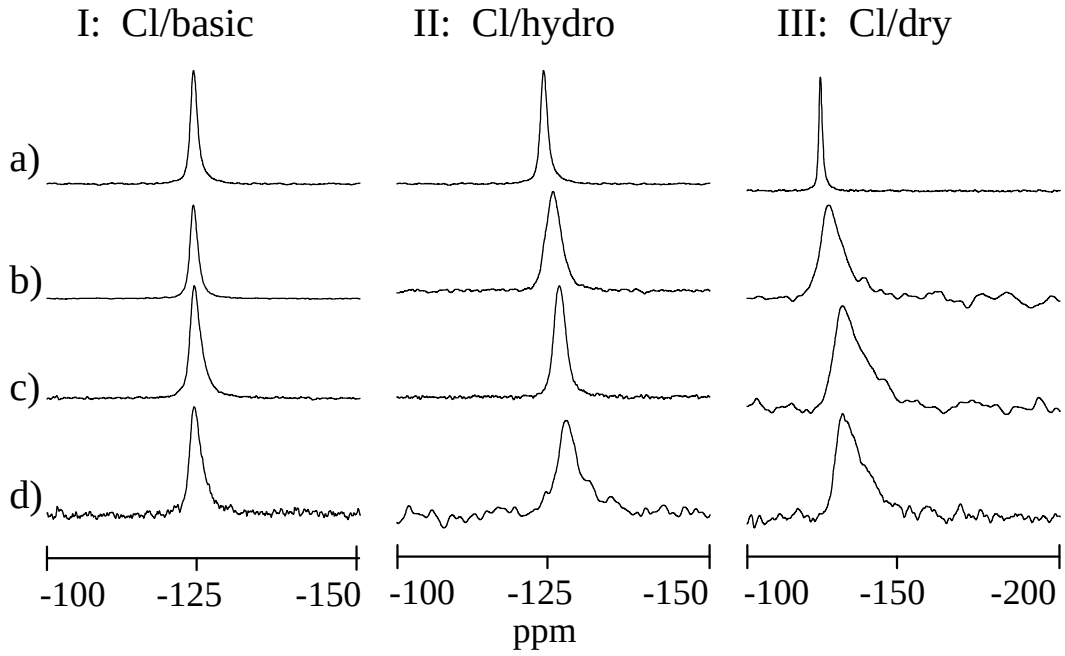

Figure 8-8: *^{35}Cl MAS NMR spectra (observed at 48.99 MHz) of the Cl/basic, Cl/hydro, and Cl/dry series. The percentages of chloro cages, identical for all three series within the same row: (a) 98%, (b) 73%, (c) 45%, (d) 16%.*

The ^{35}Cl resonances of Cl/basic sodalites are given in Figure 8-8I and vary only very little (δ = -123.3 ± 0.1 ppm) in chemical shift. Their linewidths increase from 120 Hz to 240 Hz from pure Cl to 45 % and 16% Cl containing sodalites. The intensity of the resonances decreases with decreasing Cl content in the sample, which is visible in the increased S/N ratio, although for sample 8-8Id four times as many FIDs were acquired compared to 8-8Ia. In the series of Cl/hydro sodalites (Figure 8-8II), the chemical shifts decrease from -123.3 ppm to -126.7 ppm. Also the linewidth of the latter sample increase from 120 to 400 Hz. The change of chemical shifts and linewidth with the halide concentration is most obvious for the Cl/dry sodalites portrayed in Figure 8-8III, where the chemical shift decreases from -123.3 ppm to -131 ppm and the linewidths increase up to 1800 Hz. The P_Q values as determined from field dependent NMR increase corresponding to the linewidths from 0.3 ± 0.2 MHz to 1.5 ± 0.5 MHz. As for the mixed halide sodalites, these values have been determined for the peak of the lineshape and thus do not necessarily represent the average P_Q values. Also the lineshape indicates a wide distribution of quadrupolar coupling constants around the average value.

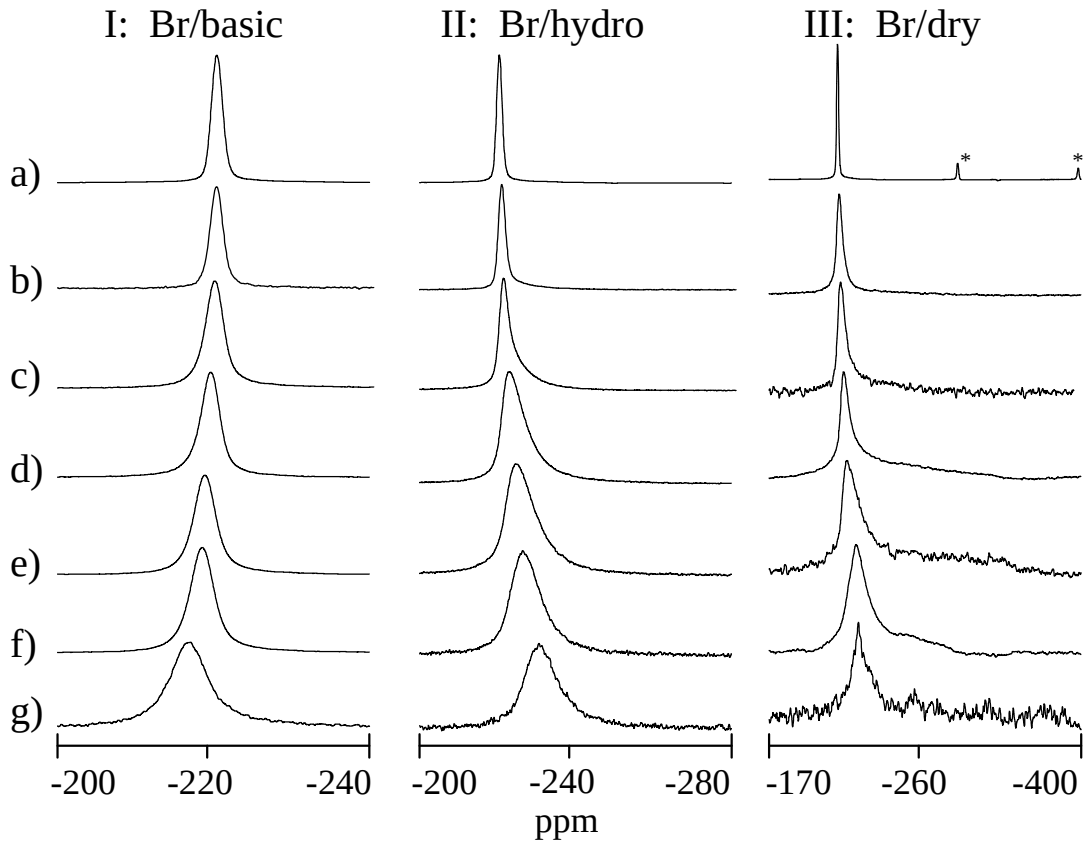

Figure 8-9: *^{81}Br MAS NMR spectra (observed at 135.03 MHz) of the Br/basic, Br/hydro, and Br/dry series. The percentages of bromo cages, identical for all three series within the same row, are as follows: (a) 98%, (b) 78%, (c) 67%, (d) 61%, (e) 45%, (f) 36%, (g) 10%.*

The ^{81}Br MAS NMR spectra of the Br/basic sodalites (Figure 8-9I) also show only a single resonance. The ^{81}Br P_Q values scatter around 0.6 ± 0.2 MHz, reflecting only weak quadrupolar coupling in this series. Nevertheless, the random distribution of the two anions in the Br/basic series produces some disorder, as revealed by line broadening effects due to distributions of chemical shifts and/or P_Q values for each sample. The ^{81}Br isotropic chemical shifts increase linearly with the decrease of the bromine content, ranging from -221 to -217.5 ppm. Samples of the Br/hydro series (Figure 8-9II) also have single peak ^{81}Br spectra but the chemical shift variation with bromine content is opposite to that in the Br/basic series, reaching δ_{cs} = –226 ppm at the lowest Br content. Concomitantly the P_Q values increase from 0.5 to 2.2 MHz.

The ^{81}Br MAS NMR spectra of Br/dry-sodalites (Figure 8-9III) show one dominant resonance with isotropic chemical shifts between -220.4 and -235.8 ppm. While the P_Q values for this series are small and increase only slightly with decrease of the bromine content (0.6-0.8 MHz), there is a dramatic increase in the resonance linewidth (from 250 to 2400 Hz at 11.7T). Furthermore samples having bromine contents below 70% display complex asymmetric

lineshapes, where the low-frequency side of the resonance extends up to –350 ppm. While such spectroscopic features are indicative of strong quadrupolar coupling, the excessive broadening suggests a wide distribution of interaction parameters precluding a more detailed analysis with simulation routines.

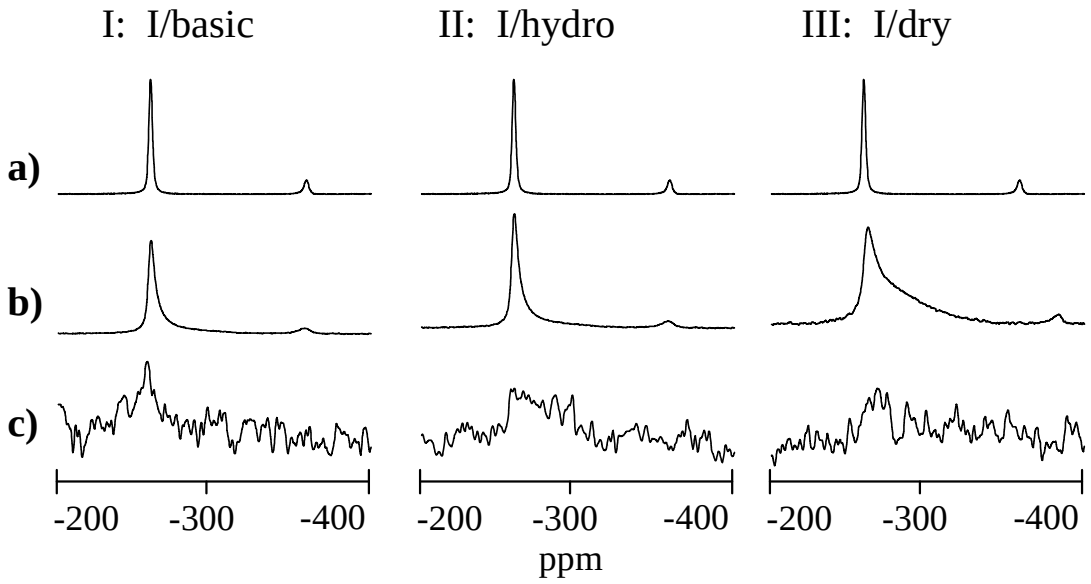

Figure 8-10: *^{127}I MAS NMR spectra (observed at 100.04 MHz) of the I/basic, I/hydro, and I/dry series. The percentages of iodo cages, identical for all three series within the same row, are as follows: (a) 98%, (b) 86%, (c) 9%.*

The ^{127}I resonances, displayed in Figure 8-10, generally show similar trends as observed above and in Chapter 7. Due to the trend of phase separation in these systems, single-phase samples with only very high or very low iodine concentration are available. While the data for the lowest iodine concentration can hardly be evaluated due to the low signal to noise ratio, the 86% I containing sodalite shows ^{127}I resonances similar to the ones of pure I-sodalite but with about twice the linewidth. The ^{127}I spectrum of the 86% I/dry sodalite shows a strong low-frequency shoulder indicating a wide distribution of quadrupolar coupling constants.

8.1.3 Sodium

Other than in the mixed halide sodalites, where sodium is always coordinated by three framework oxygen atoms and the halide ion, sodium in salt-free cages occurs in three substantially different environments. In order to assign these resonances it is necessary to first discuss these different coordinations of the sodium environments as portrayed in Figure 8-11:

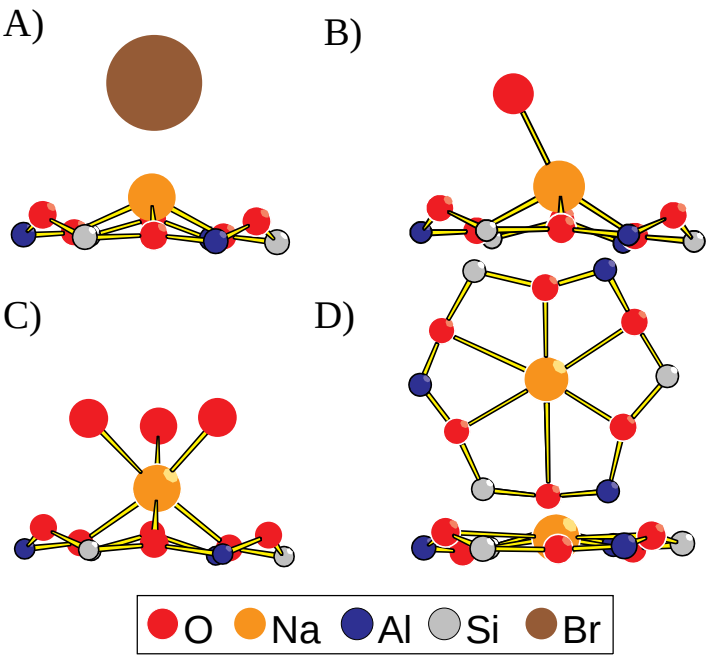

Figure 8-11: *The four substantially different sodium environments found in mixed salt-bearing/salt-free sodalites.* ***A)*** *sodium in a cage occupied by a halide anion.* ***B)*** *sodium in a basic cage coordinated to one of the two oxygen atoms of the* $H_3O_2^-$ *anion. The oxygen atom plotted occupies one of three equivalent sites and is mobile at room temperature. The hydrogen atoms are not plotted for simplicity.* ***C)*** *Sodium in a hydro cage according to the crystal structure by Felsche*[10]*. Hydrogen atoms are not plotted.* ***D)*** *sodium sites in the cubic phase (high temperature phase) of dry sodalite.*

Sodium cations in *halide* cages (Figure 8-11A) are coordinated by three framework-oxygen atoms and one bromine anion. Within *basic* cages Na^+ cations are surrounded by the three framework-oxygen atoms and one extra-framework oxygen (Figure 8-11B). According to low temperature crystallographic data on pure basic sodalite, this extra-framework oxygen, a part of the $H_3O_2^-$ anion, is separated from the Na^+ cation by 2.4 Å.[12] In *hydro* cages, sodium is surrounded by three framework-oxygen atoms at a distance of about 2.5 Å and three (out of four) water molecules at similar distances (Figure 8-11C).[12] Finally, sodium cations in *dry* sodalite cages are coordinated by the three framework-oxygen atoms at a distance of 2.355 Å and three additional ones at distances of about 2.95-3.05 Å of the same 6-ring (Figure 8-11D). Due to the lack of coordination from the direction of the cage center, the four-coordinated environment, as preserved for the earlier sodium sites in halide cages, is completely removed for sodium in *dry* cages.

The ^{23}Na MAS NMR spectra of the halide/basic series are presented in Figure 8-12I to 8-14I. From the compositional trends it is obvious that the high-frequency resonances have to be assigned to sodium in halide containing cages, while the low frequency resonances can be assigned to sodium in the different salt-free environments. As expected in Cl/basic sodalites the resonances from sodium in halide and basic cages overlap strongly. In fact, in this series, the resonance shifts are very similar and can only be deconvoluted due to the much broader lineshape of the ^{23}Na resonance from basic cages. In addition peaks at about –3 and –10 ppm

are visible in several spectra of this series. These resonances result from sodium in hydro cages and sodium hydroxide on the crystallite surfaces, respectively. The latter resonance disappears quickly, when the sample is rinsed with distilled water. Unfortunately, this also leads to an exchange of basic for hydro cages, topotactically transforming the material, and changing the lattice parameters. In order to avoid the latter effect, the impure sodium spectra had to be accepted. The fraction of the ^{23}Na resonance assigned to sodium in hydro cages is less than 5 % in all spectra, although to the eye of the reader it might appear stronger, which is due to the underlying broad lineshape from sodium in basic cages.

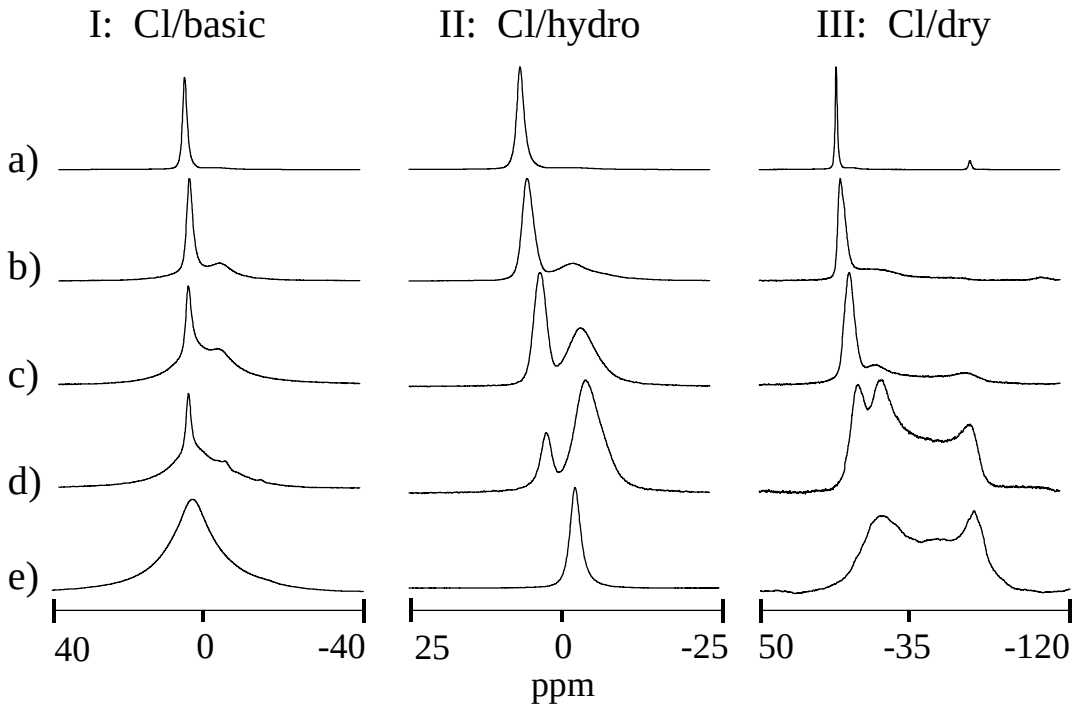

Figure 8-12. *^{23}Na MAS NMR spectra (observed at 132.26 MHz) of the Cl/basic, Cl/hydro, and Cl/dry series. The percentages of chloro cages, identical for all three series within the same row, are: (a) 98%, (b) 73%, (c) 45%, (d) 16%, (e) 0%.*

The ^{23}Na NMR spectrum of the halide/basic sodalite sample containing 98% Br^- anions (sample I-a) is characterized by a chemical shift of 7.5 ppm and a P_Q of 0.7 MHz, in good agreement with the literature.[52] For lower bromine contents, the determination of P_Q values by the two-field method becomes more difficult owing to extensive peak overlap. Nevertheless approximate P_Q values of 0.7 ± 0.1 and 0.6 ± 0.2 MHz can be estimated for ^{23}Na sites in *bromo* and *basic* cages, respectively.

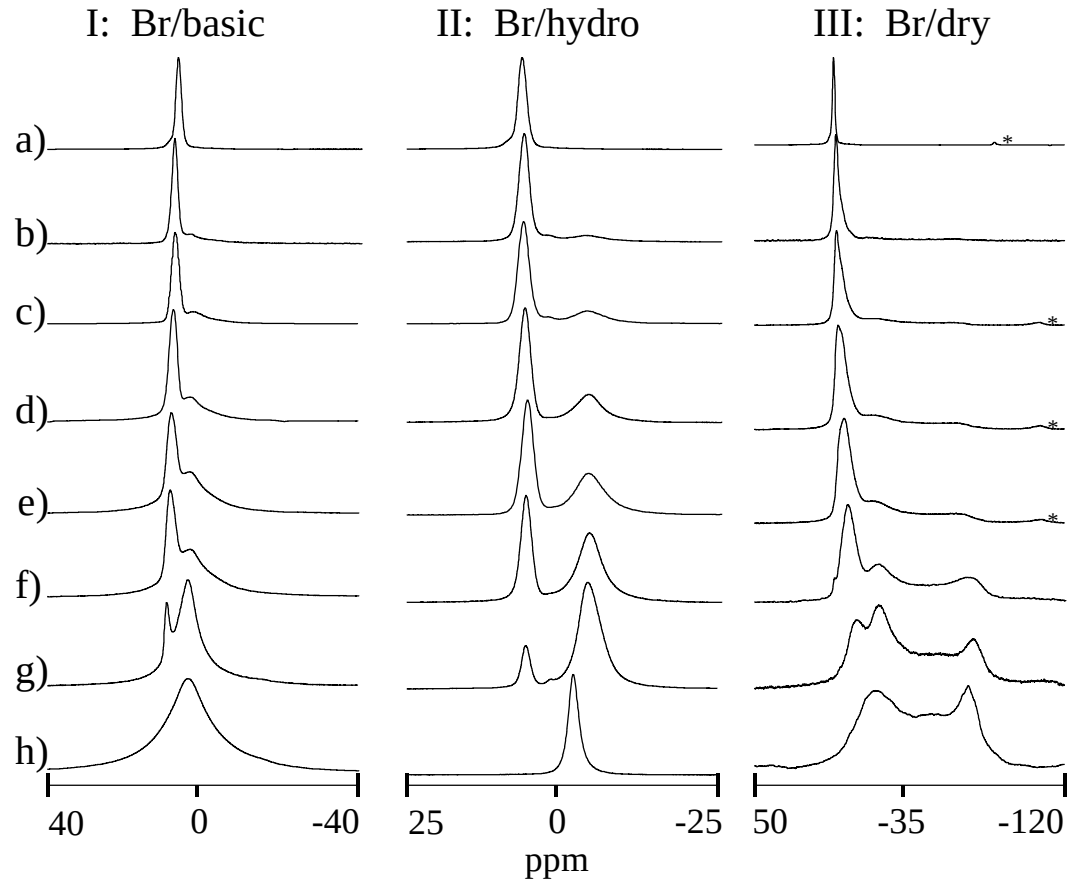

Figure 8-13. *^{23}Na MAS NMR spectra (observed at 132.26 MHz) of the Br/basic, Br/hydro, and Br/dry series. The percentages of bromo cages, identical for all three series within the same row, are: (a) 98%, (b) 78%, (c) 67%, (d) 61%, (e) 45%, (f) 36%, (g) 10%, (h) 0%. Spinning sidebands are marked by asterisks.*

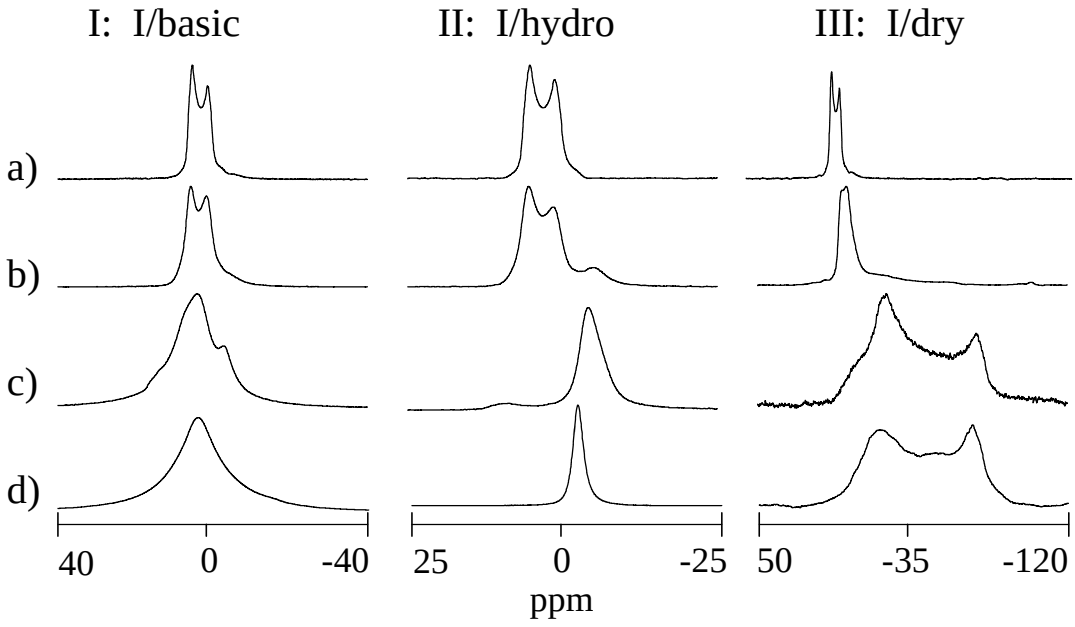

Figure 8-14. *^{23}Na MAS NMR spectra (observed at 132.26 MHz) of the I/basic, I/hydro, and I/dry series. The percentages of iodo cages, identical for all three series within the same row, are: (a) 98%, (b) 86%, (c) 7%, (d) 0%.*

In the I/basic sodalite series, a strongly quadrupolar broadened lineshape (C_Q = 1.75 MHz) can be observed and assigned to sodium in iodine containing cages similar to the case of mixed halide sodalites in Chapter 7. The chemical shift of this resonance changes from 7.6 ppm in pure I-sodalite to about 10 ppm for the sample with the lowest iodine concentration. The latter spectrum is dominated by a broad symmetrical resonance similar to the ^{23}Na resonance of basic sodalite. High and low-frequency shoulders are observed, which can be attributed to sodium in iodo and hydro cages. Due to the strong overlap and the low overall intensity, it was not possible to extract quadrupolar coupling or chemical shift data for the latter two peaks.

The ^{23}Na MAS NMR spectra of halide/hydro-sodalites in Figure 8-12II to 8-14II show two resonances assigned to sodium in *halide* and *hydro* cages, whose lineshapes are well separated from each other. The resonances from sodium cations in *hydro* cages are characterized by P_Q parameters between 1.5 and 1.7 MHz, as determined by both the two-field method and TQ MAS NMR (see Figure 8-15a and b). The resonance shift of the latter resonance changes between –5.5 ppm in I/hydro sodalites (Figure 8-14IIb) and –2.2 ppm in Cl/hydro sodalites (Figure 8-12IIb). This effect can mainly be ascribed to changes in the quadrupolar coupling parameters, while the chemical shifts of the latter resonances only vary between –1 and 0 ppm. For pure hydro sodalite we obtain δ_{cs} = 0 ± 0.1 ppm and P_Q = 1.1 ± 0.1 MHz.

The sodium resonances originating from halide occupied cages change according to the cage diameter similar to the case of mixed halide sodalites and will be discussed below.

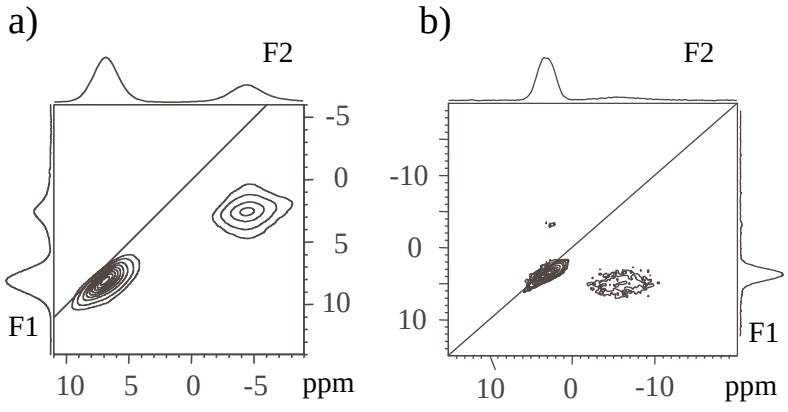

Figure 8-15: *^{23}Na TQ MAS NMR spectra observed at 105.81 MHz.* ***a)*** *Br/hydro sodalite corresponding to Figure 8-13IIf.* ***b)*** *Cl/hydro sodalite corresponding to Figure 8-12IIc.*

The ^{23}Na NMR spectra of halide/dry sodalites (Figure 8-12III to 8-14III) show two dominant lineshape components. Again the high frequency resonances can be assigned to sodium cations in *halide* cages. For sodium in Cl/dry sodalites, the largest variation of resonance shifts between 6.5 and –5.7 ppm is observed, resulting from chemical shifts between 7.0

and –2.4 ppm and quadrupolar coupling constants between 0.4 and 1.5 MHz from pure Cl to 16% Cl containing Cl/dry sodalites, respectively. For Br/dry sodalites quadrupolar coupling constants between 0.7 and 1.8 MHz with corresponding chemical shifts of 0.5 to 7.4 ppm are observed, for pure Br and 9% Br containing Br/dry sodalites. The MAS lineshapes, recorded at 52.9 MHz in this series, reveal a strong peak asymmetry indicating a superimposed distribution of P_Q values for this site (data not shown). While the quadrupolar lineshape of nearly pure iodine sodalites is well resolved, reflecting C_Q = 1.75 MHz, the presence of dry cages causes distortions to this resonance, first removing the singularities for the ^{23}Na spectrum of the sample containing 15% dry cages and creating a broad hump in the case of the sample containing 92% dry cages. While NMR parameters cannot be well extracted from these spectra, it appears, as if the chemical shift as well as the quadrupolar coupling constants increase along with an increasing fraction of dry cages.

The second lineshape component, characterized by strong second-order quadrupolar broadening effects, is attributed to sodium ions located in *dry* cages. The corresponding lineshape can be simulated with quadrupolar coupling constants between 5.4 and 5.8 MHz and asymmetry parameters close to zero (see Figure 8-16). These results are consistent with values previously published for pure dry sodalite (P_Q = 5.9 MHz).[67]

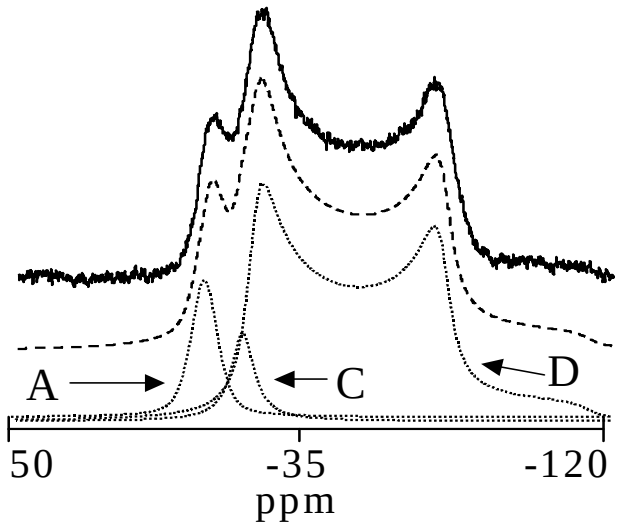

Figure 8-16: *132.26 MHz spectrum of Br/dry sodalite with 10 % of bromo cages (Figure 8-13IIIg) (solid line), simulated spectrum (dashed line), and de-convoluted lineshape components belonging to sodium in A: bromo cages, C: hydro cages and D: dry cages (dotted curves).*

It was also possible to obtain a ^{23}Na TQ MAS NMR spectrum of this 11% bromine containing Br/dry sodalite as shown in Figure 8-17. Maximum rf-power had to be used and 2048 FIDs per t_1 slide had to be acquired to this end. Although the strong quadrupolar lineshape dominates the 1 D spectrum (Figure 8-13IIIg) the corresponding intensity is rather small in the TQ MAS spectrum due to the unfavorable excitation probability of the triple quantum transition in case of such large coupling constants. Nevertheless, the resonance can be

observed and a P_Q value of 5.8 MHz can be derived from the F_1 and F_2 shifts of the center of gravity. The spectrum also reveals the 1.8 MHz quadrupolar coupling constant of the resonance at 4.5 ppm which has been ascribed to sodium in Br cages. The latter resonance shows a low frequency shoulder, which can either be interpreted as the result of a large distribution of coupling constants or a superimposed separate resonance with a quadrupolar coupling constant of 2.5 MHz and a chemical shift of –11 ppm overlapping with the high-frequency resonance. This signal might result from strongly distorted maybe containing n < 4 water molecules. The peak at F1 = -10 and F2 = -25 ppm might have similar origin, but its small overall intensity (when corrected for the effect of the quadrupolar coupling constant) indicates that it should not play a significant role in understanding the 1D NMR spectrum.

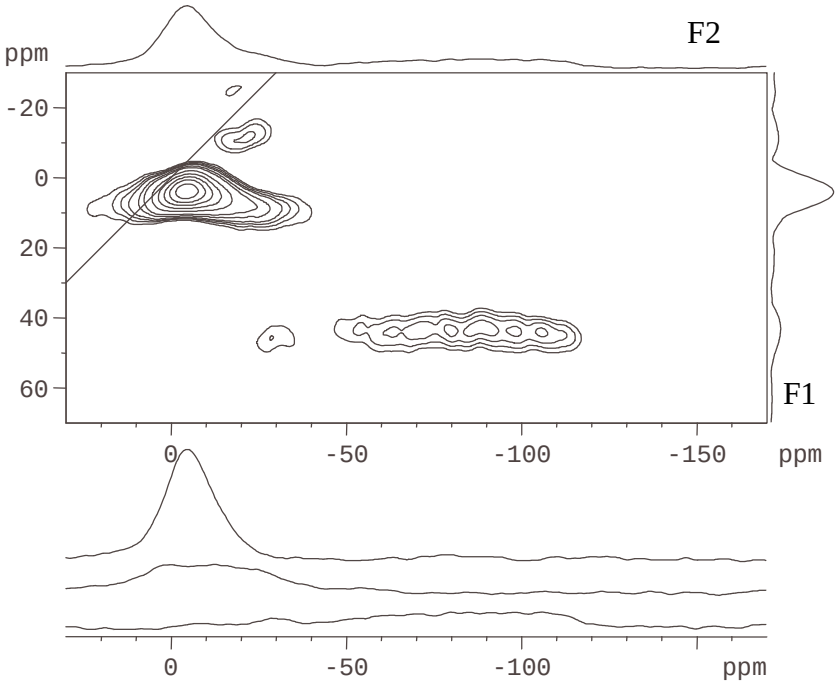

Figure 8-17: *^{23}Na TQ MAS NMR spectra of 11% Br containing Br/dry sodalite acquired at 104.22 MHz. The slices shown below have F_1 frequencies of 5 ppm, 10 ppm and 42 ppm, respectively. At this point it is not clear, if the lower frequency resonances belong to different slices or are just the consequence of a distribution of quadrupolar coupling parameters.*

8.2 Discussion of the Observed NMR Spectra.

In addition to the monotonic changes in the structural (lattice) parameters, which affect chemical shifts of the NMR resonances of both the framework and the extra-framework species within each series and have mostly already been discussed along the mixed halide sodalite series, in this chapter the discussion will focus on the second aspect of the solid solution effects concerning the electric field gradients produced by the disorder, which gives rise to additional sites and/or amplified nuclear electric quadrupolar interactions. Thus both of these aspects will be discussed for all nine solid solution series, considering both the effects on the framework and the local environments of the extra-framework ions.

8.2.1 Solid Solution Effects on the Framework

When the water molecules are removed from the cages of hydro-sodalite, the sodalite framework expands rather than contracts (see Figure 6-1). Similarly, the lattice of salt-free sodalite is expanded in comparison with that of salt-bearing sodalites. The underlying reason for this unusual behavior is the Coulomb repulsion between the charge compensating alkali cations. In the absence of the central anion or some polar molecular species such as water, the unscreened Coulomb repulsion pushes the alkali cations away from the center of the sodalite cage. This in turn increases the average Al-O-Si bond angle leading to lattice expansion. Because of the unusually large Al-O-Si bond-angles, the aluminosilicate framework of dry sodalite is strained and eager to absorb small atoms or molecules that can help screen Coulomb repulsion.

As shown above, the topotactic transformations lead to a removal of the observed equivalence degeneracy of the aluminum sites. In order to rationalize the existence of several distinct ^{27}Al resonances in the Br/hydro and Br/dry series, it is necessary to consider the local aluminum environments.

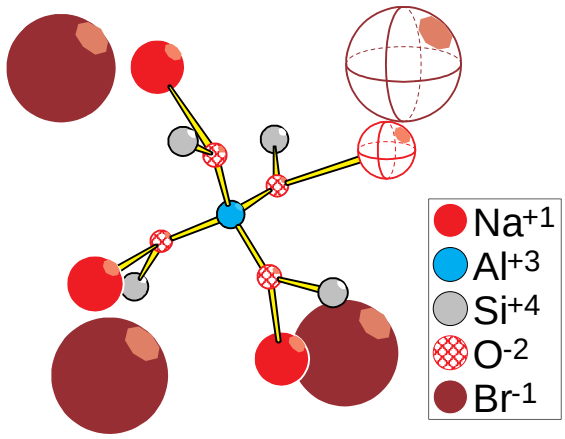

Figure 8-18: *Aluminum environment in mixed salt-bearing/salt-free sodalites. While in the lower and left three salt bearing cages, all central positions as well as all sodium sites, which are linked to the oxygen atoms of the AlO_4 tetrahedra are occupied, this is not the case in the fraction of the cage in the upper right corner. However, even if this cage lacks a central anion, the probability of the vacant sodium site is only 25%, since still three framework-charge compensating sodium ions are present in the salt-free cage.*

As shown in Figure 8-18, each aluminum site is located at the joint of four sodalite cages. Different environments result from different distributions of the two types of neighbors. If the degeneracy of the aluminums sites is removed by different central anions in the bordering cages, a binomial distribution of aluminum sites according to the fractions of cage types can be expected. Figure 8-19 shows several simulations for aluminum site distributions. The binomial intensity distributions expected for the aluminum sites dependent on different cage types are given in column b), where the numbers on the x-axes correspond to the number of salt-bearing cages neighboring the aluminum site. Model b) predicts that the main intensity is shifted towards aluminum resonances corresponding to fewer salt-bearing neighbors with

decreasing halide content. In the cases of mixed halide sodalites and mixed halide/basic sodalites only one aluminum site could be resolved, indicating that these differences do not affect the aluminum resonances to generate multiple resonances.

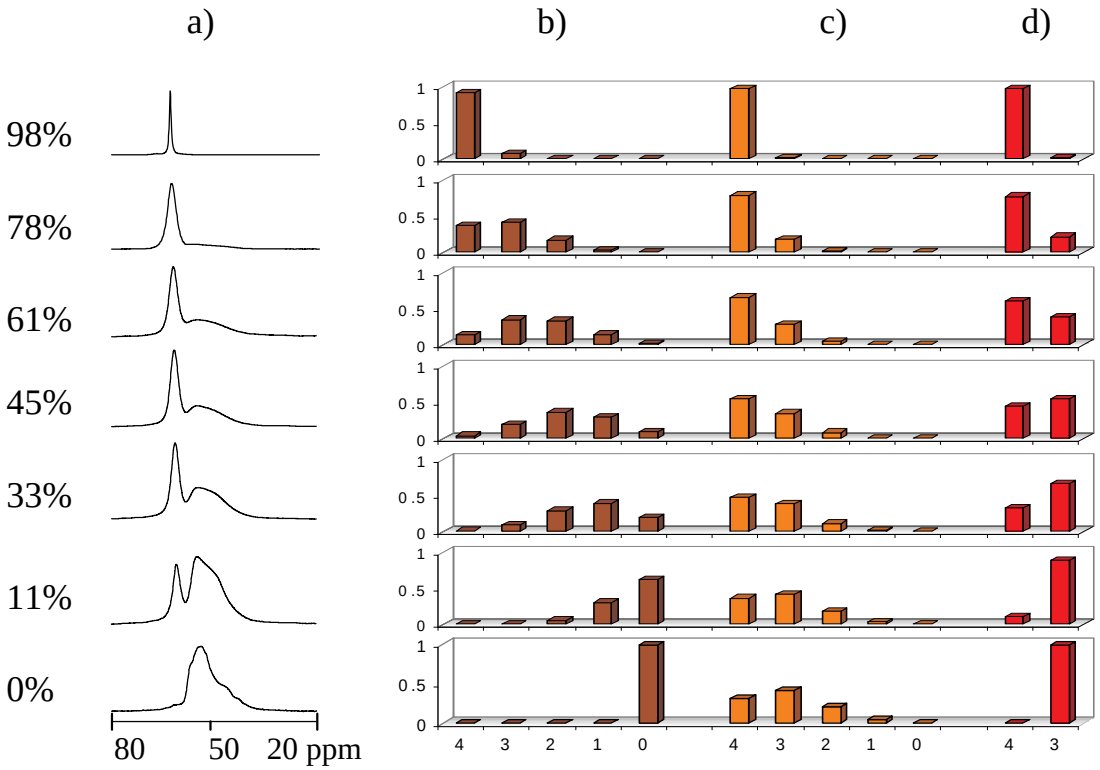

Figure 8-19: a) *the ^{27}Al MAS NMR spectra of Br/dry sodalites with halide fractions according to the left column.* ***b)*** *probabilities for 4 to 0 salt free cages neighboring the aluminum site, according to the halide fraction and binomial distribution.* ***c)*** *probabilities of 4 to 0 unoccupied sodium sites neighboring the aluminum site, according to the given halide fraction and binomial distribution of salt-free cages.* ***d)*** *Same probabilities as in c), but with the restriction of a maximum of one vacant sodium site per associated aluminum atom.*

Also, as shown in Figure 8-18, each aluminum atom is bound to four oxygen atoms each linked to a sodium site in a different sodalite cage. This sodium site is always occupied if the cage is salt-bearing (or basic), but if the cage is salt-free, however, the sodium site next to the aluminum-bound oxygen atom is vacant with a 25% probability. Statistically also a distribution of i = 0 to 4 vacant sodium sites linked to the framework aluminum can be expected, the probability, *P(i)* given by:

$$P(i) = \sum_{v=i}^{4} P(v) \cdot \binom{v}{i} \cdot \left(\frac{1}{4}\right)^{i} \cdot \left(\frac{3}{4}\right)^{v-i} \qquad \text{Equ. 8-1}$$

Here *P(v)* is the probability that *v* of the 4 neighboring cages are salt-free, according to the overall halide fraction. While the resulting probabilities given in column c) behave more similar to the experimental data than the probabilities of column b), the residual probability of the aluminum environments with four occupied sodium sites for pure dry sodalite is in

contrast to the observed experimental data. This is an indication that the vacant sodium sites are not statistically distributed throughout the sodalite lattice. (It should be noted that some order is of course present due to the fact that each salt-free cage has only one vacant sodium site. This however, does not necessarily affect the distribution around the aluminum site, since aluminum is neighboring sodium sites in four different cages, thus still zero to four vacant sites are possible. While the latter effect affects the probabilities for spatially close other aluminum sites, these effects are likely to average out statistically over the whole crystallite.)
A distribution where only two possible aluminum sites exist in these systems can be realized under the restriction that no more than one vacant sodium site neighboring each aluminum are allowed. The corresponding binary distribution is given in Figure 8-19d. In fact, the corresponding probabilities agree well with the integrated peak intensities in the ^{27}Al NMR spectra of Br/hydro and Br/dry sodalites, after correcting the systematic error arising from the large differences in the QCC-values.[39] The occurrence of only two sites is also in accordance with the ^{27}Al TQ MAS NMR spectra as shown in Figure 8-6 an 8-4, where only two sites could be resolved, but the existence of overlapping resonances in the low-frequency lineshape could not completely be excluded. This conclusion is also consistent with recent structure refinements of pure dry sodalite.[13,14] In this material the sodium ions are strictly ordered, such that each aluminum site is linked to only one unoccupied sodium site. Thus it can be concluded that a similar type of short range order exists in the mixed halide/dry sodalites, while the long range order is disturbed by the halide filled cages precluding observation by X-ray diffractometry.
Also for mixed halide/hydro sodalites such an order is expected and in agreement with the TQ MAS and VT NMR data. While at 373 K the ^{27}Al NMR spectrum on 30% Br containing Br/hydro sodalite shows only two quite narrow resonances, at 273 K the low-frequency resonance is much broader (see Figure 8-4), what could be caused either by a distribution of quadrupolar coupling parameters or by overlapping ^{27}Al resonances. As will be shown below it is likely that the sodium vacancies are also ordered in this system and a wide distribution of ^{27}Al quadrupolar coupling parameters occurs as the result of “freezing” water molecules inside the hydro cages.

As already shown in Chapter 7, the chemical shifts of the aluminum resonances are correlated with the average Al-O-Si bond angles and are therefore dependent on the cell edge of the sodalite unit cell. So far, the linear relation had only been tested on sodalites with a single aluminum resonance.

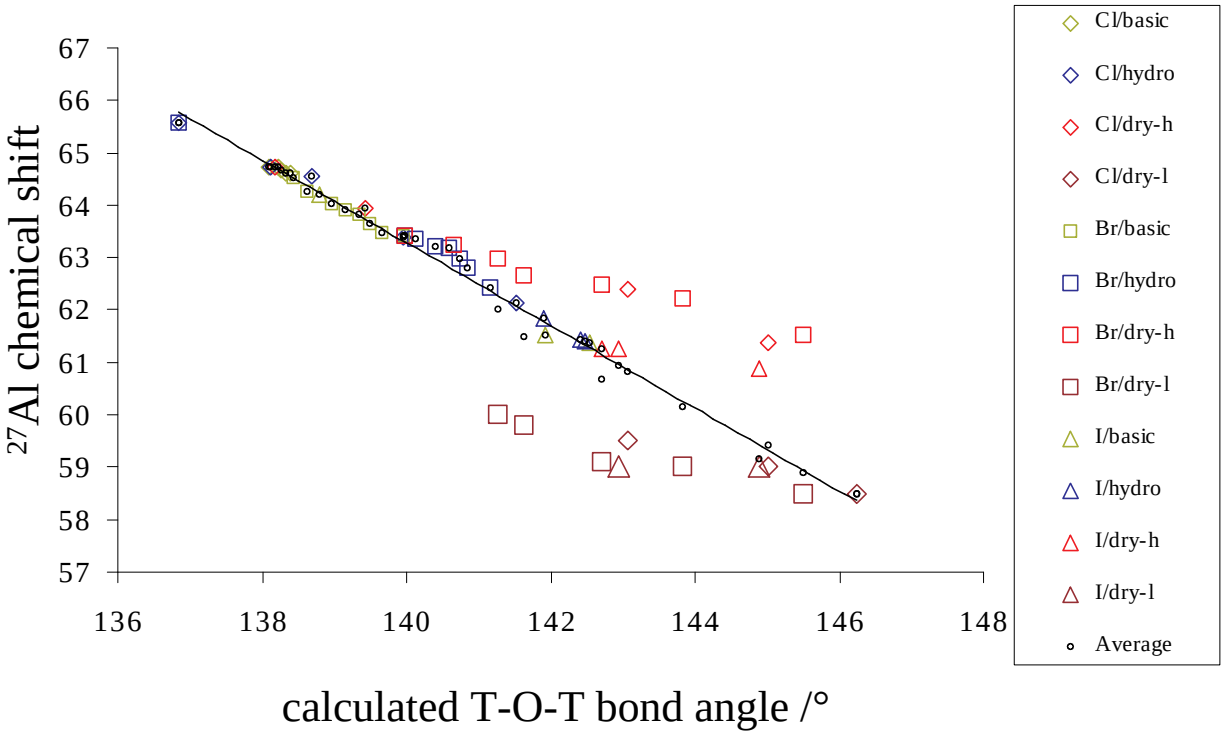

Figure 8-20: *^{27}Al MAS NMR chemical shift versus average Si-O-Al bond angle calculated from the lattice constant for all three series. The spectra of mixed halide/dry sodalites contain two ^{27}Al NMR resonances with chemical shifts. The chemical shift of the high frequency resonances (halide/dry-h) is always plotted in orange and the corresponding shifts of the low frequency resonances (halide/dry-l) are marked in purple. The small open circles give the average ^{27}Al chemical NMR shift of each spectrum (see text for details).*

Figure 8-20 gives the chemical shifts of all the ^{27}Al resonances observed in the nine series of halide-containing sodalite solid solutions. For mixed halide/basic and halide/hydro sodalites, the correlation of δ = 168 ppm – 0.74 ppm/° between average Al-O-Si bond angle and chemical shift is confirmed, indicating that even in the halide/hydro sodalite series, the framework is in average not significantly distorted due to the absence of 25% of sodium ions. While in this series, two ^{27}Al resonances can be distinguished that still have similar chemical shifts, the two ^{27}Al resonances of the halide/dry series are further characterized by significant chemical shift differences (and quite different P_Q values of 1.5 MHz and 4.4 MHz). For these resonances, the slopes in the plot of chemical shift versus average Al-O-Si bond angle are significantly smaller than expected from the average Al-O-Si bond angle as calculated from the lattice constant. The slope also decreases from Cl/dry to Br/dry to I/dry sodalites. A similar trend is observed for the low frequency resonances, but at smaller absolute chemical shift values. Here the experimental error is about ± 1 ppm owing to significant site distribution effects.

It turns out that even for halide/dry sodalite solid solutions, the correlation with the average T-O-T bond angle is maintained, if the weighted average of the chemical shifts of the two ^{27}Al resonances of halide/dry sodalites are plotted (see open circles in Figure 8.20). This indicates that the average T-O-T bond angle corresponds to that predicted from locally different lattice constants, while local deviations from the average T-O-T bond angle are detectible. In order to rationalize these observation, the P_Q values of the various aluminum sites were simulated on the basis of a point charge model,[67] using nuclear parameters given in Table 4-I. While this model is more suited for ionic environments, it has been shown for other nuclei[86,87] that such an approach is capable of mimicking the effect of electron density distributions in bonding orbitals within the first coordination sphere. The adjustable parameter in this procedure is the effective charge on the oxygen atoms, reflecting the polarity of the Al-O bonds. To reproduce the experimental value of C_Q = 0.7 MHz in bromo sodalite, the oxygen charge had to be adjusted to –1.6e in these calculations. Due to the covalent nature of the Al-O bond, this value is far from –0.67e that can be derived in ionic systems following the procedure by Brown and Altermatt.[66] This discrepancy shows the limitations of the point charge model, yet we find this simple model is useful in comparing relative magnitudes of quadrupolar coupling constants for the different aluminum sites. Following the predictions of Brown and Altermatt,[66] the charge of oxygen next to a vacant sodium site in Br/hydro sodalite was increased by –0.3e to account for the missing Na-O bond. This resulted in a C_Q value of 2 MHz in good agreement with our experimental findings.

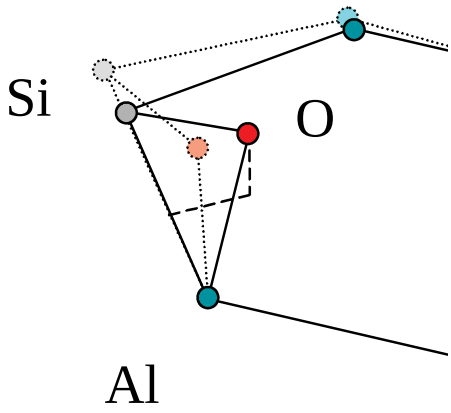

Figure 8-21: *Distorted fraction of an $Al_3Si_3O_6$-ring. If the attracting sodium ion is gone, the electrostatic repulsion from the three oxygen atoms as well as the expansion of the cage caused by the unscreened electrostatic repulsion of the remaining three sodium ions, are likely to move the oxygen atom away from the center of the cage. For the computations it was assumed that the orientation of the Si-Al vector remains, while the T-O-T bond angle increases and the T-T-O angles decrease, causing distortion of the TO_4 tetrahedra as well as an increase of the average T-O-T bond angle.*

In order to simulate P_Q = 4.4 MHz of the ^{27}Al site linked to the vacant sodium site in Br/dry sodalite, one of the four Al-O-Si bond angles was expanded by 22^o as indicated by Figure 8-21. This was accomplished in our simple model by keeping the original orientation of the Al-

Si vector while increasing the average Al-O-Si bond angle of the aluminum site by about 5.5°. Within the sodalite lattice such an operation requires dislocation of the T atoms from their crystallographic sites, which affects other T-O-T but also O-T-O bond angles. According to Vogel et al,[88] the change in the O-Si-O bond angle affects only the chemical shift anisotropies, but not the isotropic values. Projecting these findings to the ^{27}Al NMR shifts of our system as shown in Figure 8-20, we propose that the chemical shift difference between the two aluminum sites in the halide/dry series arises from differences in the average Si-O-Al bond angles. In this case, the 3.3 ppm difference in chemical shift observed for the two ^{27}Al resonances corresponds to a difference of about 4.5° in average Al-O-Si bond angle of the two sites. This is in reasonable agreement with the difference in average T-O-T angles (5.5°) deduced from the analysis of the quadrupolar interactions. The smaller slopes observed in Figure 8-20 for each site within the halide/dry series suggest that these angles change only slightly. For these series, the main compositional effect concerns the population ratio of these sites. As noted above, the universal correlation of chemical shift with the average Al-O-Si bond angle is still obeyed, however, only if the average shift of both sites, weighed by their population ratio is plotted.

8.2.2 Solid Solution Effects on the Extra-framework Species

As already shown in Chapter 7, the halide NMR resonances are a sensitive tool for the observation of the alkali-halogen distance. Figure 8-22 plots the ^{35}Cl chemical shifts versus the Na-halide distances calculated from the lattice constants.

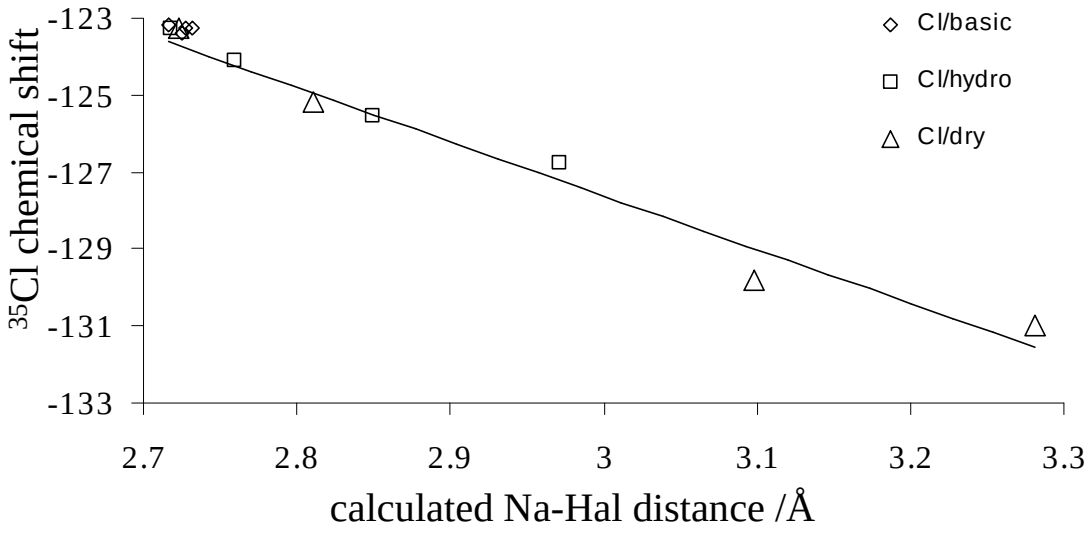

Figure 8-22: *^{35}Cl chemical shift of mixed Cl/salt-free sodalites as a function of the Na-Cl distance as computed from the lattice constant.*

The chemical shifts reflect the behavior of the cell edge increasing from pure chloro sodalite to Cl/hydro and further to Cl/dry sodalites. The observed slope of 15.3 ppm /Å is in good agreement with the observed 17.6 ppm/Å from the mixed halide sodalites in Chapter 6. Actually the slope observed here has an internal error of about 2 ppm/Å due to uncertainty in the shift of the Cl/dry sodalites with small halide concentrations. This is due to the fact that meaningful quadrupolar coupling constant values could only be determined from the peak maxima of the field dependent spectra.

Likewise, Figure 8-23 reveals a universal correlation of the ^{81}Br chemical shift with the Na-Br distance with a slope of –35.7 ppm/Å for all three mixed Br/salt-free solution series, again in good agreement with the data observed for mixed halide sodalites. Other than for ^{35}Cl in the Cl/salt-free series, the P_Q values of the ^{81}Br resonances in the Br/hydro series are significantly larger than in the two other series indicating a distortion of the tetrahedral symmetry. As already seen in Chapter 6, the ^{81}Br resonances are more sensitive to an inhomogeneous environment than the ^{35}Cl resonances. While in the Br/basic and the Br/dry series, the P_Q values remain below 1 MHz, these values extend up to 2.2 MHz in the Br/hydro series. The distribution of vacant sodium sites in the neighboring cages cannot be the origin of this effect observed in the Br/hydro series, since it can also be expected for the Br/dry series.

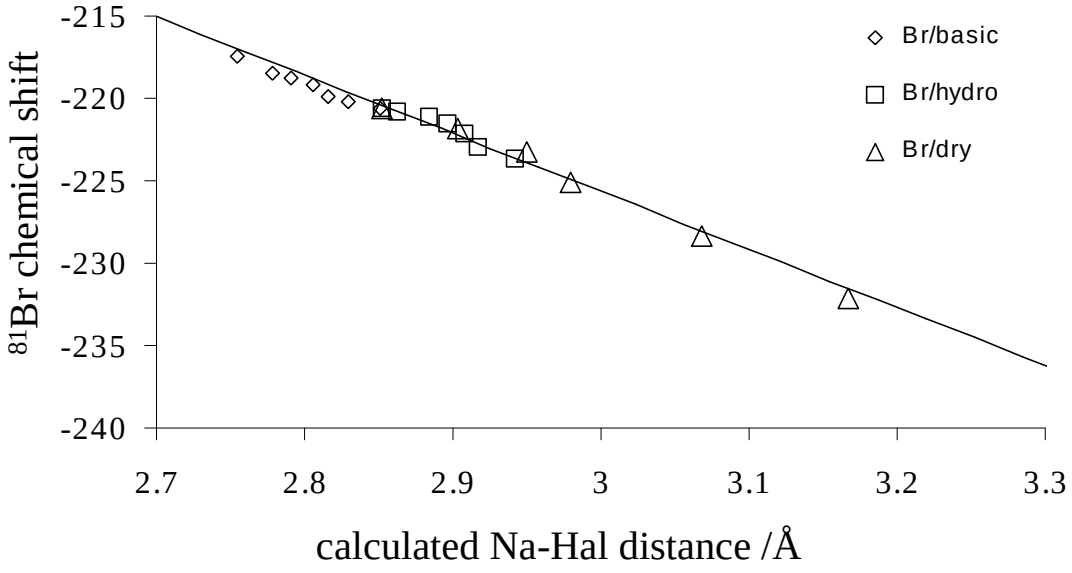

***Figure 8-23**: ^{81}Br chemical shift as a function of the calculated Na-halide distance.*

The ^{81}Br spectra of several Br/dry sodalites also show an additional low-frequency shoulder, what is difficult to assign. The origin of the relatively large ^{81}Br linewidths in the spectra of

these samples is more difficult to explain, considering that the Br^- anions populate sites with T_d symmetry. The quadrupole moment of ^{81}Br is larger than for the other nuclei studied here, which makes its NMR resonances more sensitive to structural perturbations. Also it is conceivable that the Br^- anions in enlarged *bromo* cages do not reside in the center of the sodalite cage, a situation similar to rare earth ions in endohedral fullerenes.[89] The EFG is the smallest in the center of the sodalite cage but rises sharply elsewhere. A displacement of the Br^- anions from the center of the sodalite cages would therefore lead to strong quadrupolar effects, which are expected to increase with increased cage size, in agreement with the experimental findings.

The data set of the ^{127}I resonances in mixed I/salt-free sodalites is quite limited. Between the samples with 98 and 86 % iodine only minimal differences in the shift of the dominant resonance can be observed. The ^{127}I resonances of the 7% iodine containing sample are extremely weak. This can be understood on the basis of the much larger nuclear electric quadrupole moment of ^{127}I compared to ^{35}Cl and ^{81}Br. Even slight deviations from a cubic local environment will produce strong quadrupolar interactions, resulting in broad lineshapes. Only a broad low-frequency shoulder is visible in the ^{127}I NMR spectrum of 86% I containing I/dry sodalite, which is likely to be due to similar effects as discussed for the Br/dry sodalites above.

As already shown for the mixed halide sodalites, the ^{23}Na chemical shifts of sodium in halide occupied cages can be understood to be controlled by the Na-halide distances. The chemical shifts of sodium in halide occupied cages are plotted in figure 8-24a. For the same Na-halide distance, the deshielding increases from chlorine to bromine to iodine. The data points, however, are more scattered than for the mixed halide sodalites, thus preventing reasonable exponential fits of the data. Approximate linear fits yield slopes of –17, -20 and –27 ppm/Å for sodium with chlorine, bromine and iodine as the central cages anion. These slopes can be compared to –19, -24 and –34 ppm/Å for the corresponding environments in mixed halide sodalites, if a simplified linear fit is applied to those data. If only mixed halide/basic and halide/hydro sodalites are taken into account, the values of the slopes always agree within 2 ppm. Thus, the differences are mostly due to the experimental data points from mixed halide/dry sodalites. This discrepancy can be understood if one assumes local cage size variations such that the halide filled cages are on average slightly smaller and the dry cages are slightly larger than expected. In such a case, the Na-halide distances calculated from the experimental lattice constants are overestimated leading to systematically smaller slopes.

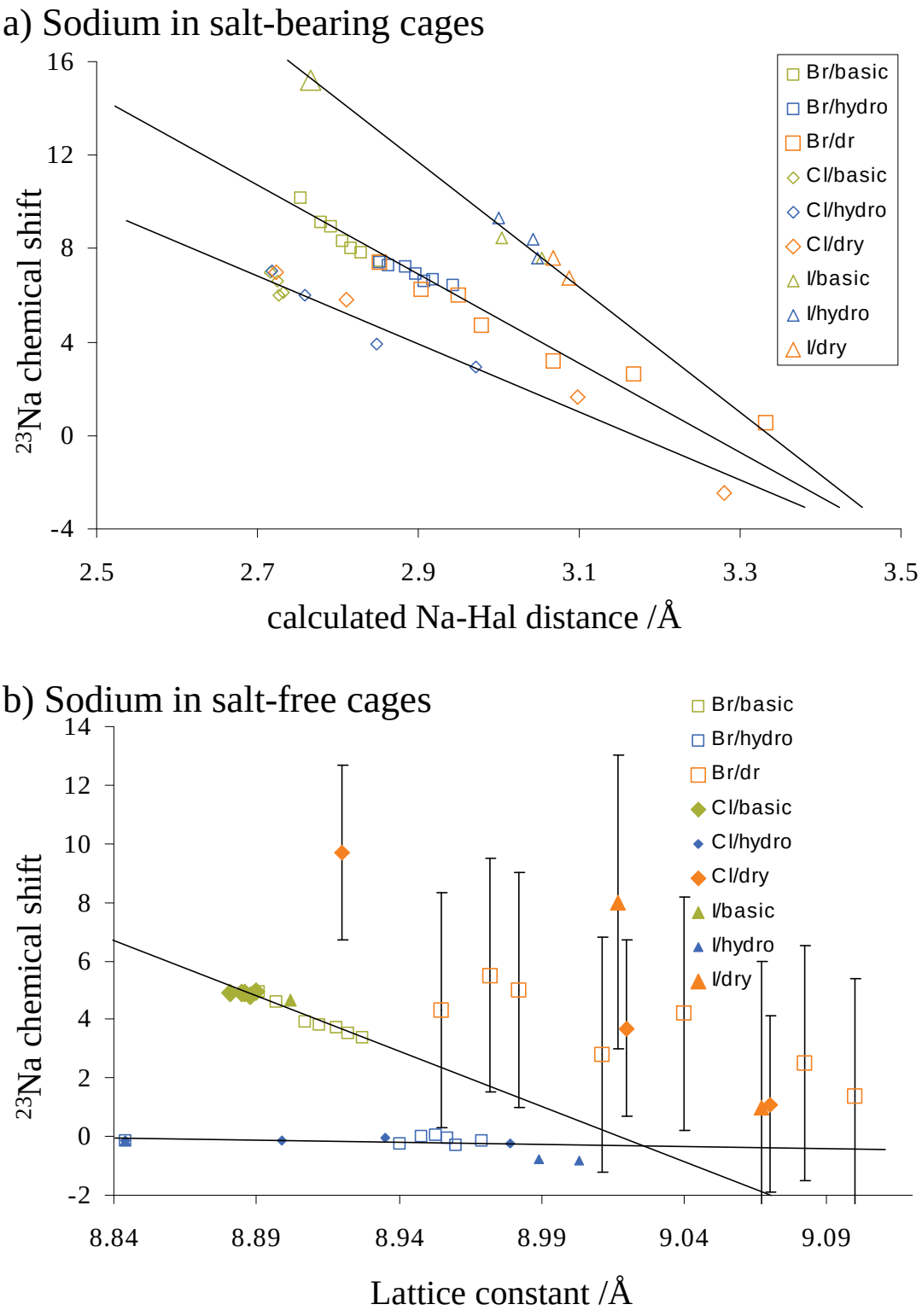

Figure 8-24: *^{23}Na chemical shifts of mixed salt bearing/salt-free sodalites.* ***a)*** *chemical shifts of sodium in salt bearing cages. While the symbol represents the type of halide cage, the color gives the type of salt free cage.* ***b)*** *^{23}Na chemical shifts of sodium in basic and salt-free cages. The color denotes the type of salt-free cage and the symbol the corresponding halide. The experimental errors are about the size of the symbol with the exception of the ^{23}Na resonances of dry cages, where the overlap with the high frequency resonance precludes an exact determination of CQ (±0.2) and η (± 0.1), resulting in fairly large errors of the chemical shift.*

The ^{23}Na chemical shifts of sodium in salt-free cages are plotted in Figure 8-24b. The chemical shift of sodium in basic cages is quite similar to sodium in chlorine occupied cages. In addition a slope of about 17 ± 2 ppm /Å can be observed when the chemical shift is plotted against the calculated Na-center distance. In Figure 8-24b, however, the chemical shift is plotted versus the cell edge, since no single central ion exists in these cages. As show in Chapter 3 the relation between Na-center distance and cell edge can be considered linear over small variations in the cell edge.

For sodium in hydro cages, no obvious correlation between the lattice parameters and the chemical shift is observed. The chemical shifts near 0 ppm reflect a coordination environment similar to that of a hexaquo complex. In contrast to the sodium environments in other cages, sodium ions in *hydro* cages are octahedrally coordinated with six oxygen atoms, three of which belong to the framework oxygen and the other three to water molecules. This sodium environment is not expected to change much with lattice parameters, consistent with the ^{23}Na chemical shift behavior observed. One has to keep in mind, however, that the observed resonance shifts vary between –1.0 and –5.5 ppm and differ mainly in the contribution of the quadrupolar shift resulting from quadrupolar coupling constants between 1.05 and 1.8 MHz.

For Br/dry sodalites, the chemical shifts of sodium in *dry* cages scatter between –2 and 10 ppm and suggest a relation between lattice constant and ^{23}Na chemical shifts of $\delta = 472$ ppm $- a_0$[Å] ·52 ppm/Å. The relation, however, has to be evaluated with care. Due to the overlap of the sodium resonances in the halide bearing and dry cages, the onset of the resonance with the strongly quadrupolar broadened lineshape cannot be extracted with precision. In contrast, the low-frequency shoulder of the signal with P_Q values of about 5.8 MHz had to be used. Based on this reference point, changes of 0.4 MHz in P_Q change the chemical shift by about 20 ppm. The data points plotted for dry sodalites in Figure 8-24b were extracted from the spectra assuming similar nuclear quadrupolar coupling constants of about 5.7 MHz, which were only slightly modified to increase the quality of the fit. However, these values are uncertain by about 10 to 15 ppm due to potential changes in the quadrupolar coupling constants throughout the series, which cannot be detected with higher precision.

Besides the GAUSSIAN computations, the simple point charge model discussed earlier was used to calculate the ^{23}Na quadrupolar coupling constants (C_Q) from the structural data. The point charges have been determined following the procedure by Brown and Altermatt,[66] resulting in -0.67e, -0.90e, -1.30e, and -0.89e for framework-oxygen, oxygen in H_2O, oxygen in $H_3O_2^-$, and bromide anion, respectively. Using the ^{23}Na nuclear parameters listed in Table

4-I, quadrupolar coupling constants of 0.6 MHz, 0.7 MHz, 2.0 MHz, and 5.5 MHz were calculated for sodium sites in bromo, basic, hydro and dry cages, respectively. These values are in very good agreement with the experimental data in Table 8-I. We note that the variations of electric field gradients with lattice parameters in this series are generally small while the increase of P_Q values for sodium in bromo cages of the Br/dry series with decreasing Br^- content is noticeable and cannot be explained simply by the distance change. It is possible that the sodium ions in salt-bearing cages of Br/dry sodalites are dislocated from the center of their six rings, as in the case of pure dry sodalite.[13] It is also possible that the Br^- anions are displaced from the center of the sodalite cages. Since the observed field gradients can be produced by a large variety of structural arrangements, no specific structural information can be extracted from the experimental data.

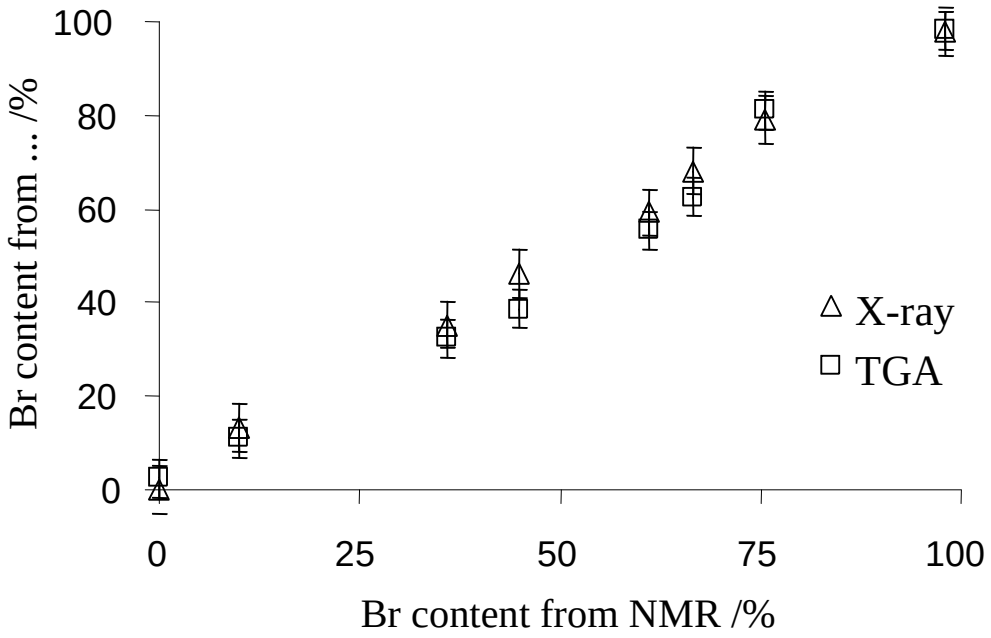

Figure 8-25: *Fraction of bromine filled cages as determined from TGA and x-ray diffractometry compared to those determined from quantitative ^{23}Na MAS NMR on mixed Br/hydro sodalites.*

A very important accomplishment of this study was to utilize the ^{23}Na MAS NMR spectra of mixed halide/hydro sodalites as a convenient gauge of the sample's chemical composition. It was found that the halide content in mixed sodalites can be determined from sodium NMR data in good agreement with the more traditional methods listed such as TGA and XRD. The ^{23}Na MAS NMR signal of the sodium cations in halide cages is well separated from the sodium resonance in hydro cages. By choosing a small (π/6) flip-angle and sufficiently large relaxation delay times (t>5 s), the fractional areas of both resonances in Figure 8-12II to 8-

14II can be used for accurate determination of the bromine content. The values need to be adjusted for the sodium cage content since halide cages contain four sodium cations while hydro cages have only three of them.

8.3 Ion and Molecular Dynamics in Mixed Halide/Salt-free Sodalites

8.3.1 The Pure Hydro and Br/hydro Sodalite Systems

As can be seen in Figure 6-1, a substantial difference exists between mixed halide/hydro sodalites and pure hydro sodalite. While the lattice constant of the former approached a value of 8.97 Å for small halide concentrations, the pure hydro sodalite has a lattice constant of 8.844 Å at room temperature, which is the smallest observed for all sodium based sodalites. It was assumed that cooperative hydrogen bonding is the reason for this effect,[56] but ^{1}H MAS NMR spectra show chemical shifts of 4.5 and 4.3 ppm for the latter two systems, indicating that no substantial difference in hydrogen bond strength exists. Figure 8-26 shows the ^{1}H MAS NMR spectra of 28% bromine containing Br/hydro sodalite and pure hydro sodalite.

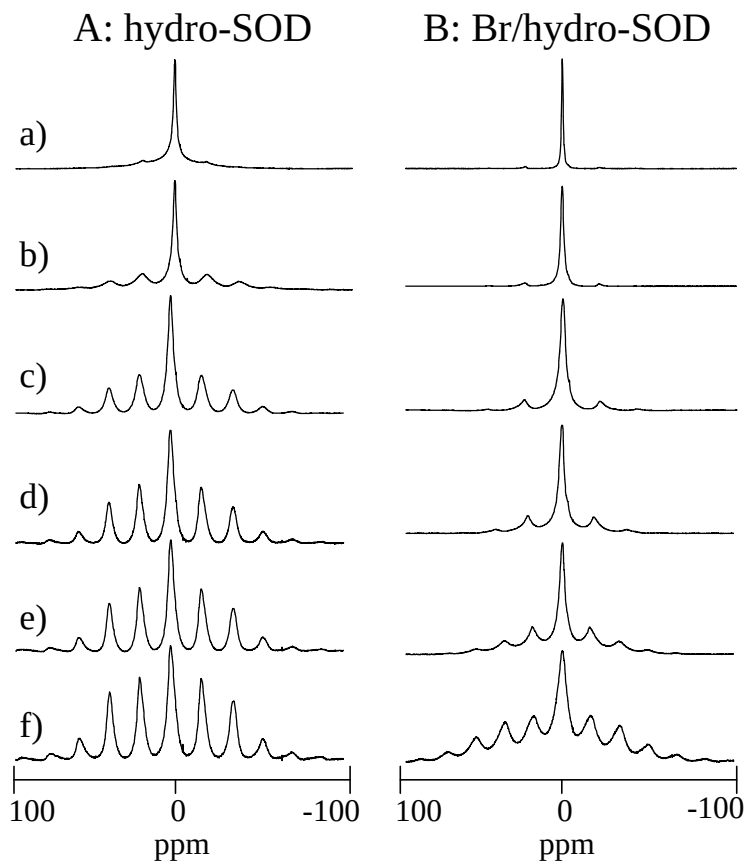

Figure 8-26: *^{1}H MAS NMR spectra of Br/hydro and pure hydro sodalites between 170 K and 370 K. All the spectra were acquired at 400.11 MHz at spinning speeds of 7000 Hz. Spectra of comparable temperature are plotted next to each other. The exact temperatures for column A and B are: a) 370 K, 370 K; b) 330 K, 340 K; c) 270 K, 290 K, d) 240 K, 250 K, e) 210 K, 210 K; f) 170 K, 180 K, respectively.*

While in both systems the chemical shifts change only by about 0.2 ppm between 170 K and 370 K, the most striking difference between the spectra of the two sodalites arise in the

intensities of the spinning sidebands at similar temperatures. In addition, the spinning sidebands of the pure hydro-sodalites have a linewidth of 1900 Hz at the lowest temperature, while the corresponding sidebands of the mixed Br/hydro sodalite are more than twice as wide (3900 Hz). For all low temperature spectra, fifth order sidebands at a distance of 35 kHz of the central transition can be observed. The relative intensity of the outer sidebands compared to the inner ones is slightly reduced at higher temperatures.

The ^{27}Al MAS NMR spectra of pure hydro sodalite show single resonances with low frequency shoulders at low temperatures. The linewidths decrease from 640 Hz at 180 K to 268 Hz at 370 K, to increase again slightly to 323 Hz at 410 K. The resonance shift is about 63.6 ppm at 250 K and below and decreases with increasing temperature down to 61.2 ppm at 410 K.

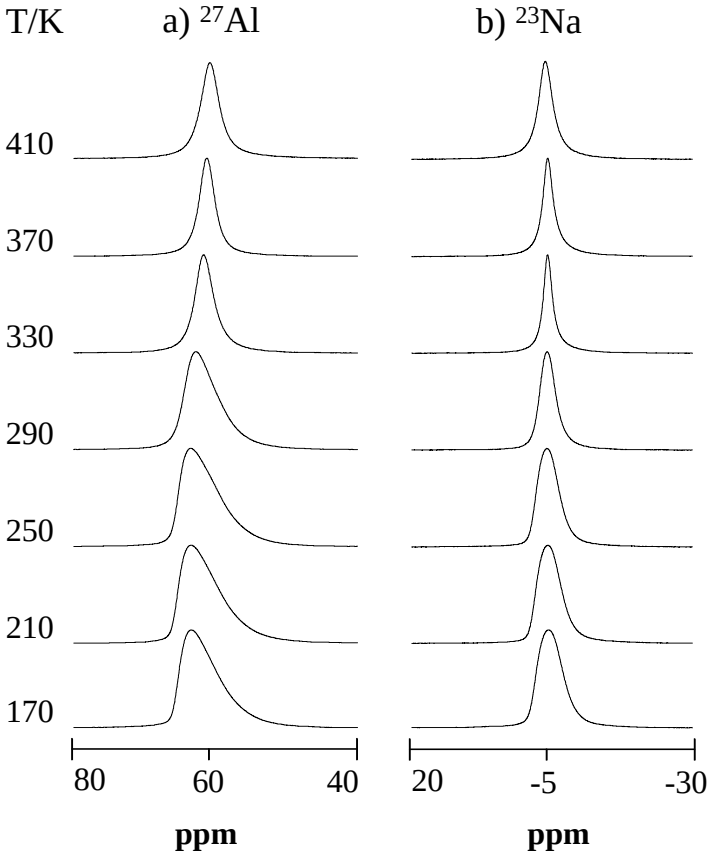

Figure 8-27: *^{27}Al, and ^{23}Na spectra of pure hydro sodalite. The spectra were acquired at 104.23 and 105.81 MHz, respectively. The spinning speed was 7000 Hz in all cases. For this sample data was only acquired up to 410 K due to the fact, that above this temperature, the sodalites looses water, expanding the gas volume in the closed spinner. A special spinner cap was then designed, allowing gas exchange. The latter one was, however, only applied in subsequent experiments like the VT NMR analysis of Br/hydro sodalite, which is plotted in Figure 8-28.*

The ^{23}Na MAS NMR spectra also show only a single resonance in this temperature region. Similar to the ^{27}Al data, the minimum linewidth of 202 Hz is found at 330 K and increases towards higher and lower temperatures to 533 Hz at 170 K and 322 Hz at 410 K. The ^{23}Na chemical shift varies only little over the observed temperature region and changes from -4.4 ppm at 170 K to –3.8 ppm at 410 K.

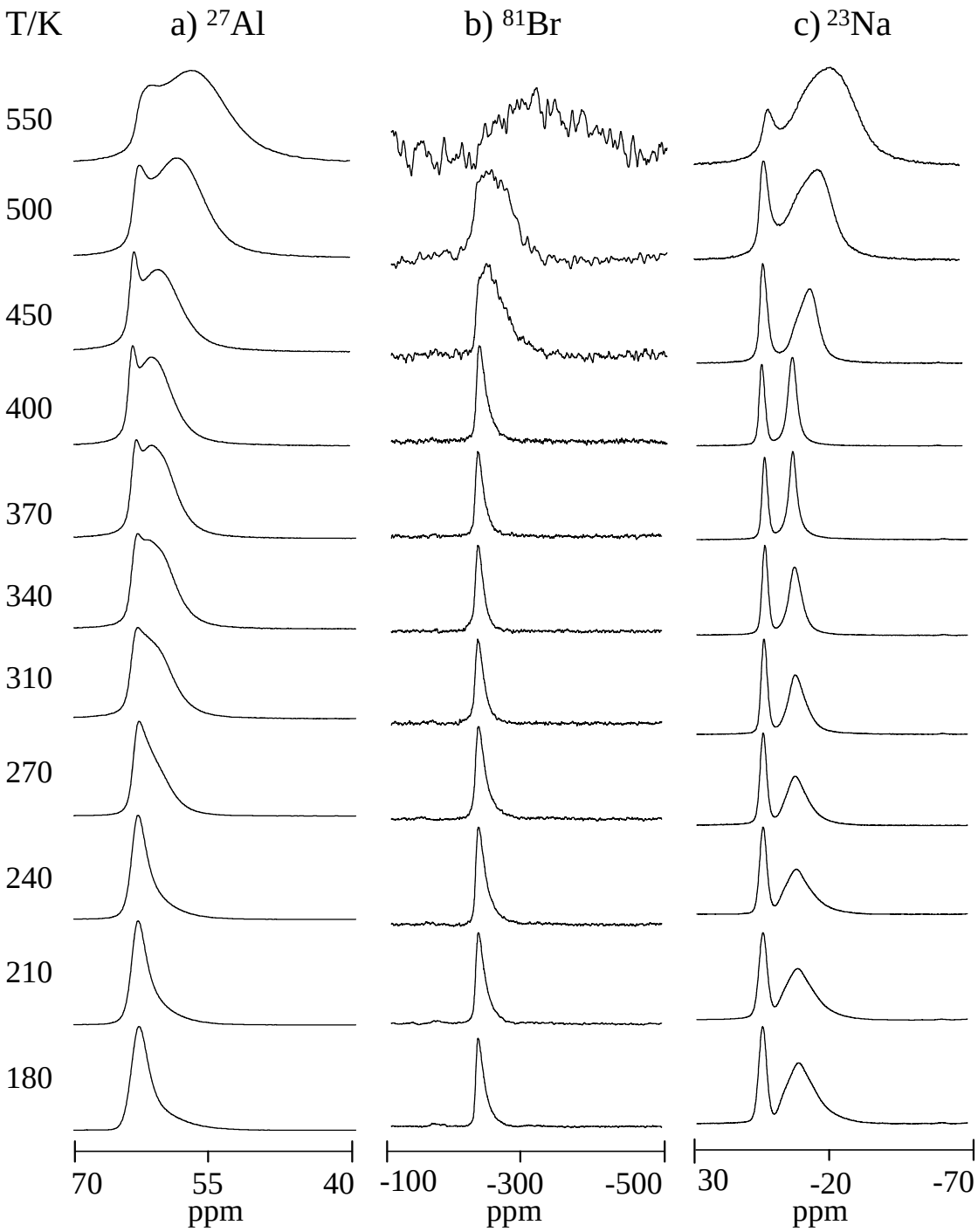

Figure 8-28: *^{27}Al, ^{23}Na and ^{81}Br spectra of 28% Br containing Br/hydro sodalite. The spectra were acquired at 104.23, 105.81 and 108.03 MHz, respectively. The spinning speed was 7000 Hz in all cases.*

The temperature dependent ^{27}Al MAS NMR spectra of a 27% Br containing Br/hydro sodalite are given in Figure 8-28 a). At low temperatures the spectra show a single resonance at 62.1 ppm with a shallow low-frequency shoulder. Between 240 K and 270 K this shoulder becomes more pronounced and at 370 K a separate peak at 60.3 ppm can be identified. At higher temperatures the center of gravity of this resonance is shifted to lower frequencies up

to 56.7 ppm at 550 K. Above 400 K, also the high frequency resonance is shifted towards lower frequencies, while its relative intensity decreases. The latter effect indicates a fusion of these two peaks and will be discussed below.

The room temperature ^{27}Al TQ MAS NMR of Br/hydro sodalite shows the existence of two sites with distinct chemical shift and quadrupolar parameters. The ^{27}Al TQ MAS NMR shown in Figure 8-29 a), acquired at 450 K, reveals the nature of the low frequency resonance. The high frequency resonance has a chemical shift of 63.0 ppm and P_Q = 1.2 MHz. The lineshape of the low frequency resonance is smeared along a ridge with an approximate slope of –10/17 indicating a distribution of the quadrupolar coupling parameter. Accordingly the shifts in F_1 and F_2 correspond to δ = 62.8 ppm and P_Q = 2.5 MHz, and δ = 63.2 ppm and P_Q = 3.3 MHz, for the center of gravity and the low frequency maximum, respectively.

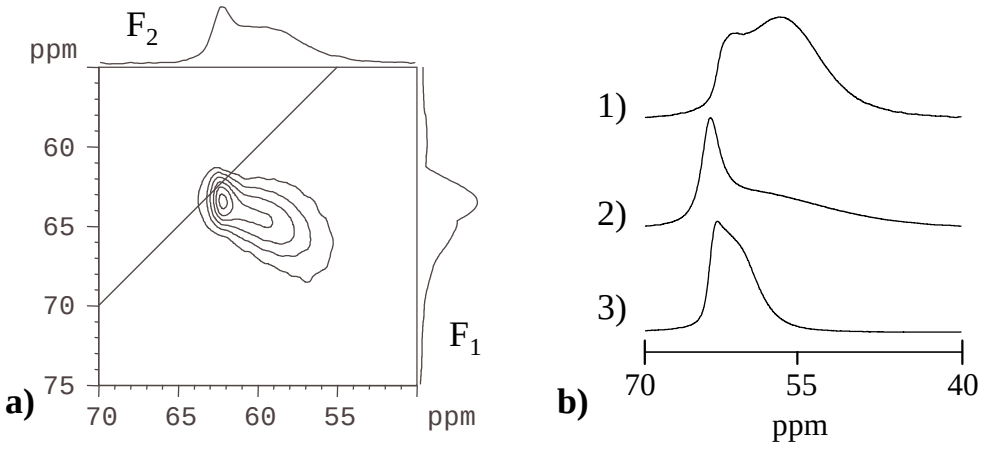

Figure 8-29: *^{27}Al MAS NMR spectra of a 28% bromine containing Br/hydro sodalite acquired at 104.23 MHz.* ***a)*** *TQ MAS NMR acquired at 450 K, the diagonal indicates $F_1 = F_2$.* ***b)*** *1D MAS NMR spectra: 1) at 550 K, 2) and 3) at 310 K. While spectrum 3) is before heating, spectrum 2) was recorded, after the sample had cooled down from 550 K under nitrogen.*

Figure 8-29 b) indicates the irreversibility of the processes that have taken place during the heating of the sample under nitrogen atmosphere. The high frequency component of the spectrum regains its previous intensity after cooling. In contrast, the shoulder due to the low frequency fraction is excessively broadened towards lower frequencies after cooling.

The ^{81}Br NMR spectra observed from the Br/hydro sodalite and shown in Figure 8-28 column b) shows only a single resonance. Between 180 K and 400 K, neither the linewidths nor the chemical shifts change dramatically. However, the linewidth has a slight minimum at 340 K with 1.4 kHz, while at 400 K and 180 K it is about 1.7 kHz. The shift of the resonance peak varies from –227.7 to – 228.5 ppm between 180 K and 400 K, respectively. Above 400 K, the linewidth increases from 4.4 kHz at 450 K to 16.7 kHz at 550 K; also the resonance shift of the center of gravity changes from –240 ppm at 450 K to –315 ppm at 550 K. The extreme

linebroadening and the unfavorable Boltzmann distribution cause a drastic reduction of the signal to noise ratio.

The ^{23}Na MAS NMR spectra displayed in Figure 8-28 c) show two resonances, which have already been identified earlier in this chapter as due to sodium in bromide cages (high frequency) and sodium in hydro cages (low frequency). Except for the highest temperatures, the high frequency resonance shows small shifts towards lower frequencies, which will be discussed later in more detail. Its linewidth has a minimum of 245 Hz at 370 K and increases towards higher and lower temperatures to 540 Hz at 550 K and 370 Hz at 180 K, respectively. The low frequency resonance shows a similar minimum of 359 Hz at 370 K and increases to significantly larger values of 1300 Hz at 180 K and 2560 Hz at 550 K. As can be seen from Figure 8-30, the heating process (under nitrogen atmosphere) irreversibly changes both resonances. The high frequency resonance remains about 420 Hz wide and the low frequency resonance also shows a much more extended low frequency shoulder.

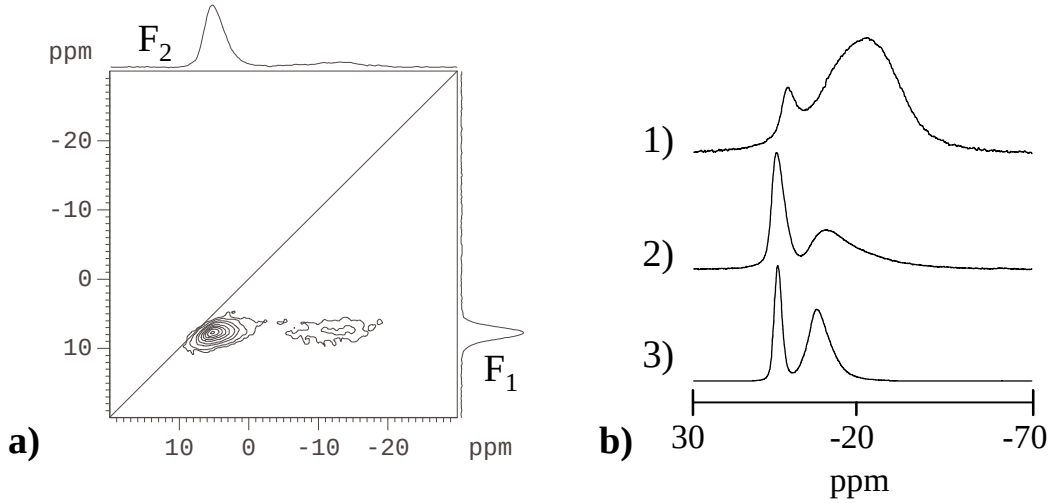

Figure 8-30: *^{23}Na MAS NMR spectra of a 28% bromine containing Br/hydro sodalite acquired at 105.81 MHz.* ***a)*** *TQ MAS NMR acquired at 450 K, the diagonal indicates $F_1 = F_2$.* ***b)*** *1D MAS NMR spectra: 1) at 550 K, 2) and 3) at 310 K. While spectrum 3) is before heating, spectrum 2) was recorded, after the sample had cooled down from 550 K under nitrogen.*

A ^{23}Na TQMAS NMR spectrum acquired at 450 K, shown in Figure 8-30 a), shows similar NMR parameters for both resonances as the room temperature one shown in Figure 8-15. The chemical shift of the high frequency resonance is δ = 6.8 ppm with P_Q = 0.8 MHz; the low frequency resonance is characterized by δ = -0.2 ppm and P_Q = 2.4 MHz. Although the lineshape of the low frequency resonance is not typical, even for a strongly broadened resonance with P_Q = 2.4 MHz, the 2D spectrum does not indicate any other components.

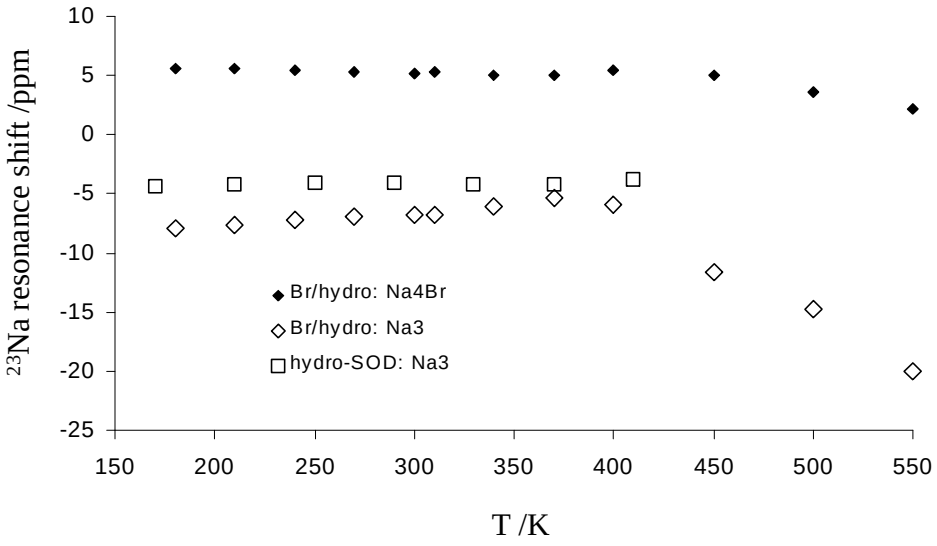

Figure 8-31: *Temperature dependent ^{23}Na NMR resonance shifts of hydro and Br/hydro sodalite recorded at 105.81 MHz.*

Figure 8-31 gives the resonance shifts of the ^{23}Na resonances of both sodalites as a function of temperature. For the pure hydro sodalite, the ^{23}Na resonance shift is temperature independent up to 400 K. The some is true for the high frequency resonance of the ^{23}Na spectra of the Br/hydro sodalite. The low frequency resonance however shifts slightly to higher frequencies between 180 K and 400 K. Above 400 K, both resonances of the Br/hydro sodalite shift to lower frequencies. This effect is more pronounced in the low frequency resonance, most likely due to the fact that the quadrupolar coupling constant of this site also increases as it is shown by the TQ MAS data given in Figure 8-30. A decrease in the quadrupolar shift between 180 K and 370 K also explains the observed increase of the resonance shift.

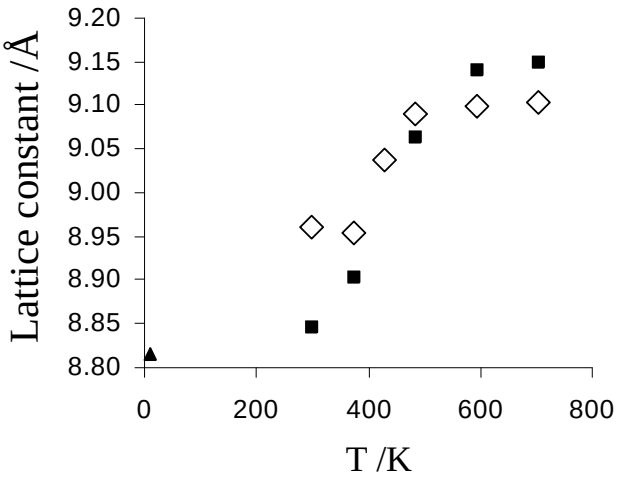

Figure 8-32: *Temperature dependent x-ray diffraction patterns of pure hydro sodalite (solid squares) and 28% Br containing Br/hydro sodalite (open diamonds). The data point at 10 K has been taken from the literature.*[90]

Both sodalites were also studied by temperature dependent x-ray diffractometry and the resulting lattice constants are plotted in Figure 8-32. The peaks of the Br/hydro sodalite are on average about twice as wide as in the case of the pure hydro sodalite, which is ascribed to the disordered nature of this material, where, as discussed earlier, small domains with slightly

different lattice parameters may be formed. For the pure hydro sodalite, the dehydration process between 100°C and 300°C can be watched in situ, revealing the large lattice expansion of about 0.34 Å or 13 % in unit cell volume, which was detected by Felsche and Luger as the difference between hydro and dry sodalite.[10] A similar but less pronounced effect (with an increase in lattice volume of about 4.5%) is observed for the Br/hydro sodalite between 100°C and at 210°C.

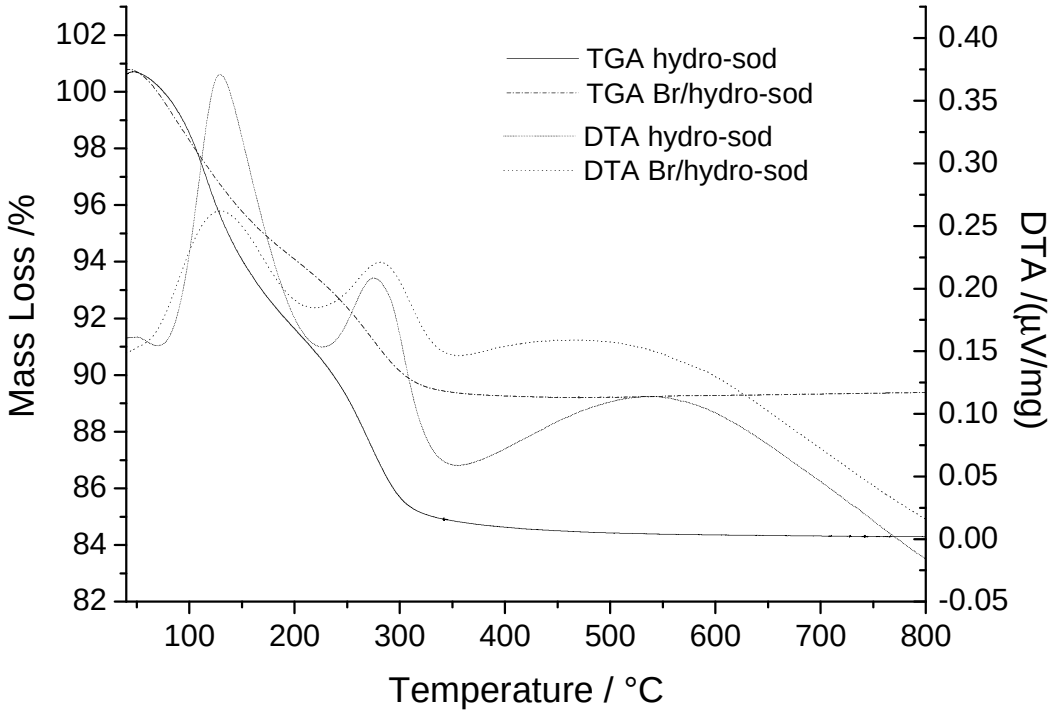

Figure 8-33: *TGA of pure hydro sodalite and 28% Br containing Br/hydro sodalite. The dashed curves give the mass loss according to the left y-axis; the dotted curves are proportional to the temperature difference between sample and reference, indicating exothermal (up) and endothermal (down) transitions.*

The TGA data indicates that the loss of water occurs at similar temperatures and over the same temperature range in both sodalites. The DTA signals of both sodalites have peaks at 115 °C and 280°C indicating endothermic transitions of the sodalite lattice corresponding to the evaporation of water molecules in two steps. In the case of the Br/hydro sodalites, these peaks are broader and slightly less in intensity. While the mass loss below 100 °C has to be ascribed to surface water, the loss of mass above 100 °C can be ascribed to removal of cage water molecules from the sodalite crystallites. The latter point marks the significant difference between the two sodalites, where the pure hydro sodalite looses 14.0 % of its mass and the Br/hydro sodalite looses 9.8 % of its mass. According to Equation 4-1b, the latter values correspond to halide contents of – 1% for the hydro sodalite and 31 % for the mixed Br/hydro sodalite, respectively. These results are in good agreement with 0 % and 28 % Br content determined by x-ray and NMR. Thus, above 370 K no significant difference concerning the

water molecules in these sodalites can be detected, in agreement with the data plotted in Figure 8-26.

Discussion

To understand the sideband pattern of the proton resonances in Br/hydro and pure hydro sodalite the dipolar interactions between the protons have to be considered, causing dipolar broadening of the static lineshape, which, in case of a two-spin interaction displays a Pake doublet with a splitting according to the dipolar coupling constant. Static NMR spectroscopic investigations have been undertaken in 1983[91] and came to the conclusion that the water molecules in pure hydro sodalite are completely rigid below 160 K. Investigations of the T_2 relaxation time lead to the conclusion that one rotational mode is active between 160 K and 250K; above 250 K isotropic rotation and above 350 K even isotropic motion was inferred. No structural phenomena were suggested, although different filling factors were investigated. Later Stein et al[29] found that the lattice constant of pure hydro sodalites is exceptionally small, compared to mixed Br/hydro sodalites at room temperature and ascribed this effect to structural hydrogen bonding.

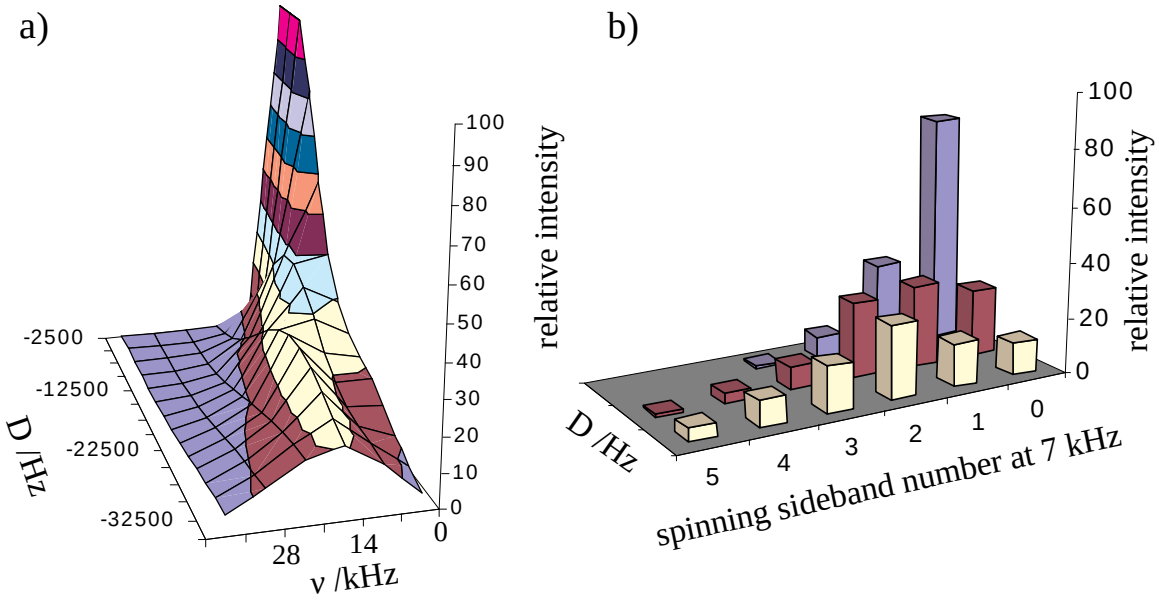

Figure 8-34: *Simulation of the proton NMR sideband pattern for protons interacting with another single spin simulated by SIMPSON.* ***a)*** *high frequency half of the sideband envelope as a function of the dipolar coupling constant D.* ***b)*** *simulated sideband intensities for the first five spinning sidebands (x-axis, 0 corresponds to the center of gravity of the spectrum) at a spinning frequency of 7000 Hz. Intensities for spectra due to dipolar coupling constants of –10, -20 and –30 kHz are plotted (from back to front).*

In this study, proton spectra were simulated based on spinning speeds of 7000 Hz and various dipolar coupling constants, between 0 and 35 kHz, the latter corresponding to two interacting protons at a distance of 1.51 Å, as it is found in gaseous water molecules. The sideband

intensities are given in the block diagram of Figure 8-34. With increasing dipolar coupling constant, the Pake doublet structure becomes increasingly evident.

It was found that the sideband patterns of both sodalite samples at low temperature are best represented by the simulation with a dipolar coupling constant of 19500 Hz. This value corresponds to a H--H distance of 1.8 Å. This value is much larger, than e.g. for regular ice (1.61 Å)[91] and also than the value of 1.54 Å determined 1983 from static NMR.[91] On the other hand, it agrees well with a value of 1.79 Å found by neutron diffraction as the D--D distance of deuterium oxide loaded hydro sodalite, which has the same room temperature lattice constant as regular (hydrogen oxide loaded) hydro sodalite.[28]

The MAS centerband seen in Figure 8-26 can now be interpreted as a superposition of a MAS centerband originating from the Pake doublet and a sharp line arising from isotropically reorienting water. Evaluation of the spectra was undertaken by fitting the ratio of the first and second sideband to the experimental data (under the condition that the total spectral width of the simulated spectrum also agrees with the experimental data). If the dipolar coupling constant is known (from the fit), the simulation also delivers the ratio of the central peak and the first sidebands due to the static water. Over the range studied, the ratio of the intensity of the central line compared to the first sideband is fairly insensitive to the dipolar coupling constant and remains at a value around 0.8. Thus the central peak intensity can be deconvoluted into the parts resulting from static and the isotropically rotating protons. Figure 8-35 shows the values of these ratios as a function of the coupling constant.

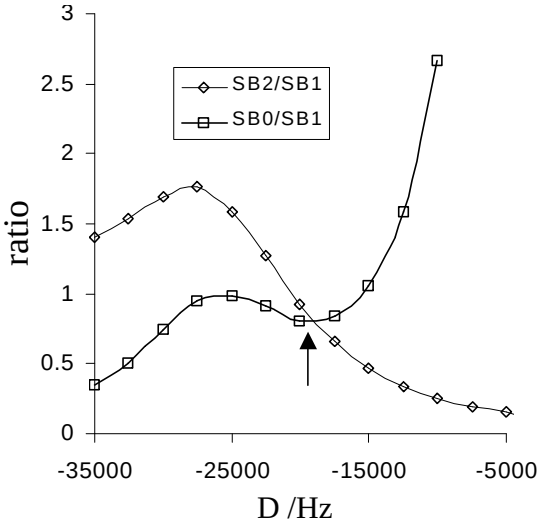

Figure 8-35: *The intensity ratios of the first sideband compared to the central transition (squares) and compared to the second side-band under MAS conditions, at a spinning speed of 7000Hz and as a function of the H--H dipolar coupling constant. The arrow marks the experimentally found D value.*

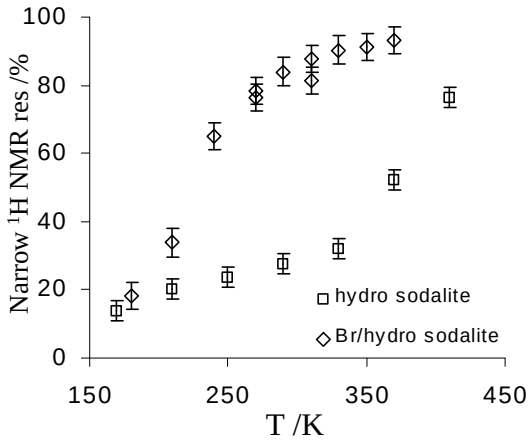

Figure 8-36: *Fractional contribution of the isotropically mobile proton in the ^{1}H MAS NMR spectra to the total signal area of Br/hydro and pure hydro sodalites.*

From Figure 8-36 it can be seen that, at a given temperature, the fractional areas of the static and the mobile hydrogen atoms differ drastically between the two sodalites. While the fraction of static water molecules approaches 0 already at 270 K for the mixed Br/hydro sodalite, in the case of pure hydro sodalite, this value is not even reached at about 410 K.

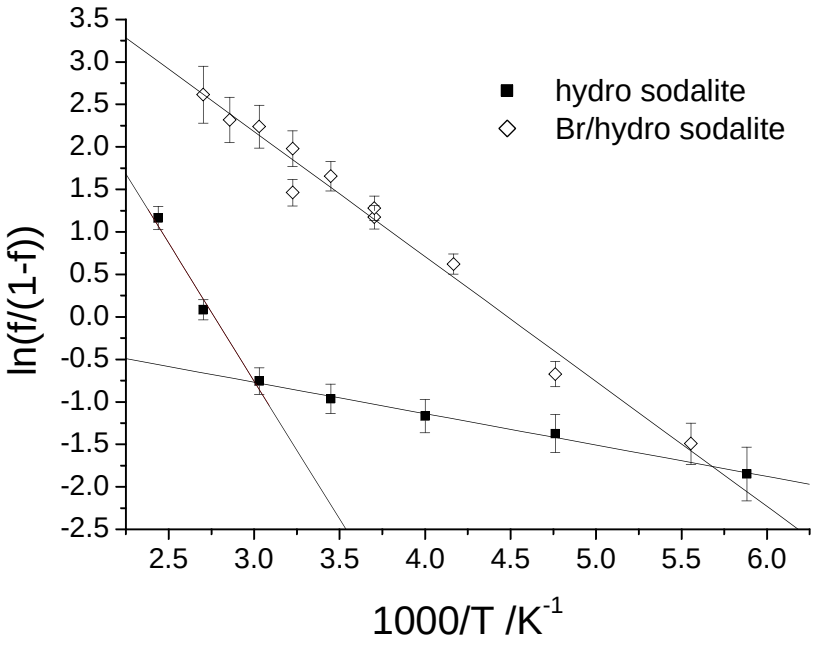

Figure 8-37:
Arrhenius plot of the ratio of the narrow and the broad lineshape areas in the ^{1}H spectra of hydro and Br/hydro sodalite. The slopes are measures of the activation energy:
12.1 ± 0.7 kJ/mol *for the Br/hydro sodalite;*
3.1 ± 0.7 kJ/mol *for the low temperature phase of hydro sodalite below 330 K and*
27 ± 5 kJ/mol *for the high temperature phase above 330 K.*

The logarithmic plot in Figure 8-37 clearly shows that the water molecules in Br/hydro sodalite and hydro sodalite experience different energy barriers in order to become mobile. From TGA measurements it is known that hydro sodalite looses two of its four cage water molecules between 100 °C and 200 °C. Thus it can be concluded, that at 370 K in both sodalites, water is mobile and can migrate between the cages. The energy necessary to reach this state is by a factor of 2.5 lower for the Br/hydro sodalite. The 27 kJ/mol necessary in pure hydro sodalite already almost compares to the 40 kJ/mol evaporation energy of regular water at 373 K. Below 330 K only a small fraction of the water in hydro sodalite exists in the mobile state with an activation energy of only 3.1 kJ/mol, comparable to the 6 kJ/mol necessary to melt ice at 273 K. It is interesting to note that at about 250 K, where the onset of the lattice expansion occurs, no anomalies in the in the proton spectra are observed. Thus, it is reasonable to conclude that below 250 K most water molecules are in a frozen state, where the excited water molecules are mobile only within one cage. Only above 330 K the thermal energy is sufficient to allow the water molecules to penetrate the 6-ring windows. In Br/hydro sodalite the activation energy (12 kJ/mol) is significantly smaller than in pure hydro sodalite and the water mobility is increased substantially. All of these findings support the idea, that

the unusually small lattice constant of pure hydro sodalite (8.844 Å at RT) arises from inter cage bonding effects arresting the H_2O molecules. Since, from the similar chemical ^{1}H NMR shifts of the protons in both sodalites (4.1 ppm and 4.3 ppm for the pure hydro and Br/hydro sodalite, respectively), a significant difference in hydrogen bonding can be excluded, an alternate possibility is the inter-cage interaction between sodium and water. This idea is supported by the fact that pure silver exchanged hydro sodalite has a lattice constant of a_0 = 8.950 Å,[92] rather similar to the low-halide concentration limit of the halide sodalites of 8.97 Å. In addition an attractive interaction between the water-oxygen and sodium of a neighboring cage has been proposed by Shannon.[93] However, the data presented here only allow to conclude that the presence of bromine substantially reduces the energy necessary for inter-cage water migration.

As shown earlier, the ^{27}Al chemical shift is a sensitive probe for the average T-O-T bond angle and thus for the cell edge length in these sodalite systems. Exploiting the fact, that the quadrupolar parameter for ^{27}Al resonances of these sodalites do not significantly vary in the temperature range observed (see Figure 8-29), approximate chemical shifts can be extracted for each resonance based on the data at room temperature and 450 K. Equation 6-2, giving a relation between T-O-T angle and the chemical shift (δ) can be converted into a relation between the lattice constant (a_0) and the chemical shift according to Equation 3-1 due to the fact that over the small observed data range the T-O-T bond angle and cell edge are proportional to the first order of accuracy.

$$a_0 = 11.513\ \text{Å} - \delta(^{27}\text{Al})\ [\text{ppm}] \cdot 0.0407\ \text{Å/ppm} \qquad \text{Equ. 8-2}$$

From the weighted average of all resonances in each spectrum the lattice constants can be computed according to Equation 8-2 and the resulting data is given in Figure 8-36. These lattice constants, determined by NMR, agree fairly well with those determined by x-ray diffraction.

While for hydro sodalite, the onset of lattice expansion already occurs at about 250 K, the lattice constant of the Br/hydro sodalites does not increase significantly below 400 K, however, above 450 K a significant increase is visible. It is interesting to note that the Br/hydro sodalite starts expanding at a temperature, where the pure hydro sodalite has reached exactly the same cell edge length of about 8.96 Å during its expansion process. At higher temperatures, the lattice constants derived from the ^{27}Al NMR of the Br/hydro sodalite are

systematically smaller than the cell edges derived from the x-ray data. A reason for this effect might be the difference in water evaporation during the x-ray and the NMR experiments. The Br/hydro sodalites had a large surface area exposed to a nitrogen atmosphere during the x-ray data acquisition, while during the acquisition of the NMR data, just a hole of 0.5mm in diameter allowed the water to leave the spinner. The latter conditions might have resulted in a less efficient water removal during the NMR data acquisition. The final high temperature lattice constant of pure hydro sodalite is larger than that of Br/hydro sodalite. This is expected from the solid solution behavior of the Br/dry systems.

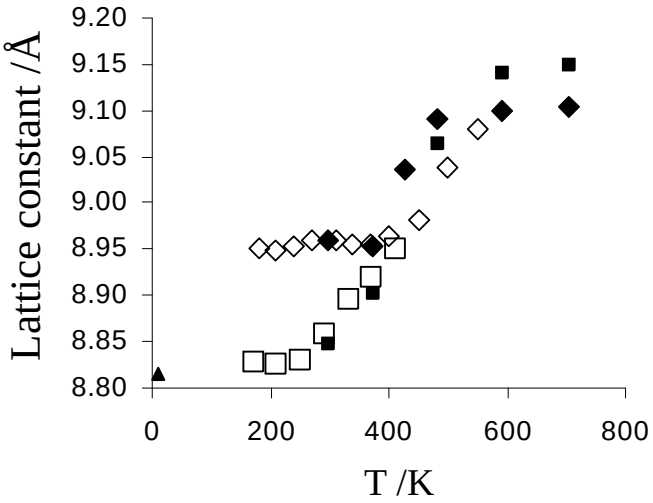

Figure 8-36: *Temperature dependent ^{27}Al resonance shifts converted into lattice constants according to Equation 6-2 (empty symbols) and lattice constants determined by x-ray diffractometry (solid symbols). The data of the pure hydro sodalites is symbolized by squares, while the data points corresponding to the Br/hydro sodalite are marked by diamonds.*

The ^{27}Al and ^{23}Na linewidth minima in both systems at about 350 K can be understood considering the motional states of the water molecules. Below 350 K an increasing number of water molecules is able to rotate isotropically with increasing temperature, removing anisotropies within the sodalite cage and averaging out distortions of the neighboring framework atoms, arising from multiple next nearest neighbor environments. If, as suggested by Ernst,[91] the water molecules are mobile between the cages, the number of water molecules per cage can vary, causing distorted cages and thus leading to broader resonance lines of the framework atoms. This becomes even more obvious at temperatures above 450 K, where it is known from TGA that water leaves the sodalite crystallites, resulting in variable cage occupancies approaching the state of dry sodalite. The TQMAS spectrum of Br/hydro sodalite acquired at 450 K (shown in Figure 8-29 a) indicates this process. While the chemical shift of all spectral components is about 63 ppm indicating an undistorted lattice, quadrupolar coupling constants continuously vary between 2 and 3.3 MHz. As discussed earlier, the variation of P_Q without a change in the chemical shift indicates different sodium occupancies at the oxygen atoms about the aluminum. While at room temperature the data indicate that

only one vacant sodium site per aluminum occurs, the high temperature TQMAS suggests that at these temperatures, the ordering of vacant sodium sites no longer exists, resulting in aluminum atoms with various associates vacant sodium sites.

The ^{81}Br NMR resonances in Br/hydro sodalites observed show a weak temperature dependence below 400 K. This is expected, due to the fact that the lattice constant does not significantly vary in the range between 180 K and 400 K. Compared to Br/basic and Br/dry sodalites, the ^{81}Br resonance of Br/hydro sodalites generally shows stronger quadrupolar coupling parameters and thus an increased linewidth. Thus the halide resonance is sensitive to asymmetries in the neighboring cages and therefore it is not surprising that its linewidth has a minimum at 370 K most likely caused by motional narrowing due to the motion of the water molecules. For temperatures higher than 400 K, the linewidth dramatically increases. As will be shown below, this can be explained by the mobility of sodium ions. Sodium ions changing from a halide containing cage into a hydro cage remove the tetrahedral symmetry of the halide site, causing strong quadrupolar broadening and fluctuating electric field gradients causing T_2 relaxation.

The ^{23}Na resonance of pure hydro sodalite does not change significantly between 170 and 370 K, although the lattice constant changes by more than 0.1 Å. As discussed earlier, its chemical shift is about 0 ppm at room temperature and agrees well with the chemical shift of sodium in hydro cages of mixed halide/hydro sodalites. Apparently the chemical shift of sodium at this site is invariant to changes of the cage diameter and always similar to the shift of the sodium standard. This is also in agreement with the behavior of the corresponding ^{23}Na chemical shift in the Br/hydro sodalite systems. For the linewidth the same trend can be observed as for aluminum and bromine. The decrease between 170 and 330 K is due to motional narrowing, probably induced by the motion of the water molecules.

In the Br/hydro sodalite system also a linewidth minimum occurs for both ^{23}Na NMR resonances at 370 K. While the linewidth of the high frequency resonance, ascribed to sodium in bromine cages is comparable to the corresponding one in mixed Br/Cl sodalites, the linewidth of the low frequency resonance, ascribed to sodium in hydro cages, is significantly greater than in pure hydro sodalites. At 370 K this effect is 75 % (202 Hz to 357 Hz) and it increases with decreasing temperature to 160 % (510 Hz to 1310 Hz)

It is likely that the water molecules freeze at disordered positions giving rise to multiple sodium environments. At elevated temperatures also an increase of the low frequency resonance linewidth occurs, along with an increase in the quadrupolar coupling and low

frequency shift. Above 450 K also a significant low frequency shift of the high frequency resonance can be observed. Along with this effect goes a change in relative intensity of the high frequency resonance, indicating ionic exchange between both sites. When compared to mixed halide sodalites (Chapter 7), it is interesting to note that in Br/hydro sodalites such an isotropic ion mobility already starts 150 K lower. This could be understood owing to two reasons. First, hydro cages contain a vacant sodium site and second the Na-O distance in hydro cages is about 0.2 Å larger than in halide filled cages. Thus, the ions are more loosely bound and have more attractive sites to jump to than in the case of mixed halide sodalites. Unfortunately it is not possible to observe sodium mobility within the hydro cages directly. However, the large distribution of P_Q values found in the ^{27}Al TQ MAS NMR (Figure 29a) indicates that this type of hopping is already allowed before inter cage jumps occur.

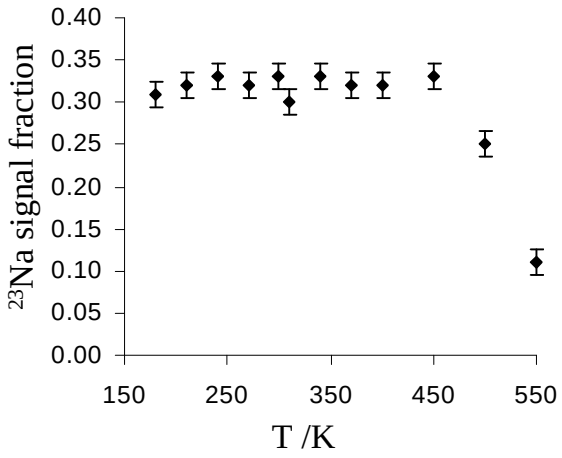

Figure 8-38: *Temperature dependence of the fractional integral area of the low frequency resonance in the ^{23}Na NMR spectra of 28% bromine containing Br/hydro sodalites. While the fractional area is 0.33, the resulting fraction of bromine filled cages is 28% due to the fact that hydro cages contain 25 % less sodium (one ion).*

The irreversibility of the ^{23}Na spectrum after heating to 550 K and cooling under nitrogen is the result of the loss of motional narrowing due to water removal. 550 K is not sufficient to remove all four water molecules. Since for pure hydro sodalite TGA shows that the crystallites loose two water molecules per cage below 470 K and another two between 470 K and 670 K, it is reasonable to assume that on average one to two water molecules per cage remained inside the sample. Thus, it is not surprising that sodium in such hydro cages experiences a much more asymmetric environment, resulting in stronger quadrupolar broadening, which leads to the observed lineshape. After exposure to air for about 2h, the spectrum is identical with the room temperature spectrum observed before heating, indicating full rehydration.

8.3.2 Dry and Br/dry Sodalites.

The same sample studied in the preceding paragraph have been dried for 8 hours under vacuum to yield dry and Br/dry sodalites.

While the VT NMR spectra of Br/dry sodalite are shown in Figure 8-39, the ^{23}Na and ^{27}Al spectra of pure dry sodalite are not shown. Up to 550 K, these spectra are similar to spectra of dry sodalites of pure dry sodalites, shown in Figure 8-1-IIIe, 8-2-IIIe and 8-3-IIIe. The NMR spectra of the Br/dry sodalites, in contrast, show several interesting characteristics:

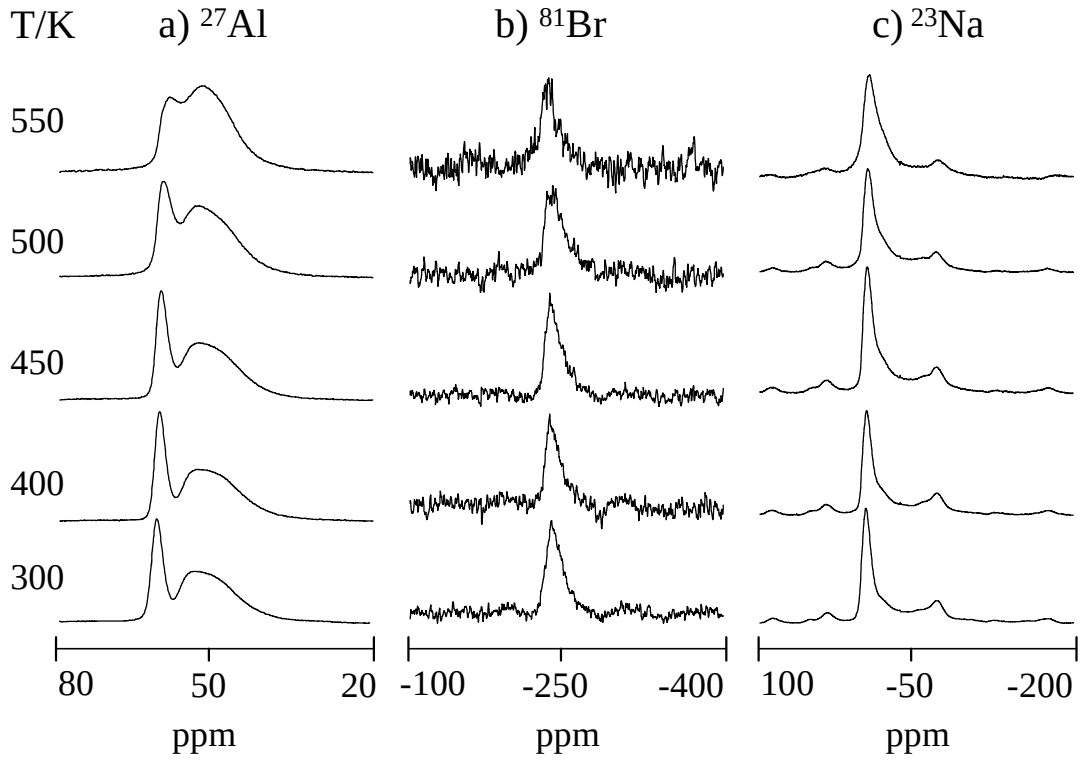

Figure 8-39: *^{27}Al, ^{23}Na and ^{81}Br spectra of 28% Br containing Br/dry sodalite. The spectra were acquired at 130.29, 132.26 and 135.03 MHz, respectively. The spinning speed was 7000 Hz in all cases.*

The ^{27}Al NMR spectrum shows two resonances, which already have been assigned above. The high frequency resonance is shifted to lower frequencies with increasing temperature and shows a linewidth minimum at 400 K. The low frequency resonance with a P_Q value of 4.4 at room temperature has a chemical shift of 58.0 ± 0.3 ppm up to 500 K, and is shifted to 57.1 ppm at 550 K. Its lineshape becomes significantly more broadened at 500 K, but can still be fitted with a P_Q value of 4.2 MHz. All spectra can be satisfyingly fitted with two lineshape components, however a occurrence of a third peak with an intermediate shift can not be

excluded from the experimental data. The fractional share of the high frequency peak is about 26 % below 500 K and 23 % an 18 % at 500 K and 550 K, respectively.

The ^{81}Br NMR resonances, observed do not significantly shift with temperature. The mean value is –237.5 ± 0.5 ppm. A deviation is only found at 550 K, where the resonance is shifted to –232 ± 3 ppm and the linewidths is reduces to 2200 Hz (compared to 2600 Hz at all other temperatures).

The two resonances, visible in the ^{23}Na NMR spectra of this Br/dry sodalite suffer from overlap with spinning sidebands due to the spinning speed of only 7000 Hz and the large expansion of the resonance with about 5.9 MHz. The fractional shares are about 50% for all spectra except the one at 550 K, where the fraction strong quadrupolar coupled resonance is only 34 %. (The fact that the fraction do not resemble the composition of the sample is due to the large P_Q value of 5.9 MHz and the reduced excitation probability.) Similar to the ^{27}Al spectra, the lineshape of the ^{23}Na spectra above 450 K could also be simulated by three components with the additional having an intermediate shift of about –15 ppm accounting for the linewidth increase of the high frequency component. In this case, however, the data becomes ambiguous and thus does not allow for quantitative analysis.

The Br/dry sodalite is an ideal material to test for mobility of sodium in dry sodalite cages. From the temperature dependent NMR spectra of pure dry sodalite, it can only be concluded that no jumps between vacant and occupied sodium sites within a single cage occur below 550 K. Assuming a two site jump process, the quadrupolar coupling constant observed for sodium ions, which change sites within one sodalite cage is expected to be 50% of the value of immobile sodium ions due the change of 109° in the principal axis orientation of the EFG resulting from such a jump.[94] Jumps through a 6-ring window change the EFG tensor seen by the sodium ion by 180°. The resulting P_Q parameter then has the same absolute value but different sign, which unfortunately cannot be detected by NMR because it is only sensitive to the absolute value of P_Q. In the case Br/dry sodalites, however, the situation is much more advantageous from the NMR point of view. Due to the two different sodium resonances, exchange of sodium ions between the two types of cages becomes directly detectable by ^{23}Na NMR and indirectly detectable by ^{27}Al NMR. As shown above, the two ^{27}Al resonances occurring in these spectra have different chemical shifts and quadrupolar coupling constants due to the fact that the AlO_4 tetrahedra linked to a vacant sodium site are slightly distorted, compared to the ones that have all their four sodium sites occupied.

The ^{27}Al NMR spectra of Figure 8-39 show the two peaks starting to fuse with one another above 450 K. This effect indicates an averaging of aluminum sites on the NMR timescale.

Thus it is plausible to conclude that the sodium ions become mobile at about 450K and the two aluminum sites become similar and experience the influence of a fractional vacant sodium site averaged over the time of the NMR experiment. Within the same temperature range the linewidth of the ^{23}Na high frequency resonance develops a low frequency shoulder. This observation might signify to a new resonance, resulting from an exchange between the two sodium sites in this mixed Br/dry sodalite.

Thus, the temperature dependences of the aluminum spectra of Br/dry sodalite indicate that sodium becomes mobile at elevated temperatures. In addition the ^{23}Na NMR spectra suggest that at the temperatures observed, this mobility is mainly due to two site jumps through six-ring windows, rather than due to "tetrahedral" jumps between the sites of a single sodalite cage. Of course such a process or similar ones also have to take place, since the site on the opposite to an occupied sodium site (with respect to the six-ring window) cannot be permanently occupied by sodium. Therefore a jump (with an orientation change of 70.5° of the EFG principle axis) to a neighboring vacant sodium site is necessary, (also resulting in a reduction of the P_Q value of 50% with respect to the value of immobile sodium[94]).

9 Mixed Halide/Electro Sodalites

As known from the literature and already discussed in Chapter 4-2 dry sodalites take up sodium vapor to form Na_4^{3+} centers. The additional electron is delocalized over the cage and screens the Coulomb repulsion between the sodium ions to allow lattice contraction from 9.1Å in dry sodalite to 8.86Å in electro sodalite. The lattice constant for the pure F-center containing sodalite has not yet been unambiguously determined, and values of 8.881 Å,[95] 8.8634 Å,[96] and 8.860 Å[97] appear in the literature. The electro sodalite is called "black sodalite" due to its color or "sodium electro sodalite" (SES).[98] The alkali centers in such electro sodalites have an unpaired electron in a σ like molecular orbital generated by the four alkali ions. The electron density of such a center extends beyond the boundaries of the sodalite cage. EPR investigations of sodalites with isolated F-centers show a 13-peak hyperfine structure due to the four sodium nuclear spins of 3/2, characterized by hyperfine coupling constants of 31.0 , 28.4 and 24.7 G for Cl, Br and I sodalites, respectively.[99,100] While coupling with the framework nuclear spins has not been reported so far, a super-hyperfine coupling of about 1 G was observed and attributed to sodium ions neighboring F-center containing cages.[101] As shown by Engelhardt, NMR of the framework nuclei ^{29}Si and ^{27}Al allows investigation of much smaller coupling constants due to paramagnetic hyperfine shifts of the NMR resonances, which arise from paramagnetic electron density at the sites of the observed nuclei, due to the delocalization of the Na_4^{3+} σ-electron. While a ^{23}Na MAS NMR spectrum on partially doped SES has been published,[59] only two sets of overlapping peaks were found and had to be assigned in a highly speculative way. In addition, NMR on mixed halide/electro sodalites offer a unique opportunity to measure the electron density at the center of the neighboring cages, thus providing estimates of the magnetic coupling constants between neighboring and next nearest neighboring cages. Representative samples of all three mixed halide/electro sodalite series have been prepared and studied by NMR.

9.1 Experimental Observations

9.1.1 ^{27}Al and ^{29}Si MAS NMR

Figure 9-1 presents the ^{27}Al spectra of three series of mixed halide/electro sodalites, where all of the salt-free cages have been doped with sodium. Each spectrum shows a variety of peaks; the actual peak positions and relative intensities can be found in Table 9-I.

Figure 9-1 (previous page): *^{27}Al MAS NMR spectra of mixed halide/electro sodalites at 104.23 MHz and spinning speeds of 15 kHz (blue curves). To allow an easy identification of the multiple resonances contributing to the spectra, the fitted lineshapes (red curves) with all their components (colored lines) are also included.* ***I:*** *a) 16% , b) 40% and c) 86% Cl containing Cl/electro sodalites prepared from the Cl/dry sodalites I(b,c,d) in Figure 8-1.* ***II:*** *a) 28% , b) 54% and c) 73% Br containing Br/electro sodalites prepared from the dry sodalites similar to II(b,c,d) in Figure 8-2.* ***III:*** *a) 9% and c)84% I containing I/electro sodalites prepared from the I/dry sodalites I(b,d) in Figure 8-3.*

While the quadrupolar broadened resonance around 50 ppm, which was found in halide/dry sodalites has disappeared, the spectra of these electro sodalites show about seven new resonances on the high frequency side. The intensity distribution of these resonances shifts with decreasing halide content towards the high frequency resonances as expected. A closer look allows distinction between four sharp peaks at about 64, 73, 78 and 84 ppm and four broader peaks at about 98, 116, 129 and 138 ppm. The line widths of the peaks within these sets decrease with increasing paramagnetic shift.

Exposure to air causes a decrease of intensity of the high frequency resonances, while the intensities of the peaks with smaller resonance shifts increase. When the data is fitted, usually a small but broad resonance with a shift between 60 and 50 ppm has to be included to optimize the fitting curve to the spectra.

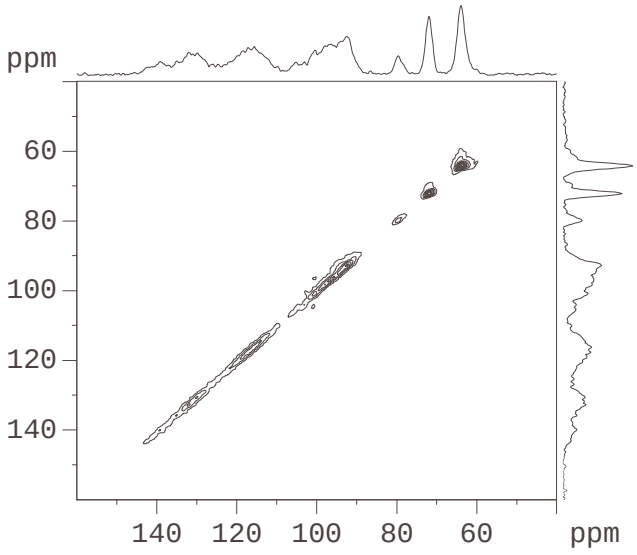

Figure 9-2: *^{27}Al TQ MAS NMR spectra of sample IIc (73%Br containing Br/electro sodalite). The spectrum was recorded at 104.23 MHz at a spinning frequency of 15 kHz; 512 FIDs were accumulated for the F_2 spectra with relaxation delays of 1s. 192 spectra were acquired for the F_1 dimension.*

All observed shifts show only minor and equal quadrupolar shift contributions reflecting coupling constants around 0.8 MHz. Values of this magnitude are also observed for other sodalites with tetrahedral extra framework symmetry, such as mixed halide or halide/basic sodalites. A representative ^{27}Al TQ MAS NMR spectrum is given in Figure 9-2. All the peaks are slightly shifted from the 1:1 diagonal indicating small and similar quadrupolar shifts of about 0.3 ppm throughout the whole spectrum. Thus the paramagnetic electron density does not alter the electric field gradients at the nuclear sites.

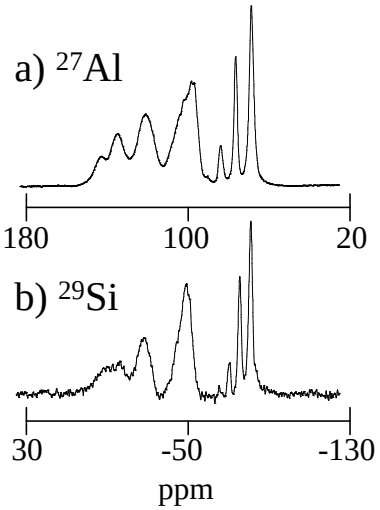

Figure 9-3: *^{27}Al and ^{29}Si MAS NMR spectra of a 73% Br containing Br/electro sodalite recorded at 104.23 and 79.46 MHz, respectively, at a spinning speed of 13 kHz. The spectral range shown is 160 ppm in both cases.*

peak	resonance shift		hyperfine shift	
	^{27}Al	^{29}Si	^{27}Al	^{29}Si
0^0	63.9	-86.0	0.0	0.0
0^1	71.8	-80.5	7.9	5.5
0^2	79.3	-75.4	15.4	10.6
0^3	86.4	-70.3	22.5	15.7
1	96.8	-54.1	32.9	31.9
2	116.9	-33.4	53.0	52.6
3	131.0	-22.2	67.1	63.8
4	140.1	-14.4	76.2	71.6

Table 9-II: *comparison of paramagnetic shift contributions in the ^{27}Al and ^{29}Si MAS NMR spectra shown in figure 5-7-3. The resonance shifts subtracted are 63.9 ppm and –86.0 ppm for ^{27}Al and ^{29}Si, respectively. The paramagnetic contributions of the ^{29}Si shifts are always about 10% smaller than for the ^{27}Al shifts. The peak assignment is explained in the text.*

Figure 9-3 compares the ^{27}Al and ^{29}Si spectra of the same sample as Figure 9-1-IIc, and Table 9-I gives the paramagnetic shifts, relative to the resonance with the lowest chemical shift.

9.1.2 MAS NMR of the Central Anions

The ^{35}Cl, ^{81}Br and ^{127}I spectra of the halide resonances of the mixed halide/electro sodalites are given in Figure 9-4. As in the case of ^{27}Al NMR two sets of resonances can be observed and the intensities are shifted to the higher frequency resonances with decreasing halide content. Up to 5 sharp peaks with rather small paramagnetic shifts can be resolved in some spectra, while up to 8 broad lineshape contributions can be found in the region of large paramagnetic shifts. The observation of spectra in samples with low halide contents is hampered by poor signal to noise ratios because of the low spin probe concentration. Up to 128k scans had to be acquired in the cases of the lowest halide contents.

Figure 9-4 (next page): I *^{35}Cl MAS NMR spectra of mixed Cl/electro sodalites recorded at 39.19 MHz. a) 16% , b) 40% and c) 86% Cl containing Cl/electro sodalites prepared from the Cl/dry sodalites I(b,c,d) in Figure 8-1 column I.* ***II:*** *^{81}Br MAS NMR spectra of mixed Br/electro sodalites recorded at 108.03 MHz. a) 28%, b) 54% and c) 73% Br containing Br/electro sodalites prepared from the Br/dry samples similar to sodalites II(b,c,d) in Figure 8-1 column II.* ***III:*** *^{127}I MAS NMR spectra of mixed I/electro sodalites recorded at 80.03 MHz. a) 9% and c) 86% I containing I/electro sodalites prepared from the I/dry sodalites I(b,d) in Figure 8-1 column III. To allow an easy identification of the multiple resonances contributing to the spectra, the fitted lineshapes (red curves) with all their components (colored lines) are also included in all spectra.*

The ^{35}Cl NMR spectra have resonances between –122 and 0 ppm. A broad signal at ~ -120 ppm shows up in all cases. The frequency separation between the peaks decreases only slightly with increasing resonance shift, compared to the corresponding effect observed for the ^{27}Al spectra. The resonances in the ^{81}Br NMR spectra are spread between –220 and + 106 ppm, thus covering a range 2.7 times as wide as observed for the Cl/electro sodalites. In the case of I/electro sodalites, due to reasons explained before no phase pure samples with medium halide concentrations are available. Also, for the high and low halide containing samples clustering can be expected due to the large separation factor. Thus in the ^{127}I spectra only a few peaks can be observed compared to the halide spectra of the other halide/electro sodalites. Besides the usual sodalite ^{127}I resonance at –260 ppm, spectrum IIIc shows a sharp peak at –200 ppm and a broader peak at –100 ppm. The remaining resonances are due to spinning sidebands of the dominant peak at –260 ppm. The NMR spectrum of the 9 % iodine containing sodalite shows additionally a sharp resonance at 500 ppm. The range in between these two extremes shows an elevated baseline which might be interpreted as the overlapping and thus not resolved signals of a multiplet similar to the ones observed for ^{35}Cl and ^{81}Br.

9.1.3 ^{23}Na MAS NMR

The ^{23}Na NMR spectra observed for all three series are given in Figure 9-5, and the data of the fitted resonance lines are given in Table 9-I. All the spectra show a high frequency resonance, which moves towards higher frequencies for mixed halide/electro sodalites, with higher halide atomic number. The observed chemical shifts are around 90, 120 and 150 ppm at room temperature for Cl/electro, Br/electro and I/electro sodalites, respectively. Also several spectra show a small broad resonance at 50 to 60 ppm. Furthermore a resonance multiplet consisting of up to 16 resonances is found between 45 and 0 ppm. While these multiplets are best resolved for the Cl/electro series, where 11 distinct components can be distinguished, the resolution decreases for the Br/electro sodalites, and for I/electro sodalites only a broad hump with no distinguishable components is observed. The low frequency side of the multiplet shows a shoulder in many spectra, which extends to about – 30 ppm. Assignment of these peaks to sodium sites in the lattice is not straightforward and will be presented below in the Discussion section.

Figure 9-5 (next page): *^{23}Na MAS NMR spectra of mixed halide/electro sodalites at 105.81 MHz and at spinning speeds of 15 kHz (blue curves). To allow an easy identification of the multiple resonances contributing to the spectra, the fitted lineshapes (red curves) with all their components (colored lines) are also included in all spectra.* ***I:*** *a) 16% , b) 40% and c) 86% Cl containing Cl/electro sodalites prepared from the Cl/dry sodalites I(b,c,d) in Figure 8-12.* ***II:*** *a) 28% , b) 54% and c) 73% Br containing Br/electro sodalites prepared from the Br/dry sodalites similar to II(b,c,d) in Figure 8-13.* ***III:*** *a) 9% and c) 86% I containing I/electro sodalites prepared from the I/dry sodalites I(b,d) in Figure 8-14.*

The spectral range shown contains all the observable ^{23}Na resonances. A resonance at 4120 ppm can be assigned to a Knight shifted ^{63}Cu signal, resulting from copper in the coil of the probe. The decreasing signal to noise ratio with decreasing halide content indicates that not all of the ^{23}Na nuclei in the sample contribute to the observed signals. The ^{23}Na nuclei, which are part of the Na_4^{3+} centers are expected to show paramagnetic shifts of about 5000 to 10000 ppm, as can be derived from their hyperfine coupling constant values observed in EPR.[102] A tenacious search between 0 and 20000 ppm, with accumulations of 32k scans and spectral widths of 4000 ppm was unsuccessful. It is suspected that the Na_4^{3+} spins elude detection since the nuclear spin-lattice relaxation through fluctuating magnetic fields, originating from the paramagnetic electron is likely to be extremely fast. Figure 9-6 shows a representative ^{23}Na TQ MAS NMR spectrum, indicating similar and weak quadrupolar coupling (ca. 0.6 MHz) for all of the resonances of the spectrum.

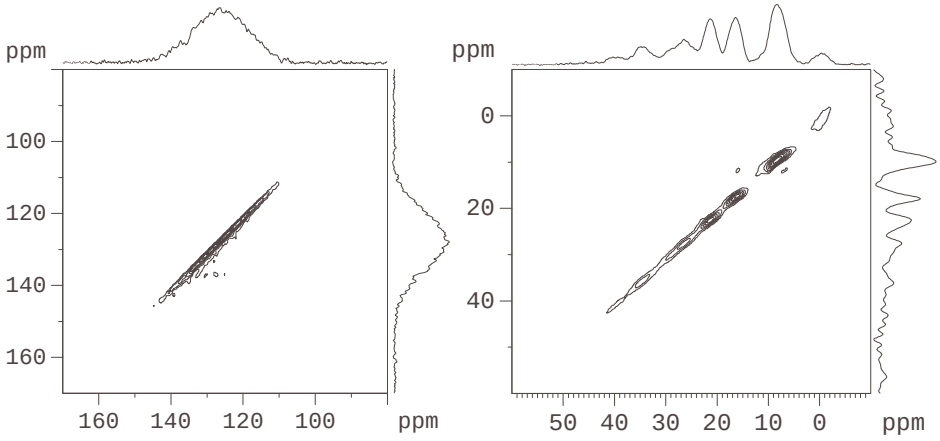

Figure 9-6: *^{23}Na TQ MAS NMR spectrum of the sample 9-4 IIc. While the left spectrum shows the region around 120 ppm (A-resonance) with a single broad signal, the right spectrum shows the region dominated by the multiplet peaks (B-resonances). The spectrum was recorded at 105.81 MHz at a spinning frequency of 15 kHz; 512 FIDs were accumulated for the F_2 spectra with relaxation delays of 1s. 128 spectra were acquired for the F_1 dimension. All the peaks are slightly shifted from the 1:1 diagonal indicating small and similar quadrupolar coupling of ^{23}Na with $P_Q \sim 0.6$ MHz.*

9.2 Discussion

9.2.1 The Framework Atoms

Discussion of Resonance Shifts

The T atoms in the sodalite structure are located at the joints of four sodalite cages and thus can have up to four Na_4^{3+} centers as nearest neighbors (nn) at a distance of about 5.0 Å, slightly depending on the cell edge length. In addition, via each neighboring T atom, the T atom of interest is linked to another cage with a next-nearest neighboring (nnn) F-center at a distance of about 8.1 Å. Thus the T atom is surrounded by four nearest and four next nearest

neighbors. Eight additional cages are at distances of 10.3 Å but appear to be of negligible significance to the observed spectrum. The shifts observed in the ^{27}Al MAS NMR spectra shown in Figure 9-1 have been explained by paramagnetic electron density at the site of nuclei[19] (see Equation 2-50) caused by the delocalized electrons of the Na_4^{3+} centers (for further proof see Section 6-3). Consequently, they are ascribed to environments with different numbers of neighboring cages occupied by such Na_4^{3+} centers, with diffuse electron density distribution. The peaks were assigned according to the number of Na_4^{3+} centers occupying nearest neighboring or next nearest neighboring cages and the assignment is visualized in Figure 9-7.[19]

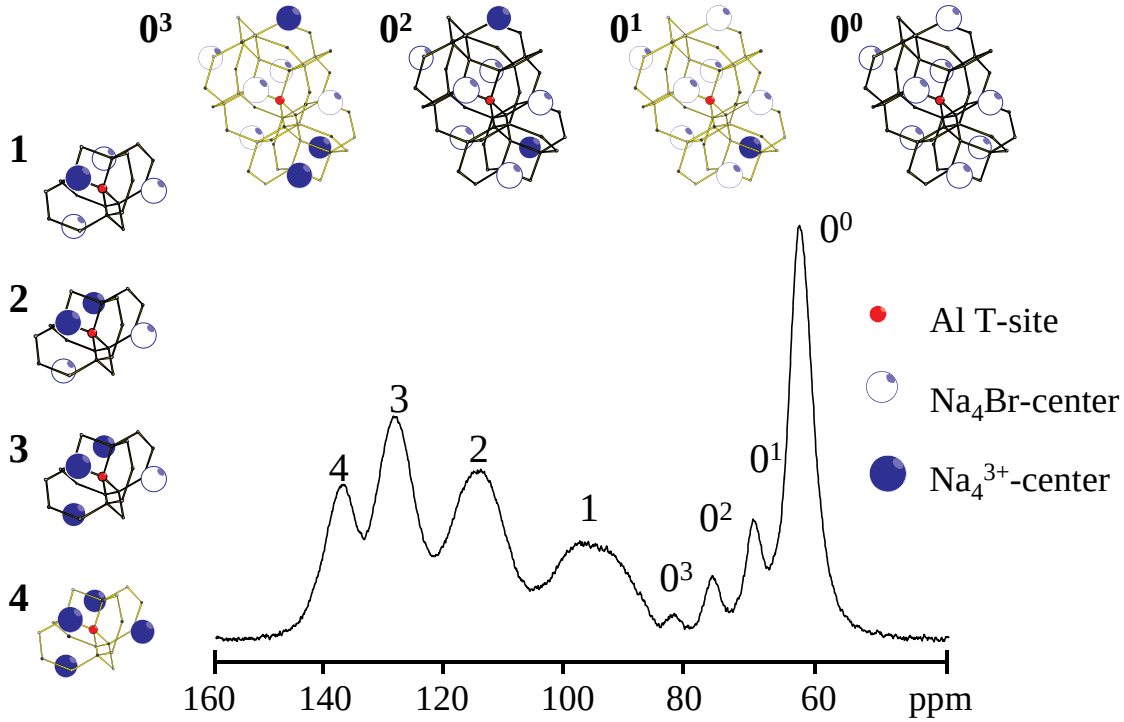

Figure 9-7: *Peak assignment for T atoms in electro sodalites. The ^{27}Al MAS NMR spectrum of Br/electro sodalite is given as an example. The peak at 64 ppm as also found in other sodalites with tetrahedral symmetry is due to T atoms with no Na_4^{3+} centers in their direct neighborhood and has the label 0^0. The 0^1, 0^2, 0^3, and 0^4 peaks are due to aluminum sites next to one to four occupied nnn cages, while none of the directly neighboring cages is occupied by a Na_4^{3+} center. The peaks assigned the numbers 1 to 4 are caused by ^{27}Al nuclei directly connected to one to four Na_4^{3+} center bearing cages. The spectrum shown is taken from a partially decomposed Br/electro sodalite. Due to decomposed F-centers, the intensities of the 0 peaks are over-represented compared to the expected values from a binomial distribution.*

Thus the peak number gives the number of nn Na_4^{3+} centers and the superscript is equal to the number of nnn Na_4^{3+} centers. The peaks 1 to 4 are therefore no single resonances, but overlaps of resonances from nuclei with n nearest neighbor Na_4^{3+} centers and nn = 0 to 4 next nearest neighbor Na_4^{3+} centers. This sub-splitting can actually be observed for the ^{27}Al spectra Ic and IIc in Figure 9-1, where in the number 1 resonance a peak can be resolved at the low

frequency side which has to correspond to one nn and zero nnn Na_4^{3+} centers. That the linewidths of the resonances as well as the frequency differences between neighboring resonances decrease with increasing paramagnetic shift can be explained by the fact that the electrons, which are the origins of the paramagnetic shifts, experience repulsive forces from other electrons. This electron-electron repulsion can be described by a repulsion parameter U_n according to Equation 3-18, where the number of electrons interacting with a given F-center is equal to n-1.

It is thus reasonable to assume, that the hyperfine shift (δ_n/n) contribution due to each neighboring F-center is given by:

$$\frac{\delta_n}{n} = \frac{\delta_1}{U_n} = \frac{\delta_1}{1+(n-1)\cdot a} \qquad \text{Equ. 9-1}$$

where δ_1 is the hyperfine shift caused by only one neighboring F-center and *a* is a fitting parameter. The observed shift due to n neighboring F-centers of the number n resonance is then simply given by $\delta_n = n\delta_1/U_n$. A plot of $n\delta_1/\delta_n$ as a function of n should thus give a linear relation as demonstrated in Figure 9-8:

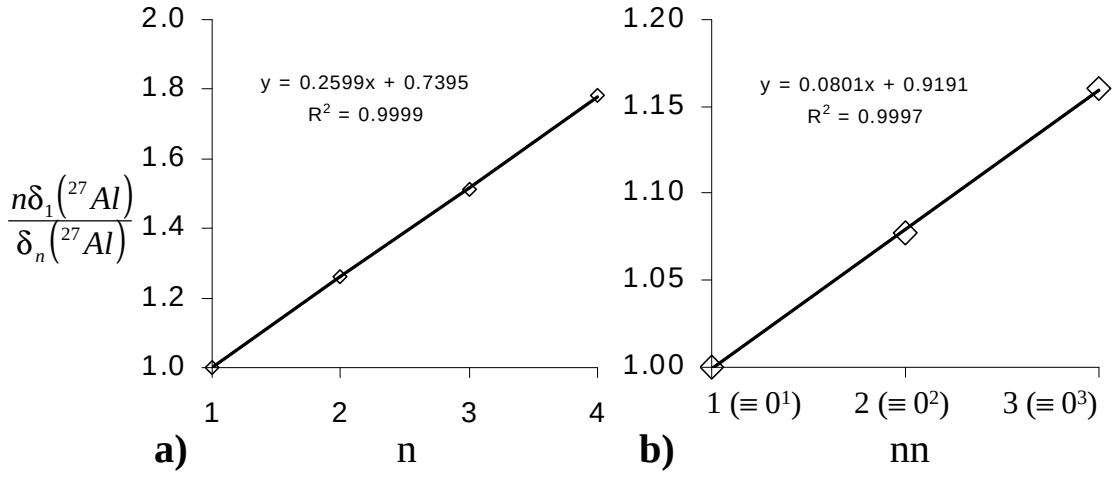

Figure 9-8: *Fits of the electron-electron repulsion parameter: $n\delta_1/\delta_n$ for the experimental ^{27}Al resonance shifts subtracted by the shift of the number 0 peak is plotted versus the number of interacting electrons.* ***a)*** *gives the relation for nearest neighbors: δ_1 = 33.3 ppm; U_n = 1 + (n-1)*0.260 and* ***b)*** *for next nearest neighbors: δ_1 = 8.0 ppm; U_{nn} = 1 + (nn-1)*0.081. In order to increase the precision, δ_1 and δ_n are the average shifts over all observed spectra in Figure 9-1.*

As shown in Figure 9-8, the agreement between the repulsion model and the experimental data is excellent, indicating that the observed shift is indeed due to paramagnetic electron density, experiencing a repulsive potential. The data set (eight ^{27}Al spectra) is too small, to confidently differentiate between the repulsive potentials of the three mixed halide/electro sodalite series, since the results are all very similar. A reason could be that with increasing

lattice constant (from Cl to Br to I), two opposing effects are expected. On the one hand, when the lattice constant increases, the distance between F-centers increases and thus the overlap integrals should decrease resulting in less repulsion. On the other hand, an increase in lattice constant is also expected to increase the Na-Na distance of sodium ions forming the F-centers. This would lead to an increase in delocalization or smearing of the F-center, again tending to increase the overlap with its neighbors.

As mentioned previously, the resonances of the peaks 1 to 4 consist of 5 resonances each, due to the possible nnn environments. Therefore it should be possible to extract the exact contributions of nn and nnn to the observed hyperfine shifts. Thus Equation 9-1 can be modified to account for all nn and nnn contributions:

$$\delta_{n,nn} = \frac{n\delta_{1n} + nn\delta_{1nn}}{1 + (n-1)\cdot a_n + (nn-1)\cdot a_{nn}} \qquad \text{Equ. 9-2}$$

where $\delta_{n,nn}$ is the shift caused by a specific environment with n nearest and nn next nearest neighboring F-centers and a_n and a_{nn} are the corresponding overlap integral parameters. δ_{1n} and δ_{1nn} are the hyperfine shifts due to one nn F-center and no nnn F-center, and no nn F-center and one nnn F-center, respectively. While $a_{nn} = 0.081$ and $\delta_{1nn} = 8$ ppm are known from Figure 9-8b, the corresponding values for the nearest neighbors cannot be extracted from Figure 9-8a, since first and second nearest neighbor effects are intermixed. However, for the samples with large halide concentration the hyperfine shift of the 1^0 peak can be determined to be $\delta_{1,0} = 28$ ppm. For the samples containing less than 10 % halide ions, the number 4 peak can be expected to mainly consist of contributions due to environments of 4 next and 4 next nearest neighbors, thus allowing to estimate $\delta_{4,4}$ to be about 75 ppm. Inserting these values into Equation 9-2 results in an overlap integral parameter of $a_n = 0.227$. Thus, the hyperfine shift for ^{27}Al for any specific nn and nnn environment is given by:

$$\delta_{n,nn} = \frac{n\cdot 28 + nn\cdot 8}{1 + (n-1)\cdot 0.227 + (nn-1)\cdot 0.081}\ ppm \qquad \text{Equ. 9-3}$$

As a result we find that the electron density at the aluminum nucleus caused by nearest neighboring interaction is about 3.5 times larger than the value due to next nearest neighbor interaction.

So far, the third neighbor sphere has not been taken into account. A test for a possible influence of the 8 F-centers at a distance of 10.3 Å on the resonance shift of the T-atom of interest is a correlation between lattice constants and resonance shifts. Since only very limited x-ray data is available, the resonance shift data for the number 0 resonances as given in Table

9-I were corrected for the quadrupolar shift (based on the P_Q values from the corresponding halide/basic sodalites) and converted via Equation 8-2 into the cell edge a_0. The resulting lattice constants were plotted versus the halide fractions as shown in Figure 9-9. The agreement between expected solid solution behavior of the lattice constant and the experimental data is quite good, supporting the hypothesis that the hyperfine shift of second next nearest neighbors is negligible. Such hyperfine shifts would produce a high-frequency contribution and application of Equation 9.4 would thus lead to systematically smaller lattice constants compared to those expected from solid solution behavior.

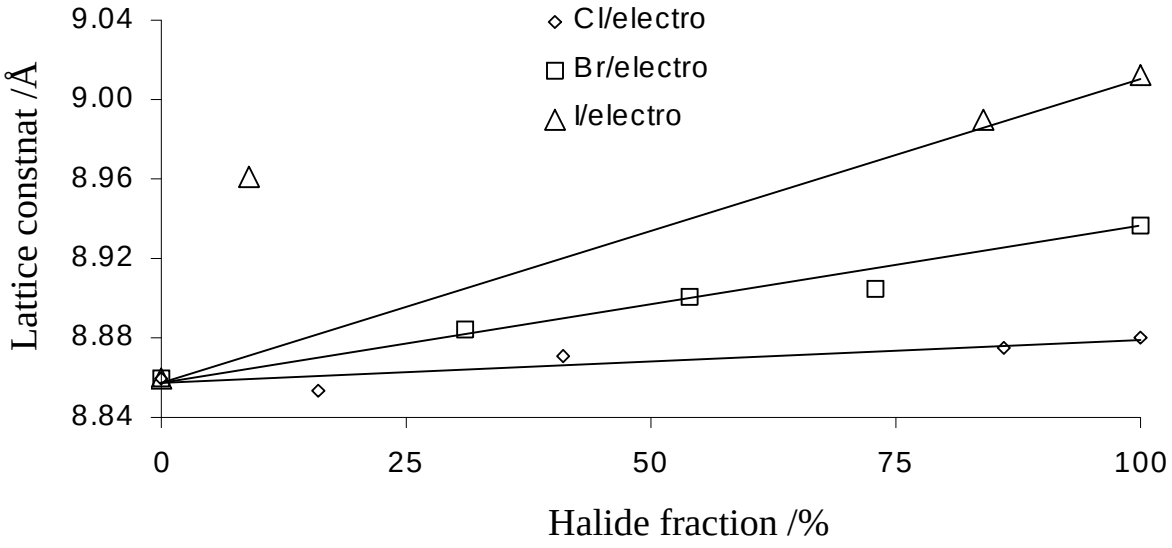

Figure 9-9: *Lattice constants of various halide/electro sodalites, derived from the ^{27}Al resonance shifts of the number 0 resonances, plotted against the halide content. The lines symbolize perfect obedience of Vegard's rule under the assumption that the actual lattice constant of pure SES is 8.8636Å.*[96]

Within the experimental error of the computed cell edges for the Cl/electro and Br/electro sodalites there is no indication for a deviation from Vegard's rule, as observed for halide/hydro sodalites. In the case of I/electro sodalites, however, the computed lattice constant for the 9% I containing sample is almost 0.1 Å larger than expected. This can, however, be understood by the observed domain separation in I/electro sodalites. The signal at 62.5 ppm is therefore most likely due to domains with a high iodine concentration, causing locally enlarged cages compared to the sample average.

As representatively shown by Figure 9-3, the ^{29}Si and ^{27}Al spectra of the same sample are very similar. Both show two sets of four (five) resonances, which is very reasonable, due to the fact that these T atoms occupy crystallographic sites with identical symmetries. A closer look, however, indicates, that the ^{29}Si hyperfine shifts are slightly smaller than the corresponding ^{27}Al shifts. This finding is especially obvious for resonances due to nnn F-centers. In the latter case, the ^{29}Si shifts are 30% (!) smaller as plotted in Table 9-II, while the hyperfine shifts due to nearest neighboring F-centers are quite similar for the number 1

resonance. The difference in the shifts of the number 4 resonance can thus be explained due to the smaller hyperfine shift contribution of nnn F-centers to the overall shift (see Equation 9-3). Certainly the striking difference in the nnn hyperfine shifts cannot be ascribed to nuclear effects, since the shift solely depends on the electron density and not on nuclear parameters. Thus one explanation might be the shorter Si-O distance (compared to the Al-O distance), screening the silicon nuclei more effectively against electron distribution along the Si-Al direction, while the screening towards the center of the directly neighboring cages is not affected.

Discussion of Peak Intensities

If the mixed halide/electro sodalites are perfect solid solution systems with a binomial population distribution, it is possible to simulate the peak intensities just from the halide fraction according to Equation 3-5. A 3D block diagram illustrating the relation between peak intensities and halide content is given in Figure 9-10.

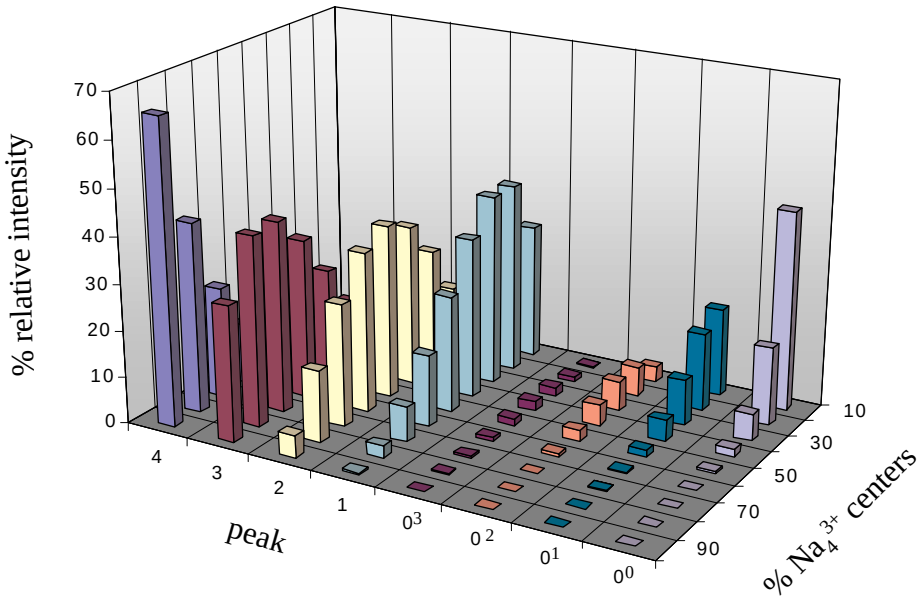

Figure 9-10: *Probabilities of the 8 distinguishable environments for T atoms in halide/electro sodalites according to the fraction of halide filled cages. Computations were undertaken for a binomial distribution and two classes of neighbors. For n > 0 probabilities of different (nn, nnn) environments have been summed up into one value. While the x-axis gives the peak assignment, the y-axis gives the percentage of F-centers, and the z-axis gives the probability in percent.*

When this data is compared to the experimental spectra a disagreement in the number 0 peaks and especially the number 0 peak at about 64 ppm is obvious for several spectra. Besides a departure from binomial distribution in the samples, this effect is most likely caused by imperfectly doped parts of the sample. This might be due to residual water or hydroxide

persisting through the topotactic transformations or to ^{27}Al at cages close to the surface, where Na_4^{3+} centers have been destroyed through oxidation by oxygen or water. However, these discrepancies are small and can be mostly neglected, by considering only the n = 1 to 4 peaks in the comparison between theoretical and experimental intensity distributions.

Thus by analyzing the intensity information of these spectra, the agreement between experimental and theoretical peak intensities is excellent for Cl/electro sodalites (h values of 1% according to the growth model in Chapter 5-1) and still very good for Br/electro sodalites (h = 5% on average). The peak intensities of the ^{27}Al spectra of I/electro sodalites do not agree with the computed intensities based on the overall halide fraction. This is, however, in good agreement with the halide inclusion data gained on mixed iodo sodalites so far, where high separation constants are observed. Thus, although the x-ray data of these high or low iodine containing mixed sodalites do not indicate phase separation, from the ^{27}Al MAS NMR peak intensity distribution analysis the occurrence of separation is obvious.

Taking all this information into account, it is possible to simulate the ^{27}Al MAS NMR spectra of mixed halide/electro sodalites, where the peak positions can be computed from Equation 9-3 and the intensities are in accordance with the binomial distribution of two groups of four neighbors.

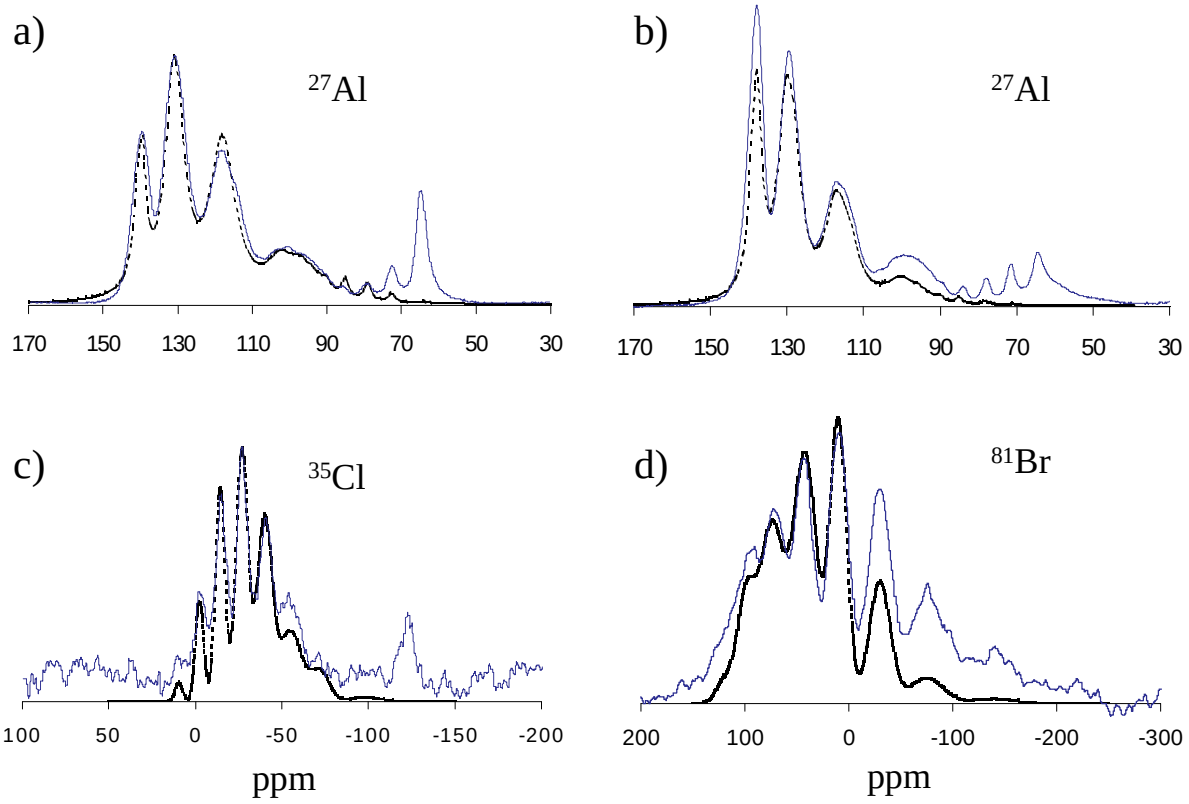

Figure 9-11: *Simulated NMR spectra (dashed lines) compared to the experimental NMR spectra (solid lines) of mixed halide/electro sodalites. Spectrum a) and c) are of 40% Cl containing Cl/electro sodalite; Spectra b) and d) are of a 28 % Br containing Br/electro sodalite.*

9.2.2 The Central Halide Environments.

The halide resonances as portrayed in Figure 9-4 show a similar characteristic as the ^{27}Al spectra of the same samples with a set of large and a set of small hyperfine shifted resonances. This can again be understood by an analysis of the various halide environments possible. Each halide has two groups of neighbors as portrayed in Figure 9-12: eight next neighbors connected through a six-ring window at a center to center distance of $0.866a_0$ and six next nearest neighbors connected through four-ring windows at a distance of a_0. The observed peaks can now be assigned in a similar way as the ^{27}Al resonances, where the peaks number 1 to 8 are due to halide ions, which have between one and eight F centers at the closest 6-ring, neighboring at distances of $\sqrt{3}a_0$. The resonances due to environments with no F-centers among their eight 6-ring neighbors are labeled 0 to 0^6, where the superscript is identical with the number of 4-ring neighboring cages occupied by F-centers at distances of a_0.

a) **b)**

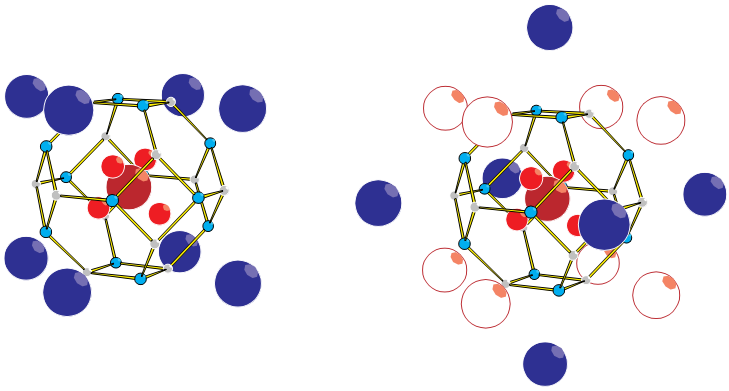

Figure 9-12:
Halide environments in mixed halide/electro sodalites. The halide ions at the centers of the sodalite cages have 14 direct neighbors. ***a)*** *eight cages are separated by 6-ring windows at distances of* $0.866a_0$ *and* ***b)*** *six cages are separated by 4-ring windows at distances of* a_0*, where* a_0 *is the cell edge and varies between 8.864 and 9.012 Å in these series.*

A closer look at the 6-ring neighbors allows further distinction into two groups, where one has an F-center sodium atom at the connecting 6-ring, while for the other F-centers a sodium ion of the Na_4Hal^{3+} center is linked to the inner side of the connecting 6-ring window. This, however, seems to have no observable effect on the electron density at the site of the halide nucleus. Also other than in the tetrahedral coordination of the T-atoms, environments with n F-centers as nearest neighbors are not necessarily equivalent. For example for n = 2 there are 3 different arrangements, for n = 3 there are 4 and for n = 4 there are 4. Again the differences in electron density at the sites of the halide nuclei can apparently not be resolved for these arrangements.

The sizes of the hyperfine shifts can be fitted using an electron-electron repulsion potential according to Equation 9-1. Figure 9-13 shows the fits for the types of neighboring F-centers:

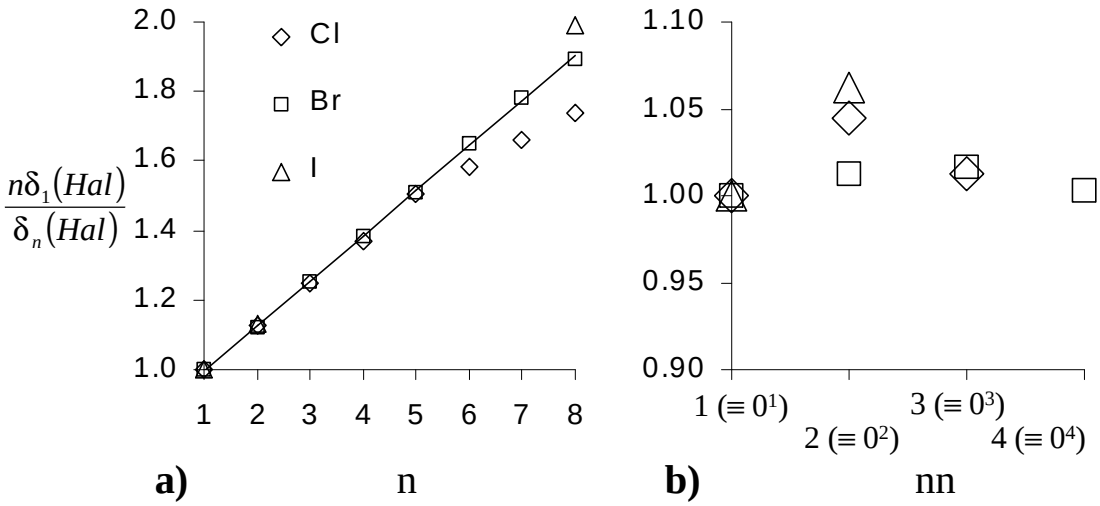

Figure 9-13: *$n\delta_1/\delta_n$ for the hyperfine shift contributions to the halide resonances of **a)** n, the number of nearest F-centers and **b)** nn, the number of next nearest F-centers. The line shown in a) is a linear fit for the ^{81}Br resonances with a repulsion potential of U = 1 - 0.13(n-1) and an undisturbed hyperfine shift of δ_1 = 82 ppm. For the nn neighbors the repulsion is absent (U = 1 within the margin of experimental error as plotted in b).*

A striking finding is, that within the plotted correlation, the otherwise very different halide shifts fall almost together into the same data points. While the correlation with the repulsion effect of the main resonances is excellent for Br/electro sodalites, it is quite good for Cl/electro sodalites. In addition for the first five resonances, the $n\delta_1/\delta_n$ values for Cl and Br/electro sodalites are almost identical. For the stronger shifted ^{35}Cl resonances the repulsion potentials appear weaker than the linear rule predicts. For the I/electro sodalites, only two data points exist, which are in good agreement with the ^{81}Br data. It is interesting to note that the value for the repulsion parameter in these 8 neighbor environments is about 1/8 while in the 4 neighbor environment of the T atoms it is about ¼.

For the four-ring neighbors, no repulsion effect can be observed within experimental error. A possible reason for this is that the 4-ring windows are separated from each other by the 6-ring windows, thus the electron densities penetrating through the 4-ring windows are unlikely to strongly overlap with each other. The ratio of hyperfine shifts caused by 6-ring and 4-ring neighbors is 3.5, 3,7 and 3,0 for Cl, Br and I/electro sodalites, respectively. This might allow a good guess for the ratios of J_n and J_{nn} in Equation 3-20 and will be useful in the interpretation of the magnetic data presented in the following section.

Figure 9-14 gives an idea of the theoretical distribution between the intensities of these resonances as a function of F-center concentration. As can be seen from Figure 9-14,

observation of the whole multiplet cannot be expected for a given composition. This is in contrast to the aluminum spectra, where for most halide concentrations all 5 main resonances can be observed. Since, as discussed above, the main resonances are principally composed of seven sub-peaks themselves, not only the peak intensities, but also the positions of these main peaks depend noticeably on the F-center concentration.

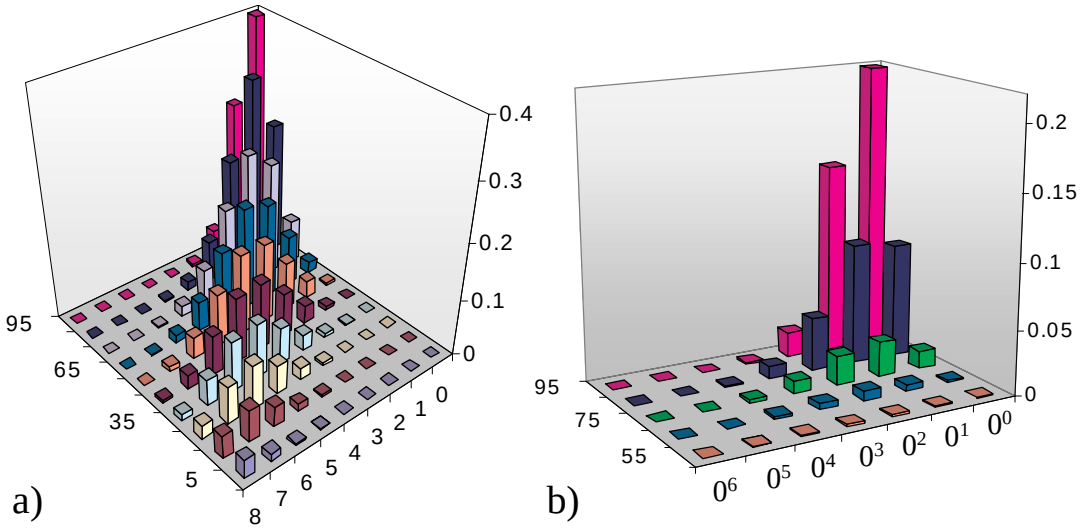

Figure 9-14: *Probabilities of F-center environments of halide filled cages. The x-axes give the peak assignment, the y-axes give the halide fractions in %, and the z-axes indicate the probability of the corresponding resonances.* ***a)*** *Probability distribution for the eight 6-ring neighbors.* ***b)*** *Probability distribution for the six 4-ring neighbors, according to the F-center concentration given and under the assumption of a binomial distribution of both species throughout the lattice.*

Another finding is that for the halide resonances the paramagnetic shifts per F-center increase strongly with increasing halide atomic number. This finding corresponds with the well-known fact that Knight shifts of metals also increase with atomic number. Indeed, the ratios are somewhat similar to the ratios of Knight shifts in those alkali metals that are isoelectronic with the halide anions. This point is still under investigation, and the ^{39}K and ^{71}Ga NMR of mixed K and Ga exchanged halide/electro sodalites might shed additional light onto the origin of this effect.

9.2.3 Sodium Environments in Mixed Halide/Electro Sodalite Solid Solutions

The assignment of the ^{23}Na resonances in the mixed halide/electro sodalites is a bit more challenging than the assignment of the T atom resonances. Therefore it is first necessary to consider the possible locations of Na_4^{3+} centers with respect to the ^{23}Na nucleus under

investigation. The positions of the 10 nearest cage centers to a sodium site are portrayed in Figure 9-15:

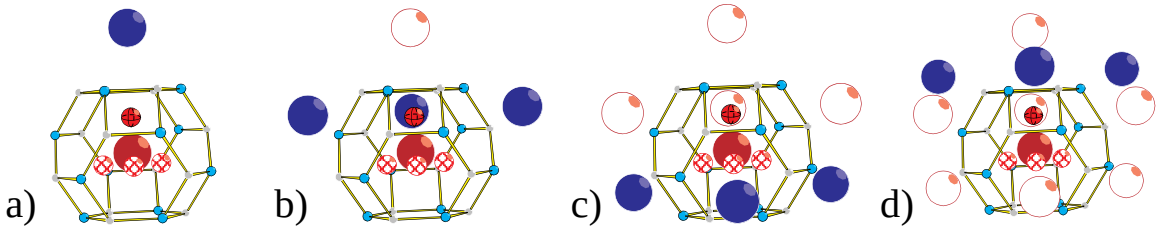

Figure 9-15: *The environment of sodium in mixed halide/electro sodalites.* ***a)*** *sodalite cage with a central anion (large, dark) and the sodium ion of interest (small, dark) slightly above. The residual three sodium cations of the same cage are slightly below the anion (white with black crosses). The closest neighboring cage center at a distance of 4.9 Å is symbolized by a dark sphere.* ***b)*** *three next nearest neighbors behind 6-ring windows at distances of 7.3 Å and are portrayed as dark spheres. The nearest neighbor is, for reference, symbolized by an empty sphere.* ***c)*** *three "6-ring" neighbors at distances of 8.7Å.* ***d)*** *three "4-ring" neighbors at a distance of 7.8 Å. The next neighbors at a distance of 10 Å and cages with larger distances have not been plotted due to the unlikeliness of their significance to the problem.*

From Figure 9-15 it becomes obvious that a large variety of resonances can be caused by distribution of Na_4^{3+} centers among the four different neighbor groups. Considering the fact that the sodium resonances of the ^{23}Na nuclei forming the Na_4^{3+} center are not detected, the resonance with the strongest frequency shift can be assigned to those sodium nuclei, which are only separated from a Na_4^{3+} center by a 6-ring window at a distance of 4.9 Å (resonance A). The fact that its resonance shift increases from Cl/electro to Br/electro to I/electro sodalites is also consistent with the fact that the lattice constant increases in the same direction, pushing the sodium ions closer to the 6-ring window. [As already discussed in Chapter 5-3 the decrease in the Na-window distance is much more important than the increase of the distance between the cage center and the 6-ring window, which is only proportional to the change in the lattice constant. Thus the resulting Na-Na_4^{3+} distance *decreases* with increasing cell edge.] Similar to the number 4 resonance of the ^{27}Al spectra, the broad lineshape of resonance A is the result of overlapping resonances. In this case the latter are caused by different F-center environments which all have the direct neighbor at 4.9 Å in common.

The resonance with the second largest high frequency shift is the one between 50 and 60 ppm (resonance CA), the intensity and shift of which appear correlated with the halide concentration. Close inspection of the various samples indicates a correlation between its intensity and the intensity of the resonance at about 0 ppm. Therefore it will be discussed along those lines below.

Between 45 and 5 ppm a multiplet of up to 15 resonances is found (B resonances). Fortunately the ^{23}Na spectra of Cl/electro sodalites are well resolved and offer an insight into the nature of those resonances. Even better resolution than for the main peaks is achieved for the first high frequency sideband due to the absence of the broad overlapping signal contribution around -10 ppm. Figure 9-16 portrays the sideband and the fit according to the following assignment.

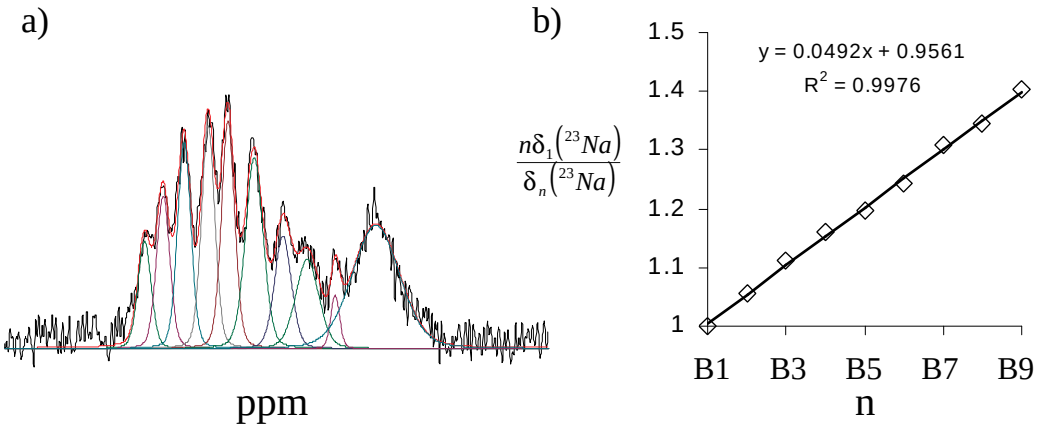

Figure 9-16: a) *First high-frequency spinning sideband of the ^{23}Na multiplet between 45 and 5 ppm of sample Ib according to Figure 9-1. Analysis of the spectrum resolves 10 peaks and, with the exception of the first peak, a symmetric distribution around the center of gravity of the residual multiplet.* ***b)*** *Plot of $n\delta_1/\delta_n$ according to Equation 9-1 for the 10 peak multiplet with respect to the peak number. The resulting repulsion parameter is U = 1+ 0.05(n-1), where n corresponds to the peak number B_n.*

Considering the three groups of neighbors with different paramagnetic shift contributions α, β, and γ, the possible number of resulting peaks can be computed and are given in Table 9-III.

hyperfine couplings			combinations	peaks
α	β	γ	4*4*4	64
α	α	β	4*(4+3)	28
α	α	α	4+3+3	10
α	β	0	4*4	16
α	α	0	4+3	7
α	α/3	0	4*4-3	13
α	2α/3	0	4*4-2	14
α	α/2	0	4*4-6	10

Table 9-III. *Possible numbers of peaks in the multiplet resulting from different hyperfine coupling constants α, β and γ from Na_4^{3+} centers at the sites portrayed in Figure 9-11b-d.*

As it is highly unlikely that those three groups of neighboring F-centers have the same hyperfine coupling with the sodium under investigation, the only model resulting in a ten peak multiplet is the last one, where one coupling constant is by coincidence only half the size of the other one. Thus, only two of the neighbor groups appear to produce significant electron density at the sodium site. While the larger hyperfine coupling can be ascribed to the F-centers at 7.3 Å distance, the smaller coupling is likely to result from the group of 4-ring neighbors at distances of 7.8 Å. As shown in Figure 9-16, the paramagnetic shifts of the peaks

associated with these multiplets can also be fitted well to a repulsion parameter according to Equation 9-1, from which paramagnetic hyperfine shifts of 12 and 6 ppm for the two species can be deduced. The situation was slightly simplified, as all parameters for F-centers causing the larger hyperfine shift were approximated by twice the value of the F-centers with the smaller contribution. Thus, generally the two hyperfine shift contributions can be determined from the first two high frequency shifted resonances with respect to the unaffected ^{23}Na resonance of mixed halide/salt-free sodalites. For Br/electro sodalites, these are 12.5 and 8 ppm, respectively, resulting in a multiplet of strongly overlapping resonances, which can apparently be well reproduced by simulations based on the two hyperfine shift contributions, the repulsion potential from Cl/electro sodalites and a binomial distribution of F-centers between the two groups of three neighboring cages. In case of the I/electro sodalites, the multiplet is not well resolved at all. Besides the domain separation and the resulting effect on the intensity distribution of the resonances, the ^{23}Na NMR spectra of I/electro sodalites also show strong quadrupolar coupling preventing a more detailed analysis.

So far all the resonances with paramagnetic shifts could be assigned and two resonances at lower frequencies, compared to the "regular" Na-halide resonance are remaining. The intensity of the peak at 0 ppm (resonance **C0**) increases dramatically after the samples have been exposed to air. Thus this peak can be assigned to cages with decomposed F-centers. From the results of Chapter 6 it is known that the deshielding of the ^{23}Na nuclei inside a sodalite cage decreases with the size of the central cage anion. Thus it is likely that the peak at 0 ppm in halide/electro sodalites is due to sodium in cages with a rather small anion, such as oxygen or OH^-. The peak at 60 to 50 ppm (resonance **CA**) can then be assigned to such decomposed cage sodium sites which are linked to an F-center via a 6-ring window, similar to the situation for sodium in halide cages giving the **A** resonance, just with a Na-F-center distance of about 6.0 Å. It is reasonable to assume that such surface cages can shrink to better accommodate the small anion and thus the distance between sodium and the neighboring F-center increases, causing a less intense paramagnetic shift, compared to sodium in halide cages. It can be expected that a similar multiplet as for the B resonances exists for resonance C0, however, due to the fact that these resonances would only result from sodium sites in decomposed F-centers at the interfaces between doped and decomposed parts of the crystallites, their overall probability is likely to be quite small.

The broad resonance at the low frequency side of the spectrum (resonance **D**) can be assigned to an overlap of resonances due to sodium in OH^- and $_3O_2^-$ containin ca es as well as ca es with a partially destroyed framework. The ^{23}Na resonance of sodium in OH^- containing cages

(which are available through annealing basic sodalites at 400°C)[12] has a precise quadrupolar lineshape with a C_Q value of 2 MHz, an η of 0 and a chemical shift of –4 ppm. The broad signal observed in the spectra of Figure 9-5 might therefore have the same origin, but be exposed to more site distribution effects, due to the fact that the decomposition of the F-centers causes massive distortions in the lattice and possibly destruction of the latter. Figure 9-17 gives a comprehensive overview over the discussed ^{23}Na resonances.

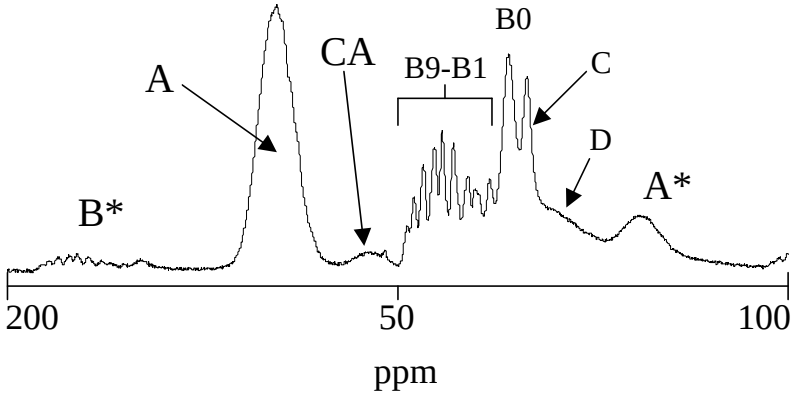

Figure 9-17: *Assignment of the observed ^{23}Na resonances in sodium spectra of halide/electro sodalites. The representative spectrum shown is for a 45% Cl containing Cl/electro sodalite (Figure 9-4Ib). For the corresponding environments causing the resonances A-D see text.*

While all resonances observed in the ^{23}Na spectra of mixed halide/electro sodalites can be assigned to certain sodium environments, only the most high frequency shifted resonance and the multiplet between 45 and 5 ppm are due to sodium sites within the solid solution phase of halide and F-center occupied cages. According to the model explained above, we can thus simulate the intensities of these resonances as portrayed in Figure 9-18.

Figure 9-18: *Theoretical relative intensity distributions among the A and B resonances in the ^{23}Na spectra of mixed Cl/electro sodalites according to a binomial distribution. Obviously the total intensity of all observed resonances decreases with increasing F-center concentration due to the unobserved ^{23}Na resonances of sodium forming the Na_4^{3+} centers.*

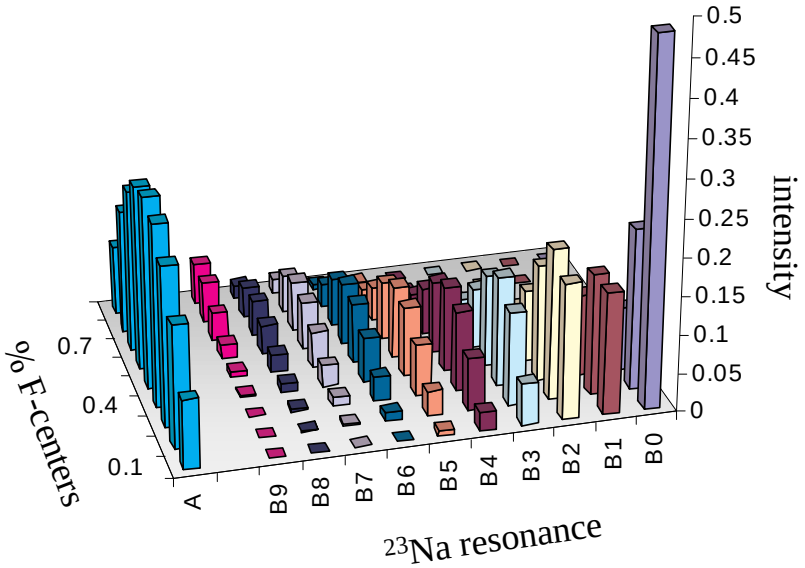

Although the intensity distribution of the sodium resonances could be used to characterize the distribution of F-centers within the sodalite lattice, the influence of decomposed cages and the

reduced number of available nuclei do not allow more than qualitative comparisons between the theoretical and experimental intensity distributions. On the other hand, the multiple sodium sites at different distances to F-centers allow an experimental observation of the electron density distribution of the F-center. The observed ^{23}Na NMR hyperfine shifts are, as discussed in Chapter 3, proportional to the electron density at the site of the nucleus. Thus this density is proportional to the electron density at the surface of the sodium ions, allowing a plot of relative electron density as a function of the distance between the nuclei and the center of gravity of the F-center. Such a plot is given in Figure 9-19, where the linear behavior indicates an exponential decay of the electron density from the center of gravity of the F-center towards the cage boundaries and even beyond. The characteristic length of the decay is r_0 = 0.8 Å in this case. This is in fine agreement with theoretical investigations on the F-centers, which have recently been published and also find s character of the paramagnetic electron.[23]

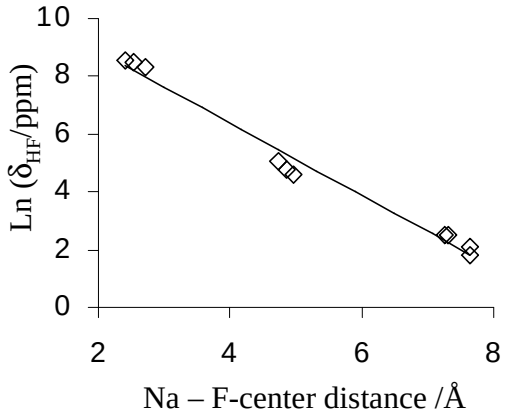

Figure 9-19: *^{23}Na NMR hyperfine shifts as a function of Na-F-center distance. The shifts of the sodium nuclei in Na_4^{3+} centers (data points below 3 Å) are computed from the EPR hyperfine coupling constants according to Equations 2-50.*

Sodalite	neighbor	Na-Fc-dist	HF-shift
Cl-SOD	F-center	2.42	5140
	nn	4.96	98
	nnn	7.25	12
	nnnn	7.64	6
Br-SOD	F-center	2.54	4760
	nn	4.87	120
	nnn	7.3	12.5
	nnnn	7.65	8
I-SOD	F-center	2.71	4100
	nn	4.72	155
	nnn	7.37	
	nnnn	7.66	

Table 9-IV: *^{23}Na NMR hyperfine shifts in various sodalites. The distances have been calculated according to the lattice constants of all the phases in which the couplings were observed. Where no crystallographic data was available the calculations were based on Vegard's rule and the fractional compositions. The data is plotted in Figure 9-19.*

Furthermore, the experimental data is in nearly quantitative agreement with spin densities calculated for sodium nuclei in dry cages that are neighboring F-centers.[23] (In this analysis, the sodium positions in the dry cages were assumed to be the same as in the F-centers, just with one vacant site. Although this is highly unrealistic, such sodium coordinates are actually very similar to the sodium positions in chloro sodalites.) The values are comparable to the shifts given in Table 9-III and are 0.0169, 0.0014 and 0.0006 au (atomic units) for ^{23}Na next

to and F-center, next nearest to an F-center by a 6-ring window and by a 4-ring window, respectively.

9.3 Temperature Dependent NMR Studies

Recently low-temperature static NMR data of partially doped electro sodalite have been published[78] indicating a Weiss temperature of –150 K for the number 4 peak, while the shift of the number 0 peak was temperature independent. As shown in Chapter 3, the Weiss temperature is a function of the number of neighboring paramagnetic electrons as well as their mutual coupling constants (J_{nn} and J_{nnn}). Therefore different Weiss temperatures are expected for different halide concentrations and environments and thus only variable temperature NMR can distinguish between the contributions of electron density and electron-electron interaction to the hyperfine shift. Two sodalite samples showing all five major aluminum resonances (28 % Br/e-sodalite and 40% Cl/e sodalite) were studied. The bromine sodalite was exposed to air prior to the VT experiment allowing for an in-situ observation of the decomposition of further F-centers, while the chlorine sodalite was kept under argon.

9.3.1 Experimental Results and Observations

Br/Electro Sodalite:

The high temperature NMR spectra are shown in Figure 9-18. The sample is the same as the one from which the NMR spectra in Figure 9-(2,4,5)IIa originate, but it had been exposed to air prior to the high temperature experiment leading to an increase in the peaks at the low frequency side of the spectrum, due to decomposed F-centers, as discussed above. While for the temperatures between 300 K and 500 K the high frequency shifted resonances move to lower frequencies with increasing temperature, no changes in the relative intensities of the resonances can be observed.

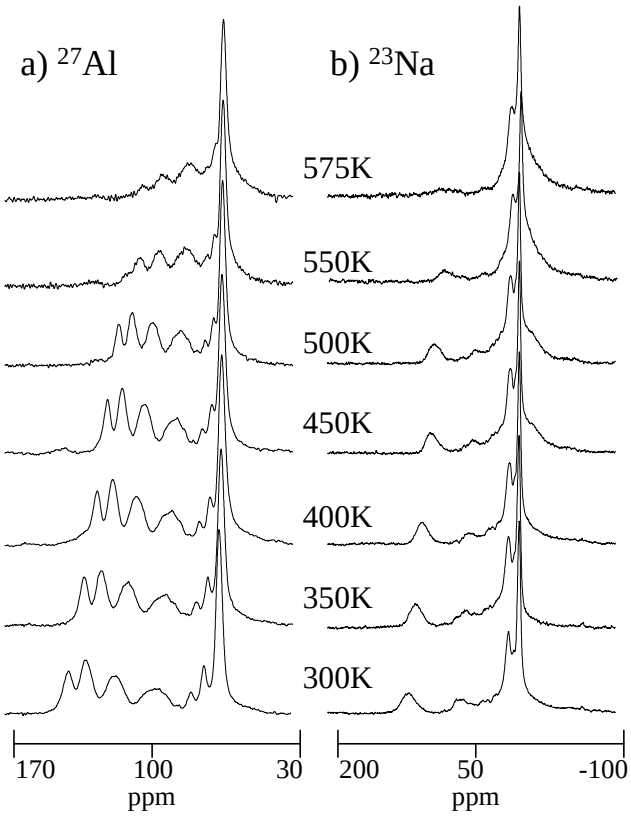

Figure 9-20: *VT MAS NMR spectra of 28% Br containing mixed Br/electro sodalite.* ***a)*** *^{27}Al and* ***b)*** *^{23}Na spectra, observed at 104.29 and 105.81 MHz, respectively. The spinning speed was 6500 Hz at all temperatures and varies between ± 1 and ± 15 Hz at 300 K and 575 K, respectively. 512 scans were acquired with relaxation delays of 0.5 s. The temperatures are constant within ± 0.1 K and accurate to within 1 %.*

The ^{27}Al spectra taken at 550 K and 575 K show significantly different intensity distributions compared with the spectra at lower temperatures. While the intensities of the peaks number 4 and 3 have dropped, the relative intensities of the number 0 and 1 peaks have increased. A similar observation can be made in the ^{23}Na spectra, where the A resonance has almost disappeared at 575K and the resonances around 0 ppm have increased.

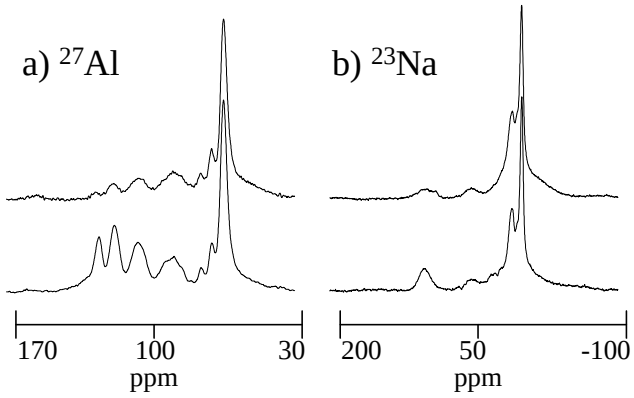

Figure 9-21: *^{27}Al and ^{23}Na MAS NMR spectra observed at 400 K. The lower spectra were observed before heating the sample to 575 K and the upper ones during the cooling process.*

As shown by Figure 9-21, the temperature dependent frequency shifts are reversible, while the spectral intensities of those samples that were cooled down to 400 K from 575 K are still similar to the intensities at 575K (shown in Figure 9-20). An exception might be the A resonance in the sodium spectra. While its intensity relative to the other resonances in the 400

K spectrum after heating is still smaller than in the spectrum prior to the exposure to 575 K, the latter intensity appears to be relatively stronger than in the spectrum taken at 575 K, indicating a reversible change in intensities, stronger than the expected temperature dependence due to Boltzmann distribution.

Cl/Electro sodalite:

The temperature dependent ^{27}Al and ^{23}Na NMR spectra of the Cl/e sodalite generally show similar trends as in the case of the Br/e sodalite, however, within the range of 200 to 550 K the observed changes in the spectra are fully reversible.

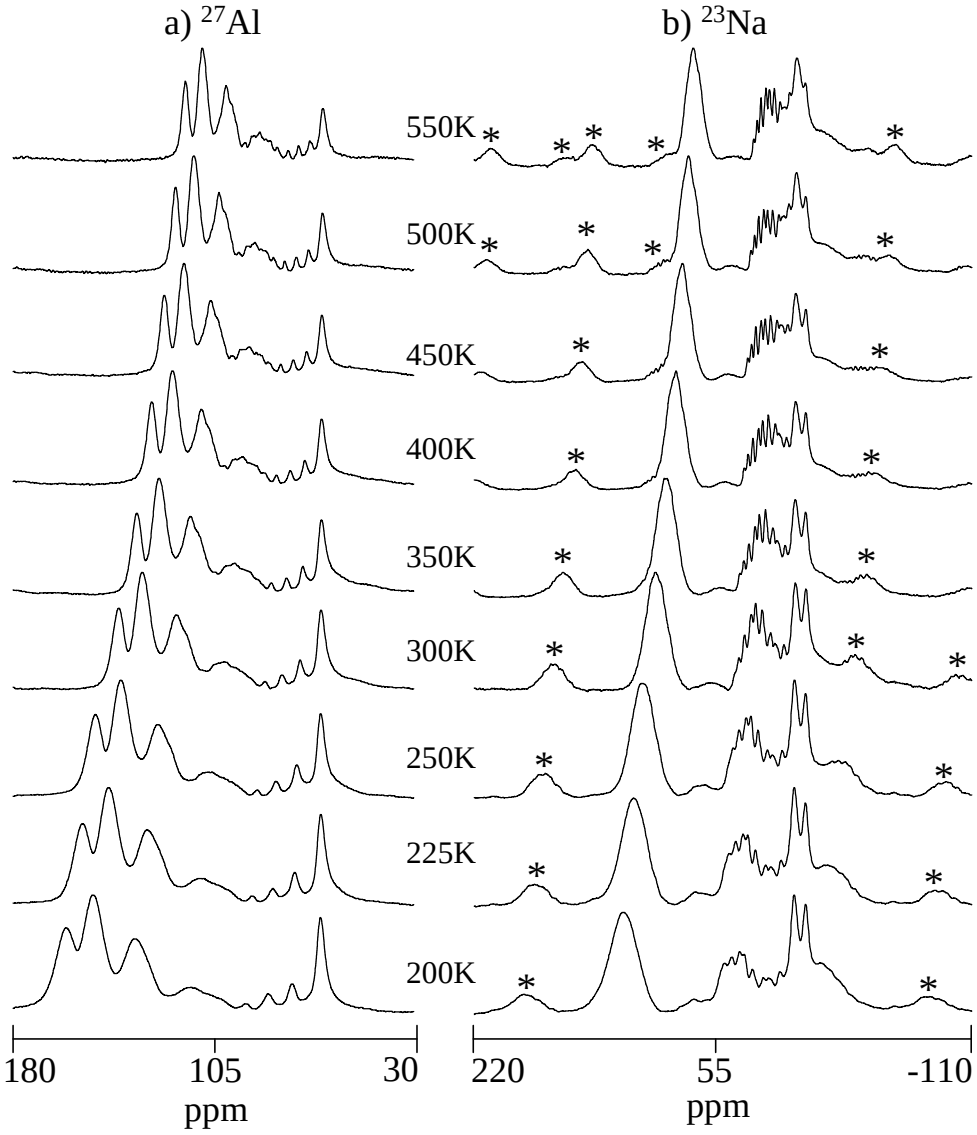

Figure 9-22: *^{27}Al and ^{23}Na VT-NMR spectra of a 40% Cl containing Cl/electro sodalite, observed at 104.23 and 105.81 MHz at spinning speeds of 7000 Hz. The spinning sidebands of the major resonances in the ^{23}Na NMR spectra are marked with asterisks.*

While the ^{23}Na NMR spectra of this Cl/e sodalite show the best resolved B-peak multiplet of all mixed electro sodalites studied, it is interesting to note that, although the magnitude of the hyperfine shifts decreases with temperature, their linewidth is reduced even more, allowing for the observation of the 0^4 and the 1^{nn} peaks in the ^{27}Al NMR spectrum. In order to extract more information from these spectra a detailed investigation of the hyperfine shifts will be presented in the Discussion section.

9.3.2 Discussion

Sodium Mobility

For temperatures below 500 K, the intensity distribution among the peaks in the ^{23}Na and ^{27}Al spectra remains unchanged, indicating that the overall and the local structure of the sample does not change. The variation of peak intensities of the observed resonances between 500 K and 550 K, however, indicates decomposition and possible rearrangement of the F-centers. Since the sample was already partially decomposed it is reasonable to assume that oxygen and water are present at the outer spheres of the crystallites and become sufficiently mobile to penetrate further into the crystallites to oxidize F-centers. While this effect explains the irreversible intensity change of the resonance intensities, the reversible change of the A resonances in the ^{23}Na spectra is likely to be due to an increased mobility of sodium ions in and next to F-centers. This is in good agreement with the onset of doping observed during the preparation of the sample at about 525K, since mobile sodium ions are mandatory to allow the migration of F-centers into all empty (or dry) cages of the sodalite lattice. Thus HT NMR allows an in situ observation of the processes relevant in the doping mechanism.

Hyperfine Shifts.

Since the chemical shift is to the first order temperature independent, the shift changes observed for the number 0^0 ^{27}Al NMR peak could be due to hyperfine shifts caused either by the vicinity of more distant F-centers or by thermal expansion of the lattice and thus an increase in the T-O-T bond angle. Since, as shown in the previous section, it is plausible to neglect the influence of more distant (nnnn) F-centers, the temperature dependence of the number 0^0 resonance is best explained by an increase in the T-O-T bond angle. Between room temperature and 500 K the ^{27}Al resonances of both sodalites are shifted by only 0.7 ppm indicating an increase of 0.025 Å in lattice constant. While compared to the salt-free sodalites discussed in Chapter 8 (up to 0.25 Å) this increase is rather small, it compares well to the lattice expansion of Cl/Br sodalite (0.035 Å) discussed in Chapter 7. It is then interesting to

note, that no abrupt increase of the cell edge is observed at around 525 K, where the doping process becomes possible due to the sodium mobility.

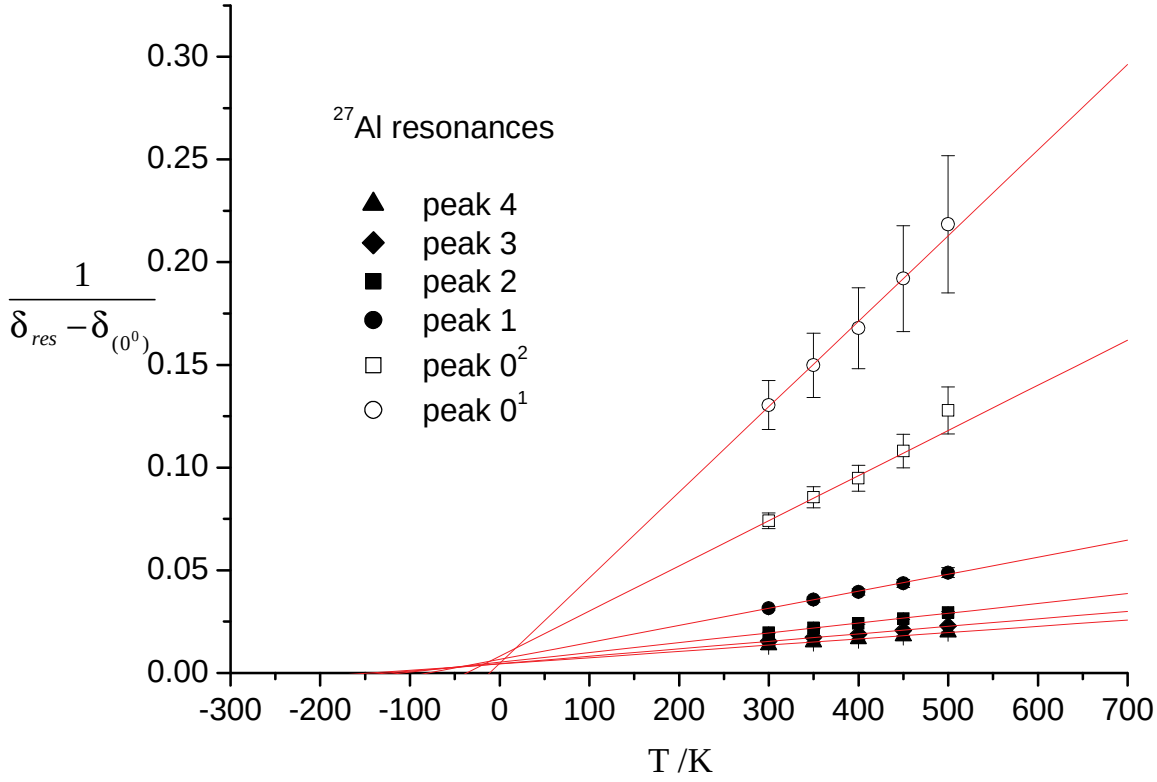

a)

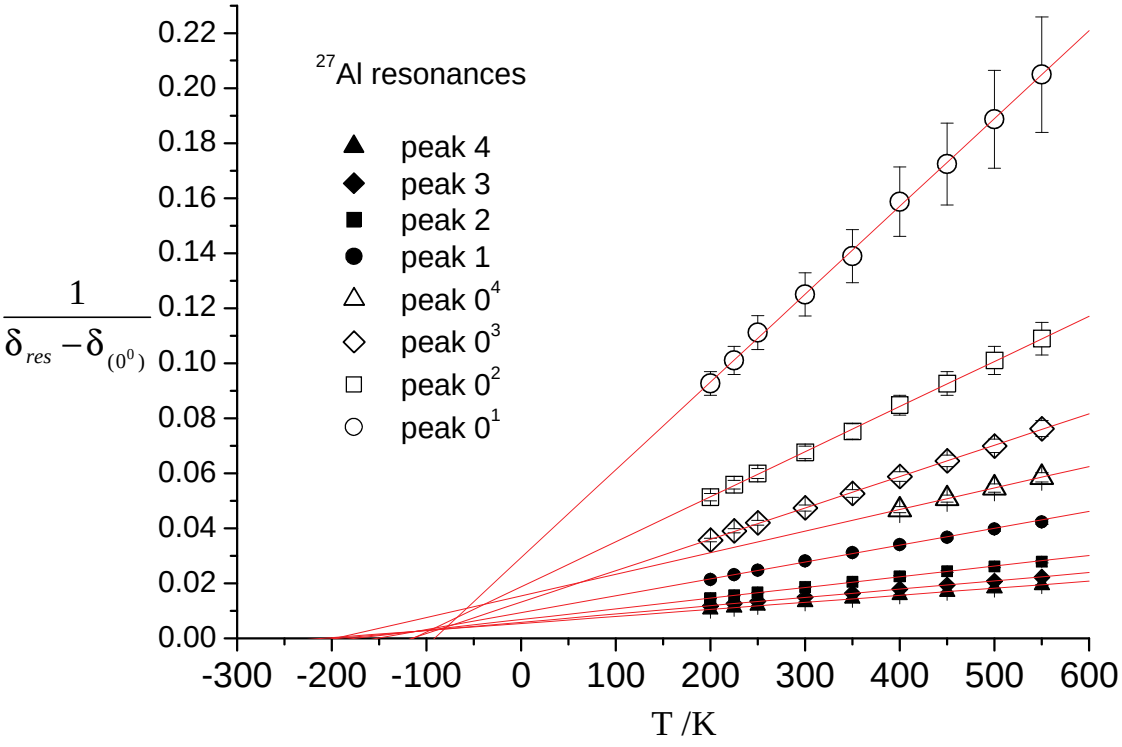

b)

Figure 9-23: *Temperature dependence of the ^{27}Al hyperfine NMR shifts of* ***a)*** *28% Br-containing Br/electro sodalite and b) 40% Cl containing Cl/electro sodalite. Resonances obeying the Curie-Weiss law show linear slopes with the Weiss temperature as the y-axis offset. The slopes are a function of the hyperfine coupling constant according to Equation 9-5. The resulting data is given in Table 9-V.*

As shown in Figure 9-2, the quadrupolar shift contribution is similar for all ^{27}Al resonances observed in halide/electro sodalites. Thus, the hyperfine shift of all observed resonances can be extracted by subtraction of the resonance shift of the 0^0 ^{27}Al resonance. As can be seen from Equation 2-50 the hyperfine shift is related to the Weiss temperature of the electrons as well as the electron density at the nucleus observed. A plot of $1/\delta$ against the temperature is expected to show a linear relation and yields the Weiss temperature as the x-axis-offset, while the slope is a function of the hyperfine coupling constant A_N, which is again proportional to the electron density at the nucleus (see text near Equation 2-50)

$$\frac{1}{\delta_{HF}} = \frac{1}{A_N}\frac{g_N \mu_N}{g_e \mu_e}\frac{3k}{10^6 hS(S+1)}(T-\theta) \qquad \text{Equ. 9-5}$$

Figure 9-23 a and b plot the ^{27}Al NMR hyperfine shifts of both sodalites according to Equation 9-5. The resulting Weiss temperatures and coupling constants are given in Table 9-V.

Although the hyperfine shifts observed are affected by both different hyperfine coupling constants and Weiss temperatures, the major distinction is caused by the coupling constants, resulting from the occurrence of multiple F-centers around the nucleus observed. The hyperfine coupling constants of both sodalite samples can be plotted analogous to Figure 9-8 revealing a similar linear relation as that resulting from electron-electron repulsion.

	40 % Cl/e sodalite		28 % Br/e sodalite	
^{27}Al peak	$-\theta$ /K	A /kHz	$-\theta$ /K	A /kHz
0^1	92 ± 27	78 ± 8	11 ± 66	60 ± 10
0^2	114 ± 17	151 ± 8	40 ± 42	103 ± 13
0^3	116 ± 11	217 ± 8	-	-
0^4	185 ± 79	315 ± 48	-	-
1	152 ± 8	403 ± 10	79 ± 23	298 ± 18
2	175 ± 6	637 ± 11	108 ± 15	519 ± 20
3	193 ± 5	823 ± 11	121 ± 15	680 ± 28
4	210 ± 5	967 ± 12	140 ± 11	809 ± 24

Table 9-V: *Hyperfine coupling constants between ^{27}Al and its surrounding F-centers as well as the Weiss temperature measured for these aluminum resonances, as determined from Figure 9-24.*

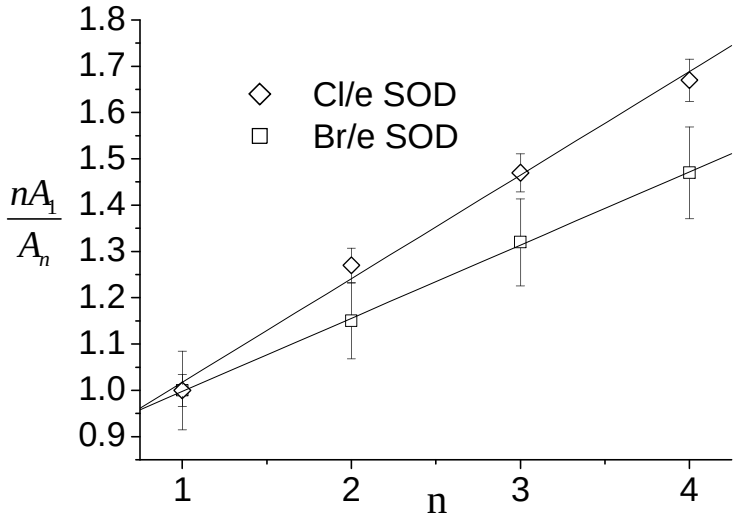

Figure 9-24: *Fits of the electron-electron repulsion factor: nA_1/A_n reflects the ratio of pure electron densities independent of the Weiss temperature. The slopes are 0.22 ± 0.02 for the Cl/e sodalite and 0.16 ± 0.04 for the Br/e sodalite.*

While the electron density at the aluminum cores changes by a factor 2.6 between the number 1 and number 4 peaks, the Weiss temperature in both cases only changes by about 33%. This can be understood as follows: The Weiss temperature observed for a given ^{27}Al resonance is a good average value arising from all electrons interacting with the nucleus. The Weiss temperature of each electron, thus, depends on the number of nn and nnn neighboring F-centers it is coupled with according to Equation 3-19. This average value, however, does not exactly equal the F-center concentration in the sodalite, since the content of mutual neighbors (neighboring the F-center as well as the ^{27}Al atom), slightly restricts the expected distribution. Table 9-VI shows the average number of nn and nnn F-centers neighboring an electron, which is part of either of the 8 aluminum environments.

	neighboring F-centers			
^{27}Al peak	6-ring out of 2	4-ring out of 2	z_{nn}(average) e.g. 28% Hal cont. SOD	z_{nnn}(average)
0^1	0	0	4.38	2.92
0^2	0	½	4.38	3.42
0^3	0	2/3	4.38	3.59
0^4	0	1	4.38	3.92
	out of 2	out of 1		
1	0	0	4.38	3.65
2	2/3	1/3	5.05	3.98
3	4/3	2/3	5.71	4.32
4	2	1	6.38	4.65

Table 9-VI: *Dependence of the average number of neighboring F-centers (see Equation 2-50) to an F-center contributing to the hyperfine shift of a given ^{27}Al resonance. The first column gives the ^{27}Al resonance and the second and third give the number of F-center occupied cages neighboring both the F-center of interest and the aluminum atom. The fourth and fifth column give the average number of six- and four-ring neighboring F-centers, based on an average F-center concentration of 72 % throughout the sample.*

Table 9-VI indicates that the average number of neighboring F-centers increases with the hyperfine resonance number. Thus from the Weiss temperatures associated with the number 1 to 4 peaks it can be concluded that J_{nn} is negative, indicating antiferromagnetic coupling. In addition from the decrease in Weiss temperatures of the resonances number 0^1 to 0^4, whose contributing F-centers have the same average number of 6-ring neighbors, but an increasing average number of 4-ring neighbors, it is obvious, that J_{nnn} is also negative. Thus all magnetic interactions within the sodalite lattice are antiferromagnetic.

A quantitative analysis of the absolute values of J_{nn} and J_{nnn} is not possible based on the temperature dependent data shown here. The model is, however, consistent with a ratio J_{nn}/J_{nnn} of about 3 to 4, which corresponds well to the ratio of the hyperfine shifts of halide nuclei exposed to a F-centers connected through 6-ring to those connected through the 4-ring window. A more detailed discussion of these considerations can be found in the following section about the bulk magnetic properties of these electro sodalites.

Based on Equation 9-5 the temperature dependent ^{23}Na NMR data could also be analyzed. While for the Cl/electro sodalite Weiss temperatures were determined for all resonances observed, the severe overlap of the B resonances in the ^{23}Na NMR spectra of the Br/electro sodalite prevented further analysis of these resonances. Thus only data for the A resonance could be extracted and is given along the data of the Cl/electro sodalite in Table 9-VII.

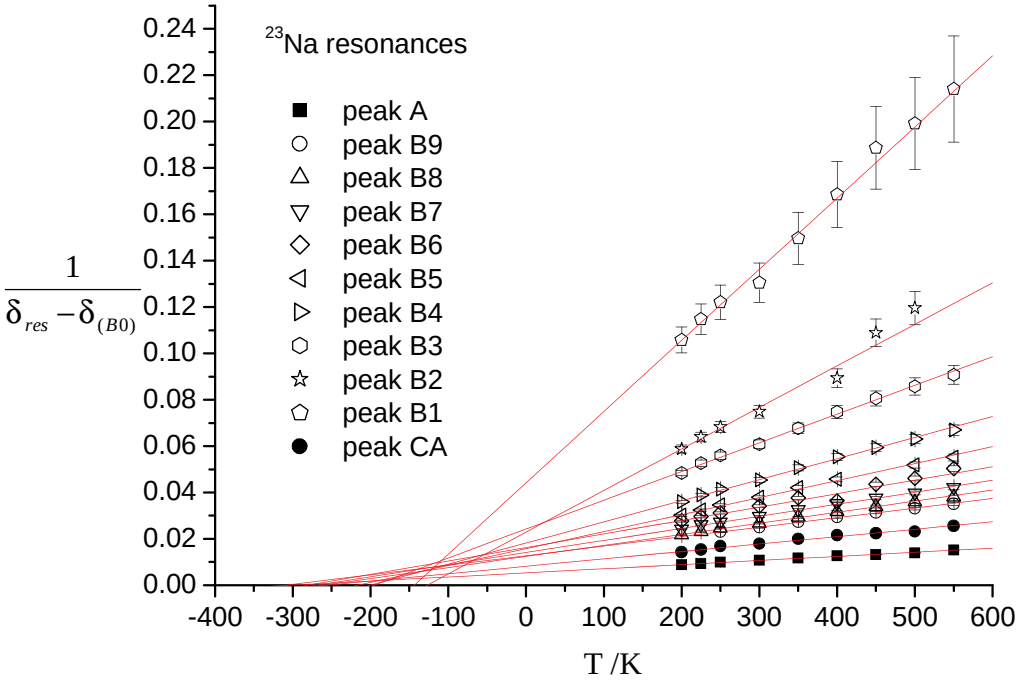

Figure 9-25: *Temperature dependence of the ^{23}Na hyperfine NMR shifts of 40% Cl containing Cl/electro sodalite. Resonances obeying the Curie-Weiss law show linear slopes with the Weiss temperature as the y-axis offset. The slopes are a function of the hyperfine coupling constant according to Equation 9-5 and the resulting data is presented in Table 9-VII.*

^{23}Na peak	θ_w /K	A / kHz
A (Cl/e$^-$)	257± 7	786 ± 14
B1	144 ± 40	82 ± 10
B2	128 ± 23	140 ± 11
B3	196 ± 20	203 ± 12
B4	201 ± 15	276 ± 12
B5	217 ± 14	343 ± 14
B6	281 ± 15	433 ± 16
B7	273 ± 12	482 ± 15
B8	263 ± 11	528 ± 14
B9	312 ±18	613 ± 24
A (Br/e$^-$)	232 ± 29	1560 ± 95

Table 9-VII: *Hyperfine coupling constants between ^{23}Na and its surrounding F-centers as well as the Weiss temperatures measured for the ^{23}Na resonances in Cl/electro sodalite (from Figure 9-24). The last line gives the values for the A resonance in the Br/electro sodalite.*

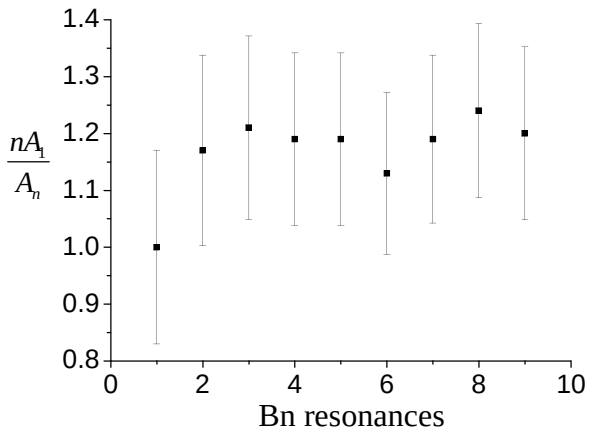

Figure 9-26: *plot of the electron-electron repulsion factor similar to Figure 9-24. The huge error bars result from the error in the coupling constant for the B1 resonance.*

An evaluation of the Weiss temperatures as well as the electron densities at the ^{23}Na nuclei is complicated by the fact, that the B resonances observed result from overlaps of resonances due to substantially different F-center environments. While up to 4 combinations of neighboring F-centers with large and small hyperfine coupling constants are possible this number multiplies through different occupation arrangements of the F-center occupied neighbors among the six possible sites. However, it can be observed, that the Weiss temperature increases with increasing peak number. It is interesting to note, that the observed Weiss temperatures exceed the maximum Weiss temperature, measured for F-centers, which magnetically interact with F-centers in all neighboring cages. A reason for this observation might be the influence of an impurity conduction band involving the sodium atoms. Metallic conductors show temperature independent Pauli susceptibility, rather than the Curie-Weiss like susceptibility. Possibly, this Pauli-type contribution leads to a less pronounced temperature dependence of the observed resonances and thus results in artificially enlarged negative Weiss temperatures, when fitting the data to Equation 9-5. However, the maximum possible precision in observation of the resonance shift combined with the complex composition of the observed ^{23}Na resonances precludes quantitative analysis of such contributions.

Also the electron density at the sodium nuclei, expressed by the ^{23}Na hyperfine coupling constants A_n shows a different behavior than that observed for the ^{27}Al nuclei. When the coupling constants are fitted according to Equation 9-1 no significant increase of the electron-electron repulsion with increasing peak number can be observed. However, the error bars

would still allow such a fit, due to the rather insecure hyperfine coupling constant A_1. On the other hand, the F-centers contributing to these hyperfine shifts statistically only partially neighbor each other, reducing their average interaction and thus the e-e-repulsion. If the hyperfine shifts themselves are plotted versus the shift number, the data can be fitted by a linear expression with a slope of 68 kHz and crossing (0,0). As a consequence almost no e-e repulsion would be expected in this system.

9.4 Bulk Magnetic Measurements

One of the most exciting effects in these mixed halide/electro sodalite systems is the relation between the microscopic magnetic interactions between single F-centers and the bulk magnetization of a whole halide/electro sodalite sample. As it has been shown by Srdanov et al.,[20] pure sodium electro sodalite is a low temperature antiferromagnet with a Néel temperature of 48 K. Temperature dependent measurements of the bulk magnetic susceptibilities of i ed r electro sodalites were underta en and the data is resented in Figure 9-27.

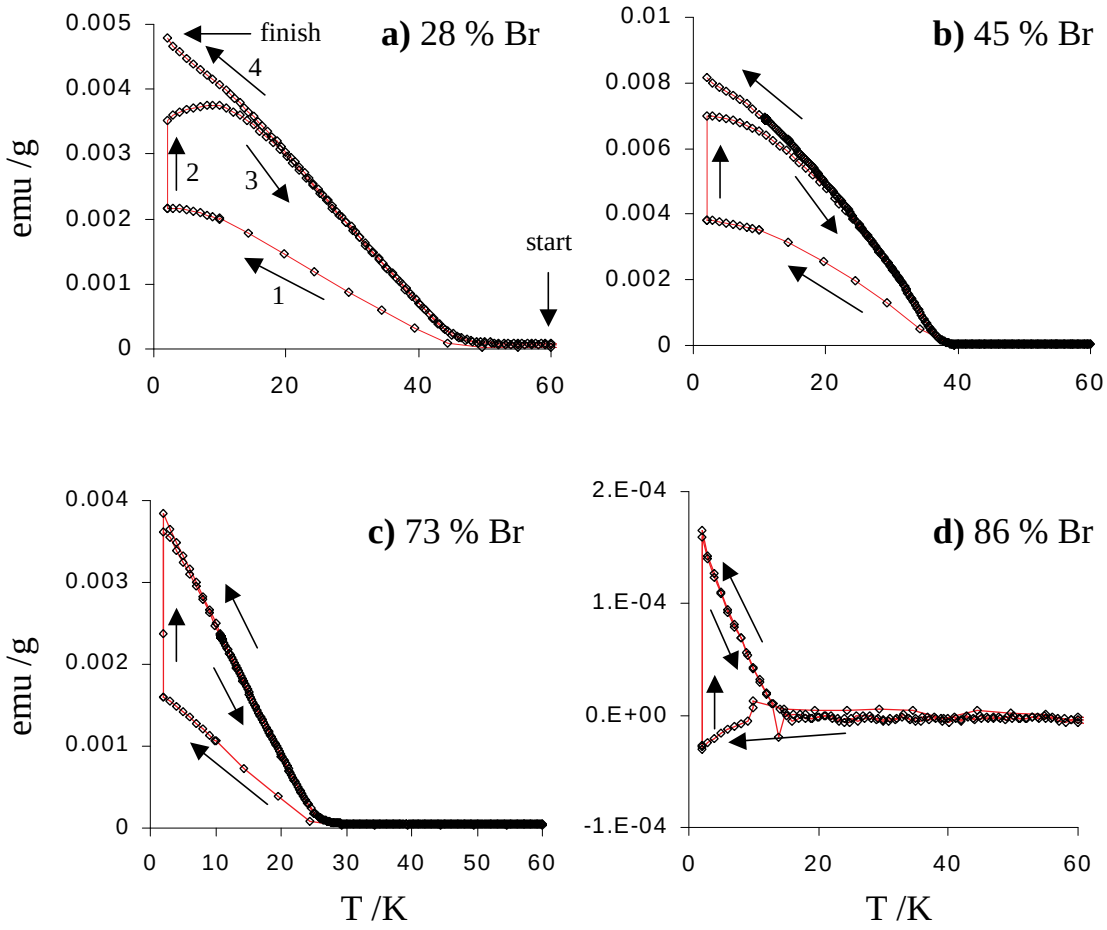

Figure 9-27: *Temperature dependent magnetic susceptibility data observed at 0 (± 0.1) and 1 mT. (Zero field cooling, see text) The arrows marc the chronology of the data acquisition. Start and finish as well as the order are representatively plotted in a).*

The most striking observation of the ZFC measurements presented in Figure 28 is that the overall magnetization shows a ferromagnetic transition. The Curie or rather onset temperature of this magnetic interaction appears to be somewhat dependent on the concentration of F-centers in the sample studied and varies between 44 K for 28 % bromine containing sodalite and 15 K for 73 % bromine containing sodalite. Even in the zero field cooling process, the overall magnetization of the samples starts to rise at these temperatures (in case *d)* even to negative values). This is most likely due to the fact, that the external magnetic field was not exactly zero, but had a residual strength of $< 10^{-4}$ T. Since the strength of the applied magnetic field (after the cooling process) was only 10^{-3} T, the magnetization caused by the residual field is likely to be a significant fraction when compared to the magnetization induced by the applied field. The deviations between the field warmed and field cooled temperature scans also increase with increasing concentration of F-centers. While for the sodalites with lower F-center concentration the field warmed magnetization is just a little smaller than the field cooled one, the sample with 28% bromine exhibits a maximum in the field warmed magnetization. The overall magnetic moment increases with increasing F-center concentration, with an exception of the sample with the lowest bromine concentration. It is also possible, that a maximum magnetization per F-center is reached at 50 % F-center concentration. Also these overall magnetic moments are only a fraction of the saturation magnetization which is $g_e \bullet S(S+1) = 1.734$ (in μ_B) per free electron. For example, for the 45% Br containing Br/electro sodalite with a molecular mass of 934 g/mol, the magnetic moment of $8 \bullet 10^{-3}$ emu/g corresponds to $2.44 \bullet 10^{-3}$ (in μ_B) per F-center. Thus the magnetization is about 0.1 % of the saturation magnetization expected for a paramagnetic spin.

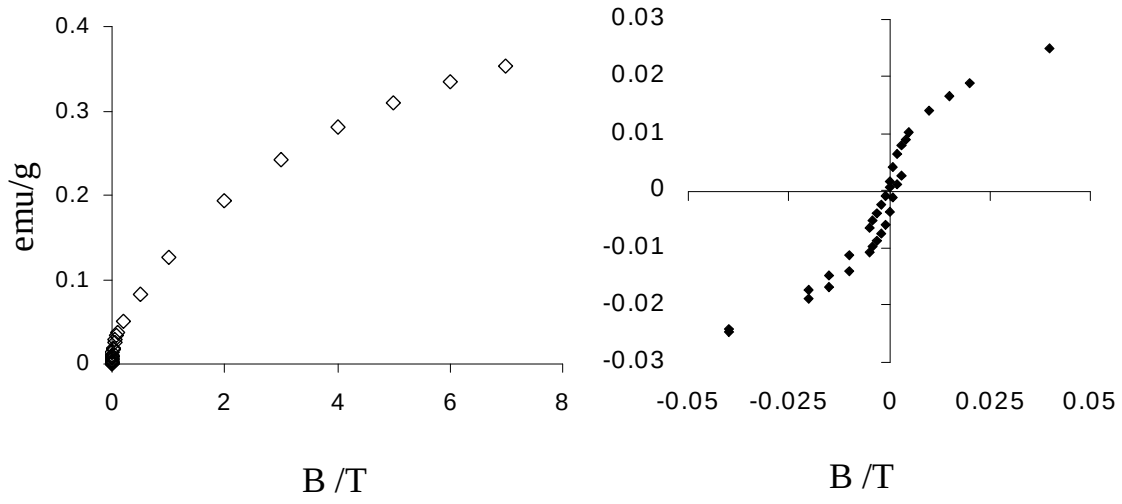

a) ***b)***

Figure 9-28 a) *Saturation experiment at 2 K and a maximum external magnetic field of 7 T on a 45 % Br containing Br/electro sodalite.* ***b)*** *Hysteresis found for the same sample, also at 2 K.*

Figure 9-28 shows field dependent susceptibility measurements performed at a temperature of 2 K on the sample with 45 % bromine content. For high magnetic fields, the onset of saturation can be observed. However, the magnetic moment per F-center at 7 T is only about 0.11 (in μ_B) and thus 6.4 % of the value expected for paramagnetic s-electron spins.

Also at 2 K, the magnetization shows a hysteresis loop with a remanence of 3 mT and a coercive field of 1.5 mT. This soft ferromagnetic behavior indicates the formation of magnetic domains and is consistent with the occurrence of a blocking temperature in the ZFC experiments.

Discussion

As shown above, the mixed Br/electro sodalites show a bulk ferromagnetic susceptibility characteristic with Curie Temperatures between 44 K and 15 K. In contrast, the pure SES is an antiferromagnet. In addition the NMR data observed for these mixed halide/electro sodalites shows, that the magnetic coupling constants between F-centers and their first and second neighbors are antiferromagnetic, which is consistent with negative Weiss temperatures observed for the overall magnetic susceptibility. To rationalize these observations the following qualitative model is proposed:

As expected for unpaired electrons, all interactions between F-centers are indeed of antiferromagnetic nature. The introduced random distribution of halide and F-center occupied cages is the reason for a variation of Weiss as well as Néel temperatures dependent on the number of neighboring F-centers to each spin. When the temperature is lowered in a magnetic field, small antiferromagnetic coupled clusters occur at a temperature defined by their average number of neighboring spins. The sizes of these clusters are likely to range from dimers to clusters with tens of spins. Due to the parallel occurrence of clusters throughout the lattice several spins are trapped in states, where each orientation is parallel and antiparallel to the same number of neighbors. Such spins are called “frustrated” spins. They cause a degeneracy of the ground state of the whole system. Without any external field, their orientation will statistically vary between the two possible alignments resulting in a zero magnetic moment of the sample. In the presence of an external magnetic field, however, the state where all frustrated spins are oriented parallel (or have a parallel component, depending on their easy axes) with the external field is lower in energy and thus the spin system freezes in this state. The resulting magnetic behavior therefore appears to be ferromagnetic. During the field cooling process, the size of the freezing clusters decreases, adding more spins which are oriented parallel with the external magnetic field to the system. The contribution of paramagnetic spins is negligibly small in the small external fields applied.

The data of the ZFC measurements can now be understood as follows. While the temperature is lowered in a zero external magnetic field, the system freezes in a state, where the frustrated spins are oriented randomly. The application of the external field is capable of reorienting paramagnetic spins as well as orienting the magnetization direction of small clusters along the external magnetic field. An increase in temperature has two effects: For small clusters, the Néel temperature is reached and they become paramagnetic and the extra thermal energy might allow larger clusters to orient their magnetization parallel (and antiparallel) to the external field with the effect that the frustrated spins are then aligned parallel to the external field. In this temperature region the total magnetic moment of the sample still increases with increasing temperature. With a further increase in temperature, an increasing number of clusters becomes paramagnetic due to the fact, that their Néel temperature is reached and the overall magnetic moment decreases. This is also in agreement with the Field dependent susceptibility data, which shows a hysteretic characteristic.

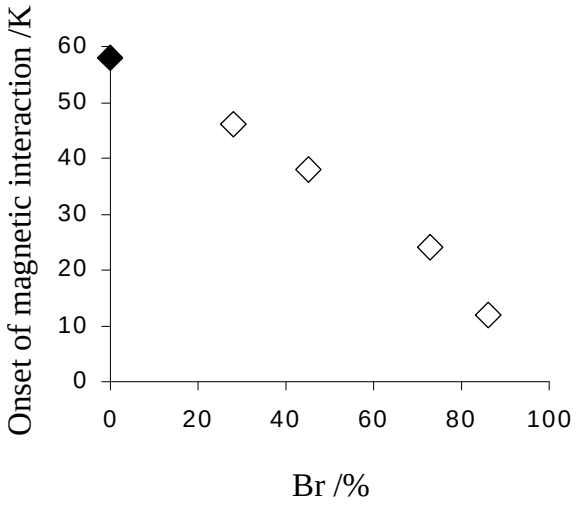

***Figure 9-29**: Dependence of the onset of cooperative magnetic coupling on the bromine concentration in mixed Br/electro sodalites. The data point corresponding to the filled black diamond was taken from the literature[20] and does not correspond to the Néel temperature, but to the onset of observable bulk antiferromagnetic coupling.*

The onset of the magnetic coupling depends on the average number of neighboring F-centers, which is linked to the overall F-center concentration. The exact interactions are rather complex, since each single F-center has a different temperature where the Néel condition is fulfilled. Still antiferromagnetic coupling does not have to occur at that given temperature if the corresponding condition is not fulfilled for a sufficient number of neighbors. Experimentally a dependence on the Br content is observed and presented in Figure 9-29.

10 Conclusion and Outlook

The purpose of this thesis was to investigate the magnetic phenomena found in mixed halide/electro sodalites, which in contrast to pure electro sodalites show a ferromagnetic instead of an antiferromagnetic transition. Within this work several ground breaking concepts were developed in order to be able to control the content of these mixed sodalite systems and it was shown that NMR is an ideal method to characterize these mixed halide sodalites.

The formation of mixed halide sodalites as well as mixed halide/basic sodalites systems was studied resulting in a growth model, which allows to predict halide incorporation during the synthesis based on two simple parameters: The selectivity factor, which describes the preference of the sodalite for a given intra-cage species and the separation factor as a measure for the occurrence of domain and phase separation due to incompatible space requirements of intra-cage species, when combined with each other in a mixed system.

The mixed halide sodalites synthesized have been proven to be a model system for the investigation of the dependence of the chemical shift on inter-ionic distances and thus valence-electron orbital overlap. While such relations were established here for the first time for ^{35}Cl, ^{81}Br and ^{127}I, in the case of ^{23}Na, the distance dependent chemical shift data could even be compared with computed ^{23}Na shieldings, resulting in excellent quantitative agreement.

While the knowledge gained on mixed halide sodalite was helpful in order to characterize mixed salt-bearing/salt-free sodalites, several new properties of these systems were discovered: Sodium in halide/hydro sodalites serves as an ideal NMR probe to directly determine the ratio of halide and hydro cages more precisely than the previously used indirect methods applying TGA or X-ray diffractometry. The vacant sodium sites in halide/dry sodalites are ordered in a way that no more than a single one is associated with an aluminum atom. The lattice constant of pure hydro sodalite is significantly smaller than in all of the mixed halide/hydro sodalite systems. The NMR investigation on mixed halide/hydro solid solutions show, that the latter effect has to be due to a cooperative phenomenon involving inter cage interactions resulting in a 15 kJ/mol lower energetic ground state of water molecules in pure hydro sodalite compared to the water molecules in mixed Br/hydro sodalites.

The temperature dependent NMR studies of these sodalites indicate an onset of ionic mobility at 550 K in mixed halide and halide/dry sodalites, while this temperature is lowered to only 400 K in water containing sodalites.

Finally a method of fully doping mixed halide/dry sodalites with sodium vapor was developed. The high concentration of about 10^{21} cages /cm^3 allows not only the observation of F-centers by NMR, but also to measure their interactions. Quantized resonance shifts were observed for ^{23}Na, ^{27}Al, ^{29}Si, ^{35}Cl, ^{81}Br and ^{127}I. The intensity distributions among the various resonances in the NMR spectra of framework atoms were found to be a good indication of the homogeneity of the sample, when compared to intensities of binomial distributions, based on the possible environments. The control of the F-center distribution allowed for the first time an assignment of the ^{23}Na resonances of doped sodalites. The identification of the sodium sites corresponding to the observed resonances thus allowed to experimentally measure the electron density distribution of an F-center. Halide NMR is another probe for the distribution of F-centers from the viewpoint of the cage center. While the intensity distributions are in perfect agreement with the data determined from framework NMR, the hyperfine shifts, when scaled properly, add the cage centers to the electron density map based on the sodium hyperfine shifts. In addition, the ratio in electron densities contributed by nearest (6-ring) and next nearest (4-ring) F-centers gives an estimate for the ratio of magnetic coupling between nn and nnn F-centers, which is not accessible otherwise.

Temperature dependent NMR of doped sodalites allowed the distinction between the contribution of magnetic interactions (Weiss temperature) and electrostatic interactions (electron-electron-repulsion) to the hyperfine shifts, indicating that both effects increase with decreasing cage diameter.

Finally the model developed could be tested on the low temperature bulk susceptibility of halide/electro sodalites, showing an F-center concentration dependent ferromagnetic transition below 50 K in contrast to the antiferromagnetic transition of pure sodium electro sodalite at 48 K. It could be shown, that all magnetic interactions in the sodalite are antiferromagnetic. Thus the resulting magnetic moments are due to frustrated spins, aligning with the external magnetic field. Based on the molecular field theory of magnetism, the concentration dependence of the Curie or rather Néel temperature can thus be conveniently explained as a result of the average number of neighboring F-centers.

The work presented has just pushed open the door of quasi “sodalite solid solution”, which allows to study interactions between nano-clusters of various materials, which are mediated by the framework and are otherwise not accessible. A more extensive VT characterization of mixed halide/electro sodalite systems, combined with the distribution based models presented in this these would offer the opportunity to quantitatively determine the magnetic coupling parameters in these systems. This issue is currently of high interest to theoretical chemists investigating the electronic structure of doped sodalites.

The study of similar potassium based systems should allow a deeper understanding of the ionic bonds, when compared to these sodium based systems. Furthermore an investigation of the properties of intra cage water in such sodalites can be expected to lead to a deeper understanding of the cooperative freezing found in pure sodium hydro sodalite.

Preliminary work by the author has shown that also potassium based mixed halide sodalites with random distribution of F-centers are accessible. The investigation of such K_4^{3+} F-centers, an comparison with the systems described here should allow to distinguish between electronic and cationic F-center properties.

11 Summary

The presented thesis was written in the context of an overall research project devoted to the creation of F-centers distributed throughout a sodalite lattice and to study the electrostatic and magnetic properties of interacting F-centers. As a material sodalite solid solution systems were chosen, since they allow for the variation of the inter-F-center distances as well as the overall F-center distribution. This was achieved by topotactic transformation of synthesized halide/basic sodalites via halide/hydro sodalites to halide/dry sodalites, where the dry cages can be transformed into F-centers by doping the material with sodium vapor. In order to be able to evaluate the data on halide/electro sodalites, it was necessary to control each step of the formation of these materials on the basis of a fundamental understanding of structural organization and dynamic properties. NMR proved to be an ideal tool to selectively study the environment and properties of each type of element occurring in these systems. With the exception of ^{16}O, all other framework and extra-framework atoms have excellent or good NMR nuclei (^{1}H, ^{23}Na, ^{27}Al, ^{29}Si, ^{35}Cl, ^{81}Br and ^{127}I). Thus, chemical shielding and quadrupolar coupling provide detailed information about the environment, while temperature dependent NMR even allows the observation of dynamic processes, like molecular motion or ion mobility.

In order to study the formation of sodalites with mixed extra-framework species, mixed halide sodalites as well as mixed basic/halide sodalites were synthesized. While the first systems show the tendency to incorporate the dominant halide species of the precursor solution over-proportionally, the latter systems generally prefer the incorporation of the halide over the basic extra framework species. Since only empirical synthesis procedures for these binary phases can be found in the literature, a growth model was developed describing the growth of these materials based on thermodynamic and kinetic considerations. The product of a sodalite synthesis can be predicted on the basis of the composition of the precursor gel and two parameters: the selectivity constant and the separation parameter. While the first one describes the kinetic effects during the formation of the crystallites resulting in the general preference of the species with the larger surface charge density ($H_3O_2^- < I^- < Br^- < Cl^-$), the latter parameter considers thermodynamic effects resulting from the strain on the framework due to the parallel accommodation of extra-framework species with different spatial requirements. While for species with similar sizes, perfect binomial distributions are expected, an increasing difference in size can lead from domain formation up to complete phase separation as it is

found in I/basic or Cl/I sodalites. On the other hand, almost perfect binomial distributions can be found in Cl/basic and Cl/BR sodalite solid solution systems. Due to Vegard's rule sodalite solid solution systems with binomial distribution and different lattice constant of their compositional endmembers can be well characterized by X-ray diffractometry, while NMR allows for detailed local structural characterization of all these sodalite phases. While a correlation between ^{27}Al or ^{29}Si chemical shifts and the average Al-O-Si bond angle has been known for over a decade, the fractional areas of the ^{23}Na NMR spectra were shown to be a suitable measure for the composition of any of these quasi binary systems. The onset of cationic mobility could also be detected by NMR at 550 K. In addition, the Na-Halide distance in mixed halide sodalites is related to the lattice constant with a high leverage. Thus these mixed sodalites serve as a model system to investigate distance dependent chemical shielding effects due to anion-cation overlap of sodium and halide nuclei without the application of high pressures or temperatures. Exponential relations between Na-halide distance and ^{23}Na chemical shielding were discovered and are in quantitative agreement with computed shieldings calculated on a Hartree-Fock based quantum mechanical model.

An exceptional feature of the sodalite as a matrix is the fact that some extra-framework species can be exchanged topotactically (without altering the framework), while others are immobile at room temperature. This allows the creation of mixed halide/hydro sodalites from mixed halide/basic sodalites. The most striking effect of these mixed halide/hydro sodalites is the violation of Vegard's rule by the pure hydro sodalite with its exceptionally small lattice constant. Water molecules in the known pure hydro sodalite are ordered at low temperature and become mobile only above room temperature. In mixed halide/hydro sodalite systems, the water molecules are already mobile around 200 K and are unable to freeze into a similar low-energy state, as they do in pure hydro sodalite. This effect is reflected in the lattice constants of these systems, which are highly temperature dependent and for hydro sodalite in the frozen state exceptionally low, compared to other water containing sodalite systems. The mobility of water in mixed Br/hydro sodalites also has an effect on the cation mobility, lowering its onset temperature by about 150 K. The extra-framework cation NMR spectra of mixed halide/hydro sodalites also serve as a convenient tool to determine the halide content easier, faster and more exactly than by conventional methods. These modified sodium sites are characterized by a chemical shift similar to aqueous sodium ions and slightly cage size dependent nuclear quadrupolar coupling constants.

The removal of water from mixed halide/hydro sodalites results in a large increase of the lattice constant due to the electrostatic repulsion of the extra framework cations, which, in this case are not screened by the water molecules. These materials show previously undetected

NMR resonances and an interesting type of disordering order. One out of three extra framework sodium sites is unoccupied since only three elemental charges per cage are necessary to compensate for the negative framework charge and no central anion exists in such cages. The vacant sodium sites order in a way that each aluminum atom has a maximum of one of its four sodium sites unoccupied. Due to the random occupation of cages by halide ions in these systems, however, no long range order is created, while in pure dry sodalites, the same microscopic order results in a macroscopic superstructure. The fundamental relation between the ^{27}Al chemical shift of aluminosilicates and the Al-O-Si bond angle is also valid in these systems, if the average chemical shift of all resonances, weighed by their fractional area is taken into account.

Halide/dry sodalites can be exposed to sodium vapor at elevated temperatures, allowing for incorporation of sodium atoms into the dry cages yielding Na_4^{3+} centers, with single paramagnetic electrons delocalized over the center of the cage and even beyond its boundaries. Although this effect has been known for some time, only the preparation of mixed halide/electro sodalite solid solution allows the investigation of interactions between these F-centers as well as between the F-centers and all other neighboring atoms. F-centers neighboring nuclei, observed by NMR give quantized paramagnetic hyperfine shift contributions to the undisturbed signals. The intensity distribution among these resonances allows an analysis of the distribution of F-centers and therefore halide ions throughout the lattice. All NMR nuclei also serve as probes for the paramagnetic electron density at their crystallographic site allowing to map the electron density distribution within the sodalite lattice on an experimental base.

Temperature dependent shift measurements allow the deconvolution of the electrostatic repulsion and the magnetic interactions between F-centers producing the magnetic coupling constants between neighboring and next nearest neighboring F-center electrons. The effects of lattice size on these parameters can also be observed. F-centers located in larger cages (as in most Br/electro sodalites compared to Cl/electro sodalites) interact less strongly with each other. This manifests in itself weather electrostatic repulsion as well as smaller average Weiss temperatures resulting from the magnetic coupling constants.

Finally, the bulk magnetic properties of mixed halide/electro sodalites deviate strongly from the antiferromagnetic behavior of pure sodium electro sodalite. Although all magnetic interactions are antiferromagnetic the overall magnetic behavior resembles that of a ferromagnet with Curie temperatures between 15 K and 45 K. The latter effect is due to frustrated spins, which occur in these systems of randomly distributed F-centers. Below the Néel temperature, the latter spins freeze into the antiferromagnetic domains, aligning rather

parallel, than antiparallel to the external magnetic field. Thus their magnetic moments add up, dominating the macroscopic magnetic moment of the sample to showing a temperature dependent magnetization characteristic similar to ferromagnets or superparamagnets.

12 Literature

1)Brogger, C.; Bockstrom, H. *Z. Kristallogr.* **1890**, 209.

2)Pauling, L. *Z. Kristallogr.* **1930**, *74*, 213.

3)Löns, J.; Schulz, H. *Acta Crystallogr.* **1967**, *23*, 434.

4)Johnson, G. M.; Weller, M. T. *Inorg. Chem.* **1999**, *38*, 2442-2450.

5)Breck, D. W. *Zeolite Molecular Sieves*; Wiley: New York, 1973.

6)Trill, H.; Eckert, H.; Srdanov, V. I. *J. Am. Chem. Soc.* **2002**, *124*, 8361 - 8370.

7)Bukin, V.; Makarov, Z. *Geochem. Int.* **1967**, *4*, 19 - 28.

8)Hassan, I.; Grundy, H. D. *Acta. Cryst.* **1983**, *c39*, 3-5.

9)Wiebke, M.; Engelhardt, G.; Felsche, J.; Kempa, P. B.; Sieger, P.; Schäfer, J.; Fischer, P. *J. Phys. Chem.* **1992**, *96*, 392-397.

10)Felsche, J.; Luger, S.; Bearlocher, C. *Zeolites* **1986**, *6*, 367.

11)Lugar, S.; Felsche, J. *Acta Crystallogr.* **1984**, *A40*, C116.

12)Engelhardt, G.; Felsche, J.; Sieger, P. *J. Am. Chem. Soc.* **1992**, *114*, 1173-1182.

13)Shannon, S. R.; Campell, B. J.; Metiu, H.; Blake, N. P. *J. Chem. Phys.* **2000**, *113*, 10215 - 10225.

14)Campbell, B. J.; Delgado, J. M.; Cheetham, A. K.; Iversen, B. B.; Blake, N. P.; Shannon, S. R.; Latturner, S.; Stucky, G. D. *J. Chem. Phys.* **2000**, *113*, 10226-10239.

15)Zhdanov, S. P.; Buntar, N. N.; Egorova, E. N. *Dokl. Akad. Nauk SSSR* **1964**, *154*, 419.

16)Faughnan, B.; Gorog, P.; Heyman, P.; Shidlovsky, J. *Advances in Image Pickup and Display*; Wiley: New York, 1981.

17)Barrer, R. M.; Cole, J. F. *J. Phys. Chem. Solids* **1968**, *29*, 1755-1758.

18)Hodgson, W. G.; Brinen, J. S.; Williams, E. F. *J. Chem. Phys.* **1967**, *47*, 3719-3723.

19)Engelhardt, G.; Feuerstein, M.; Sieger, P.; Markgraber, D.; Stucky, G.; Srdanov, V. *J. Chem. Soc. ,Chem. Commun.* **1996**, 729-730.

20)Srdanov, V. I.; Stucky, G. D.; Lippmaa, E.; Engelhardt, G. *Phys. Rev. Lett.* **1998**, *80*, 2449.

21)Sankey, O. F.; Demkov, A. A.; Lenosky, T. *Phys. Rev. B* **1998**, *57*, 15129-15139.

22)Blake, N. P.; Metiu, H. *J. Chem. Phys.* **1998**, *109*, 9977.

23)Windiks, R.; Sauer, J. *Phys. Chem. Chem. Phys.* **1999**, *1*, 4505-4513.

24)Windiks, R.; Sauer, J. *J. Chem. Phys.* **2000**, *113*, 5466-5476.

25)Mydosh, J. A. *Spin glasses : an experimental introduction*; Taylor & Francis: London ; Washington, DC, 1993.

26)Barrer, R. M.; Cole, J. F. *J. Chem. Soc (A)* **1970**, 1516 - 1523.

27)Weller, M. T.; Wong, G. *Eur. J. Solid State Inorg. Chem.* **1989**, *26*, 619-633.

28)Sieger, P. *1:1 Alumosilicat- und Alumogermanat- Sodalithverbindungen $[A_aX_xM_m]_2[Al_3(Si,Ge)_3O_{12}]_2$ mit salzartigen Gastkomplexen $A_aX_xM_m$*; Universität Konstanz: Konstanz, 1992, pp 139.

29)Stein, A.; Ozin, G. A.; Stucky, G. D. *J. Am. Chem. Soc.* **1992**, *114*, 8119-8129.

30)Samoson, A.; Lippmaa, E.; Pines, A. *Mol. Phys.* **1988**, *65*, 1013.

31)Wu, Y.; Sun, B.; Pines, A.; Samoson, A.; Lippmaa, E. *J. Magn. Reson.* **1990**, *89*, 297.

32)Mueller, K.; Baltisberger, J.; Wooten, E.; Pines, J. *J. Phys. Chem.* **1992**, *96*, 7001.

33)Frydman, L.; Harwood, J. S. *J. Am. Chem. Soc.* **1995**, *117*, 5367.

34)Slichter, C. P. *Principles of Magnetic Resonance*; 3 ed.; Springer-Verlag: Berlin, 1990.

35)Bloembergen, N. *Physica* **1950**, *16*, 95.

36)Bertini, I.; Luchinat, C. *NMR of Paramagnetic Molecules in Biological Systems*; Benjamin/Cummings Publ. Comp.:, 1986.

37)Knight, W. *Phys. Rev.* **1949**, *76*, 1259.

38)Abragam, A. *The Principles of Nuclear Magnetism*; Clarendon Press: Oxford, 1961.

39)Massiot, D.; Bessada, C.; Coutures, J. P.; Taulelle, F. *J. Magn. Reson.* **1990**, *90*, 231.

40)Maricq, M. M.; Waugh, J. S. *J. Chem. Phys.* **1979**, *70*, 3300.

41)Maricq, M. M.; Waugh, J. S. *Chem. Phys. Lett.* **1977**, *47*, 327.

42)Jakobsen, H.; Skibsted, J.; Bildsoe, H.; Nielsen, N. *J. Magn. Reson.* **1989**, *85*, 173 - 180.

43)Engelhardt, G.; Kentgens, A. P. M.; Koller, H.; Samoson, A. *Solid State Nucl. Magn. Reson.* **1999**, *15*, 171 - 180.

44)Man, P. *Phys. Rev. B* **1998**, *58*, 2764 - 2782.

45)Amoureux, J. P.; Fernandez, C.; Steuernagel, S. *J. Magn. Reson.* **1996**, *A 123*, 116.

46)Taylor, D. *Mineral. Mag.* **1972**, *36*, 593-604.

47)Hassan, I.; Grundy, H. D. *Acta Crystallogr.* **1984**, *B40*, 6-13.

48)Engelhardt, G.; Luger, S.; Buhl, J. C.; Felsche, J. *Zeolites* **1989**, *9*, 182-186.

49)Newsam, J. M. *J. Phys. Chem.* **1987**, *91*, 1259-1262.

50)Jacobsen, H. S.; Norby, P.; Bildsoe, H.; Jakobsen, H. J. *Zeolites* **1989**, *9*, 491-495.

51)VanderKlink, J. J.; Veeman, W. S.; Schmid, H. *J. Phys. Chem.* **1991**, *95*, 1508-1511.

52)Nielsen, N. C.; Bildsoe, H.; Jakobsen, H. J.; Norby, P. *Zeolites* **1991**, *11*, 622-632.

53)Jelinek, R.; Chmelka, B. F.; Stein, A.; Ozin, G. A. *J. Phys. Chem.* **1992**, *96*, 6744-6752.

54)Jelinek, R.; Stein, A.; Ozin, G. A. *J. Am. Chem. Soc.* **1993**, *115*, 2390-2396.

55)Stein, A.; Meszaros, M.; Macdonald, P. M.; Ozin, G. A.; Stucky, G. D. *Adv. Mater.* **1991**, *3*, 306-309.

56)Stein, A.; Ozin, G. A.; Macdonald, P. M.; Stucky, G. D.; Jelinek, R. *J. Am. Chem. Soc.* **1992**, *114*, 5171-5186.

57)Dann, S. E.; Weller, M. T. *Mater. Chem.* **1996**, *6*, 1717-1721.

58)Buhl, J. C.; Löns, J. *J. Alloys Comp.* **1996**, *235*, 41-47.

59)Engelhardt, G. *J. Am. Chem. Soc.* **1998**, 266 - 281.

60)Johnson, G. M.; Mead, P. J.; Dann, S. E.; Weller, M. T. *J. Phys. Chem. B* **2000**, *104*, 1454-1463.

61)Engelhardt, G.; Michel, D. *High Resolution Solid State NMR of Silicates and Zeolites*; John Wiley & Sons: Norwich, 1987.

62)Engelhardt, G.; Radeglia, R. *Chem. Phys. Lett.* **1984**, *108*, 271 - 274.

63)Engelhardt, G.; Veeman, W. J. *S. Chem. Soc. Chem. Commun.* **1993**, 622.

64)Weller, M. T.; Brenchley, M. E.; Apperley, D. C.; Davis, N. A. *Solid State Nucl. Magn. Reson.* **1994**, *3*, 103 - 106.

65)Depmeier, W. *Acta Crystallogr.* **1984**, *B40*, 185-191.

66)Brown, I. D.; Altermatt, D. *Acta Crystallogr.* **1985**, *B41*, 244-247.

67)Koller, H.; Engelhardt, G.; Kentgens, A.; Sauer, J. *J. Phys. Chem.* **1994**, *98*, 1544-1551.

68)Tossell, J. *Phys. Chem. Miner.* **1999**, *27*, 70 - 80.

69)Trill, H. *Sodalite Solid Solution System. Synthesis, Topotactic Transformations, an Investigation of Framewor-guest and Guest-guest Interactions*; PhD Thesis, Westfälische Wilhelms Universität: Münster, 2002.

70)Mason, J. *Multinuclear Nuclear Magnetic Resonance*; Plenum Press: New York, 1987.

71)Kondo, J.; Yamashita, J. *J. Phys. Chem. Solids* **1959**, *10*, 245.

72)Hafemeister, D.; Flygare, W. *J. Chem. Phys.* **1965**, *43*, 795 - 800.

73)Hafemeister, D. *J. Chem. Phys.* **1967**, *46*, 1929 - 1934.

74)Baron, R. *J. Phys. Chem.* **1963**, *38*, 173 - 187.

75)Ngai, L. *J. Phys. Chem. Solids* **1969**, *30*, 571 - 584.

76)Anderson, P. *Solid State Phys.* **1963**, *14*, 99.

77)Blake, N. P.; Metiu, H. *J. Chem. Phys.* **1999**, *110*, 7457-7466.

78)Heinmaa, I.; Vija, S.; Lippmaa, E. *Chem. Phys. Lett.* **2000**, *327*, 131-136.

79)Caballol, R.; Castell, O.; Illas, F.; Moreia, I. d.; Malrieu, J. *J. Phys. Chem. A* **1997**, *101*, 7860.

80)Smart, J. *Phys. Rev.* **1952**, *86*, 968 - 974.

81)Frisch, M. J.; Trucks, G. W.; Schlegel, H. B.; Scuseria, G. E.; Robb, M. A.; Cheeseman, J. R.; Zakrzewski, V. G.; Montgomery, J. A.; Stratmann, R. E.; Burant, J. C.; Dapprich, S.; Millam, J. M.; Daniels, A. D.; Kudin, K. N.; Strain, M. C.; Farkas, O.; Tomasi, J.; Barone, V.;

Cossi, M.; Cammi, R.; Mennucci, B.; Pomelli, C.; Adamo, C.; Clifford, S.; Ochterski, J.; Petersson, G. A.; Ayala, P. Y.; Cui, Q.; Morokuma, K.; Malick, D. K.; Rabuck, A. D.; Raghavachari, K.; Foresman, J. B.; Cioslowski, J.; Ortiz, J. V.; Baboul, A. G.; Stefanov, B. B.; Liu, G.; Liashenko, A.; Piskorz, P.; Komaromi, I.; Gomperts, R.; Martin, R. L.; Fox, D. J.; Keith, T.; M. A. Al-Laham; Peng, C. Y.; Nanayakkara, A.; Challacombe, M.; Gill, P. M. W.; Johnson, B.; Chen, W.; Wong, M. W.; Andres, J. L.; Gonzalez, C.; Head-Gordon, M.; Replogle, E. S.; Pople, J. A. *Gaussian98*; A.9 ed.; Gaussian Inc.: Pittsburg, PA, 2000.

82)Shannon, R. D. *Acta Crystallogr.* **1976**, *A32*, 751-767.

83)Engelhardt, G.; Sieger, P.; Felsche, J. *Anal. Chim. Acta* **1993**, *283*, 967-985.

84)Cocks, P.; Pope, C. *Zeolites* **1995**, *15*, 701 - 707.

85)Mundus, C.; Müller-Warmuth, W.; Buhl, J. C. *Eur. J. Mineral.* **1996**, *8*, 231-239.

86)Townes, C. H.; Dailey, B. T. *J. Chem. Phys.* **1949**, *17*, 782-796.

87)Jellison, G. H.; Panek, L. W.; Bray, J. P.; Rouse, G. B. *J. Chem. Phys.* **1977**, *66*, 802.

88)Vogel, C.; Wolff, R.; Radeglia, R. *Collect Czech Chem Com* **1993**, *58*, 1255 - 1268.

89)Takata, M.; Umeda, B.; Nishibori, E.; Sakata, M. *Nature* **1995**, *377*, 46 - 49.

90)Felsche, J.; Luger, S.; Fischer, P. *Acta Crystallogr.* **1987**, *C 43*, 809 - 811.

91)Ernst, H.; Pfeifer, H.; Zhdanov, S. P. *Zeolites* **1987**, *3*, 209 - 213.

92)Eiden-Assmann, S.; Schneider, A. M.; Behrens, P.; Engelhardt, G.; Mänder, H.; Felsche, J. *Eur. J. Inorg. Chem.* **2001**, 1527 - 1534.

93)Shannon, S. R.; Metiu, H. *J. Phys. Chem. B* **2001**, *105*, 3813 - 3822.

94)Schmidt-Rohr, R.; Spiess, H. W. *Multidimensional Solid State NMR and Polymeres*; Academic Press, Harcourt Brace&Company: London, 1994.

95)Srdanov, V. I.; Haug, K.; Metiu, H.; Stucky, G. D. *J. Phys. Chem.* **1992**, *96*, 9039-9043.

96)Madsen, G. K. H.; Gatti, C.; Iversen, B. B.; Damjanovic, L.; Stucky, G. D.; Srdanov, V. I. *Phys. Rev. B* **1999**, *59*, 12359 - 12369.

97)Blake, N. P.; Srdanov, V. I.; Stucky, G. D.; Metiu, H. *J. Chem. Phys.* **1996**, *104*, 8721-8729.

98)Kasai, P. H. *J. Chem. Phys.* **1965**, *43*, 3322-3327.

99)Smeulders, J. B. A. F.; Hefni, M. A.; Klaassen, A. A. K.; Boer, E. D.; Westphal, U.; Geimsar, G. *Zeolites* **1987**, *7*, 347-352.

100)McLaughlan, S. D.; Marshall, D. J. *Physics Letters* **1970**, *32A*, 343-344.

101)Breuer, R. E. H.; deBoer, E.; Geismar, G. *Zeolites* **1988**, *9*, 336.

102)Nakayama, H.; Klug, D. D.; Ratcliffe, C. I.; Ripmeester, J. A. *J. Am. Chem. Soc.* **1994**, *116*, 9777-9778.

Acknowledgements

I would like to thank Hellmut Eckert and Vojislav Srdanov for the opportunity to work on this very exciting transatlantic sodalite project, for providing financial funding and for their substantial scientific and emotional support.

Many thanks go to Rainer Pöttgen for the possibility to take advantage of a very fruitful cooperation and for valuable discussion.
I would like to thank Galen Stucky and his research group, especially Dan Bryan and Susan Latturner, for the possibility to come to Santa Barbara and for great support with the scientific as well as the non-scientific challenges during my times at UCSB.
I was happy to be introduced to the sodalite systems by Ljiljana Damjanovic, who allowed me to profit from her synthetic expertise in person and via many emails.
I am also very thankful to Jerry Hu and Jerry Chan for their effort of teaching me MQ MAS NMR in the initial stages of this project as well as for many valuable discussions. Also I would like to thank Jakob Kopp for his superb hardware support and many exciting discussions concerning the NMR Spectrometer.
For many valuable discussions and the introduction to Mößbauer Spectroscopy I would like to thank Bernd Mosel. I also appreciated the personal support and help with the TGA measurements by Karin Meise-Gresch and Wilma Pröbsting.
For support with the HT X-ray diffractometry and Rietveld analysis in Münster, I am thankful to Thomas Malcherek, Matthias Döch and Martin Valldor.
Special thanks go to Gunther Brunklaus and Wenzel Strojek for their introductions into the GAUSSIAN and SIMPSON simulation packages.
I would like to thank Christian Steif for buffering my interaction with bureaucracy and especially for the support during the acquisition of the Lindberg Blue furnace, leading to the majority of results presented in Chapter 9.

Finally, I was very happy to spend my time in the great environment of the Eckert Group in Münster including Paul Mutolo and Sophia Hayes from UCSB and all the fun people I have not mentioned so far.

Publications

1) Niepmann, D.; Pöttgen, R.; Poduska, K.; DiSalvo, F.; Trill, H.; Mosel, B.
Structure and properties of the stannides CeAuSn, $Ce_3Rh_4Sn_{13}$, and $Ce_3Ir_4Sn_{13}$
Z. Naturforsch, **2001**, *56b*, 1-8.

2) Mishra, R.; Pöttgen, R.; Hoffmann, R.; Trill, H.; Mosel, B.; Piotrowski, H.; Zumdick, M.
The Stannides RERhSn (RE = Ho-Yb) and ScTSn (T = Pd, Pt) - Structure Refinements and ^{119}Sn Mössbauer Spectroscopy.
Z. Naturforsch **2001**, *56b*, 589- 597

3) Trill, H.; Eckert, H.; Srdanov, V.
Halide NMR as a tool for structure characterisation
9. Jahrestagung der DGK 2001, Oldenbourg Verlag, München: Bayreuth, **2001**; p 112

4) Hoppe, H.; Trill, H.; Mosel, B.; Eckert, H.; Kotzyba, G.; Pöttgen, R.; Schnick, W.
Hyperfine interactions in the 13K ferromagnet $Eu_2Si_5N_8$.
J. Phys. Chem. Solids **2002** , 63, (5), 853 - 859

5) Johrendt, D.; Kotzyba, G.; Trill, H.; Mosel, B.; Eckert, H.; Fickenscher, T.; Pöttgen, R.
Magnetic and Electrical Properties, ^{151}Eu Mössbauer Spectroscopy, and Chemical Bonding of REAgMg (RE = La, Ce, Eu, Yb) and EuAuMg ,
J. Solid State Chem. **2002**, 164, (2), 201 - 209

6) Hoffmann, R.; Pöttgen, R.; Kußmann, D.; Niepmann, D.; Trill, H.; Mosel, B.
Transition Metal-Tin Ordering in SrPtSn, SrAuSn and BaAuSn and ^{119}Sn Mössbauer Spectroscopy of CaPdSn, CaPtSn and SrAuSn
Solid State Sci. **2002**, 4, (4), 481 - 487

7) Mishra, R.; Hoffmann, R.D.; Pöttgen, R.; Trill, H.; Mosel, B.
The Zintl Phase Eu_2Si
Z. Anorg. Allg. Chem. **2002**, 628, (4), 741 - 744

8) Tampier, M.; Johrendt, D.; Pöttgen, R.; Kotzyba, G.; Trill, H.; Mosel, B.
Magnetism and ^{151}Eu Mössbauer Spectra of α- and β-Eu_2GeS_4
Z. Anorg. Allg. Chem. **2002**, 628, (6), 1243 - 1245

9) Trill, H.; Srdanov, V.; Eckert, H.
Topotactic transformations of sodalite cages: Synthesis and NMR study of mixed salt-free and salt-bearing sodalites
J. Am. Chem. Soc. **2002**, 124 (28), 8361 - 8370

10) Trill, H.; Srdanov, V.; Eckert, H.
Mixed halide sodalite solid solution systems. Hydrothermal synthesis and structural characterization by solid state NMR
J. Phys. Chem., submitted.

11) Trill, H.; Srdanov, V.; Eckert, H.
Quantized contact interactions in a stochastic ensemble of F centers
Conference Proceedings, *Third international conference on Inorganic Materials*, Konstanz, **2002**

12) Pöttgen, R.; Wu, Z.; Hoffmann, R. D.; Kotzyba, G.; Trill, H.; Senker, J.; Johrendt, D.; Mosel, B.; Eckert, H.;
Intermetallic Lithium Compounds with Two- and Three-Dimensional Polyanions. Synthesis, Structure and Lithium Mobility.
Heteroatom Chemistry, **2002**, 13, (6), 506-513

13) Kranenberg, Ch.; Johrendt, D.; Mewis, A.; Pöttgen, R.; Kotzyba, G.; Trill, H.; Mosel,B.D.
New Compounds with the $ThCr_2Si_2$ Type Structure and the Electronic Structure of CaM_2Ge_2 (M = Mn–Zn).
J. Solid State Chem., in press

14) Bryan, D.; Iversen, B.; Trill, H.; Eckert, H.; Stucky, G.D.
Magnetic Properties of $Eu_4Ga_8Ge_{16}$
Chem. Mater. submitted

Table 6-I: Lattice constants, Na-Halide distances and NMR parameters of mixed halide sodalites:

a) mixed Cl/Br sodalites

				^{27}Al		^{23}Na				Halides			
Figure 5	Cl %	a_0 Å	Na-Hal Å	δ ppm	P_Q MHz	δ NaCl ppm	P_Q NaCl MHz	δ NaBr ppm	P_Q NaBr MHz	δ Cl ppm	P_Q Cl MHz	δ Br ppm	P_Q Br MHz
a	**0**	8.938	2.857	63.2	0.8			7.2	0.7			-220.6	0.7
b	**5**	8.936	2.852	63.3	0.7	3.0	0.2	7.2	0.6	-125.4	0.2	-220.8	0.3
c	**18**	8.932	2.842	63.5	0.8	3.3	0.2	7.5	0.6	-125.2	0.2	-220.5	0.4
b	**38**	8.921	2.813	63.7	0.8	4.0	0.2	8.4	0.6	-124.7	0.2	-219.4	0.4
e	**56**	8.913	2.793	63.9	0.8	4.2	0.2	9.1	0.6	-124.3	0.2	-218.6	0.4
f	**62**	8.910	2.786	64.1	0.9	4.8	0.3	9.3	0.6	-124.1	0.2	-218.3	0.4
g	**76**	8.904	2.771	64.2	0.9	5.1	0.3	9.8	0.6	-123.8	0.2	-217.7	0.3
h	**90**	8.898	2.756	64.4	0.9	5.4	0.3	10.2	0.6	-123.6	0.2	-217.3	0.3
i	**100**	8.893	2.745	64.4	0.7	6.1	0.5			-123.2	0.2		
error	± 3	± 0.001	± 0.004	± 0.2	± 0.1	± 0.2	± 0.1	± 0.3	± 0.1	± 0.2	± 0.1	± 0.4	± 0.2

b) mixed Br/I sodalites

				^{27}Al		^{23}Na				Halides			
Figure 6	Br %	a_0 Å	Na-Hal Å	δ ppm	P_Q MHz	δ NaBr ppm	P_Q NaBr MHz	δ NaI ppm	P_Q NaI MHz	δ Br ppm	P_Q Br MHz	δ I ppm	P_Q I MHz
a	**0**	9.012	3.073	61.2	0.6			7.3	1.8			-255.5	1.0
b	**6**	9.008	3.059	61.3	0.6	3.0	0.6	7.7	1.8	-226.4	0.7	-255.5	1.1
c	**25**	8.994	3.015	61.9	0.6	3.9	0.8	9.1	1.7	-225.0	1.0	-255.2	1.3
d	**46**	8.978	2.968	62.5	0.7	4.9	0.8	10.8	1.8	-223.7	0.9	-250.4	2.8
e	**65**	8.964	2.929	62.8	0.8	5.5	0.7	11.7	1.8	-223.0	0.8	-250.0	2.6
f	**77**	8.955	2.903	63.0	0.8	6.1	0.7	12.8	1.8	-222.1	0.8	-247.6	2.1
g	**86**	8.948	2.884	63.0	0.8	6.7	0.7	13.6	1.8	-222.0	0.3	-245.5	1.6
h	**91**	8.947	2.882	63.0	0.8	6.6	0.6	14.1	1.8	-221.6	0.4	-245.0	1.8
i	**100**	8.938	2.875	63.2	0.8	7.2	0.6			-220.6	0.7		
error	± 3	± 0.001	± 0.004	± 0.2	± 0.1	± 0.2	± 0.1	± 0.3	± 0.1	± 0.4	± 0.2	± 0.8	± 0.5

c) mixed Cl/I sodalites

				^{27}Al		^{23}Na				Halides			
Figure 7	Cl %	a_0 Å	Na-Hal Å	δ ppm	P_Q MHz	δ NaCl ppm	P_Q NaCl MHz	δ NaI ppm	P_Q NaI MHz	δ Cl ppm	P_Q Cl MHz	δ I ppm	P_Q I MHz
a	**0**	9.012	3.073	61.2	0.6			7.3	1.8			-255.5	1.0
b	**5**	9.007	3.056	61.4	0.7	-0.1	0.3	8.2	1.9	-128.2	0.2	-254.6	1.7
c	**6**	9.005	3.050	61.4	0.6	-0.4	0.5	8.4	1.7	-128.7	0.2	-254.4	1.5
d	**10**	9.001	3.037	61.6	0.7	-0.2	0.4	8.9	1.9	-128.4	0.2	-253.9	1.8
e	**22**	8.986	2.991	62.0	0.7	5.2	0.5	10.3	2.0	-124.1	0.2	-254.8	2.3
g	**90**	8.905	2.773	64.2	0.9	5.8	0.6	17.0	2.1	-12.8	0.2	-227.1	3.9
f	**89**	8.907	2.778	64.2	1.0	5.9	0.6	18.0	2.1	-123.7	0.2	-228.2	4.3
h	**97**	8.896	2.751	64.4	0.9	5.9	0.5	19.0	2.1	-123.4	0.2		
i	**100**	8.893	2.745	64.4	0.7	6.1	0.4			-123.2	0.2		
error	± 3	± 0.001	± 0.004	± 0.2	± 0.1	± 0.2	± 0.1	± 0.3	± 0.1	± 0.3	± 0.1	± 0.8	± 0.5

Table 6-II: ^{23}Na calculated shieldings in mixed halide sodalites as a function of the Na-halide distance for Na-O distances of 2.355 Å and 2.330 Å.

	Cell parameters		^{23}Na isotropic shieldings			
	a_0/Å	d Na-Hal /Å	Na-Cl /ppm	Na-Br /ppm	Na-I /ppm	Na-dry /ppm
Na-O = 2.355 Å	8.800	2.548	572.24	563.81	551.15	584.71
	8.850	2.656	575.14	568.07	559.54	584.76
	8.900	2.773	577.41	571.58	566.45	584.70
	8.950	2.902	579.34	574.56	572.03	584.60
	9.000	3.049	581.16	577.24	576.46	584.62
	9.050	3.220	582.98	579.81	579.90	584.85
	9.100	3.439	584.79	582.50	582.53	585.30
Na-O = 2.330 Å	8.800	2.602	572.28	564.59	553.54	583.10
	8.850	2.714	574.76	568.36	561.09	583.05
	8.900	2.836	576.87	571.52	567.25	582.92
	8.950	2.971	578.59	574.28	572.18	582.85
	9.000	3.127	580.36	576.83	576.04	582.95
	9.050	3.315	582.13	579.38	579.02	583.27
	9.100	3.575	583.90	582.15	581.32	583.81

Appendix III:

Table 7-I: Lattice constants and halide content of mixed halide/basic, halide/hydro and halide/dry sodalites

			Lattice constants /Å		
label	sample	Cl-fract	Cl/basic	Cl/hydro	Cl/dry
a)	h128	98	8.8806	8.8806	8.8806
b)	h258	87	8.882	8.897	8.961
	h260	73	8.884	8.883	
	h206	48	8.8858	8.922	
c)	h267	40	8.886	8.935	9.01
	h213	27	8.887	8.953	
d)	h268	16	8.888	8.979	9.062 (8)
e)	h227	0	8.8908	8.844	9.100 (15)

label	sample	Br-fract	Br/basic	Br/hydro	Br/dry
a)	H209	98	8.936	8.936	8.936
b)	H214	79	8.927	8.940	8.955
c)	H183	68	8.922	8.948	8.972
d)	H200	59	8.918	8.953	8.982
e)	H182	46	8.912	8.957	9.011
f)	H199	35	8.907	8.960	9.040 (6)
g)	H172	13	8.897	8.969	9.082 (7)

label	sample	I-fract	I/basic	I/hydro	I/dry
a)	h217	98	9.012	9.012	9.012
	h216	96	9.009		
	h266	95	9.006	9.009	
	h249	93	9.005		
	h265	87	8.994		
b)	h248	84	8.990	9.006	9.017
c)	h264	9	8.902	8.989	9.078 (8)
	h263	2	8.893		
error		± 3	± 0.002	± 0.002	± 0.004

Appendix IV:

Table 8-I-a: NMR parameters of mixed Cl/salt-free sodalites

δ_{iso}/ppm	Cl/basic	Cl/hydro		Cl/dry		
^{27}Al	site 1	site 1	site 2	site 1	site 2	site 3
a)	64.7	64.7		64.7		
b)	64.7	64.5		63.9		
c)	64.7	63.4		62.4		59.5
d)	64.6	62.1		61.4		59
e)	64.6	65.6				58.5
error	± 0.14	± 0.14		± 0.14		± 0.2
^{23}Na	Cl-cg	Cl-cg	basic-cg	Cl-cg	hydro-cg	dry-cg
a)	7	7	4.9	7	0	
b)	6.6	6	4.9	5.8	-0.1	10.7
c)	6	3.9	4.9	1.7	0	3.7
d)	6.1	2.9	4.8	-2.5	-0.3	1.1
e)			5		-0.1	
error	± 0.14	± 0.14		± 0.14	± 0.2	± 3
^{35}Cl	site 1	site 1		site 1		
a)	-123.2	-123.3		-123.3		
b)	-123.4	-124.1		-125.2		
c)	-123.3	-125.5		-129.8		
d)	-123.3	-126.7		-131		
error	± 0.2	± 0.2		± 0.2		

P_Q/MHz	Cl/basic	Cl/hydro		Cl/dry	
^{27}Al	site 1	site 1	site 2	site 1	site 3
a)	0.6	0.6		0.6	4.4
b)	0.6	0.7		2.1	4.4 (2)
c)	0.6	0.9		2	4.3 (3)
d)	0.6	1.5		2.1	
e)	0.6	2.2			
error	± 0.1	± 0.1		± 0.1	± 0.1
^{23}Na	Cl-cg	Cl-cg	hydro-cg	Cl-cg	dry-cg
a)	0.6	0.6		1.3	
b)	0.6	0.7	1.2	1.5	5.7 (3)
c)	0.7	0.7	1.6		5.8
d)	0.7	0.7	1.7		5.7
e)			1.1		
error	± 0.1	± 0.1	± 0.2	± 0.1	± 0.2
^{35}Cl	site 1	site 1		site 1	
a)	0.3	0.3		0.3	
b)	0.4	0.4		0.8	
c)	0.4	0.5		0.7	
d)	0.4	0.5		0.6	
error	± 0.1	± 0.1		± 0.2	

Table 8-I-b: NMR parameters of mixed Br/salt-free sodalites

δ_{iso}/ppm	Br/basic		Br/hydro		Br/dry	
^{27}Al	site 1		site 1	site 2	site 1	site 3
a)	63.4		63.4		63.4	
b)	63.5		63.4		63.0	
c)	63.7		63.2		63.0	59.5 (9)
d)	63.8		63.2		62.6	59.8 (6)
e)	63.9		63.0		62.5	59.1 (6)
f)	64.0		62.8		62.2	59.0 (5)
g)	64.3		62.4	62.4	61.5	58.0 (5)
h)	64.5			65.6	0	
error	± 0.14		± 0.14	± 0.2	± 0.14	± 0.2
^{23}Na	Br-cg	basic-cg	Br-cg	hydro-cg	Br-cg	dry-cg
a)	7.5		7.4		7.4	
b)	7.8	3.4	7.3	-0.2	6.2	4.3
c)	8	3.5	7.2	0	6	5.5
d)	8.3	3.7	6.9	0.1	4.7	5
e)	8.9	3.8	6.6	0	3.2	2.8
f)	9.1	3.9	6.7	-0.3	2.6	4.2
g)	10.2	4.6	6.4	-0.1	0.5	2.5
h)		5		-0.1		1.4
error	± 0.14		± 0.14	± 0.2	± 0.14	± 4
^{81}Br	site 1		site 1		site 1	
a)	-221.0		-221.0		-221.0	
b)	-220.8		-221.2		-222.4	
c)	-220.4		-221.8		-224.4	
d)	-219.9		-223.3		-226.4	
e)	-219.6		-225.4		-229.5	
f)	-219.2		-227.1		-233.3(3)	
g)	-218.0		-230.6(3)		-237.8(4)	
error	± 0.2		± 0.2		± 0.2	

P_Q/MHz	Br/basic		Br/hydro		Br/dry	
^{27}Al	site 1		site 1	site 2	site 1	site 3
a)	0.8		0.8		0.8	
b)	0.8		0.8		1.0	
c)	0.8		0.9		1.3	4.3 (3)
d)	0.8		0.9		1.3 (2)	4.4 (2)
e)	0.8		1		1.5 (2)	4.4
f)	0.8		1.2		1.5	4.4
g)	0.8		1.6	2.1	1.4 (2)	4.1 (2)
h)	0.8			2.2		
error	± 0.1		± 0.1	± 0.2	± 0.1	± 0.1
^{23}Na	Br-cg	basic-cg	Br-cg	hydro-cg	Br-cg	dry-cg
a)	0.7		0.7		0.7	
b)	0.6	0.7	0.7	1.5	1	5.4 (3)
c)	0.6	0.6	0.7	1.6	1.3	5.6 (3)
d)	0.6	0.6	0.7	1.6	1.3	5.5 (3)
e)	0.7	0.6	0.6	1.6	1.5	5.5
f)	0.7	0.6	0.6	1.6	1.6	5.6
g)	0.7	0.7	0.6	1.7	1.8	5.7
h)		0.8		1.1		5.8
error	± 0.1	± 0.2	± 0.1	± 0.2	± 0.1	± 0.2
^{81}Br	site 1		site 1		site 1	
a)	0.5		0.5		0.5 (1)	
b)	0.6		0.5		0.6 (1)	
c)	0.6		0.7		0.9	
d)	0.7		1.1		1.0	
e)	0.8		1.5		0.9 (3)	
f)	0.7		1.7 (2)		0.9	
g)	0.6		2.2 (2)		0.8	
error	± 0.1		± 0.1		± 0.2	

Appendix VI:

Table 8-I-c: NMR parameters of mixed I/salt-free sodalites

δ_{iso}/ppm	I/basic		I/hydro		I/dry	
^{27}Al	site 1		site 1	site 2	site 1	site 3
a)	61.4		61.4		61.2	
b)	61.5		61.4		61.2	59
c)	64.2		61.8		60.9	59
error	± 0.2		± 0.2		± 0.2	± 0.6
^{23}Na	Hal-cg	basic-cg	Hal-cg	hydro-cg	Hal-cg	dry-cg
a)	7.6		7.6		7.6	
b)	8.4	0	8.4	-0.8	6.7	8
c)	15.2(1.4)	4.6	9.3	-0.8		1
error	± 0.3	± 0.3	± 0.3	± 0.2	± 0.3	± 5
^{127}I	site 1		site 1		site 1	
a)	-217.5		-223.7		-236.9(3)	
b)	-218.8		-222.2		-228.4	
c)	-219.2		-221.6		-225.1	
error	± 0.3		± 0.3		± 0.6	

P_Q/MHz	I/basic		I/hydro		I/dry	
^{27}Al	site 1		site 1	site 2	site 1	site 3
a)	0.8		0.8		0.8	
b)	0.8		0.8		1	4.1
c)	0.8		2		1.6	4.2
error	± 0.1		± 0.1	± 0.2	± 0.1	± 0.1
^{23}Na	Hal-cg	basic-cg	Hal-cg	hydro-cg	Hal-cg	dry-cg
a)	1.8		1.8		1.8	
b)	1.9		1.8	1.8	5.3	5.3
c)	2	0.7	2.2	1.6		5.5
error	± 0.1	± 0.2	± 0.1	± 0.2	± 0.1	± 0.2
^{127}I	site 1		site 1		site 1	
a)	0.6		1.1 (1)		0.8	
b)	0.8		1.5		0.9	
c)	0.7		2.2		1	
error	± 0.1		± 0.3		± 0.2	

Appendix VII:

Table 9-I: Resonance shifts (ppm) of all peaks of the ^{27}Al, ^{23}Na, ^{35}Cl, ^{81}Br and ^{127}I NMR Spectra of mixed halide/electro sodalites. The peaks are assigned according to Chapter 9. All spectra where acquired in a magnetic field of 9.4 T.

Resonance shifs /ppm

^{27}Al peak	16 % Cl	40 % Cl	84 % Cl	28 % Br	54 % Br	73 % Br	9 % I	86 % I	error
0^0	65.2	64.6	64.8	64.4	64.0	63.9	62.5	62.0	0.2
0^1	72.9	72.6	72.7	71.5	71.3	71.8	70.4	70.4	0.3
0^2	79.4	79.5	80.2	77.9	78.1	79.3	76.8	78.2	0.3
0^3	85.2	85.4		83.9		85.8			0.3
1	98.3	99.4		98.2	96.3	96.8	94.3	96.5	0.8
2	119.6	118.1	115.2	116.3	115.0	116.9	115.2	117.7	0.6
3	130.6	131.1	130.8	129.3	128.0	131.0	128.0	130.9	0.4
4	138.7	140.3		138.1	136.6	140.1	136.9	139.3	0.2

^{23}Na peak	16 % Cl	40 % Cl	84 % Cl	28 % Br	54 % Br	73 % Br	9 % I	86 % I	error
C0	1.1	0.5	-0.7	0.4	-0.7	-0.8			0.2
0	7.4	7.6	6.7	6.1	8.1	8.0		8.6 (6)	0.2
B1		14.9	13.7						0.3
B2		19.0	18.3						0.3
B3		23.4	23.7						0.3
B4		28.6	29.9						0.3
B5	32.8	32.9	34.5						0.3
B6	35.5	36.1							0.3
B7	39.5	40.3							0.3
B8	43.1	43.9							0.3
B9	45.9	46.6							0.3
CA	64	63		68	67	70			2
A	101	98	96	121	120	127	156		1

Halide

NMR peak	16 % Cl	40 % Cl	84 % Cl	28 % Br	54 % Br	73 % Br	9 % I	86 % I	error
0^0	-120.0	-121.9	-123.9	-221.0	-218.3	-220.1	-263.4	-261.9	0.2
0^1			-116.2		-196.8	-197.9	-200.8	-206.7	0.3
0^2			-108.6		-175.6	-176.5	-145.5		0.3
0^3			-100.2		-153.6	-155.6			0.3
1	-98.2	-98.6	-96.3	-113.2	-136.6		-97.0	-97.5	1.5
2		-71.4	-75.0	-55.0	-80.2	-84.7	-10.0		1.0
3		-54.6	-53.3	-12.3	-28.3	-30.0			0.8
4		-40.1	-32.6	24.2	15.2	13.0			0.6
5	-29.3	-26.6		54.3	48.4	51.6			0.5
6	-15.2	-14.4		81.3	74.4	78.9			0.4
7	-2.9	-2.5		106.4	99.2				0.4
8	8.8	9.9		127.7	125.1		401 (1)		0.8

Appendix: VIII

Crystal Growth Simulation Program

```
#include <limits.h>
#include <stdio.h>
#include <stdlib.h>
#include <string.h>
#include <math.h>
#include <ctype.h>
#include <fstream.h>

void main()
{
int abbrcount,i,j,k,kr,kw,z,ps,c,lauf,konz;
float f,w,p,abbrbed;
/* Eingabe der Werte */

        printf("Groesse der Matrix :                                    ");
        scanf ("%i",&z);
        printf(" \n");



int cell[z+2][z+2][2];
float res[53][23];
float halcon[2];
float alcon[5][2];
float altheo[5][2];


/*Initial concentration of specis A, ps in promille (500 = 50%)*/

        ps=500;


/*sweep of separation factors*/

for(lauf=0;lauf<51;lauf++)
{

        f=(1-0.02*lauf);
        printf("f: %3.3f",f);
        kr=0;
        kw=1;
        abbrcount=0;

        /*creation of the initial matrix */

        for (i=1;i<z+2;i++)
        {
                for (j=1;j<z+2;j++)
                {
                        w=double(rand()%(1001));
                        cell[i][j][0]=0;
                        if(w<=ps)
                        {
                                cell[i][j][0]=1;
                        }

                }
        }

        /*computation of next matrix */

        for (k=1;abbrcount<10;k++)

        {

                /* Martix k*/
                halcon[kw]=0;
                for (i=1;i<z+1;i++)
                {
                        for (j=1;j<z+1;j++)
                        {
```

```
c=cell[i][j][kr]+cell[i][j+1][kr]+cell[i+1][j][kr]+cell[i+1][j+1][kr];
                        w=double(rand()%(100001));
                        p = 1000-(1000-ps)*pow((f),(c-2));
                        if (c<2)
                                {
                                p = ps*pow((f),(2-c));
                                }
                        cell[i][j][kw]=0;
                        if(w/100<p)
                        {
                        cell[i][j][kw]=1;
                        halcon[kw]=halcon[kw]++;
                        }
                }
        }
        halcon[kw]= halcon[kw]/(z*z);

                /* Introduction of periodic boundary conditions*/
                for (i=1;i<z+1;i++)
                        {
                        cell[z+1][i][kw]=cell[1][i][kw];
                        }
                for (i=1;i<z+1;i++)
                {
                        cell[i][z+1][kw]=cell[i][1][kw];
                }
                cell[z+1][z+1][kw]=cell[1][1][kw];

        /* Computation of aluminum environment*/
                for (i=0;i<5;i++)
                {
                alcon[i][kw]=0;
                }

                for (i=1;i<z+1;i++)
                {
                        for(j=1;j<z+1;j++)
                        {
                        c= cell[i][j][1] + cell[i][j+1][1] + cell[i][j+1][0] +
                        cell[i+1][j+1][0];
                        alcon[c][kw]=alcon[c][kw]+1;
                        c= cell[i+1][j][1] + cell[i+1][j+1][1] + cell[i][j][0] +
                        cell[i+1][j][0];
                                alcon[c][kw]=alcon[c][kw]+1;
                        }
                }

                for (i=0;i<5;i++)
                {
                alcon[i][kw]=alcon[i][kw]/(2*z*z);
                }

        /*abort condition*/
                abbrbed=(4*z*z);
                if(pow(100*(alcon[2][0]-alcon[2][1]),2)<10000/abbrbed)
                {
                abbrcount=abbrcount+1;
                }
        /*return jump*/
                kw=kw+1;
                kr=kr+1;
                if(kw>1)
                        {
                        kw=0;
                        }
                if(kr>1)
                        {
                        kr=0;
                        }
        }


/* Computation of binomial distribution*/
        altheo[0][kw]=pow((1-halcon[kw]),4);
        altheo[1][kw]=4*pow((1-halcon[kw]),3)*halcon[kw];
        altheo[2][kw]=6*pow((1-halcon[kw]),2)*pow(halcon[kw],2);
        altheo[3][kw]=4*(1-halcon[kw])*pow(halcon[kw],3);
        altheo[4][kw]=pow(halcon[kw],4);
```

```
        /*Results are tranferred into res */

        res[lauf][0]=k;
        res[lauf][1]=ps;
        res[lauf][2]=halcon[kw];
        res[lauf][3]=1-halcon[kw];
        res[lauf][4]=1-f;
        res[lauf][20]=0;
                for(i=0;i<5;i++)
                        {
                        res[lauf][5+i]=alcon[i][kw]*100;
                        res[lauf][10+i]=altheo[i][kw]*100;
                        res[lauf][15+i]=(-altheo[i][kw]+alcon[i][kw])*100;
                        res[lauf][20]=res[lauf][20]+pow(res[lauf][15+i],2);
                        }
        res[lauf][20]=pow(res[lauf][20],0.5);
        /* Datensausgabe Monitor*/
        printf("\n");
}


/*Saving procedure*/

        char* dat_name;
        dat_name="result.dat";


        ofstream to1(dat_name);
        for(j=0;j<51;j++)
        {
                for(i=0;i<21;i++)
                {
                to1<<res[j][i];
                to1<<" ";
                }
        to1<<j;
        to1<<endl;
        }
        to1.close();

}
}
```